

# **Determination of the beam asymmetry $\Sigma$ in $\eta$ - and $\eta'$ -photoproduction using Bayesian statistics**

**JAKOB MICHAEL KRAUSE**

Masterarbeit in Physik  
angefertigt im Helmholtz-Institut für Strahlen- und  
Kernphysik

vorgelegt der  
Mathematisch-Naturwissenschaftlichen Fakultät  
der  
Rheinischen Friedrich-Wilhelms-Universität  
Bonn

Sep 2022

I hereby declare that this thesis was formulated by myself and that no sources or tools other than those cited were used.

Bonn, .....  
Date .....  
Signature

1. Gutachterin: JUN. PROF. DR. ANNIKA THIEL
2. Gutachter: PROF. DR. JOCHEN DINGFELDER

# Acknowledgements

---

First of all I would like to thank ANNIKA THIEL for giving me the opportunity of being part of her research group since the beginning of my bachelor thesis in 2020. Now, with the formulation of this thesis, I will be finishing my academic career in Bonn. I greatly appreciate the insight into research I could gain.

I express my thanks to JOCHEN DINGFELDER who agreed to be the second referee for this thesis.

This thesis could not have been written without the help of FARAH AFZAL. After all, it was you, who recruited me again after my bachelor thesis. Over the past year we have shared our office and many fruitful discussions regarding physics (or not) were had. I am thankful that you and your masters and PhD thesis provided such excellent foundation for me to rely my work on.

Being the pioneer of the working group BECK/THIEL in all things regarding BAYESIAN statistics, PHILIPP KRÖNERT contributed the idea of what shall fill about half of this thesis and furthermore his help and guidance whenever i got stuck on the way. I am grateful that we were able to turn the thesis into this direction with your help.

Also, I express my gratitude to everybody who was included in the process of data taking, i.e. the CBELSA/TAPS collaboration and crew.

This thesis was written using the L<sup>A</sup>T<sub>E</sub>X-template ubonn-thesis which is kindly made available to the public by IAN BROCK.

I thank FARAH AFZAL, PHILIPP KRÖNERT, DOMINIC SCHÜCHTER and NIKOLAS PÄSSLER for reading my thesis and providing me with useful comments and insights.

Finally, I thank my parents, for the support throughout my whole studies, which now then officially come to an end.



# Contents

---

<b>1</b>	<b>Introduction</b>	<b>1</b>
1.1	Photoproduction of Pseudoscalar Mesons	4
1.2	Measurement of Polarization Observables	5
1.3	Introduction to BAYESIAN statistics	7
1.3.1	Notation	7
1.3.2	BAYES' theorem	8
1.3.3	MARKOV-Chain-Monte-Carlo (MCMC)	8
1.3.4	Diagnosing convergence of MARKOV-chains	10
1.3.5	Combining inferences	12
1.3.6	Posterior predictive checks	13
1.3.7	Example: Fitting data described by a $\cos(x)$ distribution	14
1.4	Current data situation	18
1.5	Motivation and Structure of this Thesis	18
<b>2</b>	<b>Experimental Setup</b>	<b>21</b>
2.1	Production of polarized high energy photon beam	22
2.1.1	Goniometer	23
2.1.2	Tagging system	23
2.2	Liquid hydrogen target	24
2.3	Detector system	25
2.3.1	Inner detector	25
2.3.2	Crystal Barrel and forward detector	26
2.3.3	MiniTAPS	27
2.3.4	ČERENKOV detector	28
2.3.5	Flux monitoring	28
2.4	Trigger	29
2.5	Software and Monte Carlo	29
2.5.1	ExPLORA	30
2.5.2	Monte Carlo	30
2.5.3	Stan	31
2.6	Datasets	31
<b>3</b>	<b>Event selection</b>	<b>33</b>
3.1	Reconstruction of events	34
3.2	Preselection and charge cut	34
3.3	Time of particles	35

3.4	Kinematic constraints . . . . .	37
3.4.1	Derivation of cut conditions . . . . .	37
3.4.2	Determination of cut ranges . . . . .	38
3.4.3	Quality of event selection . . . . .	43
3.5	Investigation of background and additional cuts . . . . .	45
3.5.1	Inspecting plausibility of background reactions . . . . .	45
3.5.2	Misidentification of background reactions . . . . .	48
3.5.3	Examination of additional cuts . . . . .	53
3.6	Summary of event selection . . . . .	56
3.6.1	Reaction $\gamma p \rightarrow p\eta' \rightarrow p\gamma\gamma$ . . . . .	56
3.6.2	Reaction $\gamma p \rightarrow p\eta \rightarrow p\gamma\gamma$ . . . . .	57
<b>4</b>	<b>Extraction of the beam asymmetries <math>\Sigma_\eta</math> and <math>\Sigma_{\eta'}</math></b>	<b>59</b>
4.1	Methods . . . . .	60
4.1.1	Event yield asymmetries . . . . .	60
4.1.2	Event based fit . . . . .	63
4.2	Determination of $\Sigma_\eta$ using Bayesian statistics . . . . .	66
4.2.1	Application of methods to toy Monte Carlo data . . . . .	66
4.2.2	Application of methods to data . . . . .	75
4.2.3	Discussion . . . . .	78
4.3	Determination of $\Sigma_{\eta'}$ . . . . .	81
4.3.1	Application of event based fit to toy Monte Carlo data . . . . .	81
4.3.2	Application of event based fit to data . . . . .	87
4.3.3	Systematic error . . . . .	89
<b>5</b>	<b>Discussion</b>	<b>95</b>
5.1	Comparison of results to existing data . . . . .	95
5.2	Comparison of results to PWA calculations . . . . .	97
5.3	Final discussion of methods . . . . .	98
<b>6</b>	<b>Summary</b>	<b>103</b>
<b>A</b>	<b>Illustration of used software tools</b>	<b>105</b>
A.1	ExPLORA . . . . .	105
A.2	Stan . . . . .	106
<b>B</b>	<b>Additional plots and calculations</b>	<b>107</b>
B.1	Statistical error for the asymmetry $A(\phi)$ . . . . .	107
B.2	Kinematic variables for each bin . . . . .	109
B.2.1	Coplanarity . . . . .	109
B.2.2	Polar angle difference . . . . .	111
B.2.3	Missing mass . . . . .	113
B.2.4	Invariant mass . . . . .	115
<b>C</b>	<b>Discussion of binned fits</b>	<b>117</b>

<b>D Investigation of posteriors without truncation</b>	<b>119</b>
<b>Bibliography</b>	<b>123</b>
<b>List of Figures</b>	<b>133</b>
<b>List of Tables</b>	<b>141</b>



# CHAPTER 1

---

## Introduction

---

The *Standard Model of Particle Physics* (SM) is the most successful model aiming to describe the particles and forces of the universe. It distinguishes between *fermions* and *bosons*. While all matter consists of fermions, bosons are particles that mediate the fundamental interactions.

Matter consists of (anti-)quarks and (anti-)leptons with three generations of each. Table 1.1 shows all elementary fermions including some of their most important properties. Only the first and lightest generation consists of stable particles, i.e. the up and down quark as well as the electron and its neutrino. All other particles are heavier and not stable, they will thus decay fast via the strong, electromagnetic or weak interaction.

There are in fact four interactions described by the SM: strong, electromagnetic, weak and gravitational interaction<sup>1</sup>, where gravitation is mentioned here for the sake of completeness; on the mass scale of elementary particles gravitation is negligible. Strong and weak interaction are restricted to a finite range of the order of the nucleon radius, whereas electromagnetic interaction and gravitation have infinite range. Each interaction has its own coupling (charge). The strong interaction is mediated by gluons and couples to the color charge.

	Generation			el. charge	color charge
	1	2	3		
<b>Quarks</b>	$u$	$c$	$t$	2/3	r,g,b
	$d$	$s$	$b$	1/3	r,g,b
<b>Leptons</b>	$e$	$\mu$	$\tau$	-1	-
	$\nu_e$	$\nu_\mu$	$\nu_\tau$	0	-

**Table 1.1:** Summary of the particles of the SM

Gluons and quarks carry color charge and thus interact strongly. However, an isolated quark or gluon has not been observed. Only color neutral bound systems of quarks are seen, which are called hadrons. Hadrons with integer spin are called mesons and those with half-integer spin are called baryons. Color neutrality demands mesons consist of at least one quark and one anti-quark and baryons consist of at least three quarks.

---

<sup>1</sup> They are ordered here according to their relative strength.

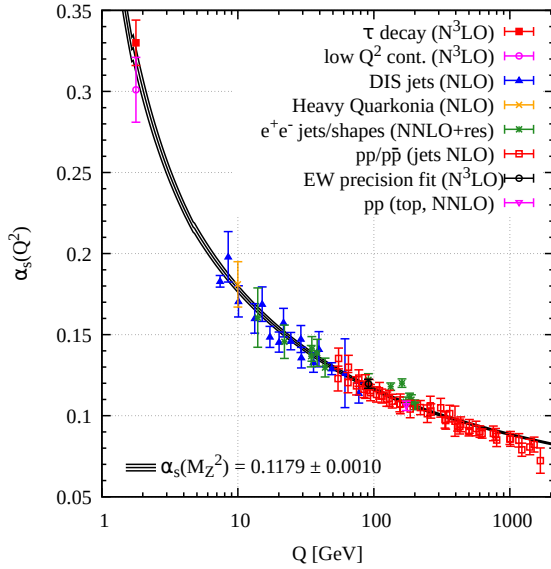


**Figure 1.1:** Running coupling of QCD depending on the momentum transfer  $Q$ . The colored data points represent different methods to obtain a value for  $\alpha_s$ . For a detailed review see [Wor+22].

As already mentioned, isolated quarks are not seen. This can be understood in terms of the strong coupling constant  $\alpha_s$ . The coupling constant is a measure of the strength of the strong interaction. Because it is highly dependent on the momentum transfer in the observed strong reaction it is also called running coupling constant, which is depicted in figure 1.1.

For low ( $< 1$  GeV) momentum transfers or large distances the coupling constant approaches infinity whereas it decreases for high ( $\gg 1$  GeV) momentum transfers or short distances. These momentum ranges are referred to as *confinement* and *asymptotic freedom*, respectively; quarks are confined to remain in a bound state since if one tried to pull them apart the color field becomes so strong it will create a new quark anti-quark pair resulting in two new bound states. On the other hand, bound quarks behave quasi-free and can be described using perturbative quantum chromodynamics (pQCD) if probed at sufficiently large momentum transfers.

It is more difficult however to describe QCD at momentum scales of  $\approx 1$  GeV since the coupling is too strong to justify a perturbative approach. Thus explicit modeling of QCD bound states is inevitable. One possibility is to describe baryons consisting of constituent quarks which are bound in a potential. Constituent quark models assume baryons are made up of three constituent quarks with effective masses differing from the bare quark mass. The effective mass is made up mostly from a sea of quark anti-quark pairs and gluons which surround the bare (valence) quarks. The explicit form of the binding potential is determined for each model.

The Bonn model [LMP01], for example, is formulated as a relativistically covariant constituent quark model. A potential increasing linearly with the distance is employed to adequately describe confinement. The binding potential between the constituent quarks is described by an instanton-induced interaction. Baryon resonances are then states with an orbital or angular excitation of one of the quarks. Figure 1.2 shows computed nucleon resonances with Isospin  $I = 1/2$  of the Bonn model [LMP01] on the left side of each column. These are compared to measured resonances and their PDG rating [Wor+22] in the middle. Uncertainties are indicated by the colored areas. The resonances are

identified by their total angular momentum and their parity  $J\pi$ . In addition also the total internal angular momentum along with isospin and again the total angular momentum  $L_{2T2J}$  is given. While

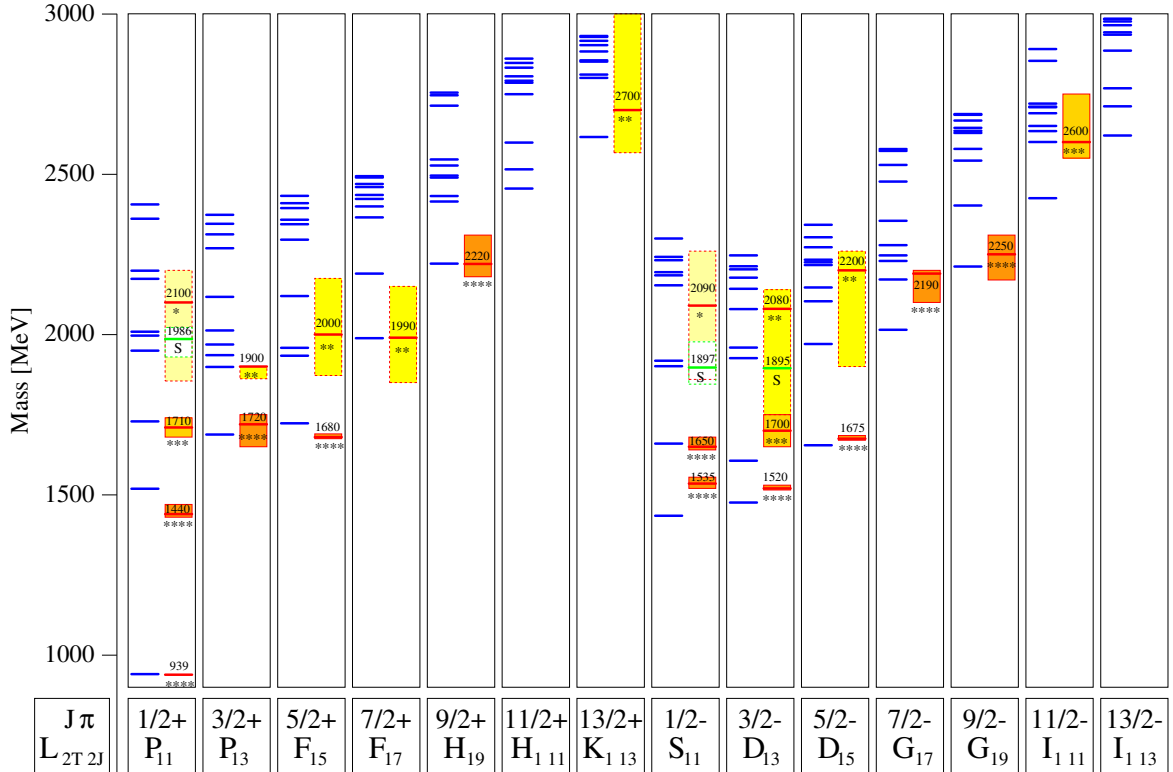


**Figure 1.2:** Calculated nucleon (isospin  $I = 1/2$ ) resonances compared to measurements. Left in each column are the calculations [LMP01], the middle shows the measurements and PDG rating [Wor+22]

generally good agreement exists for low lying resonances, especially for high masses there are much more resonances predicted than actually found. This is also known as the problem of the “missing resonances” indicating the poor understanding of QCD in the non-perturbative region. This can be due to several reasons: most of the knowledge about nucleon resonances and their properties was obtained investigating the  $\pi N$  channel, biasing the data for resonances coupling weakly to this channel [Met08]. Furthermore, the number of excited states with definite quantum numbers is related directly to the effective number of degrees-of-freedom accessible to the underlying theory [Wor+22]. As a consequence, the number of degrees-of-freedom should be obtainable by comparing the measured states to the predicted states. Since nucleon resonances decay dominantly hadronic, their resonances are broad and overlapping. Thus on one hand the determination of excitation spectra proves to be a challenge on its own, demanding sophisticated methods, such as partial wave analysis (PWA). On the other hand it is not yet clear how many effective degrees-of-freedom exist for the nucleon in a constituent quark model. They could for example be decreased if the nucleon were made up of a quark and a di-quark structure [Ans+93]. To access nucleon resonances and transitions between them for as many final states as possible the photoproduction of mesons off the proton has gained attention. Experiments dedicated to study photoproduction reactions off nucleons are located e.g. at JLAB, MAMI or ELSA. In this thesis photoproduction data taken at the CBELSA/TAPS experiment,

which is located at the accelerator ELSA in Bonn, is analyzed regarding the reactions  $\gamma p \rightarrow p\eta$  and  $\gamma p \rightarrow p\eta'$ . The theoretical foundation underlying the photoproduction of pseudoscalar mesons and the measurement of polarization observables will be discussed in the next sessions.

## 1.1 Photoproduction of Pseudoscalar Mesons

From the scattering theory point of view, photoproduction of mesons is well understood [KS03]. Figure 1.3 shows schematically the process thereof off the proton:

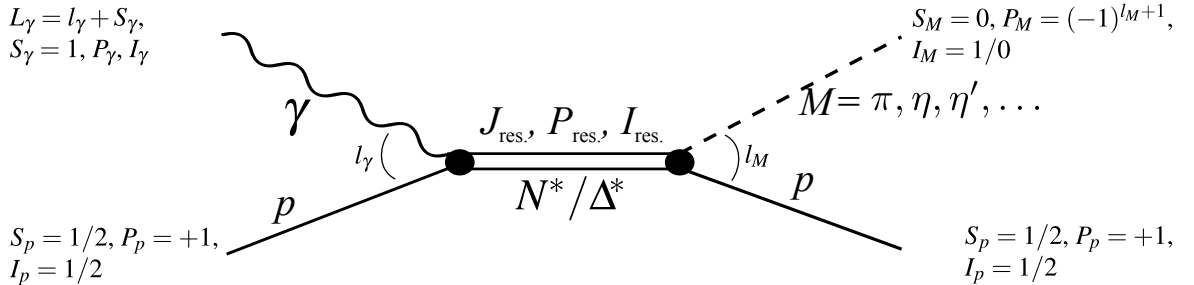


**Figure 1.3:** FEYNMAN diagram for the s-channel photoproduction of pseudoscalar mesons, adapted from [Afz19].

The analysis requires partial wave decomposition in both initial and final states [DT92] since the intermediate resonance  $N^*/\Delta^*$  has definite angular momentum, parity and isospin  $J_{\text{res.}}, P_{\text{res.}}, I_{\text{res.}}$ . The resonance is excited by a photon with (iso-) spin  $I_\gamma, S_\gamma = 1$  and parity  $P_\gamma$  coupling electromagnetically to the target proton with (iso-) spin  $I_p = 1/2, S_p = 1/2$  and parity  $P_p$ . The relative momentum is  $l_\gamma$ , such that the total momentum of the photon is  $L_\gamma = l_\gamma + S_\gamma$ . The parity of the photon depends on the multipolarity of the photon and is given by  $P_\gamma = (-1)^{L_\gamma}$  for electric ( $E$ ) or  $P_\gamma = (-1)^{L_\gamma+1}$  for magnetic ( $M$ ) photon multipoles [DT92]. Subsequently the intermediate state will have the quantum numbers  $J_{\text{res.}}, P_{\text{res.}}, I_{\text{res.}}$  and decay into a proton with spin  $S_p = 1/2$ , parity  $P_p = +1$  and isospin  $I_p = 1/2$  under emission of a meson. Here, only pseudoscalar mesons that have vanishing spin  $S_M = 0$ , isospin  $I_M$ , relative orbital angular momentum  $l_M$  und Parity  $P_M = (-1)^{l_M+1}$  are considered. Note that for  $\eta$  and  $\eta'$  mesons  $I_M = 0$ ; this exclusively limits the intermediate resonances to  $N^*$  states since the strong interaction conserves isospin [Wor+22]. The following selection rules can be derived using parity and momentum conservation [KS03; Afz19]

$$J_{\text{res.}} = L_\gamma \oplus S_p = L_\gamma \oplus 1/2, \quad (1.1)$$

$$P_{\text{res.}} = P_p \cdot P_\gamma = P_\gamma, \quad (1.2)$$

$$J_{\text{res.}} = l_M \oplus S_p = l_M \oplus 1/2 \quad (1.3)$$

$$P_{\text{res.}} = P_p \cdot P_M = (-1)^{l_M+1}, \quad (1.4)$$

where the usual rules for the coupling  $\oplus$  of angular momenta [Bar+18] apply. Thus, knowledge of the photoproduction multipoles allows the identification of contributing resonances for particular mesonic final states. Table 1.2 shows a summary of allowed quantum numbers according to the shown selection rules for the lowest order of photon multipoles ( $L_\gamma = 1$ ). The photoproduction

multipoles  $E_{l\pm}, M_{l\pm}$  indicate the relative momentum of the meson ( $l = l_M$ ) and whether the total angular momentum is obtained by adding “+” or subtracting “−” the final state momenta. Resonances are identified in spectroscopic notation by the meson momentum  $l_M$  as well as by their (iso-)spin  $I, J$  and Mass  $M$ . Note that only  $2I = 1$  resonances are listed since the mesons  $\eta$  and  $\eta'$  have vanishing isospin, so that only  $I = 1/2$  resonances ( $N^*$  resonances) may be accessed. The determination

Photon multipole	initial state $(L_\gamma^{P_\gamma}, S_p^{P_p})$	intermed. state $J_{\text{res}}^{P_{\text{res}}}$	final state $(S_p^{P_p}, l_M^{P_M})$	photoproduction multipole $E_{l\pm}, M_{l\pm}$	resonance $(l_M)_{2I2J}(M)$
$E1$	$\left(1^-, \frac{1}{2}^+\right)$	$\frac{1}{2}^-$	$\left(\frac{1}{2}^+, 0^-\right)$	$E_{0+}$	$S_{13}(M)$
$E1$	$\left(1^-, \frac{1}{2}^+\right)$	$\frac{3}{2}^-$	$\left(\frac{1}{2}^+, 2^-\right)$	$E_{2-}$	$D_{13}(M)$
$M1$	$\left(1^+, \frac{1}{2}^+\right)$	$\frac{1}{2}^+$	$\left(\frac{1}{2}^+, 1^+\right)$	$M_{1-}$	$P_{11}(M)$
$M1$	$\left(1^+, \frac{1}{2}^+\right)$	$\frac{3}{2}^+$	$\left(\frac{1}{2}^+, 1^+\right)$	$M_{1+}$	$P_{13}(M)$

**Table 1.2:** Allowed quantum numbers for the intermediate resonance state  $N^*$  in  $\eta/\eta'$ -photoproduction. Adapted from [Afz19].

of contributing multipoles which can then be used to identify nucleon resonances is challenging and requires sophisticated (model dependent) partial wave analyses (PWA). The measurement of polarization observables helps to eliminate ambiguities in PWA calculations as will be explained in the following section.

## 1.2 Measurement of Polarization Observables

Using an ansatz purely motivated by scattering theory, the differential cross section of meson photoproduction can be written as

$$\frac{d\sigma}{d\Omega} = \frac{q}{k} |\langle f | \mathcal{F} | i \rangle|^2, \quad (1.5)$$

where the matrix element is taken between initial and final PAULI spinors [Che+57] and  $q$  and  $k$  denote the momentum of the incident photon and final state meson, respectively. The photoproduction amplitude  $\mathcal{F}$  contains all relevant information regarding the scattering process connecting the initial and final state in analogy to the  $S$ -matrix that is introduced in the general discussion of quantum-mechanical scattering [PS95]. Following the notation of reference [Che+57] it can be written as a sum of the complex CHEW-GOLDBERGER-LOW-NAMBU (CGLN) amplitudes  $F_i$

$$\mathcal{F} = i(\vec{\sigma} \cdot \vec{\epsilon})F_1 + (\vec{\sigma} \cdot \hat{q})(\vec{\sigma} \cdot (\hat{k} \times \vec{\epsilon}))F_2 + i(\vec{\sigma} \cdot \hat{k})(\hat{q} \cdot \vec{\epsilon})F_3 + i(\vec{\sigma} \cdot \hat{q})(\hat{q} \cdot \vec{\epsilon})F_4, \quad (1.6)$$

where  $\hat{k}$  and  $\vec{\epsilon}$  are the momentum unit vector and polarization vector of the incident photon,  $\hat{q}$  is the momentum unit vector of the final state meson and  $\vec{\sigma}$  denote the PAULI matrices. Applying the method of partial waves onto the complex CGLN amplitudes  $F_i$  one can absorb the angular dependence into LEGENDRE polynomials  $P_l(\cos \theta)$  and derivatives thereof<sup>2</sup> and express the energy dependence solely

<sup>2</sup> Here,  $\cos \theta$  denotes the polar angle of the meson in the center of mass system.

by the photoproduction multipoles  $E_{l\pm}, M_{l\pm}$ , e.g. for  $F_1$  one finds[Che+57]

$$F_1 = \sum_{l=0}^{\infty} [lM_{l+}(W) + E_{l+}(W)] P'_{l+1}(\cos \theta) + [(l+1)M_{l-}(W) + E_{l-}(W)] P'_{l-1}(\cos \theta), \quad (1.7)$$

where  $W$  is the center of mass energy. Inserting the partial wave expansion of all CGLN amplitudes into Equation (1.5) directly connects the CGLN amplitudes and the photoproduction multipoles to the cross section which is a measurable quantity. However, the measurement of the differential cross section will give one real number which is not sufficient to unambiguously determine four complex amplitudes. To be able to access further observables that are connected to the CGLN amplitudes and the photoproduction multipoles, a polarized target and/or a polarized photon beam can be employed. In total, one may measure 16 non-redundant polarization observables [San+11] that are grouped into four categories: single polarization observables, where either the beam photon, target proton or recoil proton are polarized, and three groups of double polarization observables where two of the mentioned particles are polarized, i.e. the three groups are beam-target (BT), beam-recoil (BR) and target-recoil (TR) observables. In Table 1.3 all single and double polarization observables in pseudoscalar meson photoproduction are listed. In principle, eight carefully chosen observables allow an unambiguous determination of all CGLN amplitudes up to an overall phase [CT97], which are then referred to as a *complete experiment* [CT97; San+11]. However this academic environment does not account for measurement error [Wun18].

category	observables			
non /single	$\frac{d\sigma}{d\Omega}$	/	$\Sigma$	$T$
beam-target	$G$		$E$	$F$
beam-recoil	$O_{x'}$	$O_{z'}$	$C_{x'}$	$C_{z'}$
target-recoil	$T_{x'}$	$T_{z'}$	$L_{x'}$	$L_{z'}$

**Table 1.3:** All 16 non redundant polarization observables in pseudoscalar meson photoproduction [San+11]. Table adapted from [Afz12].

The CBELSA/TAPS experiment is able to produce a linearly or circularly polarized photon beam as well as a longitudinally or transversely polarized target. This introduces dependencies on the azimuthal angle into the differential cross section that couple to polarization observables  $\Sigma, T, P, E, F, G, H$  and the linear or circular polarization degrees of the photon beam  $p_\gamma^{\text{lin}}, p_\gamma^{\text{circ}}$  as well as the target polarization  $p_x, p_y, p_z$ [San+11]

$$\begin{aligned} \frac{d\sigma}{d\Omega} (E_\gamma, \theta, \varphi) &= \frac{d\sigma}{d\Omega} (E_\gamma, \theta) \left[ 1 - p_\gamma^{\text{lin}} \Sigma \cos(2\varphi) + p_x (p_\gamma^{\text{lin}} \mathbf{H} \sin(2\varphi) + p_\gamma^{\text{circ}} \mathbf{F}) \right. \\ &\quad \left. - p_\gamma (p_\gamma^{\text{lin}} \mathbf{P} \cos(2\varphi) - \mathbf{T}) - p_z (-p_\gamma^{\text{lin}} \mathbf{G} \sin(2\varphi) + p_\gamma^{\text{circ}} \mathbf{E}) \right]. \end{aligned} \quad (1.8)$$

In this thesis data was analyzed that was taken with a linearly polarized photon beam and an unpolarized target, so that (1.8) reduces to

$$\frac{d\sigma}{d\Omega} (E_\gamma, \theta, \varphi) = \frac{d\sigma}{d\Omega} (E_\gamma, \theta) \left[ 1 - p_\gamma^{\text{lin}} \Sigma \cos(2\varphi) \right], \quad (1.9)$$

which allows the determination of the beam asymmetry  $\Sigma$ , as is described in detail in chapter 4. The beam asymmetry can then be related to the CGLN amplitudes in order to enable the determination of photoproduction multipoles if it is multiplied by the unpolarized cross section [FTS92]

$$\widehat{\Sigma} = \Sigma \cdot \left( \frac{d\sigma}{d\Omega} \right)_0 \propto \frac{\sin^2(\theta)}{2} \Re \left[ |F_3|^2 + |F_4|^2 + 2 (F_1^* F_4 + F_2^* F_3 + \cos \theta F_3^* F_4) \right]. \quad (1.10)$$

Unlike the unpolarized cross section, the beam asymmetry, or rather polarization observables in general, is sensitive not only to the absolute values of the photoproduction multipoles squared but is also sensitive to interference terms thereof [Afz19; Wun+17]. Ultimately the photoproduction multipoles can be linked to resonance properties like mass  $M$  and width  $\Gamma$  using (model dependent) partial wave analyses that consider many observables in different final states at once. PWA calculations are also able to give predictions for polarization observables not yet measured. Expanding the database of polarization observables helps to further eliminate ambiguities in the photoproduction multipoles, which are used to identify contributing resonances, and thus adds to the understanding of the strong interaction in the non perturbative regime.

## 1.3 Introduction to BAYESIAN statistics

To determine the beam asymmetry (see Chapter 4) BAYESIAN methods are applied. This section will give a short introduction of the used concepts regarding BAYESIAN inference and the implementation of such a BAYESIAN analysis.

### 1.3.1 Notation

First of all, a probabilistic notation is introduced that will consequently be used throughout the remainder of this thesis to ease the formulation of BAYESIAN models and inferences. Hereby the BAYESIAN approach is directly applied to the context of parameter inference.

BAYESIAN parameter inference aims to draw statistical conclusions about parameters

$\boldsymbol{\theta} = \{\theta_1, \theta_2, \dots, \theta_N\}$  conditioned on observed data  $y$  in the form of probability statements [Gel+14]. The probability density of the introduced parameters  $\boldsymbol{\theta}$  given the observed data  $y$  is written as

$$p(\boldsymbol{\theta}|y). \quad (1.11)$$

Distributions that are not conditioned on other observables, i.e. marginal or prior distributions, are notated as e.g.

$$p(\boldsymbol{\theta}). \quad (1.12)$$

If a parameter  $\theta$  follows a well known probability density function (PDF) like a GAUSSIAN  $\mathcal{N}$  with mean  $\mu$  and standard deviation  $\sigma$  or Poisson distribution  $\mathcal{P}$  with mean  $\tilde{\mu}$  this is notated as

$$\theta \sim \mathcal{N}(\mu, \sigma) \quad \Leftrightarrow \quad p(\theta) = \mathcal{N}(\theta|\mu, \sigma) = \frac{1}{\sqrt{2\pi\sigma^2}} e^{-\frac{(\theta-\mu)^2}{2\sigma^2}}, \quad (1.13)$$

$$\tilde{\theta} \sim \mathcal{P}(\tilde{\mu}) \quad \Leftrightarrow \quad p(\tilde{\theta}) = \mathcal{P}(\tilde{\theta}|\tilde{\mu}) = \frac{\tilde{\mu}^{\tilde{\theta}}}{\tilde{\theta}!} e^{-\tilde{\mu}}. \quad (1.14)$$

### 1.3.2 BAYES' theorem

BAYES' theorem allows to link the conditional probabilities  $p(\boldsymbol{\theta}|y)$  and  $p(y|\boldsymbol{\theta})$  and can be formulated as [Gel+14]

$$p(\boldsymbol{\theta}|y) = \frac{p(y|\boldsymbol{\theta}) \cdot p(\boldsymbol{\theta})}{p(y)}. \quad (1.15)$$

In this context,  $p(y|\boldsymbol{\theta})$  is called the *likelihood* that the data  $y$  are described by the parameters  $\boldsymbol{\theta}$ . The second factor in the enumerator on the right hand side of Eq. (1.15) is called the *prior* of the parameters  $\boldsymbol{\theta}$ . It gives their probability density prior to acquiring any information from the model. The denominator  $p(y)$  is a normalizing constant, for which it holds

$$p(y) = \int_{\boldsymbol{\theta}} d\boldsymbol{\theta} p(y|\boldsymbol{\theta}) \cdot p(\boldsymbol{\theta}). \quad (1.16)$$

With increasing complexity of the investigated data and model, evaluating the integral (1.16) can become challenging, if not impossible. But since for a fixed dataset it is in fact only a normalizing constant, one can choose to not evaluate it to arrive at the unnormalized *posterior* on the left hand side of Eq. 1.15 and 1.17

$$p(\boldsymbol{\theta}|y) \propto p(y|\boldsymbol{\theta}) \cdot p(\boldsymbol{\theta}). \quad (1.17)$$

The posterior gives the probability density function of the parameters  $\boldsymbol{\theta}$  conditioned on the observed data  $y$ . For each parameter  $\theta_n \in \boldsymbol{\theta}$  a one dimensional marginal posterior can be determined by integrating out all other parameters [SS05]

$$p(\theta_n|y) = \int d\theta_1 \cdots \int d\theta_{n-1} \int d\theta_{n+1} \cdots \int d\theta_N p(\theta_1 \dots \theta_N|y). \quad (1.18)$$

Determining marginal posteriors is the main goal of a BAYESIAN parameter inference. They give probability densities for each individual parameter based on the observed data and are the equivalent to point estimates with error bars that are e.g. determined from a  $\chi^2$  parameter fit but at the same time yield full distributions as a result. The determination of marginal posteriors with the ansatz formulated in Eq. 1.18 can become a highly non-trivial task using analytical methods with increasing number of parameters and complexity of the investigated model, so that the use of Monte-Carlo sampling is a suitable approach.

### 1.3.3 MARKOV-Chain-Monte-Carlo (MCMC)

Consider using Eq. (1.17) to determine unnormalized marginal posteriors for all parameters  $\boldsymbol{\theta}$  without explicitly carrying out the integrations (1.18). This can be achieved by approximating the multidimensional joint unnormalized posterior  $p(\boldsymbol{\theta}|y)$  using a large number of simulation draws  $\boldsymbol{\theta}^{(s)}$  and projecting out each parameter  $\theta_n$  while ignoring all other parameters  $\theta_{k \neq n}$  [Tro08]. Thus, to perform a parameter inference, the main task is to accomplish the drawing of samples  $\boldsymbol{\theta}^{(s)}$  that follow the joint posterior in order to access the marginal posteriors.

MARKOV chains are a finite sequence of random variables  $\boldsymbol{\theta}^1, \boldsymbol{\theta}^2 \dots \boldsymbol{\theta}^S$  where for each step  $t$  the quantity  $\boldsymbol{\theta}^t$  only depends on the previous  $\boldsymbol{\theta}^{t-1}$  and is independent of all other previous chain elements [Gel+14]. Such a chain is created by starting at some initial value  $\boldsymbol{\theta}^0$  and generate new draws from a transition distribution  $T_t(\boldsymbol{\theta}^t|\boldsymbol{\theta}^{t-1})$ . The transition probabilities  $T_t$  can be constructed such that the

MARKOV chain reaches a stationary distribution which is the desired joint posterior (1.17) [Gel+14; Nor97]. A variety of algorithms exist to ensure the convergence of MARKOV chains.

### METROPOLIS-HASTINGS algorithm

A first approach is the METROPOLIS-HASTINGS algorithm [Met+53; Has70]. Here, at step  $t$  in the chain random proposals  $\theta^*$  are drawn from the transition distribution  $T_t(\theta^*|\theta)$ . To proceed in the algorithm, the ratio of posteriors

$$r = \frac{p(\theta^*|y) \cdot T_t(\theta^{t-1}|\theta^*)}{p(\theta^{t-1}|y) \cdot T_t(\theta^*|\theta^{t-1})} \quad (1.19)$$

is considered. If the new proposal  $\theta^*$  increases the posterior density, i.e.  $r > 0$ , it is accepted with probability 1, such that  $\theta^t = \theta^*$ . In the case  $r < 0$  the update  $\theta^t = \theta^*$  is only accepted with probability  $r$  and otherwise discarded so that  $\theta^t = \theta^{t-1}$  [Gel+14]. The METROPOLIS-Hastings algorithm exhibits the behavior of a random walk in the parameter space [Gel+14]. Figure 1.4 shows an example of five independent MARKOV-chains generated with the described algorithm for a two dimensional parameter  $\theta$  with a bivariate normal distribution as posterior  $\theta \sim \mathcal{N}(0, \mathbb{1}_2)$  at different stages in the simulation [Gel+14]. It is evident that MARKOV chains require a “burn-in” period before the simulation draws are a valid approximation of the target distribution that has to be chosen in the context of the applied model [Gel+14].

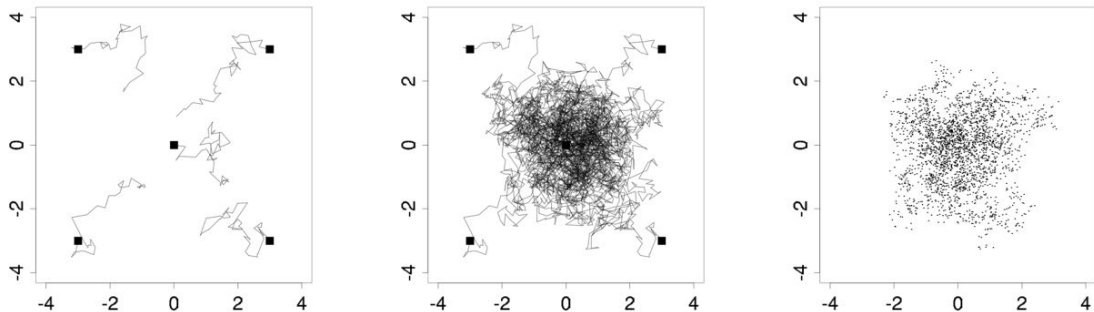


**Figure 1.4:** Five different MCMC simulations for a bivariate normal distribution, with starting points marked by black squares. Left: After 50 iterations no convergence is yet to be seen. Middle: After 1000 iterations the chains are closer to convergence. Right: Removing the first halve of simulation draws leaves a set of draws from the target distribution. Taken from [Gel+14]

### HAMILTONIAN Monte-Carlo (HMC) and No-U-Turn-Sampling (NUTS)

The random walk behavior of the METROPOLIS-HASTINGS algorithm can make computation of complex models very inefficient [Gel+14], therefore more sophisticated methods have been developed. HAMILTONIAN Monte-Carlo (HMC) [Dua+87] is an elaborate algorithm that allows to explore the parameter space much more efficient than a simple random walk. It will be described qualitatively in the following, for a detailed discussion see e.g. reference [Gel+14].

At the heart of the HMC algorithm lies an accept-reject step that is similar to the METROPOLIS-HASTINGS algorithm. To arrive at new proposals  $\theta^*$  at step  $t$  in the chain however an additional auxiliary variable  $\phi$  is introduced that has the same dimension as the parameters  $\theta$  but is independent of  $\theta$  and the data  $y$ . Introducing the new parameters leads to the joint posterior [Sta22a]

$$\begin{aligned} p(\theta, \phi|y) &= p(\theta|y) \cdot p(\phi|\theta, y) = p(\theta|y) \cdot p(\phi) \\ \Leftrightarrow -\log p(\theta, \phi|y) &= -\log p(\theta|y) - \log p(\phi) \\ \stackrel{\text{Def.}}{\Leftrightarrow} H(\theta, \phi) &:= V(\theta) + T(\phi), \end{aligned} \quad (1.20)$$

where in the last step the artificial HAMILTONIAN  $H$  has been introduced as a sum of kinetic energy  $T$  and potential  $V$ . Usually, one chooses  $p(\phi)$  to be a multivariate normal centered at 0 with covariance matrix  $M$  [Gel+14]. Applying the well known equations of motion to this HAMILTONIAN one finds

$$\frac{d\theta_i}{dt} = \frac{\partial H}{\partial \phi_i} = \frac{\partial T}{\partial \phi_i} \quad \frac{d\phi_i}{dt} = -\frac{\partial H}{\partial \theta_i} = -\frac{\partial V}{\partial \theta_i}. \quad (1.21)$$

This allows the simultaneous direct numerical integration to evolve “position” and “momentum” in  $L \cdot \epsilon$  discrete time steps with the so-called *Leap-Frog* algorithm [KN98]. Consequently  $L$  is called the number of Leap-Frog steps and  $\epsilon$  is the scale on which the time is discretized. After performing  $L$  Leap-Frog steps a proposal  $(\theta^*, \phi^*)$  is fed into a METROPOLIS-HASTINGS accept-reject step that is then used to update the current parameter value in the MARKOV chain at position  $t$ . The auxiliary momentum is discarded because it is drawn anew at the next iteration from its posterior distribution  $p(\phi)$ . When tuned right, the HMC algorithm allows for a rapid exploration of the parameter space [Gel+14]. An extension of HMC that adaptively determines the number of Leap-Frog steps, the step size  $\epsilon$  and covariance matrix  $M$  is given by the No-U-Turn-Sampler (NUTS) [HG14]. The number of Leap-Frog steps  $L$  is determined individually for each chain iteration  $t$ ; as soon as the distance between the original set  $(\theta^{(t-1)}, \phi^{(t-1)})$  and the proposals  $(\theta^*, \phi^*)$  decreases (i.e. the trajectory makes a U-Turn in parameter space) the Leap-Frog integrator is stopped. The step size  $\epsilon$  and covariance matrix  $M$  are determined during the warm-up phase and then kept fixed for all iterations that are saved for posterior inference [Gel+14].

### 1.3.4 Diagnosing convergence of MARKOV-chains

In order to quantitatively monitor the convergence of a MARKOV chain, there exist several diagnostic tools. Two of them will be introduced in the following.

#### Potential scale reduction statistic $\widehat{R}$

One way to monitor the convergence of a MARKOV chain towards its equilibrium distribution is to compare its performance to several other independent MARKOV chains [Sta22a]. Motivated by this GELMAN and RUBIN introduced the potential scale reduction statistic,  $\widehat{R}$  [GR92]. It measures the ratio of average variance of the samples within each chain to the variance of the pooled samples across all chains [Sta22a]. If all chains have reached their stationary distribution this ratio will be one and otherwise greater than one [Sta22a]. In practice one should tune the number of samples so that  $R \lesssim 1.01$  [Veh+19].

The  $\widehat{R}$ -statistic is defined for a set of  $M$  MARKOV chains  $\theta_m$  with  $N$  samples  $\theta_m^{(n)}$ . The *between-chain-variance*  $B$  is estimated as

$$B = \frac{N}{M-1} \sum_{m=1}^M \left( \bar{\theta}_m^{(\bullet)} - \bar{\theta}_{\bullet}^{(\bullet)} \right)^2, \quad (1.22)$$

where

$$\bar{\theta}_m^{(\bullet)} = \frac{1}{N} \sum_{n=1}^N \theta_m^{(n)}, \quad \bar{\theta}_{\bullet}^{(\bullet)} = \frac{1}{M} \sum_{m=1}^M \bar{\theta}_m^{(\bullet)}. \quad (1.23)$$

Further the *within-chain variance*  $W$  is averaged over all chains

$$W = \frac{1}{M} \sum_{m=1}^M s_m^2, \quad (1.24)$$

where

$$s_m^2 = \frac{1}{N-1} \sum_{n=1}^N \left( \theta_m^{(n)} - \bar{\theta}_m^{(\bullet)} \right)^2. \quad (1.25)$$

Combining the between and within chain variances into the *variance estimator*

$$\widehat{\text{var}}^+(\boldsymbol{\theta}|y) = \frac{N-1}{N} W + \frac{1}{N} B \quad (1.26)$$

one finally arrives at the *potential scale reduction statistic*

$$\widehat{R} = \sqrt{\frac{\widehat{\text{var}}^+(\boldsymbol{\theta}|y)}{W}}. \quad (1.27)$$

The previous definitions and equations can be found in a similar fashion in [Sta22a]. Advanced optimizations to the  $\widehat{R}$  statistic include the splitting of all  $M$  chains into two parts (split- $\widehat{R}$ ) to provide an additional means for detecting non-stationarity [Sta22a] and rank normalization [Veh+19].

### Monte-Carlo Standard Error (MCSE)

Given  $S$  independent simulation draws from a given MARKOV chain  $\boldsymbol{\theta}^{(s)}$  one can estimate the accuracy of the mean obtained from the posterior distribution for each parameter  $\theta_n$  as the so called *Monte-Carlo standard error* (MCSE)

$$\text{MCSE}_{\theta_n} = \frac{\text{std}(p(\theta_n|y))}{S} = \frac{\text{std}(\theta_n^{(s)})}{S}, \quad (1.28)$$

where  $\text{std}(x)$  is the standard deviation of the set  $x$ . As the mean can be sensitive to few extreme outliers of the posterior distribution, the median of the posterior may provide a better statistic to summarize a parameter inference. VETAHRI ET AL. [Veh+19] propose the following method to determine a MCSE estimate for any  $\alpha$ -quantile for a single parameter  $\theta_n$ :

1. Compute  $a$  and  $b$  as the 16% and 84% quantile of

$$B(S\alpha + 1, S(\alpha - 1) + 1), \quad (1.29)$$

where  $B(v, w) = \int_0^1 dt t^{v-1} (1-t)^{w-1}$  is the Beta-function [AS72].

2. Determine  $A$  and  $B$  as the corresponding quantiles on the original scale of draws

$$A = \theta_n^{(s')} \text{ where } s' \leq Sa < s' + 1 \quad (1.30)$$

$$B = \theta_n^{(s'')} \text{ where } s'' - 1 < Sb \leq s'', \quad (1.31)$$

where the samples  $\theta_n^{(s)}$  have been sorted in ascending order.

3. Compute the MCSE estimate of the  $\alpha$ -quantile as

$$\text{MCSE}_\alpha = \frac{B - A}{2} \quad (1.32)$$

For the remainder of this thesis the MCSE will refer to  $\text{MCSE}_{\alpha=0.5}$ . Note that the MCSE is only then a sensible quantity when it is compared to the magnitude of e.g. the mean or the median of the posterior draws. Therefore one can define the *relative MCSE* of any posterior  $p(\theta_n|y)$  as

$$\text{rel. MCSE} = \frac{\text{MCSE}}{\text{median}(p(\theta_n|y))}. \quad (1.33)$$

Each MARKOV chain element  $\theta^t$  depends on its predecessor  $\theta^{t-1}$ . However the element  $\theta^{t-1}$  is derived from  $\theta^{t-2}$  and so on. This means that the elements of the constructed chain are not completely uncorrelated, which is called *autocorrelation* [Gel+14]. In all above equations  $S$  was always specified as the number of *independent* draws from a single chain which is referred to as the *effective sample size* (ESS) in the literature [Gel+14; Veh+19]. Because of autocorrelation the effective sample size does not necessarily equal the total number of posterior draws. Determining the autocorrelation allows in turn to determine the ESS from the posterior samples using fast FOURIER transformations [Gey92; Gey11]. A detailed description thereof can be found in references [Sta22a; Gel+14].

### 1.3.5 Combining inferences

If there are several independent parameter inferences, i.e. posteriors  $p_1(\theta|y^{(1)}), p_2(\theta|y^{(2)}), \dots$ , there are several ways to combine the information from all posteriors into a single posterior distribution. The simplest approach is to combine the draws from all posteriors, effectively just increasing the sample size, and histogram them at once. This is the mathematical equivalent of summing all posteriors with equal weight [Sto61]

$$p(\theta|y) = \sum_{i=1}^N p\left(\theta|y^{(i)}\right). \quad (1.34)$$

The resulting distribution will represent the information from all posteriors and allows to evaluate the performance of a probabilistic model that is applied to several datasets when compared with according

expectations. Suppose the combined posterior  $p(\boldsymbol{\theta}|y)$  results in an unimodal GAUSSIAN, then the mean and standard deviation will represent a combined estimate of all posteriors that can be used to summarize the results of all posteriors.

An alternative way of combining probabilistic information is the so called *independent likelihood pool* [MD94] which is a fully BAYESIAN approach. Consider the combined posterior

$$p(\boldsymbol{\theta}|y^{(1)}, y^{(2)}, \dots, y^{(N)}) = \frac{p(y^{(1)}, y^{(2)}, \dots, y^{(N)}|\boldsymbol{\theta}) \cdot p(\boldsymbol{\theta})}{p(y^{(1)}, y^{(2)}, \dots, y^{(N)})}, \quad (1.35)$$

where BAYES' theorem has been applied to write the posterior as product of likelihood and prior. Since the datasets  $y^{(i)}$  are assumed independent we can write

$$p(\boldsymbol{\theta}|y^{(1)}, y^{(2)}, \dots, y^{(N)}) = \frac{\prod_{i=1}^N p(y^{(i)}|\boldsymbol{\theta}) \cdot p(\boldsymbol{\theta})}{p(y^{(1)}, y^{(2)}, \dots, y^{(N)})}, \quad (1.36)$$

and, applying BAYES' theorem once more

$$p(\boldsymbol{\theta}|y^{(1)}, y^{(2)}, \dots, y^{(N)}) = \frac{\prod_{i=1}^N p(y^{(i)})}{p(y^{(1)}, y^{(2)}, \dots, y^{(N)})} \cdot \frac{\prod_{i=1}^N p(\boldsymbol{\theta}|y^{(i)})}{p(\boldsymbol{\theta})^{N-1}} \quad (1.37)$$

$$\Rightarrow p(\boldsymbol{\theta}|y^{(1)}, y^{(2)}, \dots, y^{(N)}) \propto \frac{\prod_{i=1}^N p(\boldsymbol{\theta}|y^{(i)})}{p(\boldsymbol{\theta})^{N-1}}. \quad (1.38)$$

The above calculations can be found in a similar fashion in [BS10]. To summarize, the combined posterior can be written as a product of the individual posteriors normalized by the chosen prior. This method of combination is particularly useful when the datasets  $y^{(i)}$  are generated data that follow a particular function with known parameters. The combined posterior in a pooled likelihood model allows to evaluate at one glance if the expectations have been met. This includes the widths of the individual posteriors because only when they are a valid approximation of estimated parameter error the combined posterior will be centered around the expected value within its own width. The simple adding of posteriors does not inherently provide this information. However, the application of this method is challenging if the number of posteriors  $N \gg 1$  since the multiplication has to be carried out bin-wise; the product of posteriors is thus very sensitive to statistical fluctuations since a single empty bin will annihilate all contributions for this particular bin. The multiplication of posteriors has been implemented as a logarithmic sum.

Both presented methods are used in the context of toy Monte Carlo fits (see Chapter 4).

### 1.3.6 Posterior predictive checks

The quality of a BAYESIAN inference may be quantitatively investigated using so called *posterior predictive checks*. If the chosen model fits the data, then replicated data generated using the same model should look similar to observed data [Gel+14]. Samples  $y^{\text{rep},(s)}$  from the posterior predictive

distribution

$$p(y^{\text{rep}}|y) = \int d\theta p(y^{\text{rep}}|\theta) p(\theta|y) \quad (1.39)$$

can be drawn given posterior draws  $\theta^{(s)} \sim p(\theta|y)$  by randomly generating from the sampling distribution with the parameter draw plugged in [Sta22a]

$$y^{\text{rep},(s)} \sim p(y|\theta^{(s)}). \quad (1.40)$$

In a regression analysis with predictors  $x$  the posterior predictive distribution (1.40) can be generated for each predictor. Introducing the test-statistic  $T(y^{\text{rep}} > y)$  allows to draw conclusions about the accuracy of the prediction and thus of the chosen model. The test statistic serves as a BAYESIAN  $p$ -value  $p_B$  [Gel+14] and will be defined as

$$p_B = T(y^{\text{rep}} > y) = p(y^{\text{rep}} > y), \quad (1.41)$$

i.e. the fraction of replicated samples that exceed the original data points. Values near 0 or 1 will indicate a faulty measurement or model, while  $p$ -values near 0.5 are expected if the measurement and model agree well [Gel+14]. Additionally, one can identify overfitting if all values are near 0.5 [Gel+14]. The  $p$ -value is a quantitative means to identify discrepancies between data and model and to assess whether those discrepancies may have arisen by chance [Gel+14].

### 1.3.7 Example: Fitting data described by a $\cos(x)$ distribution

In order to summarize the previous discussion of BAYESIAN methods and also to illustrate the application thereof, the simple example of fitting data using a  $\cos(x)$  distribution will be discussed in the following. A Frequentist approach, as well as a BAYESIAN approach will be applied. In the end, key differences between both approaches are investigated.

Assume there are  $N$  precise predictors  $\{x_i\}$  and corresponding independent measurements  $\{y_i\}$  with measurement errors  $\{\sigma_i\}$ . Additionally, the data  $y$  is expected to follow a functional  $y = f(x; \theta)$  with parameters  $\theta$ . Figure 1.5 shows  $N = 15$  datapoints that follow the function  $f(x; \theta) := \theta_1 \cdot \cos(x) + \theta_2$  with GAUSSIAN noise  $\epsilon$

$$y = f(x; (\theta_1 = 1, \theta_2 = 1)) + \epsilon \quad \epsilon \sim \mathcal{N}(0, \sigma) \quad \sigma \sim \mathcal{N}(0.25, 0.05). \quad (1.42)$$

From the noisy data, the parameters  $\theta$  shall be recovered in the following.

#### Frequentist Approach

The traditional approach to this fitting problem is a  $\chi^2$  fit. Then the test statistic

$$\chi^2 = \sum_{i=1}^N \left[ \frac{y_i - f(x_i; \theta)}{\sigma_i} \right]^2 \quad (1.43)$$

can be minimized with respect to the parameters  $\theta$  giving according estimates with error bars which are calculated using error propagation from the original data points  $\{y_i\}$ . The minimization can be

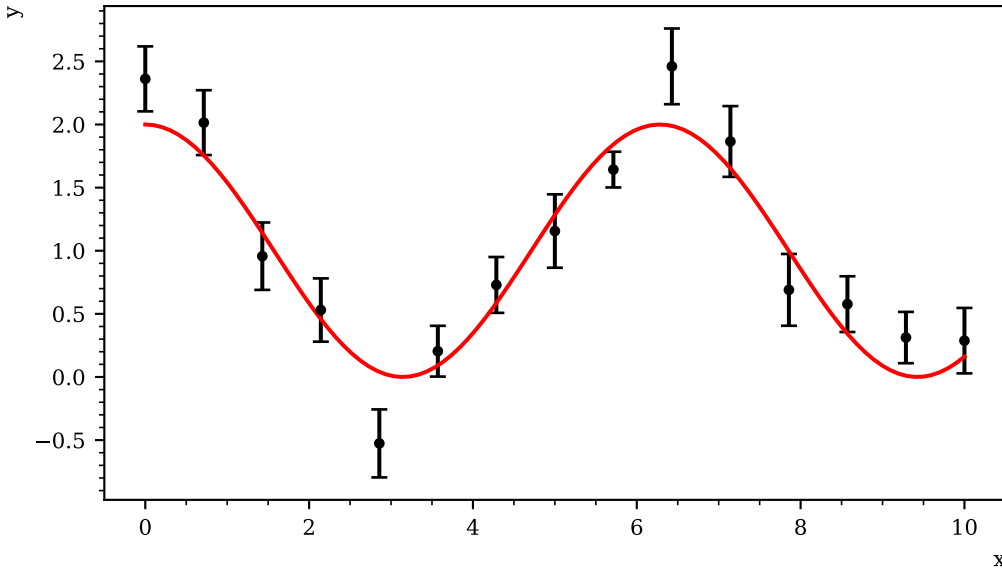


**Figure 1.5:** Randomly generated data with GAUSSIAN noise (errorbars) following the function  $y(x) = 1 \cdot \cos(x) + 1$  (red line).

solved analytically in the case of linear functions by solving the equation system

$$\frac{d}{d\theta} \chi^2 = 0$$

and otherwise numerically. The minimization of  $\chi^2$  to get best-fit estimates for the desired parameters can be motivated if one considers the likelihood  $\mathcal{L}$  that the data follow the function  $f$ . It is given by

$$\ln \mathcal{L} = -\frac{1}{2} \sum_{i=1}^N \left[ \frac{y_i - f(x_i; \theta)}{\sigma_i} \right]^2 - \sum_{i=1}^N \ln \sigma_i \sqrt{2\pi}, \quad (1.44)$$

if one assumes GAUSSIAN errors at each data point. To maximize the (log-) likelihood with respect to all parameters is then equivalent to minimizing  $\chi^2$ . As a byproduct, the  $\chi^2$  fit also gives a goodness of fit estimate which is given by  $\chi^2/\text{NDF} \approx 1$ , where NDF are the number of degrees of freedom. Significantly smaller or larger values indicate too small error estimates or a bad fit, respectively. [Bar89]

### Bayesian approach

To gather samples from the marginal posteriors  $p(\theta_1|y)$  and  $p(\theta_2|y)$  likelihood and priors have to be specified. In order to introduce intentionally vague priors that do not give significant information<sup>3</sup>

<sup>3</sup> This, of course, requires knowledge of the order of magnitude the fit parameters will take.

both parameters are assigned a standard normal distribution as a prior

$$\theta_1 \sim \mathcal{N}(0, 1) \quad \theta_2 \sim \mathcal{N}(0, 1). \quad (1.45)$$

The likelihood is determined using

$$\epsilon_n = y_i - f(x_i; \boldsymbol{\theta}) \sim \mathcal{N}(0, \sigma_i), \quad (1.46)$$

see Eq. (1.42), and the independence of all datapoints such that the likelihood evaluates to the product

$$p(y|\boldsymbol{\theta}) = \prod_{i=1}^N \mathcal{N}(f(x_i; \boldsymbol{\theta})|y_i, \sigma_i). \quad (1.47)$$

With prior and likelihood specified, samples from the joint posterior  $p(\boldsymbol{\theta}|y)$  can now be generated using MCMC. [Sta22a]

Figure 1.6 shows the fit results from a BAYESIAN fit using MCMC sampling and also from a  $\chi^2$  fit for the parameters  $\boldsymbol{\theta}$ . The point estimates with error bars correspond to a  $1\sigma$  interval of the unimodal posterior distributions. The true values underlying the simulated data are recovered by both fits.

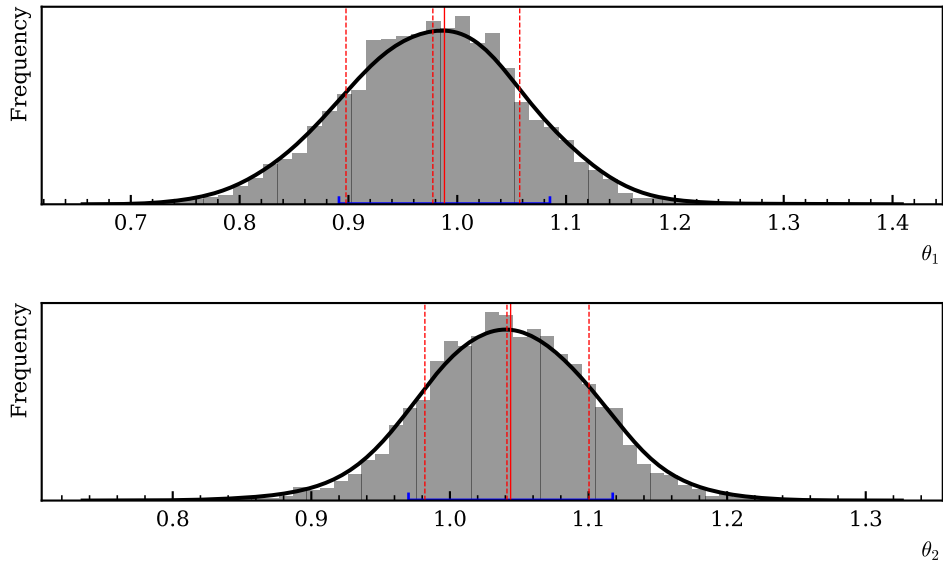


**Figure 1.6:** Marginal posteriors of the parameters  $\theta_1$  and  $\theta_2$  as obtained from MCMC sampling. The histograms represent the posterior draws, the black solid line shows a Kernel-Density-Estimate (KDE) to smooth the distribution. The solid vertical red line shows the most probable value determined from the KDE, while the dashed red vertical lines show a  $1\sigma$  interval around the mean  $\mu$ . The blue error bars show the results obtained from a  $\chi^2$  fit.

Concerning the goodness of fit, the  $\chi^2$  exhibits a value of  $\chi^2/\text{NDF} = 1.3$  which is close to 1 but also significantly greater than one, indicating only moderate goodness of the fit due to the few number of datapoints. This issue is discussed further in chapter 4 and the appendix C. For the BAYESIAN fit, a

posterior predictive check is made, see Figure 1.7. The  $p$  values are scattered around 0.5 indicating a successful and unbiased fit. The MCMC diagnostics have to be monitored for each parameter

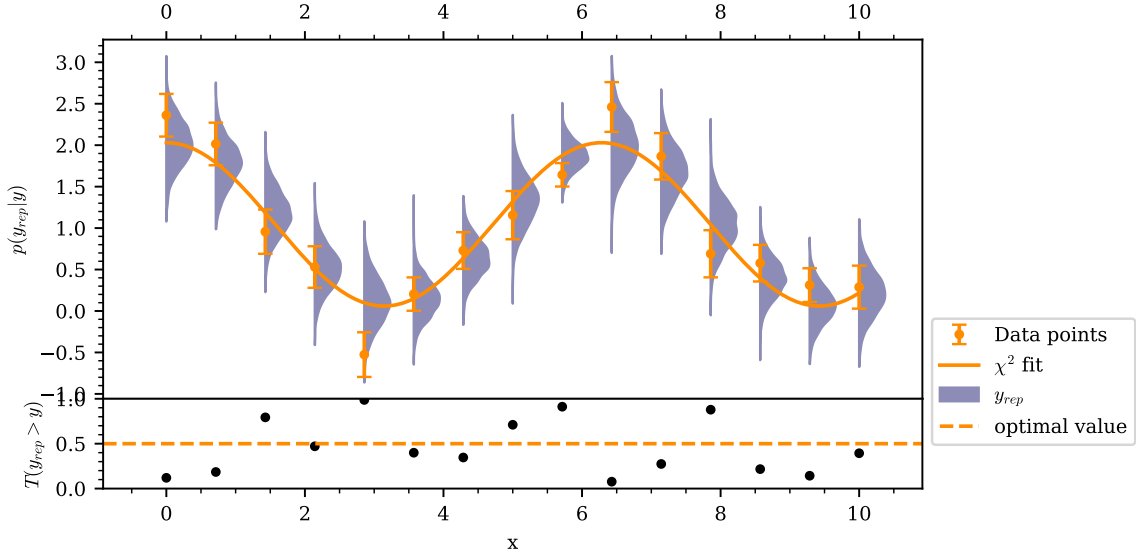


**Figure 1.7:** Posterior predictive check of the fitted model. For each drawn sample of  $\theta$  a random number according to the sampling distribution  $p(y|\theta)$  is drawn for every predictor  $x_i$ . The  $p$  value is then determined from the posterior predictive distribution.

separately. In this particular example 1000 samples from the posterior have been drawn in four independent chains. This leads to

$$\widehat{R}_1 = 1.001 \quad \widehat{R}_2 = 1.0004 \quad (1.48)$$

$$\frac{\text{MCSE}_1}{\text{median}(p(\theta_1|y))} = 0.002 \quad \frac{\text{MCSE}_2}{\text{median}(p(\theta_2|y))} = 0.001, \quad (1.49)$$

indicating good within and between chain convergence as well as good accuracy regarding the median of the marginal distributions.

Both fits give similar results, yet the approaches are inherently different; The Frequentist approach assigns probabilities based on the observed data conditioned on fixed parameters as a long-run relative frequency, the likelihood  $\mathcal{L} = p(y|\theta)$  is thus the main quantity of interest. However from a BAYESIAN perspective the complete inference is given by the posterior distribution(s)  $p(\theta|y)$  that connects prior and likelihood. Furthermore, in a Frequentist ansatz the parameters that are to be estimated are seen as unknown constants whereas in a BAYESIAN fit the parameters are in fact unknown *distributions*. Table 1.4 summarizes the core differences between a Frequentist and a BAYESIAN approach to parameter inference. [BC16]

	Frequentist statistics	BAYESIAN statistics
quantity of interest parameters are probability associated with	$p(y \theta)$ unknown constants data	$p(\theta y)$ unknown distributions parameters and data

**Table 1.4:** Key differences between BAYESIAN statistics and Frequentist statistics, contents taken from [BC16].

## 1.4 Current data situation

The data base of observables regarding  $\eta$  photoproduction off the proton has recently been expanded with a high precision measurement of the beam asymmetry at the CBELSA/TAPS experiment [Afz19; Afz+20]. This measurement will serve as reference for testing a BAYESIAN approach when determining the beam asymmetry from CBELSA/TAPS data. A detailed description of the current data situation regarding  $\eta$  photoproduction off the proton can be found in reference [Afz19]. A detailed review regarding photoproduction of pseudoscalar mesons in general is given by reference [TAW22].

The data base regarding  $\eta'$  photoproduction is scarce; the differential cross section has been measured with the CEBAF Large Acceptance Spectrometer (CLAS) at JLAB [Wil+09] and also by the CBELSA/TAPS collaboration [Cre+09] covering a large range in polar angle and beam energy. Additionally, two measurements of the beam asymmetry in  $\eta'$  photoproduction off the proton exist covering an energy range up to 1836 GeV [Lev+14; Col+17]. Different PWA fits yet claim different contributing resonances  $N^*$  where recently first hints towards a narrow resonance near the  $\eta'$  production threshold have been found [Ani+18; Tia+18]. There is consensus regarding the dominant contribution from the resonance  $N(1895)^{1/2^-}$  to  $\eta'$  photoproduction [Ani+18; Tia+18].

Within the CBELSA/TAPS collaboration, so far no attempt has been made to determine any polarization observable using BAYESIAN statistics. However, in the context of truncated partial wave analyses, which takes polarization observables as input data to determine photoproduction multipoles, there have been first approaches [Noë22; Krö22].

## 1.5 Motivation and Structure of this Thesis

This work aims on the one hand to determine the beam asymmetry  $\Sigma$  in  $\eta$  photoproduction off the proton in the energy range 1100 GeV to 1800 GeV that has been reported by the measurement [Afz19] using BAYESIAN statistics. Therefore, the same selected data are fed into the BAYESIAN analysis that were used to determine the beam asymmetry with the traditional Frequentist methods so that the results are directly comparable. Determining polarization observables via BAYESIAN statistics increases the amount of information gained from the fit result as distributions instead of point estimates become available. This is desirable since polarization observables serve as input for further analysis.

On the other hand the scarce data base regarding  $\eta'$  photoproduction is to be expanded by an additional measurement of the beam asymmetry in the beam energy range 1500 GeV to 1800 GeV. Hereby traditional Frequentist methods as well as a BAYESIAN approach are pursued.

The thesis is structured as follows: Chapter 2 will introduce the CBELSA/TAPS experiment that was used to collect the data from which the measurements of the beam asymmetry are derived. The next chapter 3 will illustrate the process of event selection of the reaction  $\gamma p \rightarrow p\eta' \rightarrow p\gamma\gamma$  and summarize the event selection of the reaction  $\gamma p \rightarrow p\eta \rightarrow p\gamma\gamma$  that is reported in reference [Afz19].

With the selected data the beam asymmetries for both reactions are then determined in chapter 4. Lastly, the results are discussed in chapter 5.



## CHAPTER 2

### Experimental Setup

In this work the beam asymmetry  $\Sigma$  is determined in the reactions  $\gamma p \rightarrow p\eta$  and  $\gamma p \rightarrow p\eta'$ , requiring a polarized photon beam and an unpolarized proton target. It is convenient to study photoproduction off a fixed target and investigate the resonances that occur in the process. The analyzed data was taken at the CBELSA/TAPS experiment located in Bonn at the EElectron Stretcher Accelerator (ELSA). In this chapter the different parts of the CBELSA/TAPS experiment that are used for the measurement of the beam asymmetry  $\Sigma$  will be presented. Figure 2.1 shows an overview of the experimental hall. All mentioned parts are discussed in detail in the following.

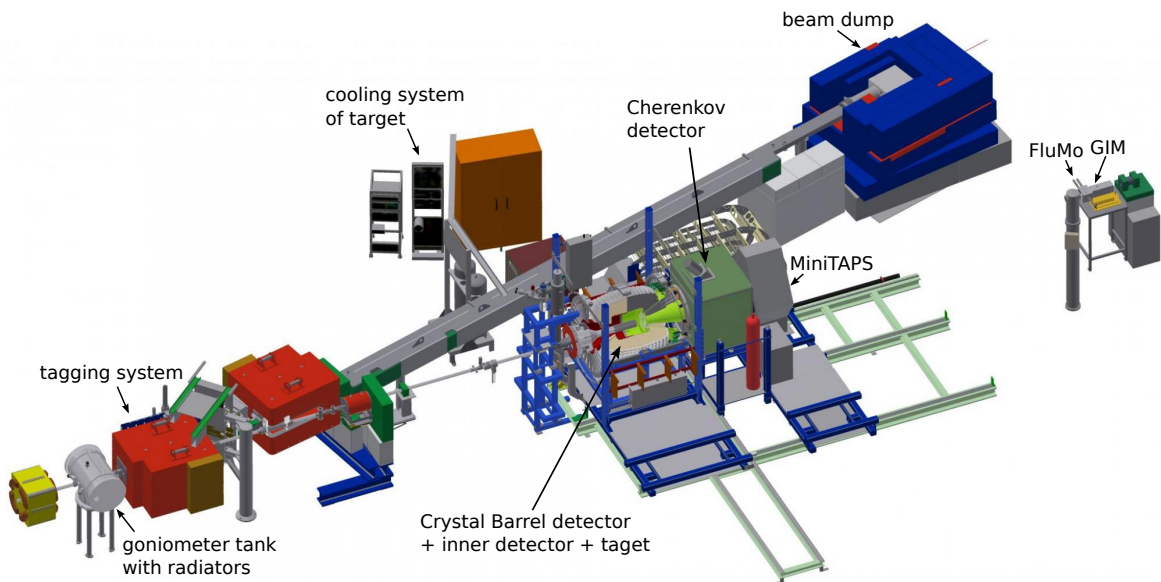


**Figure 2.1:** Overview of the experimental hall of the CBELSA/TAPS experiment. The electron beam from ELSA enters at the bottom left. M. GRÜNER in [Afz19]

High energy electrons extracted from ELSA are used to produce a polarized photon beam using the *bremssstrahlung* process (see 2.1.1). After they have been energy tagged (see 2.1.2) these photons then interact with the fixed target material (see Section 2.2) so that hadronic resonances may be excited

that will decay via the strong interaction e.g. under the emission of mesons. The resulting decay products can then be measured with a system of electromagnetic calorimeters and scintillators that is especially suited for the detection of photons (see Section 2.3). The analogue measurements are only saved for offline analysis if detector signals meet certain trigger conditions which is only the case for reactions that are of interest (see Section 2.4). This way the amount of unwanted background is minimized already during the process of data taking. Once data acquisition is finished the data may be investigated with the help of analysis software and Monte Carlo simulations tailored to the needs of the CBELSA/TAPS experiment (see Section 2.5).

## 2.1 Production of polarized high energy photon beam

To measure polarization observables in photoproduction reactions a polarized photon beam is needed which can be created using *coherent bremsstrahlung*. Bremsstrahlung is the dominating interaction of high energy ( $\mathcal{O}(1 \text{ GeV})$ ) electrons with matter [Leo94]. Electrons are decelerated in the COLOUMB field of heavy nuclei and radiate real photons, see Figure 2.2.

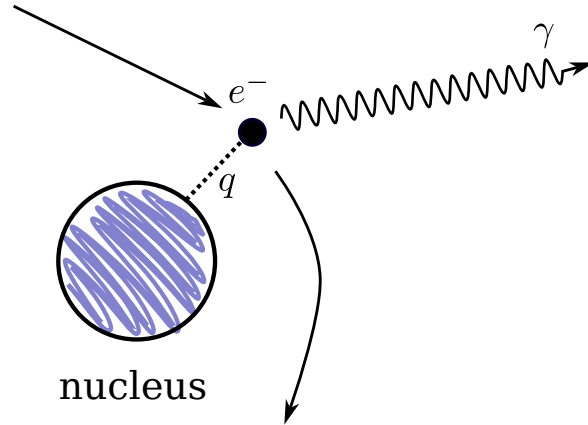


**Figure 2.2:** Illustration of the bremsstrahlung process: An electron  $e^-$  is deflected in the COLOUMB field of a nucleus in the radiator material. A photon  $\gamma$  is emitted and so the momentum  $q$  is transferred.

To conserve momentum there has to be a momentum transfer  $q$  which is negligibly small compared to the nucleon mass. If an amorphous radiator is used incoherent bremsstrahlung is produced with a continuous spectral distribution proportional to  $1/E_\gamma$ , according to the BETHE-HEITHLER cross section [Hei54]. Since the structure of nuclei in the amorphous radiator does not exhibit any periodicity, the electric field vector will not prefer any particular direction, resulting in a net polarization degree of zero for the photon beam. To achieve non-vanishing polarization degrees a crystal with periodic placement of nuclei may be used as radiator. Then, coherent bremsstrahlung is produced; the crystal can absorb the recoil only for discrete momenta  $q_n$  meeting the LAUE condition [Dem10] of the crystal lattice. This enables constructive interference between different bremsstrahl photons and at the same time fixes the deflection plane of incoming electrons, resulting in a coherent polarized photon beam. Incoherent bremsstrahlung may still occur due to impurities in the crystal structure, so that the total bremsstrahlung cross section off a crystal radiator  $\sigma_{\text{crystal}}$  is the sum of a coherent ( $\sigma_{\text{coherent}}$ ) and an incoherent ( $\sigma_{\text{incoherent}}$ ) part

$$\sigma_{\text{crystal}} = \sigma_{\text{coherent}} + \sigma_{\text{incoherent}}. \quad (2.1)$$

The process of bremsstrahlung can be modeled using ANalytical Bremsstrahlung (ANB) calculations [Nat+03]. ANB intensity spectra for a crystal and amorphous radiator are shown in Figure 2.3 on the left hand side. The right hand side shows the enhancement spectrum, which is given by dividing the two spectra. One observes that the bremsstrahlung intensity spectrum obtained from a crystal radiator

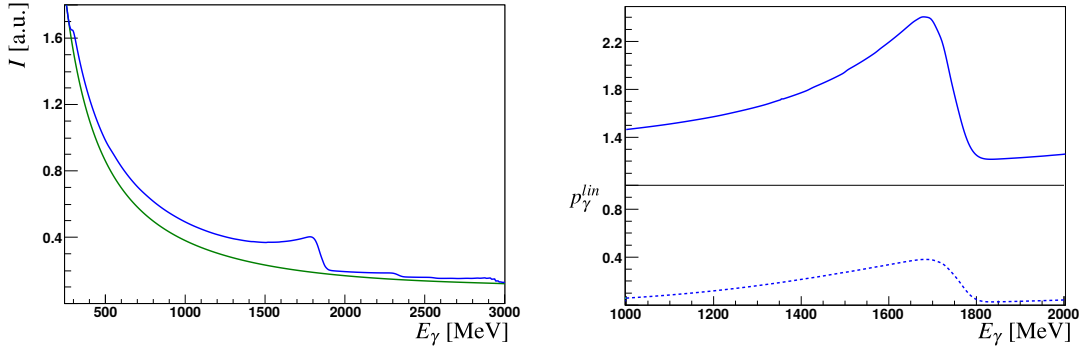


**Figure 2.3:** Left: Incoherent (green) and crystal (blue) bremsstrahlung intensities as a function of the photon energy. Right: The enhancement spectrum is given as the ratio of crystal to incoherent intensity spectrum. The dashed line at the bottom shows the calculated polarization degree. Both spectra are generated using ANB calculations. Taken from [Afz19].

is in general enhanced relative to the incoherent spectrum obtained from an amorphous radiator. In fact, using ANB calculations, the polarization degree can be determined from the enhancement spectrum. The characteristic drop in intensity in the intensity spectrum obtained from the crystal radiator is referred to as the coherent edge. It occurs because the photon energy in the kinematically allowed region of the recoil momentum that will lead to coherent bremsstrahlung is limited. The relative alignment of the radiation crystal to the electron beam determines the position of the coherent edge.

### 2.1.1 Goniometer

In order to determine the beam polarization from enhancement spectra, a diamond radiator as well as an amorphous radiator are required. Several radiators as well as beam diagnostics tools mounted inside a rotating aluminum wheel are part of the goniometer [Els+09], resting inside a vacuum tank. Depending on whether linearly polarized or unpolarized photons are needed either copper radiators of different thickness or a diamond radiator, which is located in the center of the wheel, are inserted into the beam axis, see Figure 2.4. In case a circularly polarized photon beam is required, a MØLLER polarimeter [Kam10] is used, which is also shown in Figure 2.4. The goniometer can be rotated in all directions allowing precise alignment with the incoming electron beam from ELSA.

### 2.1.2 Tagging system

Once the impinging electrons from ELSA have scattered off the radiator their energy is determined in order to measure the energy of the created photons. This is possible because the initial electron energy  $E_0 = 3.2 \text{ GeV}$  is known from ELSA. Thus, the photon Energy  $E_\gamma$  is given by subtracting the

energy of the recoil electrons  $E_e$  from  $E_0$ <sup>1</sup>

$$E_\gamma = E_0 - E_e. \quad (2.2)$$

The recoiling electrons are deflected towards the tagging system [For10] consisting of 96 overlapping scintillator bars and 480 scintillating fibers using the magnetic field of a dipole magnet with a field strength of 1.5 T. The bending radius of the electrons depends on their momenta is uniquely defined by the tagger hit position. With the position of the deflected electrons and the magnetic field strength,  $E_e$  can thus be determined. For an initial energy  $E_0 = 3.2$  GeV the scintillator bars cover an energy range of  $560\text{ MeV} < E_\gamma < 3100\text{ MeV}$  with an energy resolution of  $0.1\%E_\gamma$ - $6\%E_\gamma$ . The fibers additionally improve the energy resolution in the energy range  $416\text{ MeV} < E_\gamma < 2670\text{ MeV}$  to  $0.1\%E_\gamma$ - $0.4\%E_\gamma$ . Photomultipliers are used for the readout of the tagger bars and fibers, realizing a time resolution of  $^2\text{FWHM}_{\text{bar}} = 635\text{ ps}$  and  $\text{FWHM}_{\text{fiber}} = 1.964\text{ ns}$  [Har08]. Any electrons that have not interacted with the radiator material are deflected by another dipole magnet towards the beam dump, see Figure 2.1. Figure 2.5 shows a top-down view of the tagging system.

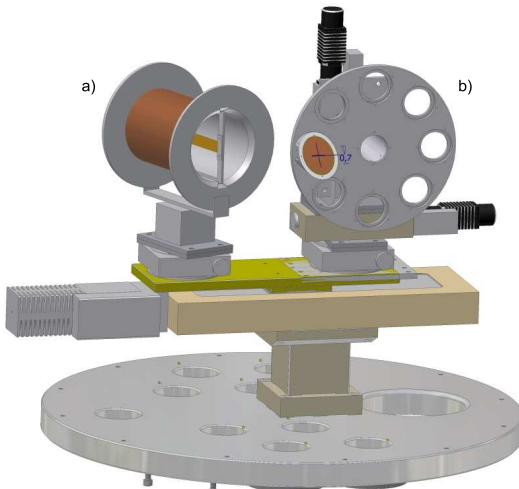


**Figure 2.4:** The goniometer holds several radiators that can be inserted onto the beam axis (b). Also available is a Møller coil with radiator (a) [Wal].

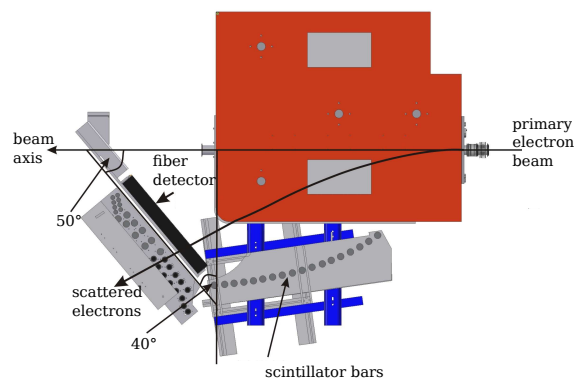


**Figure 2.5:** Top-down view of the tagging system consisting of dipole magnet (red) and scintillating bars and fibers [For10]. Electrons are deflected by the magnet after the bremsstrahlung process.

## 2.2 Liquid hydrogen target

The (polarized) photon beam impinges on a liquid hydrogen target [Ham09] which is located at the center of the crystal barrel detector, see Figure 2.1. It consists of a Kapton cell that measures 5.1 cm in length and 3 cm in diameter which is filled with liquid hydrogen. A separate cooling circuit with liquid hydrogen ensures the hydrogen that is used as target material stays liquid. Kapton is chosen as material for the target cell because the expected rate of hadronic reactions induced in the target cell is

<sup>1</sup> Hereby, the recoil energy absorbed by the nuclei is neglected.

<sup>2</sup> Full Width Half Maximum.

small compared to the expected rate from liquid hydrogen [Ham09]. Protons are bound with a binding energy of 21.4 eV in the target material, which is negligible on the scale of hadronic reaction energies, so that they can be considered free. A schematic view of the target is shown in Figure 2.6.

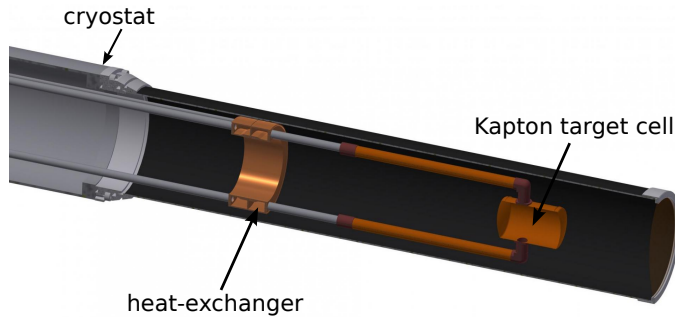


**Figure 2.6:** Schematic overview of the liquid hydrogen target. Two tubes connected to a heat exchanger and the Kapton cell allow filling it with liquid hydrogen. M. GRÜNER in [Afz19].

## 2.3 Detector system

Hadronic reactions are induced by the photon beam in the target material. As a consequence resonances are excited that decay under emission of mesons. These mesons subsequently decay to e.g. photons. The main calorimeters of the experiment, the Crystal Barrel that is complemented by the forward detector (Sec. 2.3.2) and the MiniTAPS calorimeter (Sec. 2.3.3), cover 95% of the solid angle  $4\pi$  and are especially suited for the detection of photons. Charged particles are identified by the inner detector (Sec. 2.3.1) as well as plastic scintillators mounted in front of the forward and the MiniTAPS detector that are used as vetoes. To suppress electromagnetic reactions a ČERENKOV detector is used (Sec. 2.3.4). The photon flux is measured via the Gamma-Intensity-Monitor (GIM) and Flux-Monitor (FluMo) (Sec. 2.3.5).

### 2.3.1 Inner detector

The inner detector [Fös00; Suf+05] encloses the target in a cylindrical geometry and consists of 513 plastic scintillation fibers that are placed in three layers. The outer layer is oriented along the beam axis while the inner layers are tilted by an angle of  $-24.5^\circ$  and  $25.8^\circ$ , respectively, see Figure 2.7. This structure allows to unambiguously determine the azimuthal and polar angle of a charged particle as long as at least two layers are hit. The detector is in total 40 cm long and covers a polar angle range of  $23.1^\circ < \theta < 166^\circ$  with a resolution of  $0.4^\circ$  in polar angle  $\theta$  and  $0.1^\circ$  in azimuthal angle  $\phi$ . The fibers consist of Polystyrene with a refractive index of  $n = 1.6$  and are cladded by Polymethylmethacrylat ( $C_5H_8O_2$ ) with  $n = 1.49$  [PDG]. Charged particles passing the detector will cause the emission of scintillation light by the Polystyrene molecules which is read out with photomultipliers after passing lightguides. Short decay times ensure a fast time signal and a time resolution of  $FWHM = (2.093 \pm 0.013)$  ns is reached [Har08].

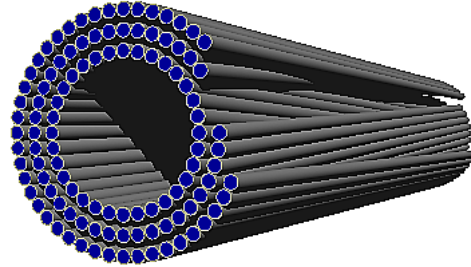


**Figure 2.7:** The inner detector with three layers of scintillating fibers. The inner two layers are tilted with respect to the outer layer. D. WALTHER in [Afz19].

### 2.3.2 Crystal Barrel and forward detector

The main calorimeter of the experiment is the Crystal Barrel detector [Ake+92]. It consists of 1320 CsI(Tl) crystals that are arranged in 24 rings facing the center of the target, see Figure 2.8. The first

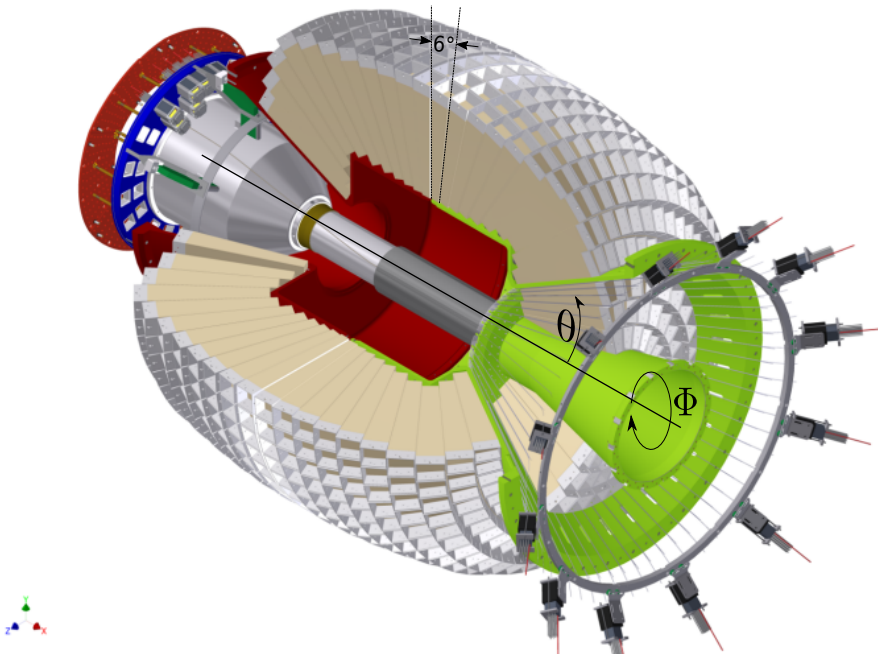


**Figure 2.8:** Crystal barrel calorimeter and forward detector are built such that they enclose the target and the inner detector. The forward detector consists of the first three rings (green base) of crystals which are additionally covered by plastic scintillators for charged particle identification. The definition of polar angle  $\theta$  and azimuthal angle  $\phi$  in the LAB system are indicated as well. D. WALTHER in [Urb17]

three rings in forward direction contain 30 crystals each and build the forward detector, covering the polar angle range  $11.18^\circ < \theta < 27.54^\circ$ . Also the 24<sup>th</sup> ring contains 30 crystals, all other rings are made up of 60 crystals. The crystals are shaped like truncated trapezoidal pyramids that cover 6° in

polar angle  $\theta$  and azimuthal angle  $\phi$ . Only in the first three and the last ring the crystals cover  $12^\circ$  in  $\phi$ . Full coverage in  $\phi$  and 80% ( $12^\circ < \theta < 156^\circ$ ) coverage in  $\theta$  are achieved by the forward detector and the Crystal Barrel. Photons from neutral mesonic decays are very high energetic and will interact with the inorganic scintillator material mainly via pair production [Leo94]. The produced electrons and positrons will themselves interact mainly via bremsstrahlung such that usually an electromagnetic shower is created upon photon impact that may spread over several crystals. Using crystals with a length of  $l = 30$  cm photons with an energy of up to 2 GeV may deposit their entire energy in the calorimeter since the  $l$  corresponds to 16.22 radiation lengths  $X_0$  [Ake+92]. The transversal spread of a shower is given by the MÓLIERE radius which is 3.8 cm for CsI(Tl) [Ake+92]. By determining the focal point of the electromagnetic showers an angular resolution of less than  $2^\circ$  can be achieved [Jun04] while the energy resolution is given by [Ake+92]

$$\frac{\sigma_E}{E} = \frac{2.5\%}{\sqrt[4]{E/\text{GeV}}}, \quad (2.3)$$

depending on the initial photon energy  $E$ . The energy loss of heavier charged particles, e.g. a proton, is described by the BETHE-BLOCH formula [Bet30]. Depending on their mass they only deposit their full energy up to a certain threshold energy above which they are characterized as Minimal Ionizing Particles (MIP).

The emitted scintillation light of crystals not belonging to the forward detector is read out using PIN photodiodes. A wavelength shifter ensures meeting the sensitive spectral range of the photodiodes. The long decay times of the scintillation light and the slow preamplifiers following the photodiodes do not allow the determination of a timing information for particles detected in the Crystal Barrel<sup>3</sup>, so that the Crystal Barrel is optimized for energy measurements.

Crystals belonging to the forward detector are read out using Photomultipliers. They provide a faster signal, such that timing information for forward detector hits is available with a time resolution of FWHM =  $(1.861 \pm 0.016)$  ns [Har08]. Additionally plastic scintillator plates are mounted in front [Wen04], allowing the identification of charged particles with an efficiency of 72% [Geh15]. Optical fibers guide the scintillation light from the plates to photomultipliers.

### 2.3.3 MiniTAPS

Since the Crystal Barrel only covers the solid angle starting at  $\theta \approx 12^\circ$ . It is supplemented by the Mini-Two-Arm-Photon-Spectrometer (MiniTAPS) [Gab+94; Str96] for polar angles  $1^\circ < \theta < 12^\circ$ . The MiniTAPS detector is placed in a distance of  $d = 2.1$  m from the target and consists of 216 hexagonally shaped BaF<sub>2</sub> crystals, see Figure 2.9. Each crystal has a length of  $l = 25$  cm which is equivalent to 12 radiation lengths [Nov91] and a width of  $w = 5.8$  cm. The chosen material has a high density and is able to withstand high reaction rates [PDG]. This is important here because most reactions will be strongly boosted in forward direction towards small  $\theta$ . Different mechanisms of scintillation allow to extract a fast and a slow component [Leo94] which are read out using photomultipliers and separately used for timing and energy information, respectively. Hereby a time

---

<sup>3</sup> As of 2014, the PIN photodiodes have been replaced by avalanche photodiodes (APD) [Hon14; Urb17], allowing a fast read out that can be used to provide timing information and also as part of the trigger.

resolution of  $\text{FWHM} = (0.872 \pm 0.006)$  ns [Har08] and an energy resolution of [Gab+94]

$$\frac{\sigma_E}{E} = 1.9\% + 0.59\% \cdot \sqrt{E/\text{GeV}} \quad (2.4)$$

is achieved. At the same time an angular precision of  $0.2^\circ$  in  $\theta$  is reached.

In front of each  $\text{BaF}_2$  crystal, plastic scintillator plates are mounted to identify charged particles. Their scintillation light is guided towards photomultipliers using optical fibers. With these scintillators a time resolution of  $\text{FWHM} = (3.06 \pm 0.05)$  ns is obtained [Har08].

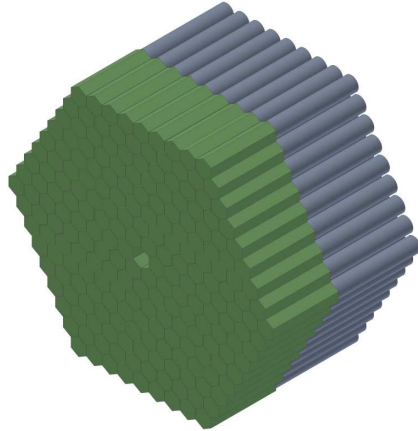


**Figure 2.9:** The MiniTAPS detector is made up of 216  $\text{BaF}_2$  crystals (grey). In front of each crystal, plastic scintillators are mounted for charged particle information. Taken from [Wal].

### 2.3.4 ČERENKOV detector

When the photon beam impinges on the proton target, not only hadronic reactions are induced but also electromagnetic reactions. Because the beam energy is very high on the scale of electromagnetic interactions, any produced electrons and positrons are highly relativistic and boosted to small polar angles. To suppress these events already during data acquisition a ČERENKOV detector [Kai07] is positioned between the MiniTAPS calorimeter and the Crystal Barrel, see Figure 2.1. It is filled with  $\text{CO}_2$  gas where ČERENKOV light is emitted by electrons or positrons above an energy of 17.4 MeV. This follows from the refractive index which is given as  $n_{\text{CO}_2} = 1.00045$  [PDG]. The emitted ČERENKOV radiation is focused on a photomultiplier using a parabolic mirror. The presence of a signal can then be used as veto during data acquisition to reduce the amount of recorded electromagnetic background. Electrons and positrons are detected with an efficiency of up to  $(99.72 \pm 0.45)\%$  [Kai07].

### 2.3.5 Flux monitoring

The FluMo and GIM detector are used to determine the total number of photons incident on the target and are located behind the MiniTAPS detector, as is shown in Figure 2.1.

The GIM detector [McG08] is made of 16  $\text{PbF}_2$  crystals placed in a  $4 \times 4$  array, see Figure 2.10. Incoming photons will interact with the material mainly via pair production [Leo94]. The produced electrons and positrons are highly relativistic and will emit ČERENKOV light that is collected

with photomultipliers. For reaction rates higher than 5 MHz the GIM detector efficiency decreases significantly. For rates above 7 MHz more than 10% of events are not registered [Har08]. To

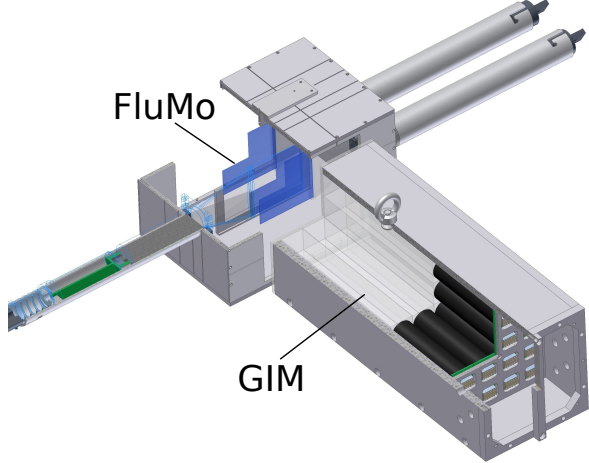


**Figure 2.10:** The two detectors FluMo and GIM are used to monitor the photon flux at different reaction rates. D. WALTHE in [Afz19].

compensate this the FluMo detector [Die08] is used as soon as deadtime effects influence the performance of the GIM detector. A converter plate made of lead, two scintillators and a veto detector are part of the FluMo detector. Impinging photons may create electron positron pairs that are detected in a coincidence measurement using the two scintillators. A plastic scintillation detector is placed before the converter plate and gives a veto signal if charged particles pass through it.

## 2.4 Trigger

To minimize the volume of data that is saved to disk for offline analysis, data is only digitized if certain predefined patterns in the detector signals are present. The search for predefined patterns is managed by the trigger of the experiment. The analyzed data sets were acquired using the *vme\_trig42c* trigger [Win06; Hof18]. The trigger requires configuration to be sensitive to hadronic photoproduction reactions and at the same time reject unwanted background events. This is achieved using Field Programmable Gate Arrays (FPGAs) which allows to split the trigger into two levels: At first level all detectors with a fast read out system (up to 250 ns) are checked for hits. At the second level the number of detected particles in the Crystal Barrel is determined using the Fast Cluster Encoder (FACE), which can take up to 10  $\mu$ s [Fle01]. It is always demanded that at least two particles are measured in either forward, MiniTAPS or Crystal Barrel detector while no veto from the ČERENKOV detector is measured. Any information from the Crystal Barrel is only available in the second level because of the slow readout.

## 2.5 Software and Monte Carlo

In order to proceed with the offline data analysis of CBELSA/TAPS, several software tools are used that are described briefly in the following.

### 2.5.1 ExPLORA

Within the CBELSA/TAPS collaboration an analysis software has been developed named *Extended Pluggable Object-oriented Root Analysis (ExPLORA)* [Sch+]. It is based on *ROOT* [BR97] and is used for reconstruction and analysis of acquired raw data. *ROOT* has been developed at CERN to deal with a high amount of data. It makes use of *C++* libraries that give it high functionality regarding statistical analyses, visualizations and data management. *ExPLORA* is also written in *C++* but is operated by the use of *xml* files. This allows user specific extensions in the form of plugins that manage e.g. the application of cuts and the filling of histograms. In order to select candidates for the reaction  $\gamma p \rightarrow p\eta' \rightarrow p\gamma\gamma$  a *C++* plugin has been written that was embedded into a *xml* file which managed the application of calibrations and reconstruction. For further analysis of the selected data, scripts in *ROOT* and *python* have been written. In Appendix A, an example *.xml* file is displayed.

### 2.5.2 Monte Carlo

In order to determine detector and analysis acceptances as well as possible background contributions it is convenient to simulate the according detector geometry and the interaction of particles with the material using the Monte Carlo technique [MU49]. Based on the CERN-developed software package *Geant3* (Geometry and Tracking) [Bru+87] a simulation of the CBELSA/TAPS experiment was developed using the Virtual Monte Carlo technique [Kal11]. Hereby the particles' interaction with the detector materials are modeled according to existing experimental data. Simulated datasets may then be analyzed in the same way as measured data in order to check consistency with the measured data as well as investigating detection efficiencies and background contributions. Table 3.2 shows the simulated datasets that were used during the analysis and how many events were generated for each reaction, respectively. The reactions  $\gamma p \rightarrow p2\pi^0 \rightarrow p4\gamma$  and  $\gamma p \rightarrow p\pi^0\eta \rightarrow p4\gamma$  proved to be responsible for background contamination after the event selection (see Chapter 3). These reactions were simulated while additionally weighting all events according to the production cross section determined from a BnGa fit [AKN+; Ani+12]. These Monte Carlos were kindly provided by P. MAHLBERG [Mah22].

Reaction	Number of events
$\gamma p \rightarrow p\pi^0$	$60 \cdot 10^6$
$\gamma p \rightarrow p\eta$	$30 \cdot 10^6$
$\gamma p \rightarrow p\omega \rightarrow p\pi^0\gamma$	$30 \cdot 10^6$
$\gamma p \rightarrow p\eta' \rightarrow p\gamma\gamma$	$30 \cdot 10^6$
$\gamma p \rightarrow p2\pi^0$	$60 \cdot 10^6$
$\gamma p \rightarrow p\pi^0\eta$	$60 \cdot 10^6$
$\gamma p \rightarrow p3\pi^0$	$30 \cdot 10^6$
$\gamma p \rightarrow p2\pi^0\eta$	$30 \cdot 10^6$
$\gamma p \rightarrow n\pi^+$	$30 \cdot 10^6$
$\gamma p \rightarrow p\pi^+\pi^-$	$30 \cdot 10^6$

### 2.5.3 Stan

All BAYESIAN fits that are presented in this thesis are performed using the programming language *Stan* [Sta22a]. *Stan* is highly functional for statistical modeling and high-performance statistical computation. Full BAYESIAN statistical inferences can be made with MCMC sampling using HMC and NUTS as well as approximate BAYESIAN inference with variational inference and penalized maximum likelihood estimation with optimization [Sta22a]. *Stan* is written in *C++* and can thus handle a large amount of data very efficiently. Interfaces for different data analysis languages are available. In this thesis, the *Python* [RP22] front-end of *Stan*, called *CmdStanPy* [Cmd22] was used. Hereby, the model is specified in a `.stan` file which is read and compiled from *Python*. All sampling statements and results can then be accessed directly from *Python*, e.g. using the package *pandas* [McK10]. MCMC diagnostics, i.e.  $\widehat{R}$  and MCSE are conveniently determined using the python package *ArviZ* [Kum+19]. The *Stan* code of the example presented in the introduction can be found in the appendix A.

## 2.6 Datasets

The data that was analyzed in the course of this thesis was taken in the period of July 2013 to October 2013. Unpolarized electrons from ELSA were incident on a diamond radiator with 500  $\mu\text{m}$  thickness with a beam energy of  $E_0 = 3.2 \text{ GeV}$  and a beam current of roughly 1 nA. Thus, linearly polarized photons were created that impinged on a liquid hydrogen target. All beam times used the *vme\_trig42c* that has been described previously.

The coherent edge position was chosen at 1750 MeV for the July and August beam times and at 1850 MeV for the September and October beam times, enabling an analysis of the beam asymmetry  $\Sigma$  in the beam energy range from  $E_\gamma \approx 1100 \text{ MeV}$  to  $1800 \text{ MeV}$ . 4919 runs were taken in total with alternating radiator orientation  $\alpha^{\parallel/\perp} = 45^\circ$ , see Figure 4.1. The photon beam polarization was determined as part of the work [Afz19] using ANB calculations, as described in Section 2.1, see Figure 2.11. Table 2.1 shows a summary of the key parameters of the 2013 beam time taken at the CBELSA/TAPS experiment.

beamtime	number of runs (h)	coherent edge position
July 2013	513 (111)	1750 MeV
August 2013	1832 (396)	1750 MeV
September 2013	1490 (323)	1850 MeV
October 2013	1084 (235)	1850 MeV

**Table 2.1:** Summary of the key parameters of the 2013 beam time at CBELSA/TAPS taken for the measurement of the beam asymmetry  $\Sigma$ . Taken from [Afz19].

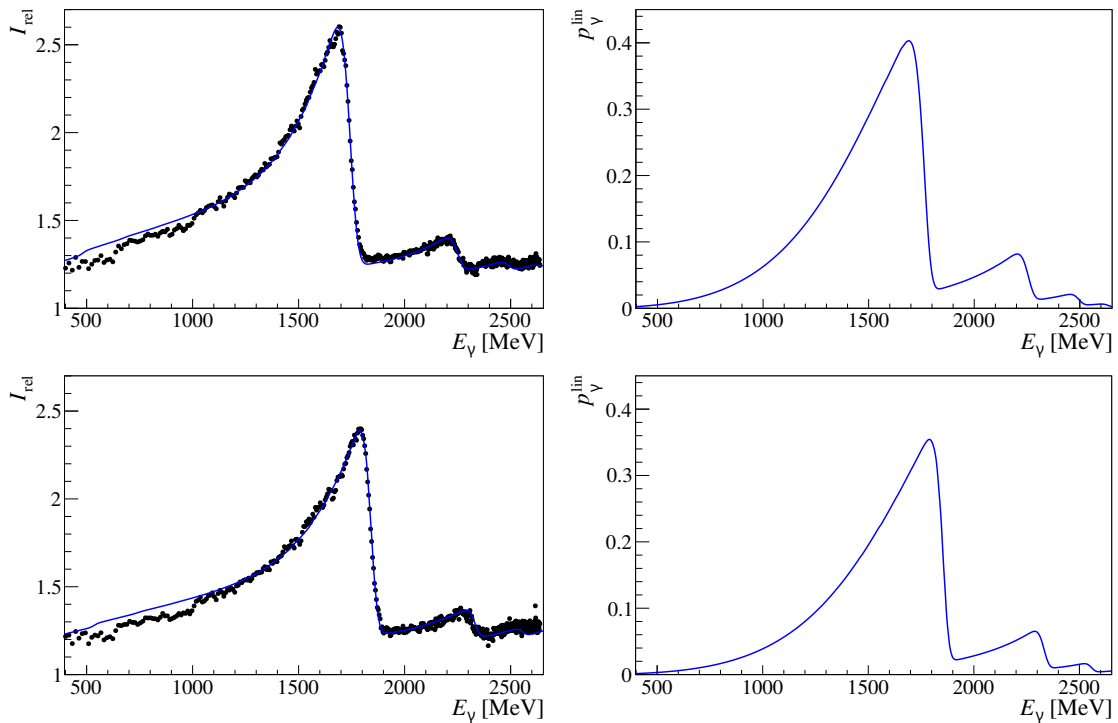


**Figure 2.11:** Comparison of the ANB calculated enhancement spectra (blue) to the measured enhancement spectra (black data points). The right hand side shows the calculated polarization degree. The upper row shows the plots for the coherent edge position at 1750 MeV and the lower row shows the coherent edge position at 1850 MeV. Taken from [Afz19].

# CHAPTER 3

---

## Event selection

---

The determination of polarization observables needs to be performed for particular reactions (cf. chapter 1), such as the photoproduction of e.g. a single  $\eta'$  meson. However, the recorded events contain data from the decay products of several possible final states in addition to combinatorial background. Thus, event candidates for the desired reaction have to be extracted before they are considered for further analysis. Table 3.1 shows the five most probable decay modes of the  $\eta$  and  $\eta'$  meson. Three decay channels of the  $\eta'$  contain final states which only contain photons and are thus reliably measurable with the CBELSA/TAPS experiment. Only the  $\eta' \rightarrow \gamma\gamma$  decay channel was considered for further analysis; the  $\omega\gamma$  channel provides negligible statistics and considering the acceptance of detecting six photons in the final state, the expected yield of the  $\eta' \rightarrow \gamma\gamma$  decays should be roughly equal to the  $\eta' \rightarrow \pi^0\pi^0\eta \rightarrow 6\gamma$  final state [Afz12]. Offering a simpler, three-particle final state, the  $\eta' \rightarrow \gamma\gamma$  channel was then favored in the course of this thesis. The  $\eta$  meson on the other hand decays dominantly into two photons making it the preferred decay channel when determining the beam asymmetry.

$\eta$		$\eta'$	
Decay mode	Branching ratio	Decay mode	Branching ratio
$\gamma\gamma$	39.36%	$\pi^+\pi^-\eta$	42.6%
$3\pi^0\gamma(\rightarrow 6\gamma)$	32.57% (31.43%)	$\rho^0\gamma(\rightarrow \pi^+\pi^-\gamma)$	28.9% (28.9%)
$\pi^+\pi^-\pi^0$	22.02%	$\pi^0\pi^0\eta(\rightarrow 6\gamma)$	22.8% (8.8%)
$\pi^+\pi^-\gamma$	4.28%	$\omega\gamma(\rightarrow \pi^+\pi^-\pi^0\gamma/\pi^0\gamma\gamma)$	2.52% (2.2%/0.21%)
$e^+e^-\gamma$	0.69%	$\gamma\gamma$	2.3%

**Table 3.1:** The five most probable decay modes of the  $\eta$  and  $\eta'$  meson. The most probable further decay with according branching ratio is shown in brackets.[Wor+22]

The process of *event selection* for the reaction  $\gamma p \rightarrow p\eta' \rightarrow p\gamma\gamma$  is outlined in the following chapter. Note that in this thesis the event selection of the  $p\eta \rightarrow p\gamma\gamma$  final state was already performed by F. AFZAL [Afz19] and the selected data are only used to determine the beam asymmetry via BAYESIAN statistics, see section 4.2. Nevertheless, a short summary of the according event selection is given at the end of this chapter, for a more detailed review, see reference [Afz19].

### 3.1 Reconstruction of events

In order to proceed with the analysis the initial and final state particles' four momenta  $p$  need to be known for every event. The employed calorimeters are capable of delivering this information; the tagger setup allows mapping fiber or bar hits to a beam photon energy. Each beam photon is assigned the mean energy  $E_\gamma$  over all tagger hits. Since the target protons are at rest, these informations suffice to determine the initial state four momenta

$$p_{\gamma, \text{beam}} = \begin{pmatrix} E_\gamma \\ 0 \\ 0 \\ E_\gamma \end{pmatrix} \quad p_p = \begin{pmatrix} m_p \\ 0 \\ 0 \\ 0 \end{pmatrix}. \quad (3.1)$$

Once a final state particle passes through sensitive detector material it will deposit a certain amount of energy by interacting with it. In most cases this will result in an electromagnetic shower that will span over several detector elements. Timely and spatially correlated showers are grouped to *clusters* using clusterfinding algorithms, depending on the hit detector. As a next step, clusters are scanned for local energy deposition maxima, which mark a *particle energy deposition* (PED), corresponding to a single particle. Clusters hereby may have more than one PED. The assigned energy  $E_i$  for each particle  $i$  is the sum of all energy depositions belonging to a PED. Furthermore, a weighted average over all crystal hits will give a polar angle  $\theta_i$  and azimuthal angle  $\phi_i$  [Dah08]. If a charged particle only hits the inner detector both angles can be calculated from at least two timely correlated fiber hits [GP08] but no energy information is gained. Finally, all informations are combined to form the four momentum of a final state particle, assuming it is massless

$$p_i = \begin{pmatrix} E_i \\ E_i \cos \phi_i \sin \theta_i \\ E_i \sin \phi_i \sin \theta_i \\ E_i \cos \theta_i \end{pmatrix}. \quad (3.2)$$

This four momentum is wrong if the detected particle is a proton since it has non vanishing mass or in case no energy has been measured at all. However, the protons energy information is not a reliable quantity since they often leave the calorimeters without depositing their entire energy. The assigned four momenta are thus only used to access their angular information. In addition to energy and momentum the CBELSA/TAPS setup allows to assign time and charge information for all particles hitting the inner, forward or MiniTAPS detector<sup>1</sup>.

### 3.2 Preselection and charge cut

Since the polarization degree can only be evaluated reliably up to 1800 MeV and the production threshold for  $\eta'$  mesons is  $E_\gamma = 1447$  MeV [Wor+22], the beam photon energy range was restricted to 1400 to 1800 MeV from the very beginning. The measured events are then generally classified depending on the number of PEDs. If three final state particles are measured, they are referred to as

<sup>1</sup> Actually, the experiment has been upgraded to provide time information for particles hitting the Crystal Barrel as well in 2017 [Urb17].

3PED events. Low energy protons however may either be only detected in the scintillators of the inner, forward or MiniTAPS detector – giving directional information from scintillator bar hits only (2.5 PED) – or lost entirely (2 PED). Only 3PED events were analyzed since the additional background contributions from 2PED and 2.5PED events exceeded the additional signal contributions. It is worth noting that 3PED events are significantly dominant for  $\eta' \rightarrow \gamma\gamma$  reactions; the production threshold for  $\eta'$  mesons at  $E_\gamma = 1447$  MeV [Wor+22] is so high energetic that the recoil proton will likely be detected. Figure 3.1 shows the distribution of the different event classes for  $\eta' \rightarrow \gamma\gamma$  production in MONTE CARLO data, with a clear preference towards 3PED events. To further improve the signal to

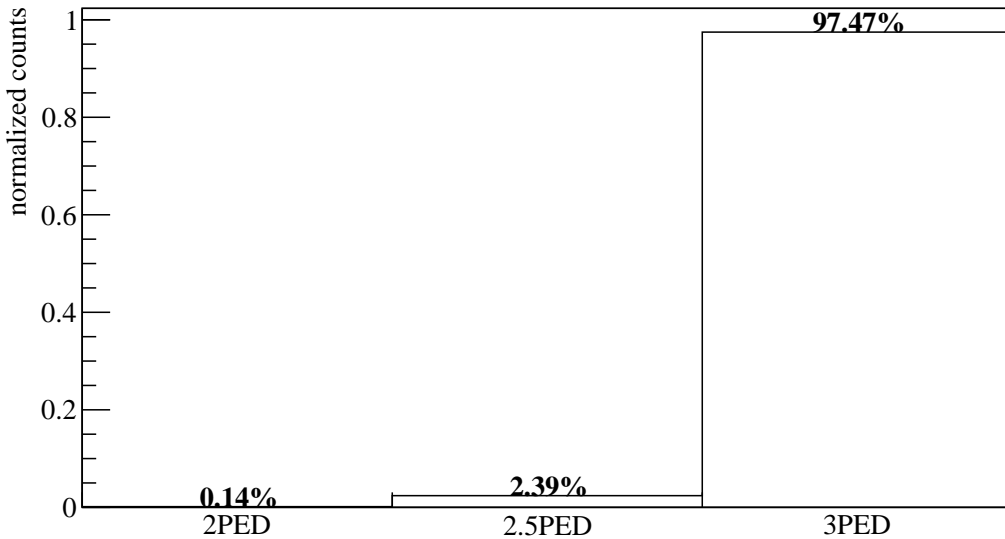


**Figure 3.1:** Distribution of event classes in  $\eta' \rightarrow \gamma\gamma$  production

background ratio, the charge information of the final state particles was utilized in the next step. In particular, to select  $\eta' \rightarrow \gamma\gamma$  reactions, one charged and two uncharged particles in the final state were demanded.

### 3.3 Time of particles

Due to its high count rate the tagging system (see section 2.1.2) will not only record beam photons which produce the detectable final state particles, but also several uncorrelated ones. To select only beam photons which will induce a photoproduction process the time information of the detected particles is used. It is shown in figure 3.2 for all particles involved in 2.5PED and 3PED events of  $\eta'$  photoproduction. In all cases prompt peaks centered around 0 ns (the trigger time) are visible. Since the final state photons move with velocity  $c$  their timing information does not underlie fluctuations, as is the case for the final state proton on the contrary. The tagged, uncorrelated beam photons are visible as flat background underneath the prompt peak in the time of the beam photon. Naturally, only coincident events may be referred to as  $\gamma p \rightarrow p\eta'$  reaction candidates for the further analysis and thus only events with time information of at least one final state particle are kept. Photons need to be

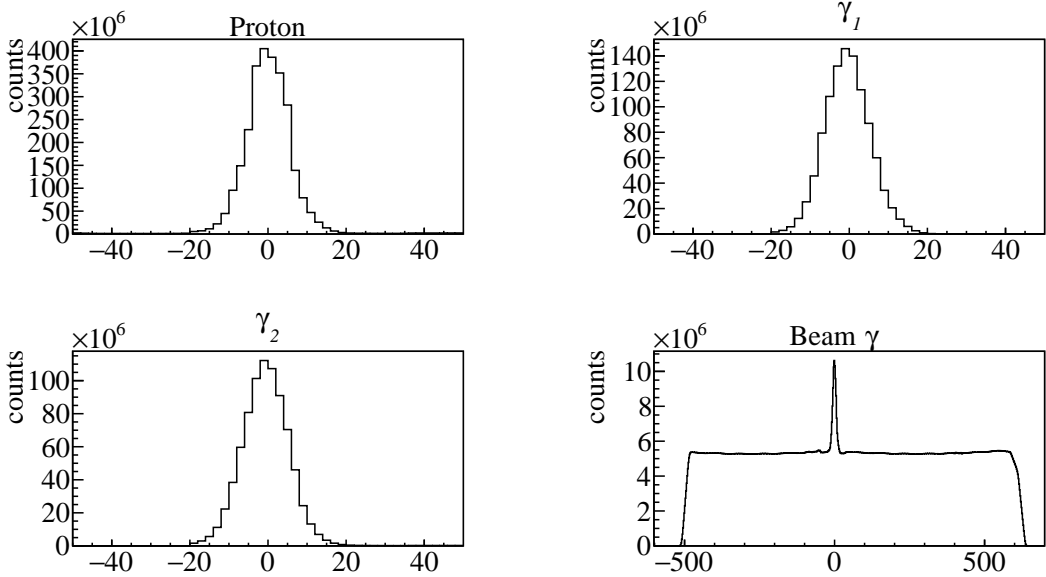


**Figure 3.2:** Time information of all final state particles and the beam photon for 3PED  $\eta'$  production

detected in the MiniTAPS or forward detector to acquire time information. To determine coincidence it is convenient to define the *reaction time*

$$t_{\text{reaction}} = \begin{cases} t_{\text{beam}} - t_{\text{meson}} & \text{meson time exists} \\ t_{\text{beam}} - t_{\text{recoil}} & \text{meson time does not exist,} \end{cases} \quad (3.3)$$

where the meson time  $t_{\text{meson}}$  is appointed either the averaged time of both decay photons or the time of a single photon if only one photon has time information.  $t_{\text{beam}}$  and  $t_{\text{recoil}}$  are the time of the beam photon and recoil proton, respectively. Figure 3.3 shows the reaction time for 2.5PED and 3PED events; a clear prompt peak centred at 0 is visible, the colored area indicates the chosen range of  $t_{\text{reaction}} \in [-8, 5]\text{ns}$ . However, this cut still contains random time background underneath the prompt peak. This may be accounted for by *sideband subtraction*, assuming the background is flat. All events residing in the prompt peak with  $t_r \in [-8, 5]\text{ns}$  will be assigned a weight of  $w_p = +1$  while sideband events with  $t_r \in [-200, -100]\text{ns} \vee t_r \in [100, 200]\text{ns}$  will be assigned a weight of  $w_s = -\frac{13}{200}$ . Events with  $t_r$  neither in the sideband nor in the prompt peak get assigned a weight of  $w = 0$ . Any histogram  $N$  that is filled in the following will then consist of prompt peak events  $N_{\text{prompt}}$  and sideband events  $N_{\text{sideband}}$

$$N = N_{\text{prompt}} + w_s \cdot N_{\text{sideband}},$$

such that the random time background underneath the prompt peak is subtracted. In addition, the time difference between meson and proton and between the two photons is demanded to be within  $[-10, 10]\text{ns}$ . All described cuts to the data, including the sideband subtraction are referred to as the *time cut* in the following.

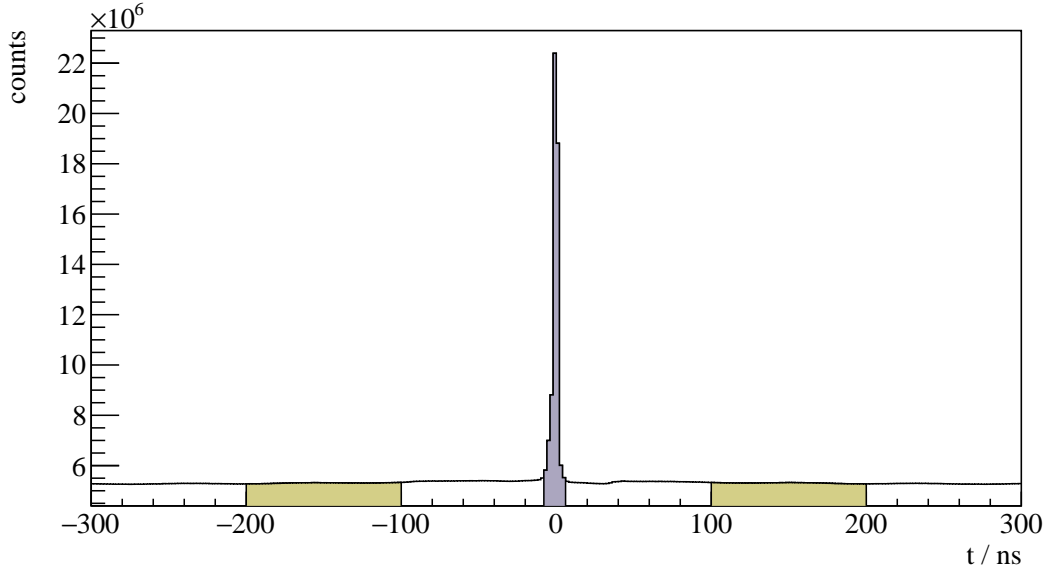


**Figure 3.3:** Reaction time  $t_r$  for 3PED and 2.5PED  $\eta'$  production. The yellow colored regions indicate the sidebands while the purple colored interval is the selected prompt peak.

## 3.4 Kinematic constraints

Up to now mainly combinatorial background caused by the amount of beam photon candidates was discussed. However one can derive kinematical constraints from energy and momentum conservation to exclusively select the desired reaction. The derivation is discussed first, followed by the determination of the derived cut conditions.

### 3.4.1 Derivation of cut conditions

Let  $p_{\text{beam}}$  and  $p_p$  be the four momenta of the initial state beam photon and proton, respectively. Then it holds

$$p_{\text{beam}} + p_p = p_{\text{recoil}} + p_{\text{meson}}, \quad (3.4)$$

with  $p_{\text{recoil}}$  being the momentum of the recoiling proton and  $p_{\text{meson}}$  the meson momentum.

#### Coplanarity

In the initial state there is vanishing transverse momentum  $p_{xy}$  since the target protons are at rest and the beam photon impinges in  $z$ -direction. Naturally, this transverse momentum has to vanish in the final state as well, such that

$$\mathcal{P}_{xy} [p_{\text{recoil}} + p_{\text{meson}}] = 0, \quad (3.5)$$

where  $\mathcal{P}_{xy}$  is the projection operator to the transverse plane. Equation (3.5) is valid if and only if meson and proton lie back to back (coplanar) in the  $x$ - $y$  plane, which is quantified by the difference of

their azimuthal angles  $\phi_{\text{meson}}$  and  $\phi_{\text{recoil}}$  being  $180^\circ$  in the laboratory-frame

$$\Delta\phi := \phi_{\text{meson}}^{\text{LAB}} - \phi_{\text{recoil}}^{\text{LAB}} \stackrel{!}{=} 180^\circ. \quad (3.6)$$

### Polar angle difference

If all initial and final state momenta are measured, the reaction described by equation (3.4) is *overdetermined*, such that one final state particle can be treated as a "missing particle"  $X$  with momentum  $p_X$ :

$$p_X = p_{\text{beam}} + p_p - p_{\text{meson}}. \quad (3.7)$$

One can then use the polar angle difference

$$\Delta\theta := \theta_{p_X}^{\text{LAB}} - \theta_{p_{\text{recoil}}}^{\text{LAB}} \stackrel{!}{=} 0 \quad (3.8)$$

as a further constraint to the data.

### Missing mass

The previously described angular cuts are only applicable if all final state particles have been detected. Independently of the detection of the recoil proton the mass of the missing particle  $m_X^2 = p_X^2$  can be determined and compared with the proton mass of  $m_p = 938.27 \text{ MeV}$  [Wor+22]. From Eq. (3.7) it follows that

$$m_X = \sqrt{(E_\gamma + m_p - E_{\text{meson}})^2 - p_{x,\text{meson}}^2 - p_{y,\text{meson}}^2 - (E_\gamma - p_{z,\text{meson}})^2}. \quad (3.9)$$

### Invariant mass

The measurement of the invariant mass of the two final state photons does also not require the measurement of the recoil proton. The knowledge of both decay photon four-momenta  $p_{\gamma_1}$  and  $p_{\gamma_2}$  suffices, since

$$m_{\text{meson}} = \sqrt{p_{\text{meson}}^2} = \sqrt{(p_{\gamma_1} + p_{\gamma_2})^2} = \sqrt{2E_{\gamma_1}E_{\gamma_2}(1 - \cos\alpha_{\gamma_1\gamma_2})}, \quad (3.10)$$

where  $E_{\gamma_i}$  are the measured photon energies and  $\alpha_{\gamma_1\gamma_2}$  is the angle between the two decay photon momenta. To select only  $\eta'$  candidates  $m_{\text{meson}} = m_{\eta'} = 957.78 \text{ MeV}$  is demanded. Remarkably, the cut on the invariant mass of the final state photons is the only one to uniquely select  $\eta'$  production candidates so far. All other cuts apply similarly to arbitrary meson photoproduction.

#### 3.4.2 Determination of cut ranges

The constraints described in the previous section must not be understood as strict equalities, cf. equations (3.5),(3.8),(3.9) and (3.10). The quantities of interest will rather describe distributions around the desired value, such that confidence intervals may be extracted by fitting to said distributions. This is done iteratively:

Let  $C_I^\chi$  be the cut operator that restrains the data  $\mathcal{D}$  such that the (generic) cut variable

$$\chi \in \{\Delta\theta, \Delta\phi, m_X, m_{\text{meson}}\}$$

lies in the interval  $I \subseteq \mathbb{R}$ , such that

$$C_I^\chi : \mathcal{D} \mapsto \mathcal{D}_{\chi \in I}. \quad (3.11)$$

After a first inspection of the data, initial guesses for the intervals  $I, J, K, L$  corresponding to the quantities  $\Delta\theta, \Delta\phi, m_X, m_{\text{meson}}$ , respectively, are made. Having established estimates for the cut ranges, new ones are estimated by investigating the distribution of one cut variable obtained from the data while all other cut variables are constrained to the previously determined intervals. For example

$$\Delta\theta \left( C_J^{\Delta\phi} C_K^{m_X} C_L^{m_{\text{meson}}} \mathcal{D} \right) \sim \text{normal}(\mu, \sigma),$$

where  $\mu \approx 0$ . This is done (with some adjustments to the fit function) for each cut variable. The parameters of the gaussian are determined from a  $\chi^2$  fit and used to assign new cut ranges. Simultaneously, Monte-Carlo (MC) data of relevant final states are fitted to match the measured values bin-wise. This is done on the one hand to check consistency between measured and MC data and on the other hand used to determine contributing background reactions. First, all mesonic final states that decay into two photons are considered, i.e.  $p\pi^0, p\eta, p\eta'$ , since the according peaks in the invariant mass spectrum will be visible. Also, a peak at the mass of the  $\omega$  (vector)-meson  $m_\omega$  will be visible; this stems from photoproduction reactions  $p\omega \rightarrow p\pi^0\gamma \rightarrow p3\gamma$  where one low energetic final state photon is lost, such that the reconstructed invariant mass still estimates the  $\omega$  mass. Further, one should investigate the impact of neutral final states, where some of the final state photons may get lost during reconstruction, as can be observed for  $p2\pi^0, p\pi^0\eta, p3\pi^0$ <sup>2</sup> production. Lastly, possible misidentification of charged particles in very frequent reactions which then mimic a  $p\gamma\gamma$  final state are examined, such as  $p\pi^+\pi^-$  and  $n\pi^+$ . Table 3.2 lists all employed MC reactions and their respective final state particles, as well as a short explanation why the particular reaction was included in the fit.

Photoproduction reaction	Final state particles	Explanation
$p\pi^0$	$p\gamma\gamma$	prominent peak in the invariant mass spectrum
$p\eta$	$p\gamma\gamma$	
$p\omega$	$p\pi^0\gamma \rightarrow p3\gamma$	
$p\eta'$	$p\gamma\gamma$	
$p2\pi^0$	$p4\gamma$	lost photons cause a "3-particle" final state
$p\pi^0\eta$	$p4\gamma$	
$p3\pi^0$	$p6\gamma$	
$p\pi^+\pi^-$	$p\pi^+\pi^-$	misidentification of charged particles, large $\sigma$
$n\pi^+$	$n\pi^+$	

**Table 3.2:** Examined MC reactions that were used in sum for the fit

To minimize the influence of any background reactions, the cut ranges are determined via fits to the scaled MC data of the  $\eta'$  final state. Table 3.3 shows which fit function and cut range was used for

<sup>2</sup> all mesons  $m$  decaying into two photons is implied:  $m \rightarrow \gamma\gamma \forall m$

each cut variable. The newly obtained intervals  $\mathcal{I}', \mathcal{J}', \mathcal{K}', \mathcal{L}'$  serve again as input for the previous

cut variable	fit function	interval range
$\Delta\theta$	GAUSS	$\mathcal{I}' = [\mu - 3\sigma, \mu + 3\sigma]$
$\Delta\phi$	GAUSS	$\mathcal{J}' = [\mu - 3\sigma, \mu + 3\sigma]$
$m_X$	NOVOSIBIRSK [Ike+00]	$\mathcal{K}' = [\mu - 2\sigma, \mu + 2\sigma]$
$m_{\text{meson}}$	GAUSS	$\mathcal{L}' = [\mu - 2\sigma, \mu + 2\sigma]$

**Table 3.3:** Fit functions and cut ranges for each kinematic variable

step. This is repeated until a certain convergence is reached, which is usually the case after two or three iterations. Since the cut ranges may vary depending on beam energy and meson direction, they are determined in bins of the beam energy and the polar angle of the meson in the center of mass system (CMS)

$$(E_\gamma, \cos \theta_{\eta'}^{\text{CMS}})^3.$$

Respecting the  $\eta'$  final state statistics, a binning of  $\Delta E_\gamma = 100 \text{ MeV}$  and  $\Delta \cos \theta = 1/3$  was chosen, spanning the energy range of 1500 to 1800 MeV. The theoretically accessible lower limit in the beam energy is provided by the production threshold of  $\eta'$  mesons at 1447 MeV [Wor+22]. Yet, the binning has to comply with the upper beam energy limit which is bound from above<sup>4</sup> by the position of the coherent edge of the beamtime. It is given by 1700 MeV and 1800 MeV for the July/August and September/October beam times, respectively. If one were to include the production threshold into the analyzed range using the same binning, more background than  $\eta'$  events are collected from the beam energy bin 1400 to 1500 MeV because the cross section  $\sigma(\gamma p \rightarrow p\eta')$  slowly rises to its maximum in this range [Cre+09], hence the chosen binning starts at 1500 MeV.

## Coplanarity

Figure 3.4 shows the coplanarity spectra for the energy bin  $1500 \text{ MeV} \leq E_\gamma < 1600 \text{ MeV}$  and all angular bins. The data points are visualized by the open circles with error bars, while the black solid histogram is a fit of  $\eta' \rightarrow \gamma\gamma$  MC. As expected, a clear peak is visible at  $\Delta\phi = 180^\circ$ , which shows only slight dependence on beam energy and meson direction. A  $3\sigma$  interval obtained from a gaussian fit is indicated by the dashed red lines. Note that only MC spectra of the  $\eta'$  final state were fitted to the data since the coplanarity gives little reference points for a correct estimation of other final states that may contribute.

## Polar angle difference

Since the meson direction correlates with the detector(s) that the final state photons hit, the polar angle difference depicts a clear directional dependence as can be seen in figure 3.5 for the energy bin  $1500 \text{ MeV} \leq E_\gamma < 1600 \text{ MeV}$  and all angular bins. In the CMS frame, meson and proton are emitted back to back. Thus, if the meson is emitted in backward direction ( $\cos \theta \sim -1$ ), the proton will be

<sup>3</sup> If not otherwise specified, from now on  $\cos \theta = \cos \theta_{\eta'}^{\text{CMS}}$

<sup>4</sup> Significantly beyond the coherent edge, the systematic error for the beam polarization degree gets too large (> 10%) while at the same time the polarization degree decreases rapidly (< 10%)

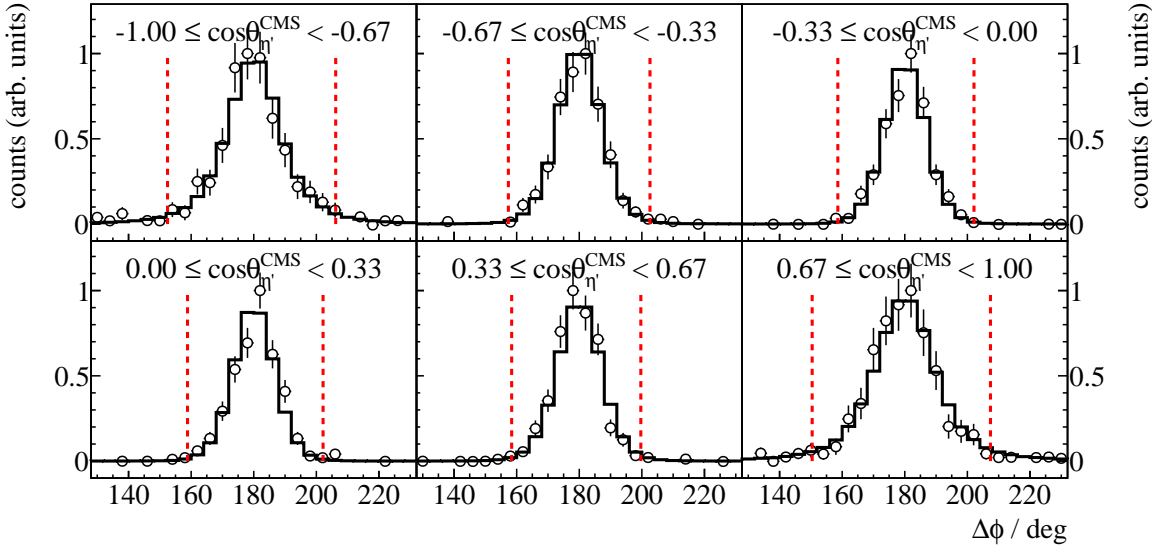


**Figure 3.4:** Coplanarity of the  $p\eta'$  final state with all other cuts applied for the energy bin  $1500 \text{ MeV} \leq E_\gamma < 1600 \text{ MeV}$ . The vertical dashed lines show the cut ranges obtained from a gaussian fit to the data (open circles). The solid black histograms represent fitted MC data of  $\eta' \rightarrow \gamma\gamma$

detected either in the forward or MiniTAPS detector, which have a better angular resolution than the Crystal Barrel calorimeter, leading to narrower distributions of  $\Delta\theta$ . The determined cut ranges are  $3\sigma$  intervals obtained from a gaussian fit to the data and are indicated by the red dashed lines. As before, no other than  $\eta'$  MC are fitted to the spectra.

### Missing mass

The missing mass spectra allow a first investigation of possible background reactions that pass the event selection. For all angular bins of the first energy bin the missing mass is shown in figure 3.6; again, the open circles are the data points with corresponding statistical error bars. The solid colored histograms are fitted MC spectra of different possible background contributions while the black histogram is the signal contribution of  $\eta' \rightarrow \gamma\gamma$  photoproduction. The turquoise histogram is the sum of all MC histograms. Generally, most of the data can be described by the  $\eta'$  MC alone, but especially towards higher masses (and higher beam energies) background contributions extend the missing mass peak as flat background. These are reactions where the reconstructed meson mass  $m_{\text{meson}}^2 = E_{\text{meson}}^2 - \vec{p}_{\text{meson}}^2$  is smaller than the  $\eta'$  mass, resulting in larger values for the missing mass. Judging from the fit to the missing mass,  $2\pi^0$  and/or  $\pi^0\eta$  photoproduction may describe the background as both show similar shapes. All other previously mentioned reactions (table 3.2) do not contribute significantly. However because the spectrum consists only of a narrow peak and the background is flat, fitting the missing mass spectra does not provide many good reference points for the fit to differentiate between contributing reactions. Few events per bin further complicate this. Better conclusions can be drawn from the invariant mass spectra as is discussed in the following. In particular, fitting the invariant mass spectra may reveal background contributions where the fit of missing mass fails to find any, as is

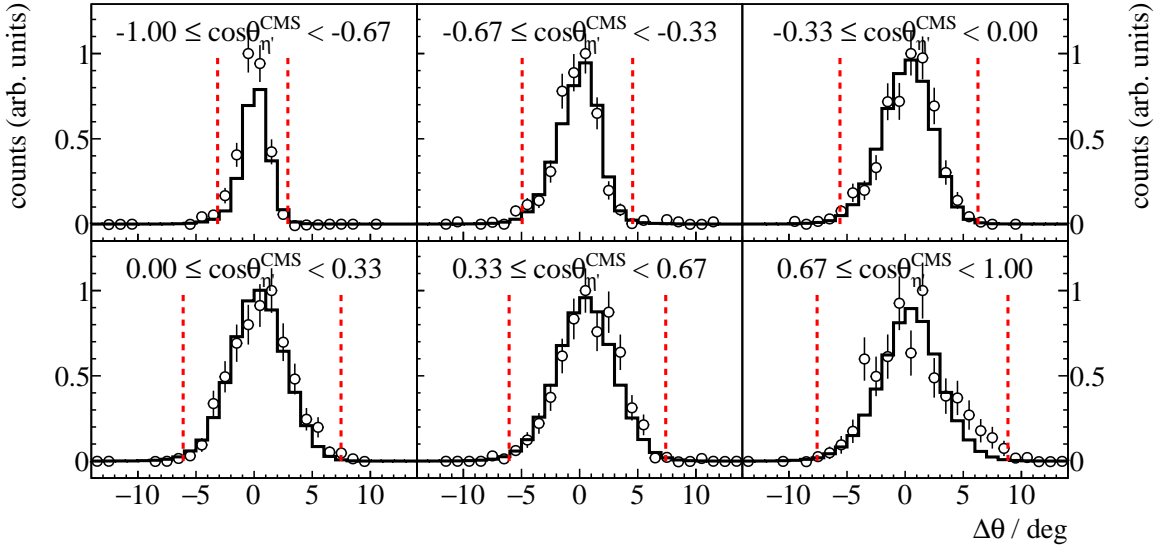


**Figure 3.5:** Polar angle difference of the  $p\eta'$  final state with all other cuts applied for the energy bin  $1500 \text{ MeV} \leq E_\gamma < 1600 \text{ MeV}$ . The vertical dashed lines show the cut ranges obtained from a gaussian fit to the data (open circles). The solid black histograms represent fitted MC data of  $\eta' \rightarrow \gamma\gamma$

the case for the bins in backward direction. The cut ranges for the missing mass are obtained from a Novosibirsk [Ike+00] fit to the data since the missing mass distribution is slightly asymmetric. However, since the tail parameter is small, still a symmetric cut of  $\pm 2\sigma$  was chosen. It was chosen narrower than the angular cuts to retain less events from background reactions.

### Invariant mass

Investigating the invariant mass spectrum of the final state photons allows to illustrate the impact of the event selection so far. As it has been mentioned all cuts considered up to this point apply to arbitrary meson photoproduction. This means that the invariant mass spectrum will depict peaks belonging to mesons produced in the considered beam energy range. This is shown in Figure 3.7 giving an overview over all energy and angular bins. All other cuts have been applied. The open circles represent data points and the different colored histograms MC data from relevant competing final states while the black histogram shows the signal contribution of  $\eta'$  MC. The turquoise histogram is the sum of all MC contributions and describes the data very well. It has again been found that no other than the shown final states contribute significantly or improve the description of data by MC spectra. As expected one can observe peaks belonging to  $\pi^0, \eta, \omega$  and  $\eta'$  photoproduction. A flat background underneath the complete spectrum is realized by  $2\pi^0$  and  $\pi^0\eta$  final state photons that have been wrongfully combined to two photons. Remarkably, the  $\pi^0, \eta$  and  $\omega$  invariant mass distributions also depict long tails towards lower and higher masses, although they contribute only marginally to the sum of all MC spectra (note the logarithmic y-Scale). At least for  $\pi^0$  production this can be explained by the fact that one low energetic photon is lost during reconstruction while the (high energetic) proton wrongfully creates two tracks of which one is then combined with the other photon

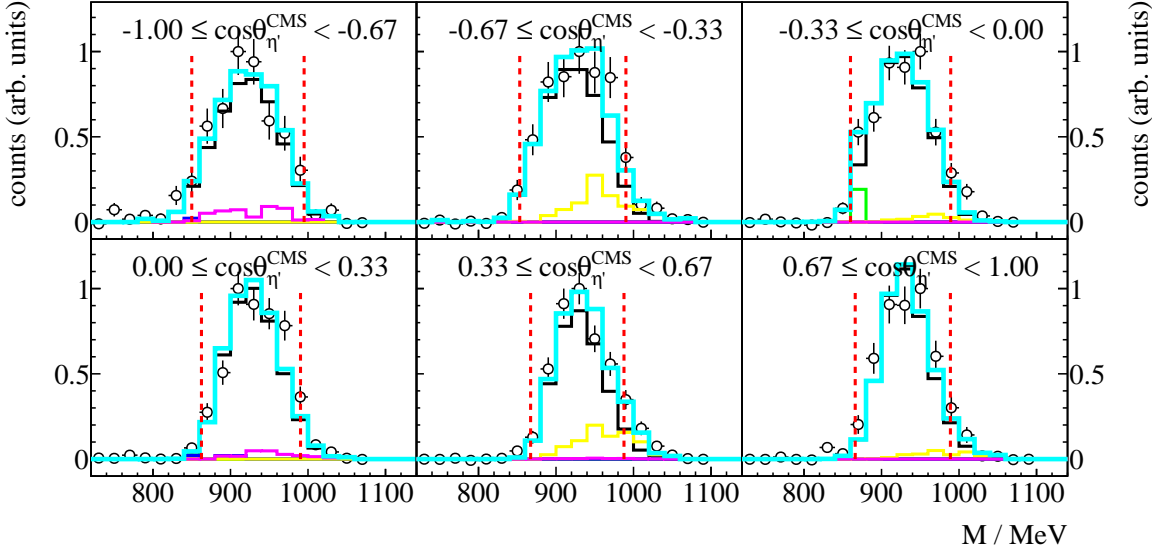


**Figure 3.6:** Missing mass of the  $p\eta'$  final state with all other cuts applied for the energy bin  $1500 \text{ MeV} \leq E_\gamma < 1600 \text{ MeV}$ . The vertical dashed lines show the cut ranges obtained from a fit to data (open circles) employing a Novosibirsk function. The solid colored histograms represent fitted MC data from relevant photoproduction reactions: in black  $\eta'$ , in green  $\pi^0$ , in red  $\eta$ , in blue  $\omega$ , in yellow  $2\pi^0$ , magenta  $\pi^0\eta$ . The turquoise histogram is the sum of all MC histograms.

as meson candidate [Afz19]. It is likely similar mechanisms are responsible for the other reactions. To finally select only  $\eta'$  photoproduction event candidates the invariant mass cut is determined again in bins of beam energy and meson polar angle. This is shown in figure 3.8 for the first energy bin with all angular bins. Here, the same color coding as before applies, but the range of the invariant mass has been reduced to only cover the  $\eta'$  peak for visibility's sake. Additionally the cut ranges, representing a  $2\sigma$  interval obtained from a gaussian fit to the  $\eta'$  MC, are shown as dashed, red lines. Considering the statistics the MC spectra still describe the data well. It is found again that the significant background contributions in the invariant mass range of interest are given by  $2\pi^0$  and  $\pi^0\eta$  photoproduction.

Appendix B.2 shows all kinematic bins for each cut variable with the corresponding cut ranges.

### 3.4.3 Quality of event selection

In order to investigate the impact of the applied cuts the detector and analysis acceptance  $A(E_\gamma, \cos \theta)$  can be investigated. It is defined as the ratio of reconstructed events  $N^{\text{rec}}(E_\gamma, \cos \theta)$  to generated events  $N^{\text{gen}}(E_\gamma, \cos \theta)$

$$A := \frac{N^{\text{rec}}(E_\gamma, \cos \theta)}{N^{\text{gen}}(E_\gamma, \cos \theta)} \quad (3.12)$$

and is shown in figure 3.9. Acceptance holes are visible in very forward and in backward direction which can be contributed to events where the proton escapes the calorimeters or is absorbed in insensitive material. Also, events close to threshold are unlikely to be reconstructed which can also be

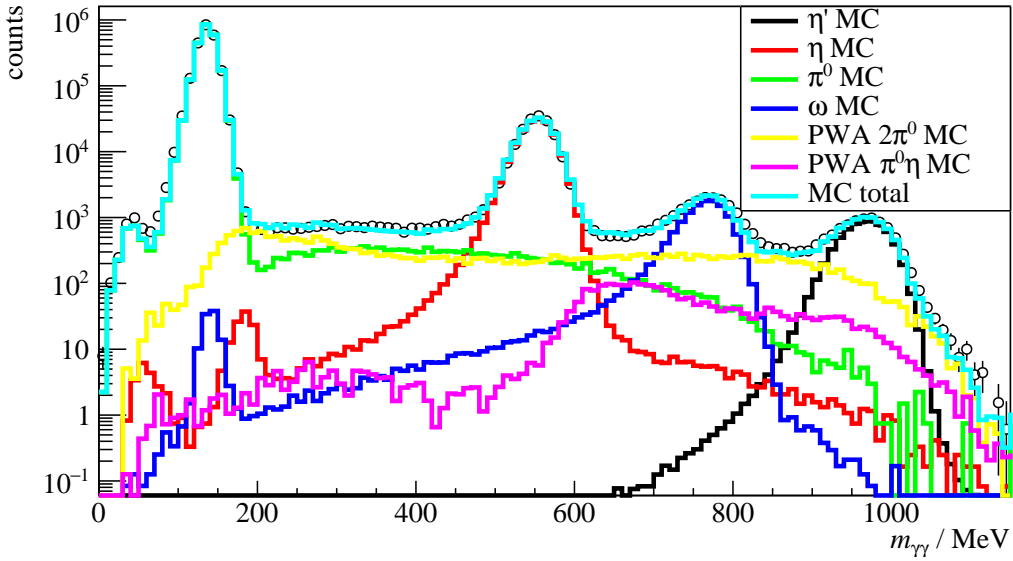


**Figure 3.7:** Invariant mass of the  $p\eta'$  final state with all other cuts applied for all energy and angular bins. The open circles represent the measured data, the solid colored histograms fitted MC data from relevant photoproduction reactions: in black  $\eta'$ , in green  $\pi^0$ , in red  $\eta$ , in blue  $\omega$ , in yellow  $2\pi^0$  and in magenta  $\pi^0\eta$ . The turquoise histogram is the sum of all MC histograms.

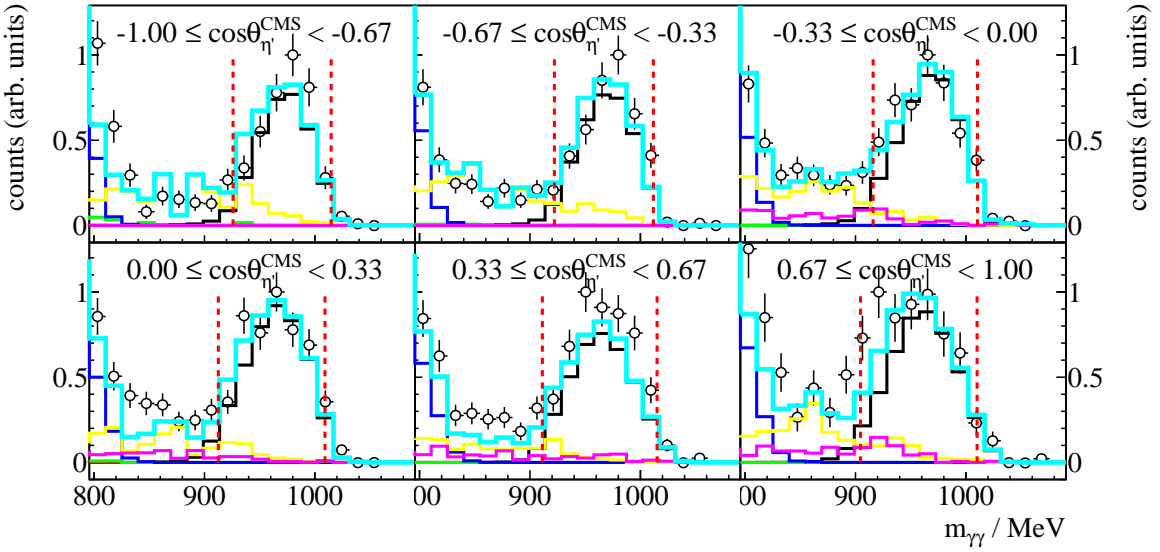


**Figure 3.8:** Invariant mass of the  $p\eta'$  final state with all other cuts applied for the energy bin  $1500 \text{ MeV} \leq E_\gamma < 1600 \text{ MeV}$ . The vertical dashed lines show the cut ranges obtained from a gaussian fit to the  $\eta'$  MC data (solid black histogram). The open circles represent the measured data, the solid colored histograms fitted MC data from relevant photoproduction reactions: in black  $\eta'$ , in green  $\pi^0$ , in red  $\eta$ , in blue  $\omega$ , in yellow  $2\pi^0$  and in magenta  $\pi^0\eta$ . The turquoise histogram is the sum of all MC histograms.

explained by low energy protons and/or low energy photons. A maximum acceptance of  $\tilde{A} \approx 0.61$  is reached which can be understood considering the cuts that have been made; each  $3\sigma$  cut retains 99% of events and each  $2\sigma$  cut 95%. Assuming detection efficiencies of 90% for the two uncharged photons and 85% for the charged proton ([Afz19; Har17]) it is evident that  $0.99^2 \cdot 0.95^2 \cdot 0.9^2 \cdot 0.85 \approx 0.61$ . In total,  $8 \cdot 10^3 \eta'$  events were extracted which nonetheless still contain background contaminations.

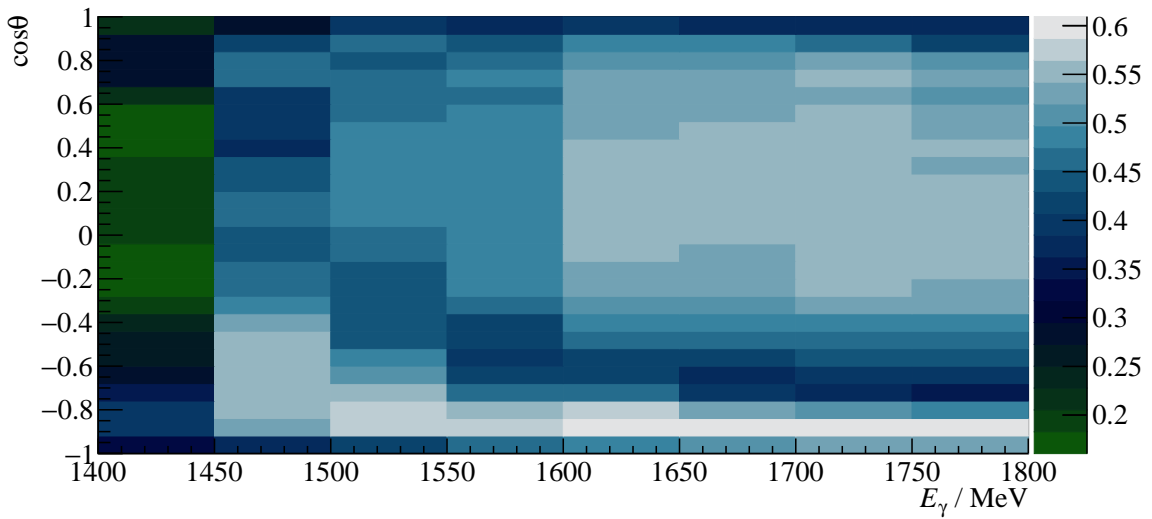


**Figure 3.9:** Acceptance for the reaction  $\gamma p \rightarrow p\eta'$  after all cuts that have been discussed so far for 2.5PED and 3PED events

In order to take this into account in the later analysis the fraction of background is determined for each bin in beam energy and meson polar angle. It is estimated as the fraction of total background MC events to total MC events and shown in figure 3.10. For most bins around 15% of all events are misidentified as  $\eta'$  events. Especially at very forward  $\cos \theta \rightarrow 1$  and backward  $\cos \theta \rightarrow -1$  angles the background contributions are significantly higher, reaching up to 45%, which can be traced back to the angular distribution of  $\frac{d\sigma}{d\Omega} (\gamma p \rightarrow p\eta')$  [Cre+09].

## 3.5 Investigation of background and additional cuts

So far the background reactions in the  $\eta'$  cut ranges have been discussed only phenomenologically as they describe the measured invariant mass spectra best. In the following the plausibility and causality of these background contributions shall be discussed. Furthermore it is investigated if the found background contributions may be reduced or eliminated by additional cut conditions.

### 3.5.1 Inspecting plausibility of background reactions

To evaluate the likelihood that the background contributions are made up of  $2\pi^0$  or  $\pi^0\eta$  production events the respective production cross sections in the inspected beam energy region and branching

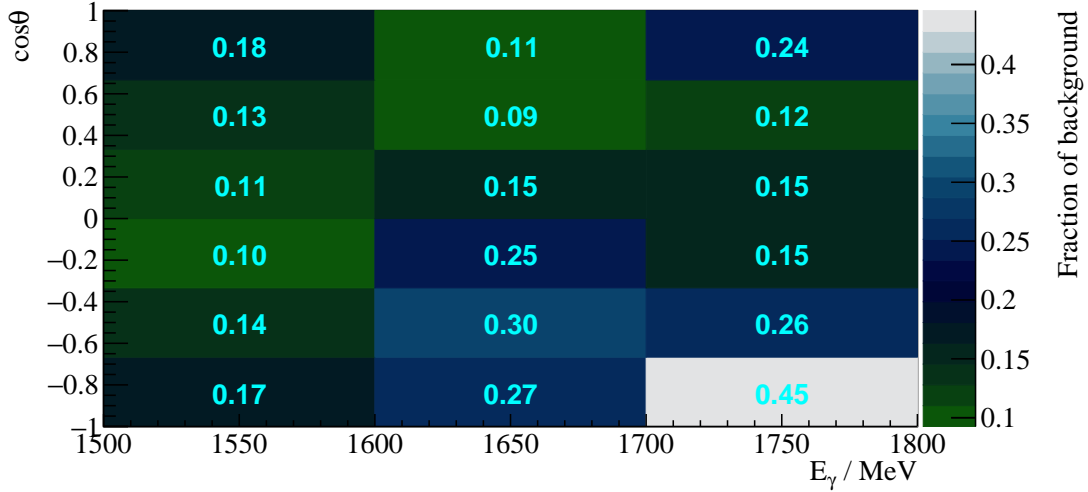


**Figure 3.10:** Fraction of background events in the analyzed beam energy and angular bins.

ratios (BR) to purely photonic final states are examined for all considered reactions, see table 3.4. Also displayed are the maximum acceptance  $\tilde{A}$ , which is additionally shown in figure 3.11 for the main background contributions, and the expected background to signal ratio. Since the total number of events is proportional to the cross section  $\sigma$ , branching ratio BR and acceptance  $\tilde{A}$ , the ratio of reconstructed background to signal events is then given by

$$R = \frac{\sigma \cdot \text{BR} \cdot \tilde{A}}{\sigma_{\eta'} \cdot \text{BR}_{\eta' \rightarrow \gamma\gamma} \cdot \tilde{A}_{\eta'}} = \frac{\sigma \cdot \text{BR} \cdot \tilde{A}}{1 \mu\text{b} \cdot 0.023 \cdot 0.61}. \quad (3.13)$$

Almost all reactions exceed  $\eta'$  photoproduction in cross section and have a higher BR to purely photonic final states. At the same time the acceptance is almost vanishing, proving that the kinematic cuts are generally very effective. However, despite vanishing acceptance, significant background ratios are expected for  $2\pi^0$  and  $\pi^0\eta$  production, based on equation (3.13). All other reactions only contribute marginally after all cuts and their contribution towards the beam asymmetry can be neglected.

Although less than 0.2% of two meson production reactions are misidentified as  $\eta'$  events they make up a notable portion of background in  $\eta'$  data, considering the according branching ratios and cross sections showed. Note that only maximum acceptances and approximations for the cross sections have been used for estimating the ratio of background events to signal events. As the acceptance and cross sections may vary depending on kinematic bin, also the actual amount of background events may yet vary. Especially in backwards direction the acceptance of  $\gamma p \rightarrow p\eta'$  events decreases due to escaping protons while at the same time the acceptance for  $\gamma p \rightarrow p\pi^0\pi^0 \rightarrow p4\gamma$  and  $\gamma p \rightarrow p\pi^0\eta \rightarrow p4\gamma$  increases in this region towards higher beam energies, see Figure 3.11.

Nevertheless, the ratios  $R$  are useful to determine the order of magnitude of background contributions. Furthermore the maximum determined ratio of background events  $b$  to total events ( $s + b$ ) (Figure

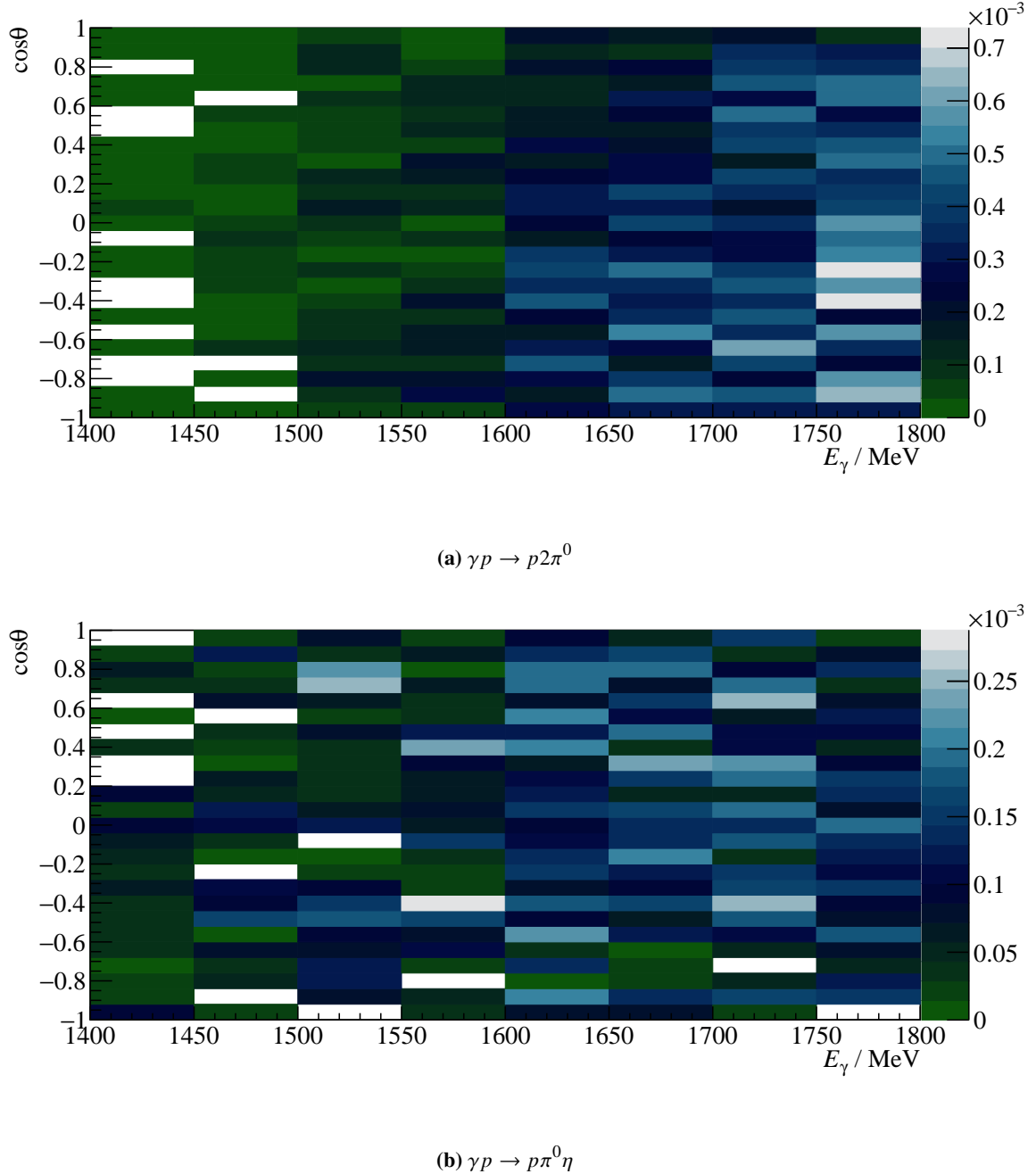


**Figure 3.11:** Acceptance for possible background contributions

reaction	$\sigma / \mu\text{b}$	BR[Wor+22]	$\tilde{A}$	$R$
$\gamma p \rightarrow p\eta' \rightarrow p\gamma\gamma$	$\approx 1$ [Cre+09]	0.023	0.61	
$\gamma p \rightarrow p2\pi^0 \rightarrow p4\gamma$	$\lesssim 5$ [Die+20]	0.9765	$2 \cdot 10^{-3}$	0.72
$\gamma p \rightarrow p\pi^0\eta \rightarrow p4\gamma$	$\lesssim 3$ [Käs+18]	0.3948	$1 \cdot 10^{-3}$	0.08
$\gamma p \rightarrow p\pi^0 \rightarrow p\gamma\gamma$	$\approx 6$ [Bar+05]	0.9882	$8.3 \cdot 10^{-7}$	$4 \cdot 10^{-4}$
$\gamma p \rightarrow p\eta \rightarrow p\gamma\gamma$	$\approx 2$ [Cre+09]	0.3996	$1 \cdot 10^{-7}$	$7 \cdot 10^{-6}$
$\gamma p \rightarrow p3\pi^0 \rightarrow p6\gamma$	$\gtrsim 3$ [Sta+11]	0.9650	0	0
$\gamma p \rightarrow p\omega \rightarrow p3\gamma$	$\approx 1$ [Mur+20]	0.0825	$1 \cdot 10^{-6}$	$7 \cdot 10^{-6}$
$\gamma p \rightarrow p\pi^+\pi^-$	$\approx 40$ [Str+76]	-	$1.3 \cdot 10^{-6}$	0.003
$\gamma p \rightarrow nn\pi^+$	$\approx 4$ [Dug+09]	-	$1.3 \cdot 10^{-7}$	$3.8 \cdot 10^{-5}$

**Table 3.4:** Total cross sections  $\sigma$  in the energy range 1500 to 1800 MeV, branching ratios (BR) to  $n\gamma$  final states, maximum acceptance  $\tilde{A}$  for signal and possible background contributions as well as the expected signal to background ratio  $R$ . References [Die+20] and [Käs+18] give the cross sections only up to roughly 1500 MeV, the given values are thus upper bounds. For the same reason, from reference [Sta+11] only a lower bound can be estimated. For all other reactions a rough mean over the energy bins of interest is built. If the references provide only differential cross sections a crude integration in each angular bin is performed. In case only very few ( $O(10^1)$ ) decays pass event selection, the acceptance is built in one global bin only for the respective reactions. This is indicated by the horizontal line.

3.10) and the corresponding value for  $R$

$$\delta = \frac{b}{s+b} = 0.45 \quad \Leftrightarrow \quad R = \frac{b}{s} = \frac{\delta}{1-\delta} = 0.81 \quad (3.14)$$

are in very good agreement with the estimated expectations from table 3.4. This justifies the previous empirical assumption to only include  $2\pi^0$  and  $\pi^0\eta$  MC as background reactions in the fit to describe the data.

### 3.5.2 Misidentification of background reactions

It has been reasonably established that the main background reactions that escape the  $\eta'$  event selection cuts are realized by  $2\pi^0$  and  $\pi^0\eta$  production. However, it remains to explain why a four-photon final state is misidentified as  $\eta'$  event so that background reducing cuts may be found. In order to do so the MC simulations of the respective final states were investigated. One observes, that for those events that passed the  $\eta'$  cuts the generated photon energies for two photons often were of order  $E_\gamma \sim O(10^1 \text{ MeV})$  and the other two of order  $E_\gamma \sim O(10^2 \text{ MeV})$ <sup>5</sup>. The reconstructed energies however only displayed energies of order  $E_\gamma \sim O(10^2 \text{ MeV})$ . During the reconstruction of final state four momenta, a minimum energy of 20 MeV per cluster is demanded. This threshold is not passed or only closely passed by  $\gamma_3$  and  $\gamma_4$  in  $2\pi^0$  production for  $\sim 60\%$  of all generated photons, see figure 3.12a. Similarly,  $\sim 70\%$  of generated  $\pi^0\eta$  events have a final state photon which does not or only closely pass the threshold of 20 MeV. Other than in  $2\pi^0$  reactions, this does only apply for  $\gamma_4$  while

<sup>5</sup> To simplify notation, from now on the four final state photons of the reactions  $\gamma p \rightarrow p2\pi^0 \rightarrow p4\gamma$  and  $\gamma p \rightarrow p\pi^0\eta \rightarrow p4\gamma$  are referred to as  $\gamma_1 \dots \gamma_4$ , where the ascending index corresponds to the photon energy in descending order

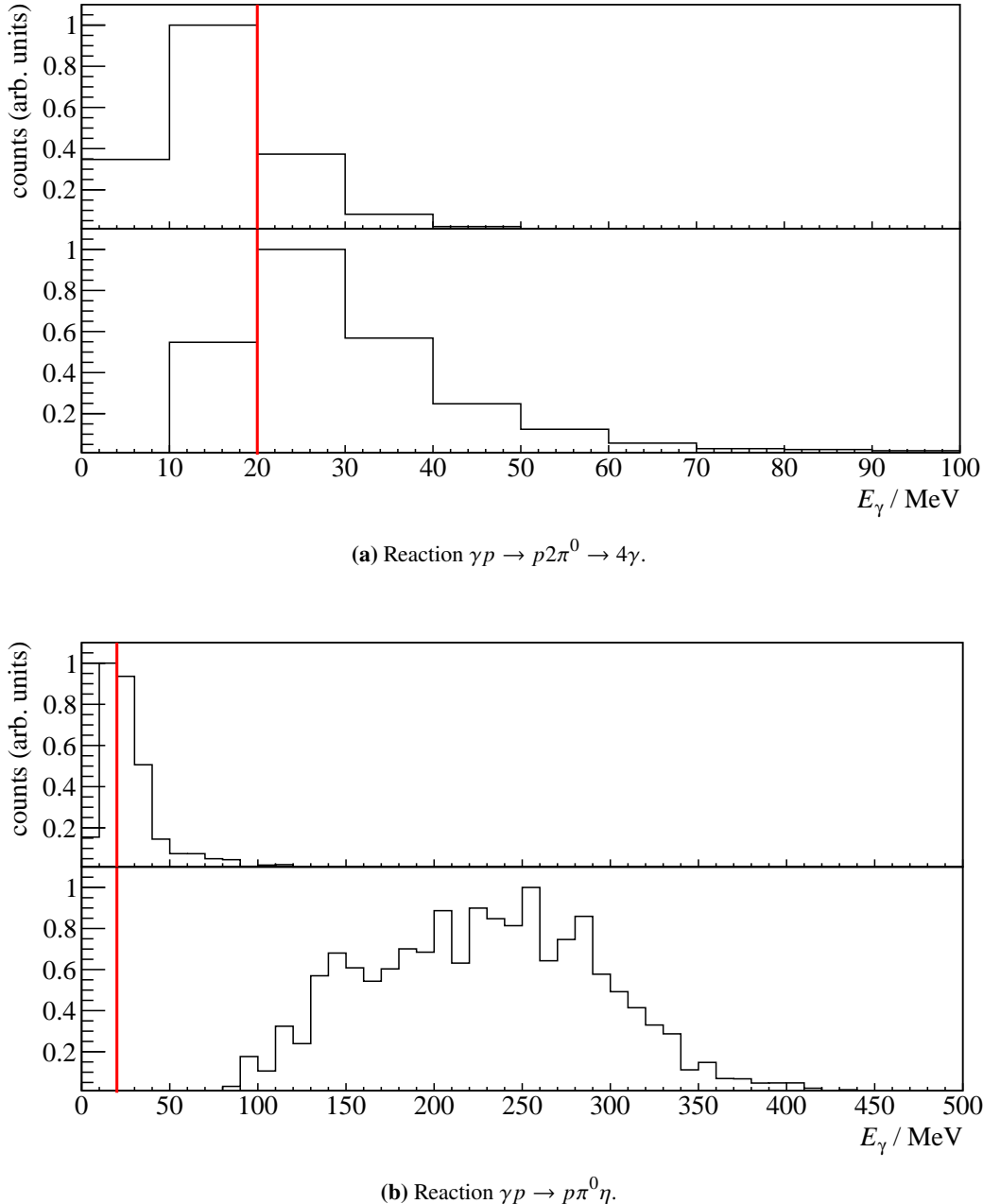


**Figure 3.12:** Generated energies of  $\gamma_3$  and  $\gamma_4$  in  $2\pi^0$  and  $\pi^0\eta$  photoproduction MC data. The threshold of 20 MeV is marked by a vertical red line.  $E_{\gamma_4}$  is shown on the top,  $E_{\gamma_3}$  is shown on the bottom of each figure.

$\gamma_3$  significantly exceeds the threshold of 20 MeV, see figure 3.12b.

At this point it is important to note that the generated energies are in general larger than the reconstructed energies because energy may be deposited in insensitive detector material. Figures 3.12a and 3.12b thus do not necessarily resemble a good approximation of how many photons actually are lost because they simply do not pass the energy threshold during reconstruction. To get a better estimate, the generated energies  $E_\gamma^{\text{gen}}$  of  $\gamma_1$  and  $\gamma_2$  are compared with the reconstructed energies  $E_\gamma^{\text{rec}}$ , see Figure 3.13. Energies that are correctly reconstructed lie on the slope of  $E_\gamma^{\text{gen}} = E_\gamma^{\text{rec}}$ , which is the case for nearly all events of  $2\pi^0$  production. However for  $\pi^0\eta$  reactions a sizable amount of events lies offside the slope towards higher reconstructed energies. This indicates on one hand that in  $2\pi^0$  production, the energies of  $\gamma_3$  and  $\gamma_4$  nearly always do not surpass the reconstruction threshold and on the other hand that photons with an energy above threshold may still be lost during reconstruction because they are falsely combined to one cluster with either  $\gamma_1$  or  $\gamma_2$  resulting in too large reconstructed energies. Too small reconstructed energies are also observed because energy may get lost in insensitive detector materials. Figure 3.14 shows the polar angle difference between  $\gamma_3$  and  $\gamma_2$  of the MC  $\pi^0\eta$  final state which clearly peaks centered at small angles, explaining why the false combination of two photons may happen during reconstruction. Similar results are found with  $2\pi^0$  production events but less distinct. It is evident that neither the two lost photons, nor the two reconstructed photons are correlated, i.e. decay products of the same meson ( $\pi^0, \eta$ ).

Considering the above one can now say that  $2\pi^0$  and  $\pi^0\eta$  events pass the  $\eta'$  event selection because

1. two uncorrelated low energy photons are lost during reconstruction and the remaining two pass the kinematic cuts by chance, since they too are uncorrelated (see figure 3.15a),
2. one low energy photon is lost. Two of the remaining three photons are combined to one in favor of the higher energetic photon since they were emitted in the same direction. The two reconstructed photons are uncorrelated and pass the event selection randomly, as shown in figure 3.15b.

These claims are indeed further validated if one examines the polar angle that is reconstructed from the falsely assigned  $\eta'$  candidates using the surviving two photon momenta. This can be compared to the generated polar angle that is built using all four final state photon momenta in the CMS  $\mathbf{p}_{\gamma_i}$ . They add up to the artificial two-meson momentum  $\mathbf{p}_m$  which in the CMS has the same magnitude but opposite direction as the recoil proton with momentum  $\mathbf{p}_{\text{recoil}}$

$$\mathbf{p}_m = \sum_{i=1}^4 \mathbf{p}_{\gamma_i} = -\mathbf{p}_{\text{recoil}}.$$

If the lost photons have very low energies and/or are emitted in the same direction as other photons one would expect the polar angle that is spanned by the four final state photons approximately agrees with the polar angle that is built using the two photons that survived event selection, such that  $\cos \theta(4\gamma) \approx \cos \theta(2\gamma)$ . This is exactly what is observed, as figure 3.16 shows for both background reactions: the generated CMS angle  $\cos \theta_{\text{gen.}}$  is plotted against the reconstructed CMS angle  $\cos \theta_{\text{rec.}}$ . The events are clearly distributed around the slope  $\cos \theta_{\text{gen.}} = \cos \theta_{\text{rec.}}$  which is indicated by the solid line. This is an important result for the later analysis: if the background contributions are taken into account quantitatively then the extracted beam asymmetry has to be corrected by the asymmetry stemming from background reactions. This is only possible if the background reactions from e.g.  $2\pi^0$

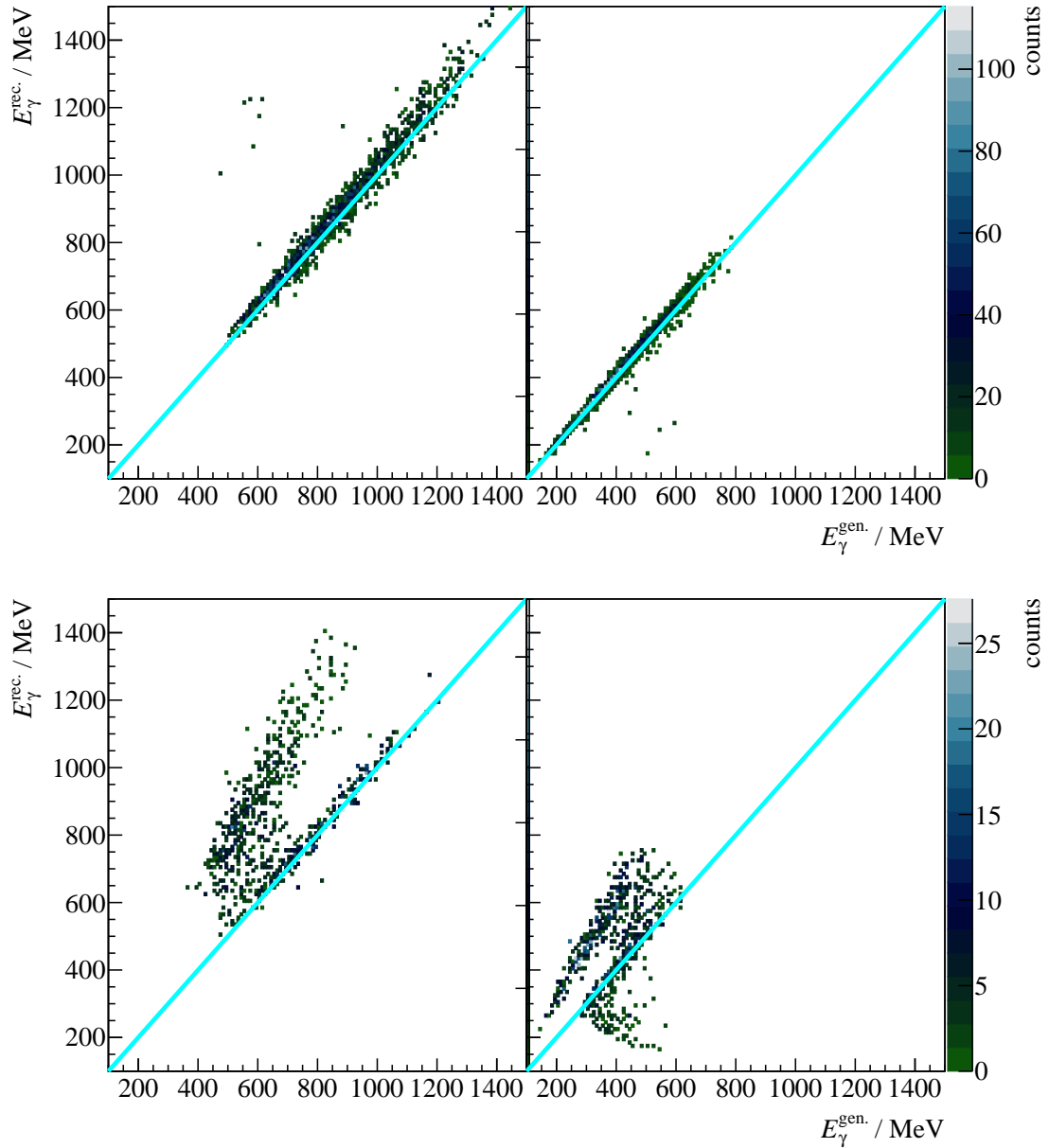


**Figure 3.13:**  $E_\gamma^{\text{gen.}}$  vs.  $E_\gamma^{\text{rec.}}$  of  $\gamma_1$  and  $\gamma_2$  for  $2\pi^0$  (top) and  $\pi^0\eta$  (bottom) production. The slope  $E_\gamma^{\text{gen.}} = E_\gamma^{\text{rec.}}$  is marked by a solid line.

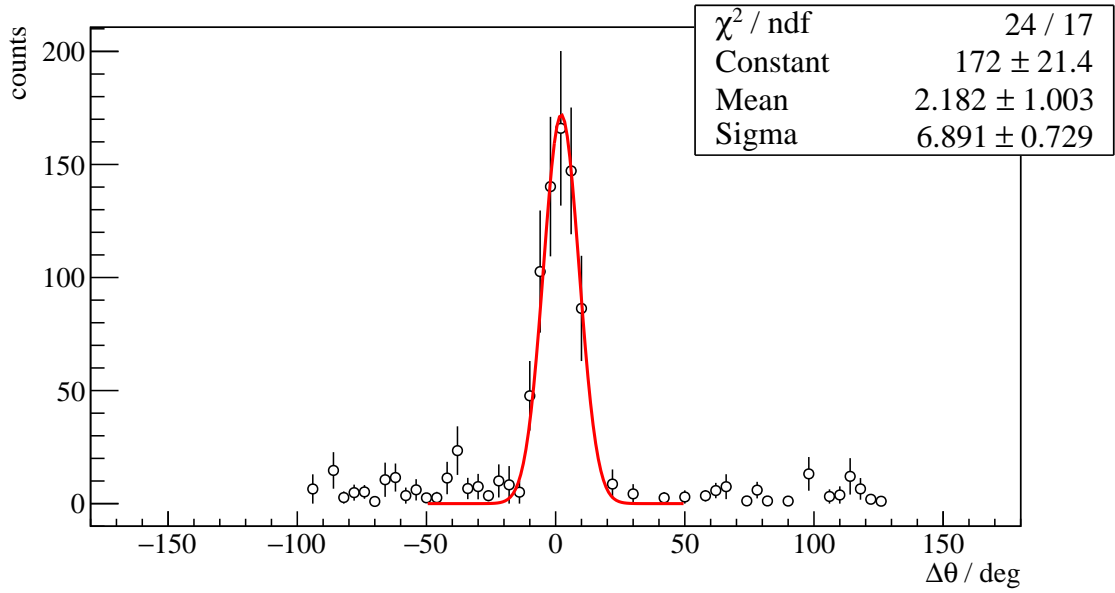


**Figure 3.14:** Polar angle difference  $\Delta\theta$  between  $\gamma_2$  and  $\gamma_3$  of the  $\pi^0\eta$  final state.

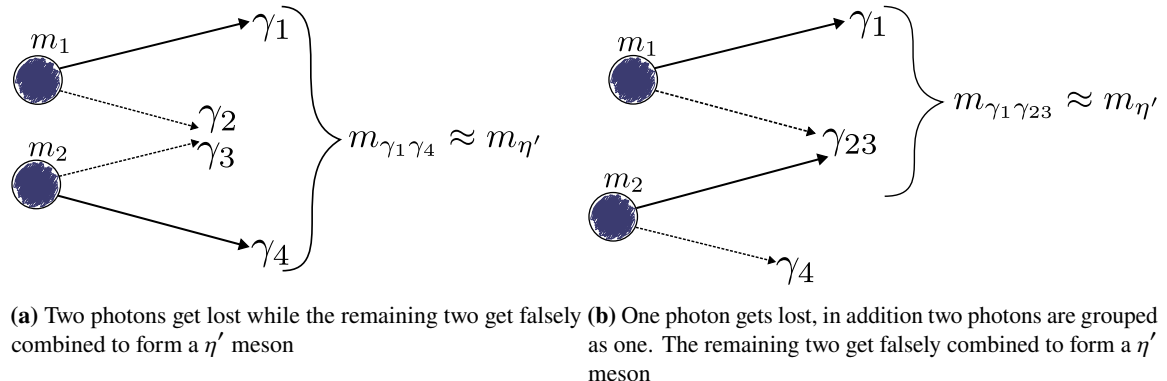


**Figure 3.15:** Illustration of the misidentification process during reconstruction. Enumeration of photons is now arbitrary.

events realize the same bins in beam energy and CMS angle as in a dedicated measurement of the beam asymmetry in the respective photoproduction reaction.

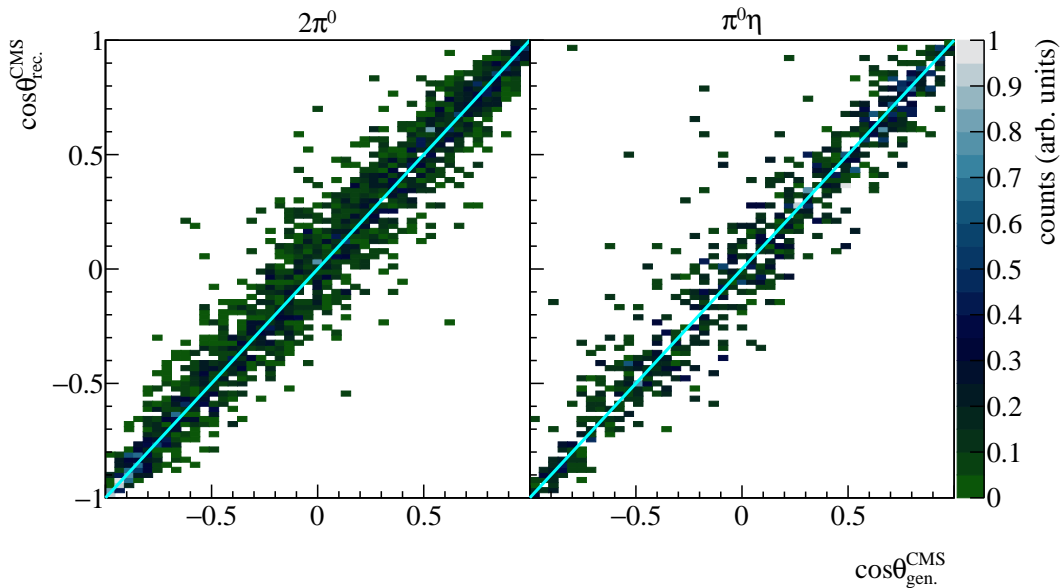


**Figure 3.16:** Generated CMS angle  $\cos \theta_{\text{gen.}}$  vs. reconstructed CMS angle  $\cos \theta_{\text{rec.}}$  for both background reactions. The slope  $\cos \theta_{\text{gen.}} = \cos \theta_{\text{rec.}}$  is indicated by the solid line.

### 3.5.3 Examination of additional cuts

Since the background contributions are significantly beyond a negligible amount it would be desirable to remove them through additional cuts that at the same time do not remove too many signal events. However, this proved to be a complicated task because the background reactions are reconstructed from real photons which happen to be in the  $\eta'$  invariant mass range. Therefore they are not distinguishable from  $\eta' \rightarrow \gamma\gamma$  photons in terms of energy, momentum (direction) or created cluster size in the calorimeter crystals. The false combination of two photons into one cluster also is not observable as such since the impact of one photon with energy  $E$  may create a cluster with cluster size  $C$  which at the same time can be created by two photons in the same direction with energies  $E_1 + E_2 = E$  and cluster sizes  $C_1 + C_2 = C$ . Thus, to find any characteristics that separate background from signal events, one has to analyze properties of either the recoil proton or the reaction kinematics as a whole.

#### Proton cut

Very close to the  $\eta'$  production threshold, the meson system is not boosted very often in forward direction as long as real  $\eta'$  mesons are produced. As a consequence the recoil proton may escape to very forward angles in the lab system which corresponds to the proton being detected in the MiniTAPS calorimeter. Falsely reconstructed  $2\pi^0$  or  $\pi^0\eta$  events have lower production thresholds such that the mesons will be boosted forward and the recoil proton is detected rather in the forward detector or the Crystal Barrel calorimeter. Figure 3.17 shows for the two energy bins (starting at 1400 MeV) the

detector that was hit by the recoil proton for  $\eta'$ ,  $2\pi^0$  and  $\pi^0\eta$  MC data. At threshold nearly all protons of  $\eta'$  events are detected in the MiniTAPS calorimeter while this is only the case for 57% of  $2\pi^0$  events and 20% of  $\pi^0\eta$  events. Towards higher energies this distribution along detectors smears out and is approximately equal for all reactions. Yet, not enough statistics are collected in the energy bin close to threshold for a cut based on the proton detector hit to have significant signal, as this bin contains less than 7% of total  $\eta'$  candidates. The poor statistics in this bin also make determining background from MC fits difficult. Thus, as has been mentioned before, the energy bin from 1400 to 1500 MeV was not included in the analysis. Consequently no cut based on proton detector hits could be applied to the remaining data. Apart from directional information near threshold protons from signal and background events could not be distinguished.

### Reaction kinematics

As has been mentioned before, the measured photoproduction reactions are in fact overdetermined, meaning that one reaction particle can be treated as missing. This can be used to calculate the beam photon energy

$$E_\gamma^{\text{calc}} = \frac{-0.5 \cdot m_{\eta'}^2 + m_p E_{\eta'}}{m_p - E_{\eta'} + |p_z|_{\eta'}}, \quad (3.15)$$

where  $m_p$  is the proton  $m_{\eta'}$  the  $\eta'$  mass,  $E_{\eta'}$  is the meson energy and  $|p_z|_{\eta'}$  is the meson momentum in  $z$ -direction. Comparing this with the measured beam energy one may tell  $\eta'$  events apart from background events where mesons with smaller masses have been produced. If equation (3.15) is used to calculate the beam energy, i.e. inserting the  $\eta'$  mass, background events from reactions with smaller masses will cause smaller calculated beam energies. The difference of measured and calculated beam energy  $\Delta E = E_\gamma^{\text{meas}} - E_\gamma^{\text{calc}}$  is shown in figure 3.18. The data points are shown as open circles and solid histograms represent fitted MC data where the turquoise histogram is the sum of all MC histograms. A broad peak centred slightly off 0 towards lower energy differences is visible because plugging in the literature values for  $m_p$  and  $m_{\eta'}$  tends to overestimate the calculated energy. It also exhibits a broad shoulder towards higher energy differences. The MC describe the data very well, consisting mainly of  $\eta'$  and  $2\pi^0$  MC, as expected. The  $\pi^0\eta$  MC describe a flat shape. The background MC show a trend towards energy differences  $> 0$ , as predicted by equation (3.15). In principle the distribution of background and  $\eta'$  MC now allow to introduce an upper bound on the beam energy difference rejecting any desired amount of background. However, simultaneously a significant amount of  $\eta'$  events have to be discarded if this cut should have remarkable influence on the background events, as is shown in table 3.5. Considering that only 8000  $\eta'$  candidates could be extracted, any cut

upper limit of $\Delta E$ / MeV	rel. loss of signal events / %	relative loss of bkg. events / %	
		$2\pi^0$	$\pi^0\eta$
0	36	71	59
50	21	53	36
100	10	33	18
150	4	15	6

**Table 3.5:** Relative loss in signal and background events if a cut on  $\Delta E$  is applied.

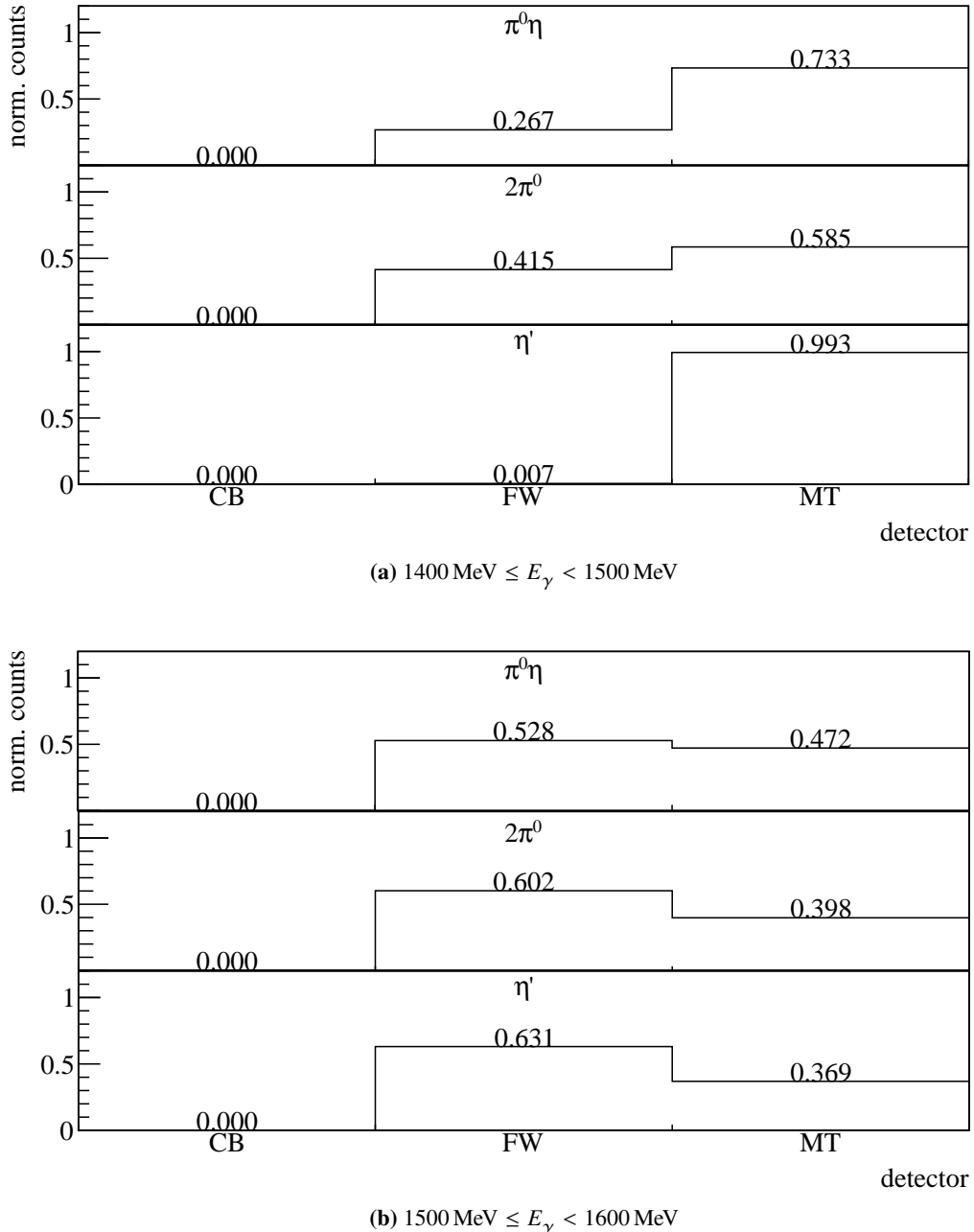


**Figure 3.17:** Detector hits of the recoil proton, as obtained from MC data for the production of  $\eta'$ ,  $2\pi^0$  and  $\pi^0\eta$ .  
 CB: Crystal Barrel, FW: forward detector, MT: MiniTAPS

removing sizable fractions of signal events will have grave impact regarding the statistical error for the later analysis of the beam asymmetry. It was decided not to imply any further cuts on the data and proceed with the selected events as described previously. Because results for the beam asymmetry in  $2\pi^0$  production are available [Mah22] it is not crucial to remove all remaining background events since the extracted beam asymmetry can be corrected proportionately, depending on the amount and type of background in a particular bin, see section 4.3.

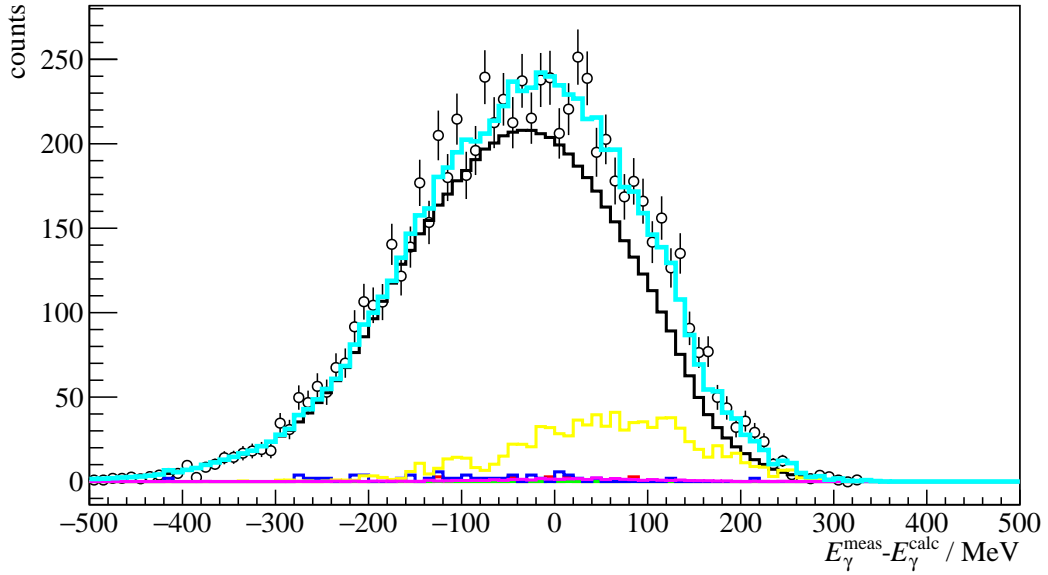


**Figure 3.18:** Difference in measured and calculated beam energy. Data points are shown as open circles, MC data as solid histograms: in black  $\eta'$ , in green  $\pi^0$ , in red  $\eta$ , in blue  $\omega$ , in yellow  $2\pi^0$  and in magenta  $\pi^0\eta$ . The turquoise histogram is the sum of all MC histograms.

## 3.6 Summary of event selection

### 3.6.1 Reaction $\gamma p \rightarrow p\eta' \rightarrow p\gamma\gamma$

The reaction  $\gamma p \rightarrow p\eta'$  could be selected successfully. Combinatorial background was removed using the time information of initial and final state particles. Furthermore, the measured energies and momenta of all final state particles were utilized when applying constraints, that were derived from energy and momentum conservation, to  $\gamma p \rightarrow \eta' \rightarrow \gamma\gamma$  event candidates. A significant amount of background still passes the event selection process which could be traced back to  $2\pi^0$  and  $\pi^0\eta$  production using Monte Carlo simulations. Very restricted possibilities to exclusively select signal from background events were found but in the end not used as they still remove sizable fractions of signal events in order to get rid of background events.

To illustrate again the impact of all applied cuts, the invariant mass summed over all angular and energy bins of the final state photons is shown again in figure 3.19 where the spectrum can be seen after each individual cut successively. While at first only slight structures in the invariant mass spectrum

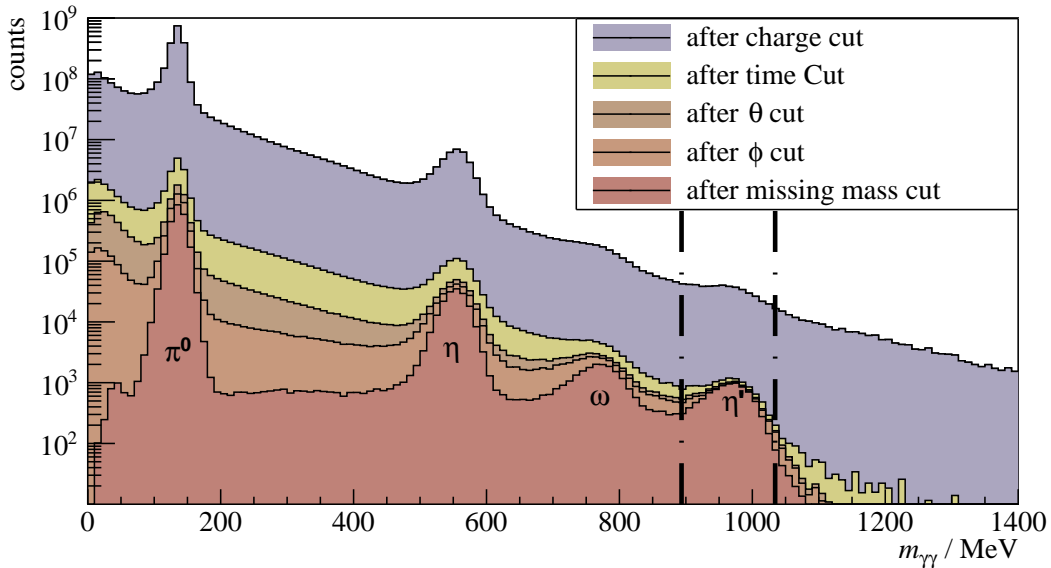


**Figure 3.19:** Invariant mass spectrum passing different stages in the event selection process. In the end clear peaks for all possibly produced mesons are visible. The vertical lines indicate the mean cut ranges over all energy and angle bins.

can be observed, in the end a clear, peak-like structure is visible, indicating the general success of the event selection that has been described in this chapter. The signal to background ratio is improved by each applied cut where the time cut clearly removes the most (combinatorial) background. Note that there are differences of three and two orders of magnitude in statistics for  $\pi^0$  or  $\eta$  meson production compared to  $\eta'$  production in the neutral decay channel.

### 3.6.2 Reaction $\gamma p \rightarrow p\eta \rightarrow p\gamma\gamma$

As has been mentioned in the beginning of this chapter, the reaction  $\gamma p \rightarrow p\eta \rightarrow p\gamma\gamma$  was subject of the dissertation [Afz19] and this thesis only uses the selected data to verify existing results with new fitting methods. A short summary of the event selection that is described in detail in reference [Afz19] will be given in the following nevertheless.

Since a three particle final state was to be investigated, the data is first of all constrained to include only 2PED, 2.5PED and 3PED events. No charge cut was applied, so that always two final state particles were combined pairwise to form a meson candidate while the remaining particle (if measured) was assigned as proton candidate. As a next step coincidence of final state particles was checked in a similar fashion to section 3.3 with the exception that depending on the hit detectors different prompt peaks and sideband ranges were selected. Afterwards the discussed kinematic variables  $\Delta\theta$ ,  $\Delta\phi$ ,  $m_X$ ,  $m_{\text{meson}}$  were used to further filter out candidates for  $\eta$  photoproduction. Hereby a binning of 60 MeV in the beam energy and 1/6 in  $\cos\theta$  was chosen. With the help of Monte Carlo simulations background contributions from single  $\pi^0$  production could be recognized. They could be explained by events where one final state photon is lost and the recoil proton falsely creates two tracks and according cuts to remove these events were made. In the end, less than 7% background contamination was

achieved in all kinematic bins. Figure 3.20 shows the invariant mass with each cut successively applied. At first only slight structures are visible, also because no charge cut is applied to the data, which increases the amount of combinatorial background. But with each cut the contributions from meson photoproduction become more distinct, indicating all in all a successful event selection.

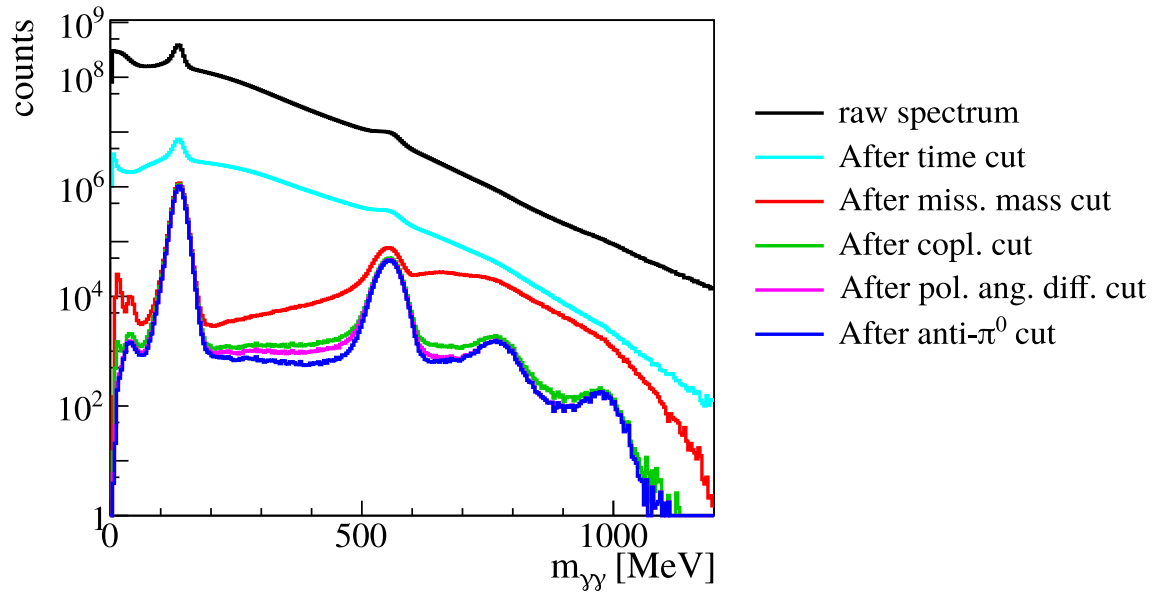


**Figure 3.20:** Invariant mass spectrum passing different stages in the event selection process. In the end clear peaks for all possibly produced mesons are visible. Taken from [Afz19].

# CHAPTER 4

## Extraction of the beam asymmetries $\Sigma_\eta$ and $\Sigma_{\eta'}$

The beam asymmetry  $\Sigma$  can be measured from data taken with a linearly polarized photon beam and an unpolarized liquid hydrogen target [San+11]. The polarized differential cross section  $\frac{d\sigma}{d\Omega_{\text{pol}}}$  is not uniformly distributed in the azimuthal angle  $\phi$  anymore as opposed to the unpolarized differential cross section  $\frac{d\sigma}{d\Omega_0}$ . It is rather modulated by a cosine dependence which scales with the polarization observable  $\Sigma$  and the (linear) beam polarization  $p_\gamma$ , see equation (4.1) [San+11].

$$\frac{d\sigma}{d\Omega_{\text{pol}}} (E_\gamma, \cos \theta, \phi) = \frac{d\sigma}{d\Omega_0} (E_\gamma, \cos \theta) \cdot \left[ 1 - p_\gamma \Sigma (E_\gamma, \cos \theta) \cos (2\varphi) \right] \quad (4.1)$$

Since the incident photon beam is polarized, photon momentum  $\vec{k}$  and polarization  $\vec{\epsilon}$  span a plane which is referred to as the beam polarization plane. This plane is tilted by the angle  $\varphi$  with respect to the reaction plane which is defined by the final state momenta. Naturally, this plane builds the angle  $\phi$  in the laboratory system. At the same time the angle of the beam polarization plane in the same reference frame is defined as  $\alpha$ . It holds

$$\varphi = \alpha - \phi. \quad (4.2)$$

Figure 4.1 illustrates definitions of all angles and planes. Theoretically the beam asymmetry can be

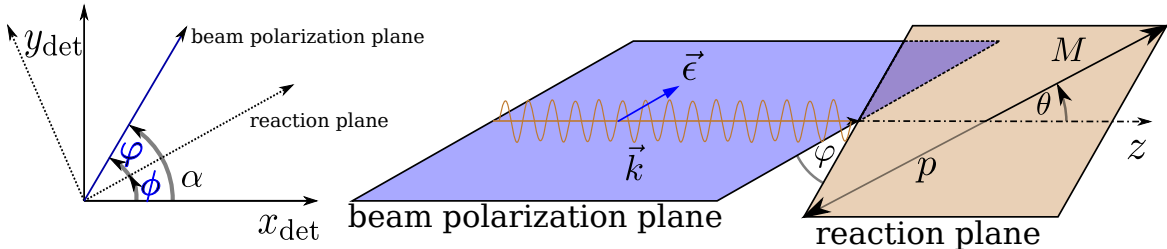


**Figure 4.1:** Left: Definition of the angles  $\alpha, \phi, \varphi$ . Right: Photon momentum  $\vec{k}$  and polarization  $\vec{\epsilon}$  define the beam polarization plane while the reaction plane is defined by the recoil proton  $p$  and produced meson  $M$ .

determined by a measurement of the cross section and a fit using equation (4.1). However, when calculating polarized cross sections, it is important to have good control over flux normalization and detector acceptance in three dimensions  $(E_\gamma, \cos \theta, \phi)$  to minimize systematical errors. To avoid

this, the measurement of asymmetries can be used to access the polarization observable  $\Sigma$  instead. Particularly, data is taken for two distinct orthogonal polarization settings corresponding to  $\alpha = \pm 45^\circ$ .

This chapter will illustrate the process of determining the beam asymmetry for  $\eta$  and  $\eta'$  photoproduction. The published results of  $\Sigma_\eta$  [Afz19; Afz+20] are used to check the accuracy and functionality of the employed bayesian methods. Bayesian methods, as well as traditional frequentist approaches are used afterwards to extract new results for  $\Sigma_{\eta'}$ . First, the determination of the beam photon polarization is briefly described, then the used methods will be presented and subsequently their application for each final state is shown, respectively.

## 4.1 Methods

The beam asymmetry has to be determined via fits to asymmetry distributions obtained from data. These are performed as either binned or unbinned fits. Both methods allow the application of Bayesian methods as will be discussed in the following. Additionally the advantages and disadvantages off all methods are compared.

### 4.1.1 Event yield asymmetries

Measurements were made in two distinct polarization settings  $\alpha = \pm 45^\circ = \alpha^{\perp/\parallel}$ . Thus, the polarized cross sections for both settings are given by<sup>1</sup>

$$\frac{d\sigma}{d\Omega_{\text{pol}}}^{\parallel} = \frac{d\sigma}{d\Omega_0} \cdot \left[ 1 - p_\gamma^{\parallel} \Sigma \cos(2(\alpha^{\parallel} - \phi)) \right] \quad (4.3)$$

and

$$\frac{d\sigma}{d\Omega_{\text{pol}}}^{\perp} = \frac{d\sigma}{d\Omega_0} \cdot \left[ 1 - p_\gamma^{\perp} \Sigma \cos(2(\alpha^{\perp} - \phi)) \right] \quad (4.4)$$

$$= \frac{d\sigma}{d\Omega_0} \cdot \left[ 1 + p_\gamma^{\perp} \Sigma \cos(2(\alpha^{\parallel} - \phi)) \right]. \quad (4.5)$$

Note that equation (4.5) holds, because

$$\alpha^{\perp} = \alpha^{\parallel} + \pi/2 \quad \text{and} \quad \cos x = -1 \cdot \cos(x + \pi).$$

Consider now taking the difference of equations (4.3) and (4.5)

$$\frac{d\sigma}{d\Omega_{\text{pol}}}^{\perp} - \frac{d\sigma}{d\Omega_{\text{pol}}}^{\parallel} = \frac{d\sigma}{d\Omega_0} \cdot (p_\gamma^{\perp} + p_\gamma^{\parallel}) \Sigma \cos(2(\alpha^{\parallel} - \phi)). \quad (4.6)$$

---

<sup>1</sup> The dependencies  $(E_\gamma, \cos \theta, \phi)$  of the polarized and the unpolarized cross sections as well as the beam asymmetry like in equation (4.1) are implied.

One can further eliminate the unpolarized cross section from this equation by dividing by the polarization weighted sum of equations (4.3) and (4.5)

$$\alpha \cdot \frac{d\sigma^\perp}{d\Omega_{\text{pol}}} + \beta \cdot \frac{d\sigma^{\parallel}}{d\Omega_{\text{pol}}} = \frac{d\sigma}{d\Omega_0} \cdot \left[ \alpha + \beta - (\alpha p_\gamma^\perp - \beta p_\gamma^{\parallel}) \Sigma \cos(2(\alpha^{\parallel} - \phi)) \right] \stackrel{!}{=} 2 \frac{d\sigma}{d\Omega_0}. \quad (4.7)$$

Since

$$\frac{d}{d\phi} \frac{d\sigma}{d\Omega_0} \stackrel{!}{=} 0 \quad \forall \phi,$$

it holds

$$\alpha p_\gamma^{\parallel} - \beta p_\gamma^\perp \stackrel{!}{=} 0 \quad \alpha + \beta \stackrel{!}{=} 2, \quad (4.8)$$

such that

$$\alpha = \frac{2p_\gamma^{\parallel}}{p_\gamma^\perp + p_\gamma^{\parallel}} \quad \beta = \frac{2p_\gamma^\perp}{p_\gamma^\perp + p_\gamma^{\parallel}}. \quad (4.9)$$

The beam asymmetry  $\Sigma$  is thus accessible via the asymmetry

$$A(\phi) = \frac{\frac{d\sigma^\perp}{d\Omega_{\text{pol}}} - \frac{d\sigma^{\parallel}}{d\Omega_{\text{pol}}}}{p_\gamma^{\parallel} \frac{d\sigma^\perp}{d\Omega_{\text{pol}}} + p_\gamma^\perp \frac{d\sigma^{\parallel}}{d\Omega_{\text{pol}}}} = \Sigma \cos(2(\alpha^{\parallel} - \phi)). \quad (4.10)$$

At this point one can now make use of the fact that in any scattering reaction the number of events  $N$  is given by the product of luminosity  $L$  and total cross section  $\sigma$  [Pov+14]

$$N = L \cdot \sigma = \Phi \cdot N_t \cdot \frac{d\sigma}{d\Omega} \cdot \Delta\Omega,$$

where  $\Phi$  is the beam flux,  $N_t$  the number of target particles and  $\Delta\Omega$  is the solid angle covered by the detector. Substituting this in equation (4.10) one can build the asymmetry  $A(\phi)$  using only the (flux-)normalized event yields  $\tilde{N}^{\parallel/\perp}(E_\gamma, \cos\theta, \phi)^2$

$$A(\phi) = \frac{\tilde{N}^\perp - \tilde{N}^{\parallel}}{p_\gamma^{\parallel} \tilde{N}^\perp + p_\gamma^\perp \tilde{N}^{\parallel}} = \Sigma \cos(2(\alpha^{\parallel} - \phi)). \quad (4.11)$$

Alternatively, the event yields  $N$  can also be normalized by integrating over the total azimuthal angle range in each bin of  $(E_\gamma, \cos\theta)$ . This normalization technique has been used in reference [Afz19] due to difficulties with the measurement of the photon flux and will also be used in this work. Using appropriate binning in  $\phi$  in addition to beam energy and meson polar angle the asymmetry can be build for all kinematic bins and the beam asymmetry then be extracted via a one-parameter<sup>3</sup> fit. The statistical errors for  $A(\phi)$  are given by GAUSSIAN error propagation (see appendix B.1).

<sup>2</sup> Again, arguments  $(E_\gamma, \cos\theta, \phi)$  are implied.

<sup>3</sup> In general one could still allow an offset to Eq. 4.11 as a second fit parameter. In ref. [Afz19] this was shown to be consistent with 0.

## Frequentist

The beam asymmetry can now be determined via a frequentist fit, where  $\Sigma$  is determined such that the  $\chi^2$  value resulting from the data points and equation 4.11 is minimized. The results are point estimates with statistical error bars that are also obtained from the fit:  $\hat{\Sigma} \pm \sigma_{\hat{\Sigma}}$ . One can show that the probability distribution of the  $\chi^2$  value, given  $n$  degrees of freedom, has mean  $n$  and variance  $2n$  [Bar89]. This means  $\chi^2/\text{NDF} \approx 1$  may be verified in order to diagnose the fit itself. Much larger values indicate a bad fit and much smaller values an overestimation of errors [Bar89]. Multiple automated minimization and calculation algorithms for  $\chi^2$  fitting are available as open source. The *Python* [RP22] module `scipy` [Vir+20] and *ROOT* [BR97] offer e.g. the methods `scipy.optimize.curve_fit` [sci] and `TH1::Fit()` [ROOa] for discrete/binned data, which were used in the analysis.

## BAYESIAN

Following section 1.3, where the basics of BAYESIAN inference were discussed, the goal of a BAYESIAN approach is to sample marginal posterior distributions for each fitted parameter from the joint posterior  $p(\theta|y)$  which depends on the observed data  $y$ . The joint posterior itself is proportional to the product of priors  $\pi(\theta)$  and likelihood  $\mathcal{L}(y|\theta)$  (BAYES' theorem). This collapses to a one parameter problem in the case of fitting the event yield asymmetries (Eq. (4.11))

$$p(\Sigma|y) \propto \pi(\Sigma) \cdot \mathcal{L}(y|\Sigma). \quad (4.12)$$

However, to be able to sample from a joint posterior, prior and likelihood need to be specified. In order not to bias the fit towards any particular values, the prior is chosen weakly-informative [Gel+14], realized by a broad GAUSSIAN centered at 0 which is truncated to the physically allowed parameter space of  $\Sigma \in [-1, 1]$ . An improper uniform prior is avoided this way following the recommendations of reference [Sta22b] although the model would in principle be suited since the beam asymmetry is designed to be constrained to a finite interval [Sta22b]. Furthermore, the likelihood is formulated assuming GAUSSIAN errors  $\epsilon_n$  with standard deviation  $\sigma_n$  at each data point  $y_n$ , which should be described by the asymmetry (Eq (4.11)) at bin  $n$   $A(\phi_n; \Sigma)$ , i. e.<sup>4</sup>

$$\Sigma \sim \mathcal{N}(0, 1)_{[-1, 1]} \quad y_n = A(\phi_n; \Sigma) + \epsilon_n \quad \epsilon_n \sim \mathcal{N}(0, \sigma_n), \quad (4.13)$$

which is equivalent to

$$\Sigma \sim \mathcal{N}(0, 1) \quad y_n \sim \mathcal{N}(A(\phi_n; \Sigma), \sigma_n). \quad (4.14)$$

---

<sup>4</sup> Reminder of the notation introduced in section 1.3:  $x \sim \mathcal{N}(\mu, \sigma) = \mathcal{N}(x|\mu, \sigma) = \frac{1}{\sqrt{2\pi}\sigma^2} e^{-\frac{(x-\mu)^2}{2\sigma^2}}$ .

Assuming all data points are independent, the likelihood of all data points now evaluates to the product of the likelihood at each data point  $y_n$  and the posterior results in

$$p(\Sigma|y) \propto \pi(\Sigma) \cdot \mathcal{L}(y|\Sigma) = \mathcal{N}(\Sigma|0, 1)_{[-1,1]} \cdot \prod_n \mathcal{N}(y_n|A(\phi_n; \Sigma), \sigma_n) \quad (4.15)$$

$$\Leftrightarrow -\ln p(\Sigma|y) = \frac{1}{2}\Sigma^2 + \frac{1}{2} \sum_n \left( \frac{y_n - A(\phi_n; \Sigma)}{\sigma_n} \right)^2 + \text{constant terms}, \quad (4.16)$$

such that all ingredients are present to form a fully BAYESIAN probabilistic model<sup>5</sup>. This model was implemented in Stan [Sta22a], directly giving access to samples from the posterior obtained with the No-U-Turn-Sampler (NUTS) [Sta22a; HG14]. Hereby, the sampling is restricted to the allowed parameter region  $\Sigma \in [-1, 1]$ . As a measure of goodness of fit, the  $p$ -values obtained from the posterior predictive distributions, as introduced in section 1.3, are reviewed. To diagnose the convergence of the MCMC fit, sensible values for  $\hat{R}$  and the Monte-Carlo standard error  $\sigma_{\text{MCSE}}$  are verified.

### 4.1.2 Event based fit

Although intuitive and easily implementable the binned fit –BAYESIAN or not– has one critical disadvantage: it is inevitable that information is lost because the asymmetry  $A(\phi)$  is a binned quantity and hence, the choice of binning influences the fit results. This is discussed in more detail in appendix C. Especially kinematic bins with low statistics show this behavior. To circumvent this problem, an *unbinned fit*, based on the likelihood function for each event, can be performed. Also, no assumptions on the distribution of statistical errors have to be made since each event is taken into account individually. Yet, the event based fit does not provide any measure of goodness of fit, so that the study of toy Monte Carlo data is essential when checking the working principle of the method.

In a polarized experiment, the azimuthal angle distribution of events is not isotropic, but modulated by a cosine term coupling to the beam asymmetry  $\Sigma$  and the beam polarization  $p_\gamma^{\parallel/\perp}$  for each setting  $\alpha^{\parallel/\perp}$ , as is expressed through the respective differential cross sections in Equations 4.3 and 4.4. Since the number of events is proportional to the cross section, the probability  $p(\phi, p_\gamma^{\parallel/\perp} | \Sigma)$  to find an event under the azimuthal angle  $\phi$  for a given bin of  $(E_\gamma, \cos \theta)$  and setting  $\alpha^{\parallel/\perp}$  is<sup>6</sup>

$$p(\phi, p_\gamma^{\parallel/\perp} | \Sigma) = \frac{\left[ 1 \mp p_\gamma^{\parallel/\perp} \Sigma \cos(2(\alpha^{\parallel} - \phi)) \right]}{\frac{1}{2\pi} \int_0^{2\pi} d\phi \left[ 1 \mp p_\gamma^{\parallel/\perp} \Sigma \cos(2(\alpha^{\parallel} - \phi)) \right]}. \quad (4.17)$$

This is only true for an idealized experiment with acceptance  $\epsilon = \text{const} \forall \phi$ , so that the acceptance  $\epsilon(\phi)$  has to be included in the probability for each event. As demonstrated in reference [Har17] a FOURIER

<sup>5</sup> Note that the sampling aims only to reflect the right proportionality of the (marginal) posterior. Thus, constant terms can be dropped and are of no further interest [Sta22a].

<sup>6</sup> Note: Normalizing  $p(\phi, p_\gamma^{\parallel/\perp} | \Sigma)$  to  $2\pi$  (or any other arbitrary constant) is sufficient for the fit as long as the integral does not depend on the fit parameters. The normalization to  $2\pi$  is chosen for better readability. However, to calculate actual probabilities, one must multiply Eq. (4.17) by  $2\pi$ .

series truncated after the fourth order is sufficient to model any occurring function

$$\epsilon(\phi) = \sum_{k=0}^4 a_k \sin(k\phi) + b_k \cos(k\phi),$$

where the detector coefficients  $a_k$  and  $b_k$  are determined from the fit. With this the measurable probability  $\tilde{p}(\phi, p_\gamma^{\parallel/\perp} | \Sigma, a, b)$  is

$$\tilde{p}(\phi, p_\gamma^{\parallel/\perp} | \Sigma, a, b) \propto [1 \mp p_\gamma^{\parallel/\perp} \Sigma \cos(2(\alpha^\parallel - \phi))] \cdot \epsilon(\phi) \quad (4.18)$$

$$= [1 \mp p_\gamma^{\parallel/\perp} \Sigma \cos(2(\alpha^\parallel - \phi))] \cdot \left( \sum_{k=0}^4 a_k \sin(k\phi) + b_k \cos(k\phi) \right), \quad (4.19)$$

where  $a := \{a_k\}_{k=0}^4$ ,  $b := \{b_k\}_{k=0}^4$ . Finally, normalizing  $\frac{1}{2\pi} \int_0^{2\pi} d\phi \tilde{p}(\phi, p_\gamma^{\parallel/\perp} | \Sigma, a, b) \stackrel{!}{=} 1$ ,

$$\tilde{p}(\phi, p_\gamma^{\parallel/\perp} | \Sigma, a, b) = \frac{[1 \mp p_\gamma^{\parallel/\perp} \Sigma \cos(2(\alpha^\parallel - \phi))] \cdot (\sum_{k=0}^4 a_k \sin(k\phi) + b_k \cos(k\phi))}{1 \pm \frac{1}{2} a_2 p_\gamma^{\parallel/\perp} \Sigma}. \quad (4.20)$$

The respective polarization setting  $\alpha^{\parallel/\perp}$  determines the sign in the normalizing constant which allows an uncorrelated estimation of the detector coefficient  $a_2$  and the beam asymmetry  $\Sigma$ . To simplify notation and implementation, Equation (4.21) can be written as *one* probability for all events – regardless of polarization setting – if the polarization values  $p_\gamma^\parallel$  are multiplied by  $(-1)$  and summarized as  $p_\gamma$ :

$$\tilde{p}(\phi, p_\gamma | \Sigma, a, b) = \frac{[1 + p_\gamma \Sigma \cos(2(\alpha - \phi))] \cdot (\sum_{k=0}^4 a_k \sin(k\phi) + b_k \cos(k\phi))}{1 - \frac{1}{2} a_2 p_\gamma \Sigma}, \quad (4.21)$$

with  $\alpha = -45^\circ$  fixed.

In section 3.3 the subtraction of uncorrelated time background was discussed via a sideband subtraction. Naturally, without binning the data, this strategy is invalid and prompt peak and sideband events have to be fitted simultaneously. Hereby it is important to consider that the random time background is realized as a flat distribution underneath the complete reaction time spectrum (cf. Figure 3.3), *including* the range of the prompt peak. The fraction of true coincident events to random coincidences is given as

$$f = \frac{N_{\text{prompt}} - w \cdot N_{\text{sideband}}}{N_{\text{prompt}}}, \quad (4.22)$$

where  $N_{\text{prompt}}$  and  $N_{\text{sideband}}$  are the number of events where the reaction time lies within the prompt peak or sideband, respectively.  $w$  is the ratio of the widths of the chosen prompt peak and sideband ranges, see section 3.3. It is now assumed that the random coincidences will exhibit an asymmetry  $\Sigma^{\text{bkg}}$  of their own and are not necessarily described by the detector coefficients  $a$  and  $b$  but rather by  $a^{\text{bkg}}$  and  $b^{\text{bkg}}$ . The probability to detect a prompt peak event  $p_{\text{prompt}}$  and the probability to measure a

sideband event  $p_{\text{sideband}}$  are then given by

$$p_{\text{prompt}}(\phi, p_\gamma | \Sigma, a, b, \Sigma^{\text{bkg}}, a^{\text{bkg}}, b^{\text{bkg}}) = f \cdot \tilde{p}(\phi, p_\gamma | \Sigma, a, b) + (1 - f) \cdot \tilde{p}(\phi, p_\gamma | \Sigma^{\text{bkg}}, a^{\text{bkg}}, b^{\text{bkg}}) \quad (4.23)$$

$$p_{\text{sideband}}(\phi, p_\gamma | \Sigma^{\text{bkg}}, a^{\text{bkg}}, b^{\text{bkg}}) = \tilde{p}(\phi, p_\gamma | \Sigma^{\text{bkg}}, a^{\text{bkg}}, b^{\text{bkg}}). \quad (4.24)$$

If there are  $n$  prompt peak and  $m$  sideband events, the joint likelihood of all events  $\mathcal{L}$  is thus given by

$$\mathcal{L} = \prod_{i=1}^n p_{\text{prompt}}(\phi_i, p_{\gamma,i} | \Sigma, a, b, \Sigma^{\text{bkg}}, a^{\text{bkg}}, b^{\text{bkg}}) \prod_{j=1}^m p_{\text{sideband}}(\phi_j, p_{\gamma,j} | \Sigma^{\text{bkg}}, a^{\text{bkg}}, b^{\text{bkg}}), \quad (4.25)$$

or, equivalently

$$\begin{aligned} \ln \mathcal{L} &= \sum_{i=1}^n \ln p_{\text{prompt}}(\phi_i, p_{\gamma,i} | \Sigma, a, b, \Sigma^{\text{bkg}}, a^{\text{bkg}}, b^{\text{bkg}}) \\ &\quad + \sum_{j=1}^m \ln p_{\text{sideband}}(\phi_j, p_{\gamma,j} | \Sigma^{\text{bkg}}, a^{\text{bkg}}, b^{\text{bkg}}). \end{aligned} \quad (4.26)$$

Again, independency of all data points is essential, when formulating a combined likelihood function this way. Eighteen<sup>7</sup> parameters have to be determined in total, either via a conventional frequentist approach or a BAYESIAN approach to this non-linear fitting problem.

## Frequentist

Best fit estimates can be derived by maximizing the likelihood  $\mathcal{L}$ , or, for computational convenience, by minimizing  $-\ln \mathcal{L}$ . The *ROOT* library [BR97] offers the method *TTree::UnbinnedFit* to perform an unbinned maximum likelihood fit on data filled in a *TTree* [ROOb], which was used to perform the fit. Minimization and statistical error calculation are performed by *MINUIT* [JR75]. Errors are hereby estimated either symmetrical from the paraboloid shape of  $(-\ln \mathcal{L})$  using the *HESSE* algorithm or asymmetric from the half-maximum values of  $(-\ln \mathcal{L})$  using the *MINOS* algorithm without making assumptions on the shape of the likelihood, if necessary [JR75].

## Bayesian

The joint posterior of all fit parameters given the data  $\phi, p_\gamma$  is

$$p(\Sigma, a, b, \Sigma^{\text{bkg}}, a^{\text{bkg}}, b^{\text{bkg}} | \phi, p_\gamma) \propto \mathcal{L}(\phi, p_\gamma | \Sigma, a, b, \Sigma^{\text{bkg}}, a^{\text{bkg}}, b^{\text{bkg}}) \cdot \pi(\Sigma, a, b, \Sigma^{\text{bkg}}, a^{\text{bkg}}, b^{\text{bkg}}), \quad (4.27)$$

where  $\pi(\theta)$  denotes the combined prior of all fit parameters which factors into each individual prior since all parameters are independent:

$$\pi(\Sigma, a, b, \Sigma^{\text{bkg}}, a^{\text{bkg}}, b^{\text{bkg}}) = \pi(\Sigma) \cdot \pi(a) \cdot \pi(b) \cdot \pi(\Sigma^{\text{bkg}}) \cdot \pi(a^{\text{bkg}}) \cdot \pi(b^{\text{bkg}}). \quad (4.28)$$

<sup>7</sup> The FOURIER series is constructed such that it holds  $a_0 = 0, b_0 = 1$ .

The priors for  $\Xi \in \{\Sigma, \Sigma^{\text{bkg}}\}$  and  $\xi \in \{a, b, a^{\text{bkg}}, b^{\text{bkg}}\}$  are again chosen non-informative, broadly centered around 0

$$\Xi \sim \mathcal{N}(0, 1)_{[-1, 1]} \quad \xi_k \sim \mathcal{N}(0, 0.1). \quad (4.29)$$

From references [Afz19; Har17] it is expected that  $\xi_k \ll 1$ , therefore the chosen widths of the priors resemble a, relatively speaking, broad distribution.

This model, consisting of the likelihood in Eq. (4.26) and the priors in Eq. (4.29), is implemented in Stan [Sta22a], so that samples from the posterior in the physically allowed region ( $\Xi \in [-1, 1]$ ) are again obtained via NUTS [HG14].

## 4.2 Determination of $\Sigma_\eta$ using Bayesian statistics

This section will now demonstrate the application of the discussed methods to obtain the beam asymmetry  $\Sigma$  for  $\eta$  photoproduction with selected data provided from reference [Afz19]. For each method only the respective BAYESIAN approach will be used and compared to the results from [Afz19] to confirm that it is a valid method. As an additional sanity check toy Monte Carlo samples are generated and analyzed.

### 4.2.1 Application of methods to toy Monte Carlo data

Although results can be compared to the already accomplished ones in reference [Afz19], verifying the correct working principle of the fitting methods is still useful. This is done by generating events that follow the expected distributions of  $N^{\parallel/\perp}$  with fixed and known parameters. With the simulated event yields the binned and unbinned fit are performed as described previously. Repeating this for a large number of times should reproduce the input parameters if the methods work as intended.

#### Event yield asymmetries

The asymmetry  $A(\phi)$  is built from the event yields  $N^{\parallel/\perp}$ , which are distributed according to

$$N^\parallel = N_0 \left[ 1 - p_\gamma^\parallel \Sigma \cos(2(\alpha^\parallel - \phi)) \right], \quad (4.30)$$

$$N^\perp = N_0 \left[ 1 - p_\gamma^\perp \Sigma \cos(2(\alpha^\perp - \phi)) \right], \quad (4.31)$$

where the parameters are chosen as  $\Sigma = 0.3$ ,  $p_\gamma^\parallel = 0.25$ ,  $p_\gamma^\perp = 0.3$ , similar to measured data [Afz19].

In each toy Monte Carlo bin the number of generated samples per setting  $N_{\text{total}}^{\parallel/\perp}$  is given by a POISSON distribution

$$N_{\text{total}}^\parallel \sim \mathcal{P}(800) \quad N_{\text{total}}^\perp \sim \mathcal{P}(1000), \quad (4.32)$$

to simulate the statistics of the  $\gamma p \rightarrow p\eta$  final state as accurately as possible [Afz19]. The samples from the distributions (4.30),(4.31) are drawn using the `TH1::GetRandom` [ROOc] function provided by `ROOT` [BR97]. The function from which samples should be drawn is integrated point wise and then normalized. The normalized integral is approximated by a parabola for each bin. A random number between 0 and 1 is generated and assigned to the according bin, where the respective parabola

is evaluated to give the desired random value. [ROOc]. In total, 10000 toy Monte Carlo bins were simulated and the asymmetry built for 12 bins in  $\phi$ , to conform with the binning chosen in reference [Afz19]. The resulting asymmetry  $A(\phi)$  is shown in Figure 4.2 for several bins as the orange data points with statistical errors according to GAUSSIAN error propagation. Additionally shown is a  $\chi^2$  fit (orange line) to the asymmetry together with posterior predictive checks as obtained from a fully BAYESIAN fit according to the introduced model (blue distributions). This BAYESIAN fit was performed employing  $n_{\text{chain}} = 4$  MARKOV chains with  $n_{\text{samples}} = 1000$  samples each. The warm-up period for each chain has the same length of  $n_{\text{warm up}} = 1000$

$$n_{\text{chain}} = 4 \quad n_{\text{samples}} = 1000 \quad n_{\text{warm up}} = 1000. \quad (4.33)$$

The goodness of fit is checked via the introduced  $p$ -values  $p = T(A_{\text{rep}} > A)$ , and are shown as black points with propagated error bars on the bottom. The optimal value of  $p = 0.5$  is marked by the dashed line and realizes the mean of the distribution of all  $p$ -values, so that one can assume good description of the data by the fits, see Figure 4.3. This replaces the investigation of the  $\chi^2/\text{NDF}$  distribution in the case of a frequentist fit, which should have a mean of 1.

To check whether the fit is unbiased and provides correct error estimation one can investigate the normalized residuals

$$\xi = \frac{\Sigma^{\text{fit}} - \Sigma^{\text{true}}}{\Delta\Sigma^{\text{fit}}} \quad (4.34)$$

in the case of a least-squares fit. Here  $\Sigma^{\text{fit}}$  and  $\Delta\Sigma^{\text{fit}}$  are the value and corresponding statistical error for the beam asymmetry as obtained from the fit and  $\Sigma^{\text{true}}$  is the true value that was used to throw the toy MC experiments. An unbiased fit with right estimation of errors yields [Bar89]

$$\xi \sim \mathcal{N}(0, 1). \quad (4.35)$$

This criterion obviously cannot be applied in the same way to a BAYESIAN fit. The fit results are distributions and therefore lack point estimates  $\Sigma^{\text{fit}}$  and errors  $\Delta\Sigma^{\text{fit}}$ . However, one can modify Equation (4.34) to the needs of a BAYESIAN fit to assess its performance:

$$\Xi = \frac{\text{median}(\{\Sigma^{\text{fit}}\}) - \Sigma^{\text{true}}}{\text{std}(\{\Sigma^{\text{fit}}\})} \sim \mathcal{N}(0, 1). \quad (4.36)$$

Instead of the point estimates  $\Sigma^{\text{fit}}$  the median of the set of all draws from the marginal posteriors  $\{\Sigma^{\text{fit}}\}$  is shifted by the true value  $\Sigma^{\text{true}}$  and normalized by the standard deviation as an error estimate for each fit. Although this is not a rigorously derived quantity it allows to identify possible bias if  $\text{mean}(\Xi) \neq 0$ . Furthermore, checking that  $\sigma \approx 1$  will affirm whether the width of the marginal posterior distributions is sensible. Figure 4.4 shows the combined  $\Xi$ -distributions of all fits and the unaltered combined posteriors shifted by the true value. As expected, both distributions are normal as a GAUSSIAN fit proves. The width of the marginal posterior distributions can be regarded as sensible since the standard deviation of the  $\Xi$  distribution  $\sigma_\Xi \approx 1$ <sup>8</sup>. This is furthermore confirmed by the

<sup>8</sup> One cannot expect to fulfill Eq. (4.35) exactly, since the errors are after all only estimates that aim to create comparability to the least squares fit.

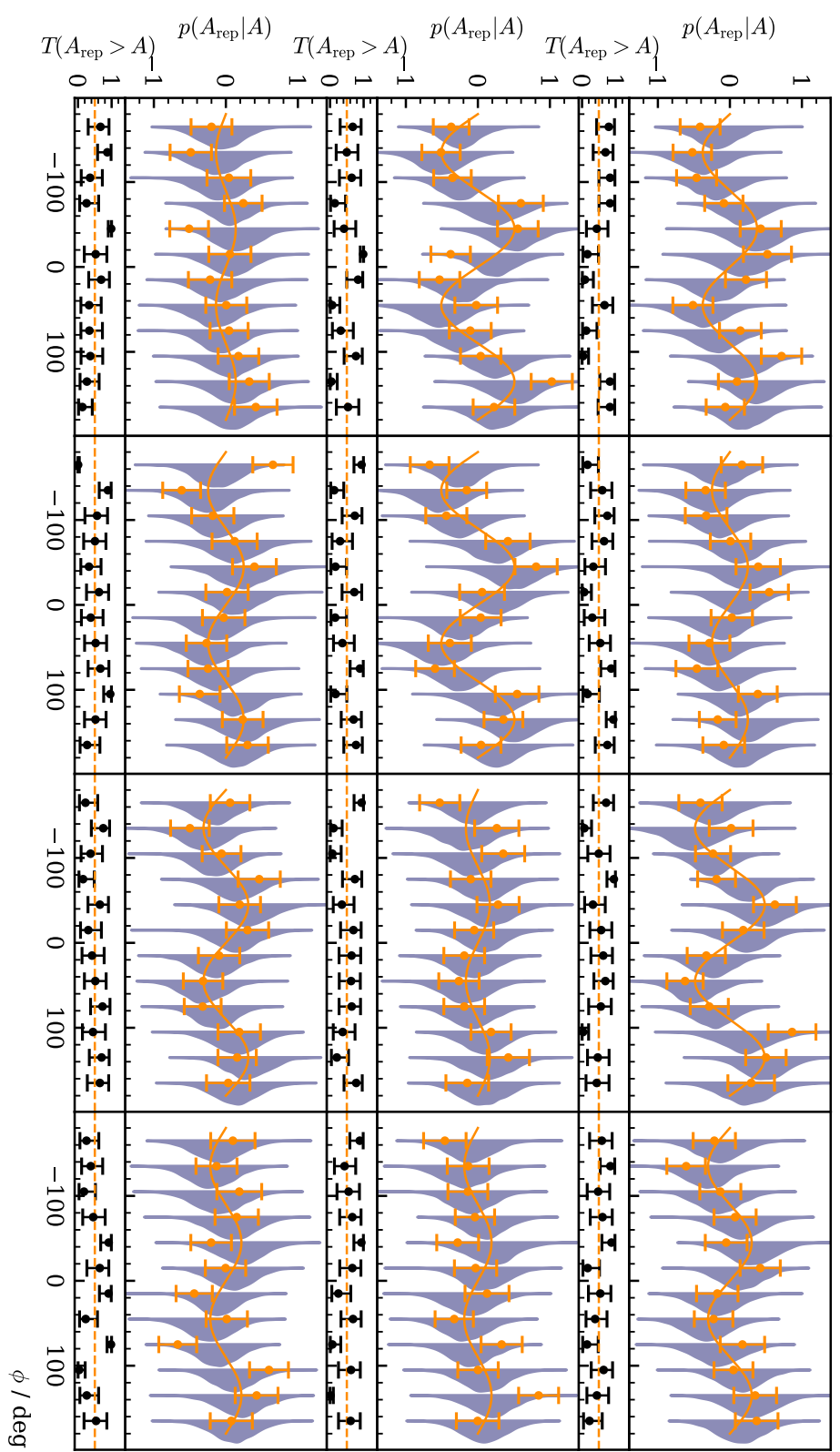


**Figure 4.2:** Posterior predictive checks  $p(A_{\text{rep}}|A)$  from a BAYESIAN fit to the event yield asymmetries for 12 toy Monte Carlo bins are shown as distributions.

The data points in the upper plot are the asymmetry  $A(\phi)$ , which was additionally fitted using a  $\chi^2$  fit (solid line). The goodness of fit is shown using  $p$ -values, which give the fraction  $T(A_{\text{rep}} > A)$  of replicated samples greater than the original measured value, with propagated statistical error bars on the bottom of each plot. The expected mean value of  $T(A_{\text{rep}} > A) = 0.5$  is indicated by the dashed line.

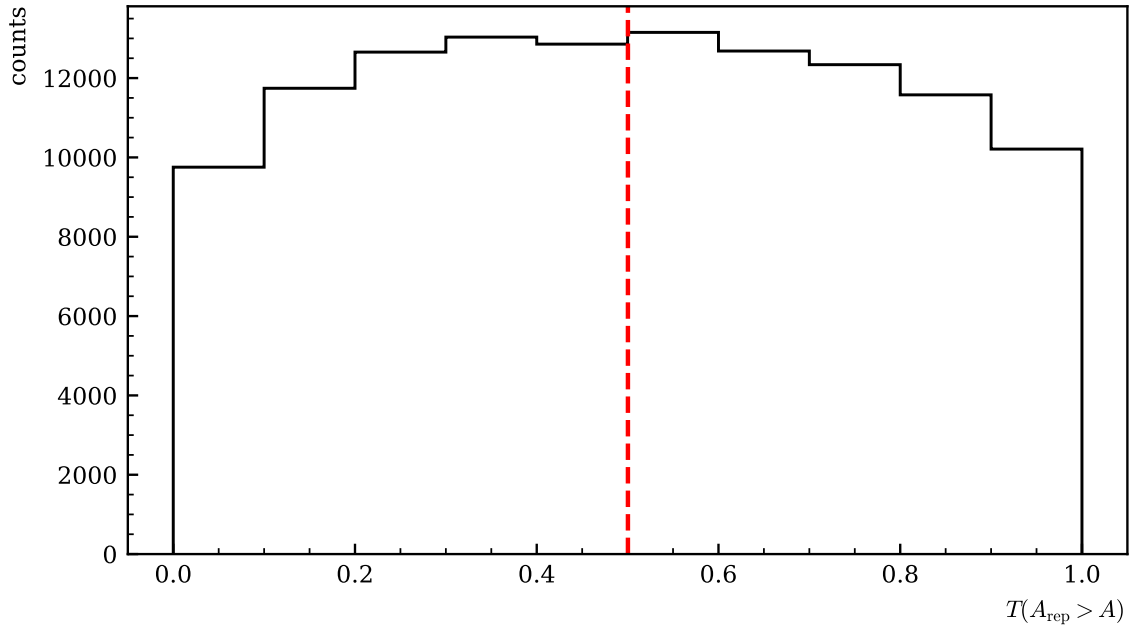


**Figure 4.3:**  $p$  values of all toy Monte Carlo bins. They are centered around their mean at 0.5, which is indicated by the dashed line, and show no bias towards higher or lower values, thus confirming an adequate fit.

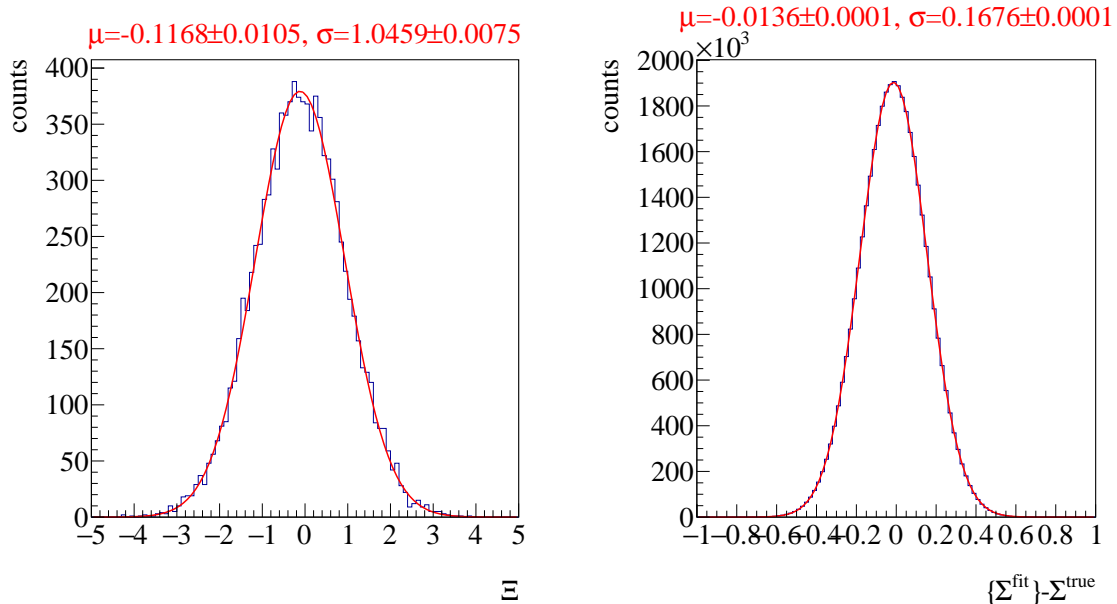


**Figure 4.4:** Left: Combined posterior distributions of all 10000 fits normalized by their respective standard deviation. Right: Unaltered combined posterior distributions of all 10000 fits. A GAUSSIAN fit was performed to determine mean  $\mu$  and standard deviation  $\sigma$  of the distributions with results given on top.

fact that  $\{\Sigma^{\text{fit}}\} - \Sigma^{\text{true}} = 0$  within one standard deviation of the GAUSSIAN. Yet, the fit results tend to underestimate the beam asymmetry, because both distributions are centered out of their statistical error at  $\mu \pm \Delta\mu < 0$ . This indicates bias towards smaller values of the beam asymmetry. Remarkably, this bias is *not* introduced by the BAYESIAN fit, but by the choice of binning and available statistics as an extensive investigation of binned fits (least squares and BAYESIAN) to toy Monte Carlo data showed. A detailed discussion thereof is given in appendix C. For now it suffices to note the origin of this bias lies in the choice of binning and is thus inevitable. And, most importantly, the introduced bias is negligible compared to the width of the posterior distributions, so that a binned fit will produce valid fit results in any case. Nevertheless this emphasizes the advantage of unbinned fitting, which is discussed in the next paragraph.

It has been established that the fit produces valid results with sensible statistical errors, i.e. widths of posterior distributions, and the description of the data is in agreement with the expectations. It remains to diagnose the convergence of the MARKOV chains to finally deem the binned fit method appropriate. For this the  $\widehat{R}$  value and the relative Monte Carlo standard error (MCSE)  $\frac{\sigma_{\text{MCSE}}}{\text{median}[p(\Sigma|y)]}$  that were introduced in section 1.3 are investigated. If  $\widehat{R} \lesssim 1.01$  one can assume that the different chains have converged and explored the same parameter space [Veh+19]. Furthermore the accuracy supplied by the number of draws from the posteriors can be evaluated with the relative MCSE. It is demanded that  $\frac{\sigma_{\text{MCSE}}}{\text{median}[p(\Sigma|y)]} \lesssim 5\%$ . This is the case for 97% of all fits, see Figure 4.5 on the left. When the fit result for the beam asymmetry is close to 0 larger values for the relative MCSE are observed. The  $\widehat{R}$  values (Figure 4.5 on the right) clearly indicate good within and between chain convergence. This means that the hyper parameters  $n_{\text{chain}}$ ,  $n_{\text{samples}}$  and  $n_{\text{warm up}}$  as chosen are well tuned, although one may increase the number of sample draws from the posterior for the fit from measured data to further suppress the relative MCSE. Then, only  $11 \cdot 12$  as opposed to 10000 fits have to be performed keeping the computational cost reasonable.

### Event based fit

Not only signal events but also contributions from random time background as well as the imperfect detector efficiency  $\epsilon(\phi)$  have to be simulated in order to test the method of event based fitting. For each polarization setting prompt peak and sideband events are drawn from the theoretical  $\phi$ -distributions  $p_{\text{prompt}}$  and  $p_{\text{sideband}}$  which are given in Equations (4.23) and (4.24). The total number of draws per setting and bin is again given by Poisson distributions and the ratio of prompt peak to sideband events is given by the time cut weights  $\{w_i\}_{i=1}^7$  employed for the actual analysis of the  $p\eta$  final state data [Afz19]. This means that seven times prompt peak and sideband events need to be simulated. The fraction of signal events within the prompt peak  $f$  was set to  $f = 0.95$ . Further, the values  $p_\gamma^\parallel = 0.25$ ,  $p_\gamma^\perp = 0.3$ ,  $\Sigma = 0.5$ ,  $\Sigma^{\text{bkg}} = -0.5$  and lastly, a random efficiency function as already chosen in reference [Afz19] were appointed. Finally the hyperparameters  $n_{\text{chain}}$ ,  $n_{\text{samples}}$ ,  $n_{\text{warm up}}$  are chosen in the same way as previously described. Table 4.1 shows a summary of all toy Monte Carlo properties. In total,  $1000^9$  toy Monte Carlo experiments are thrown. To evaluate the fit results only the posterior distributions are available. As before, the residuals  $\Xi$  are built from all fits, now for  $\Sigma$  as well as  $\Sigma^{\text{bkg}}$ . They are shown in Figure 4.6 together with the unnormalized posterior distributions. Note that the distributions are truncated towards the tails at  $\Sigma \rightarrow 1$  and  $\Sigma^{\text{bkg}} \rightarrow -1$  as implemented in the BAYESIAN fit in Stan. Also the event based fit is able to reproduce the true values within one standard

---

<sup>9</sup> The computation time for 10000 toy Monte Carlo fits would have exceeded a full week.

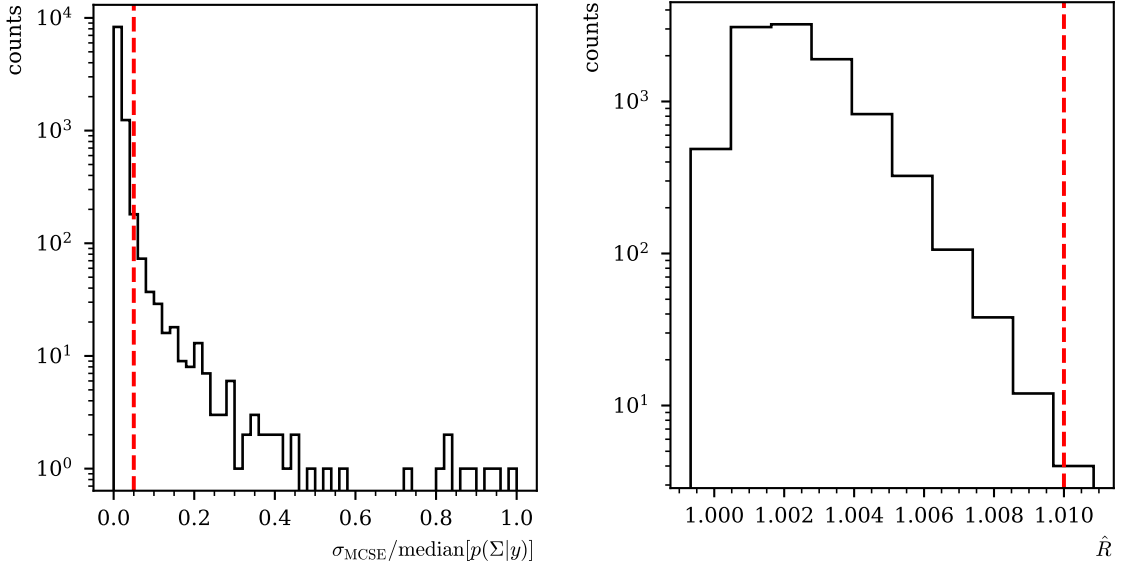


**Figure 4.5:** Left: relative error  $\frac{\sigma_{\text{MCSE}}}{\text{median}[p(\Sigma|y)]}$  associated with the parameter  $\Sigma$ . Right:  $\hat{R}$  associated with the fit parameter  $\Sigma$ . Both are shown for all 10000 unbinned fits. The critical values that should not be exceeded are marked by dashed lines.

<b>chosen parameters</b>	$p_\gamma^\parallel = 0.25, p_\gamma^\perp = 0.3, \Sigma = 0.5, \Sigma^{\text{bkg}} = -0.5, f = 0.95,$ $w_1 = \frac{15}{210}, w_2 = \frac{8}{210}, w_3 = \frac{4}{210}, w_4 = \frac{10}{210}, w_5 = \frac{14}{210}, w_6 = \frac{6}{210}, w_7 = \frac{11}{210}$
<b>simulation draws</b>	$7 \cdot N_{\text{total},i}^\parallel \sim \mathcal{P}(800), 7 \cdot N_{\text{total},i}^\perp \sim \mathcal{P}(1000) \quad  _{i=1}^7$
	signal in prompt      background in prompt      sideband
	$N_{\text{total}}^{\parallel/\perp} \cdot f$ $N_{\text{total}}^{\parallel/\perp} \cdot (1-f)$ $N_{\text{total}}^{\parallel/\perp} \cdot (1-f) \cdot 1/w_i$
<b>efficiency function</b>	$\epsilon(\phi) = 1/10.5 \cdot (9.3 + 0.28 \cdot \cos \phi + 0.24 \cdot \sin 3\phi)$
<b>hyperparameters</b>	$n_{\text{samples}} = 1000, n_{\text{chain}} = 4, n_{\text{warm up}} = 1000$

**Table 4.1:** Summary of the complete setting of all toy Monte Carlo experiments for the event based fit. Values and table layout adapted from [Afz19].

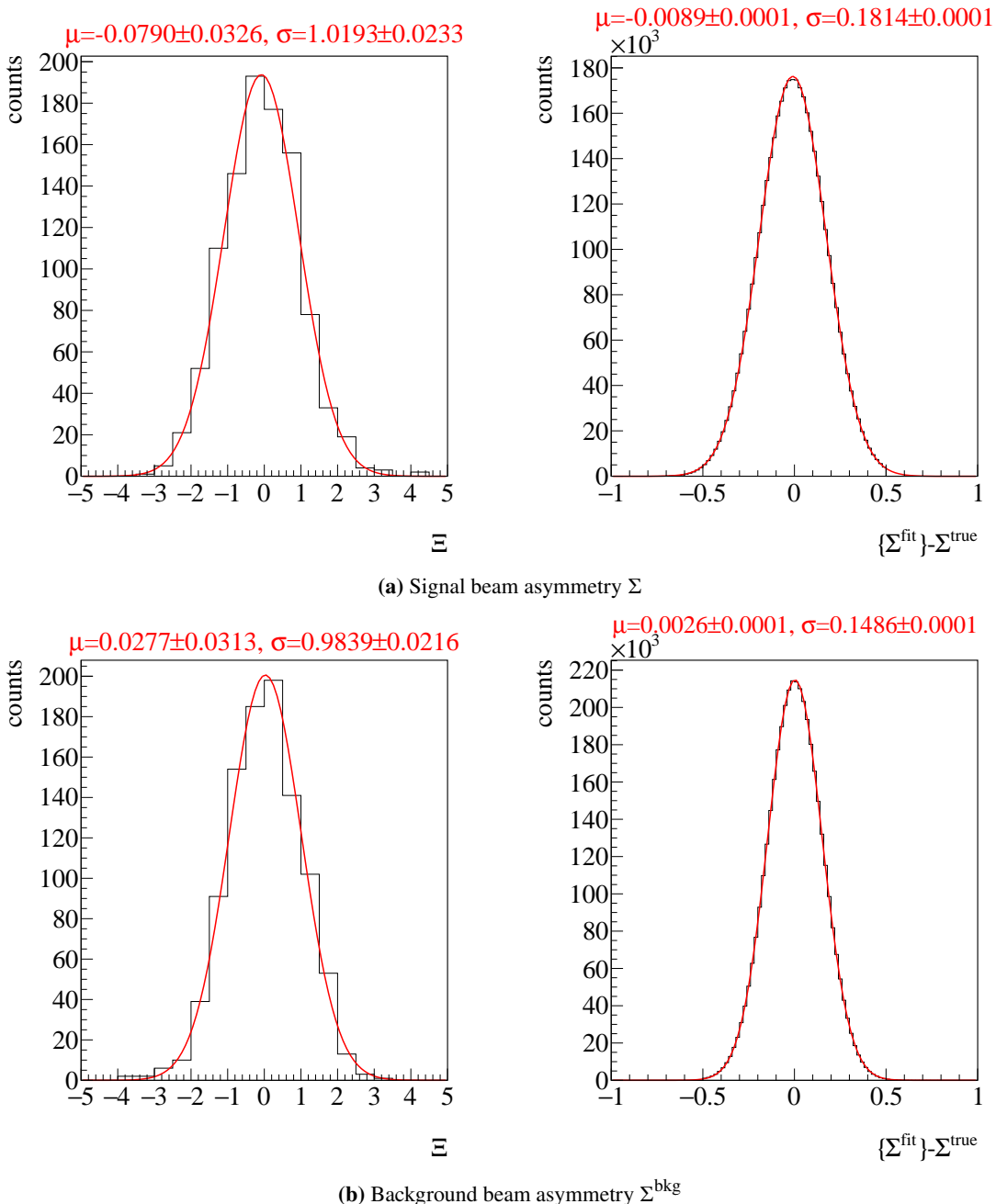


**Figure 4.6:** Combined posteriors for the beam asymmetries  $\Sigma$  and  $\Sigma^{\text{bkg}}$  from all 1000 event based fits. Left: Residuals  $\Xi$  Right: Unnormalized posterior distributions. A GAUSSIAN fit is performed on the distributions with results for mean  $\mu$  and standard deviation  $\sigma$  on top.

deviation of the posterior distribution  $\sigma_{\text{posterior}}$ . Only slight bias towards smaller values of the signal beam asymmetry is seen, but again with negligible effect on the results in comparison to the widths of the distributions. Additionally, the mean of the distributions are 0 within  $3\sigma$  of their statistical error and the errors are estimated correctly, since  $\sigma_{\text{posterior}} = 1$  within the statistical error. Note that the background beam asymmetry is estimated closer to its true value than the signal beam asymmetry because there are more random background events than signal events.

If the total amount of posterior distributions is not too large one might also combine them in a *pooled likelihood* approach (see subsection 1.3.5). This is shown in Figure 4.7 for both determined asymmetries. Because the true asymmetries are within  $1\sigma$  of the resulting distribution one can finally

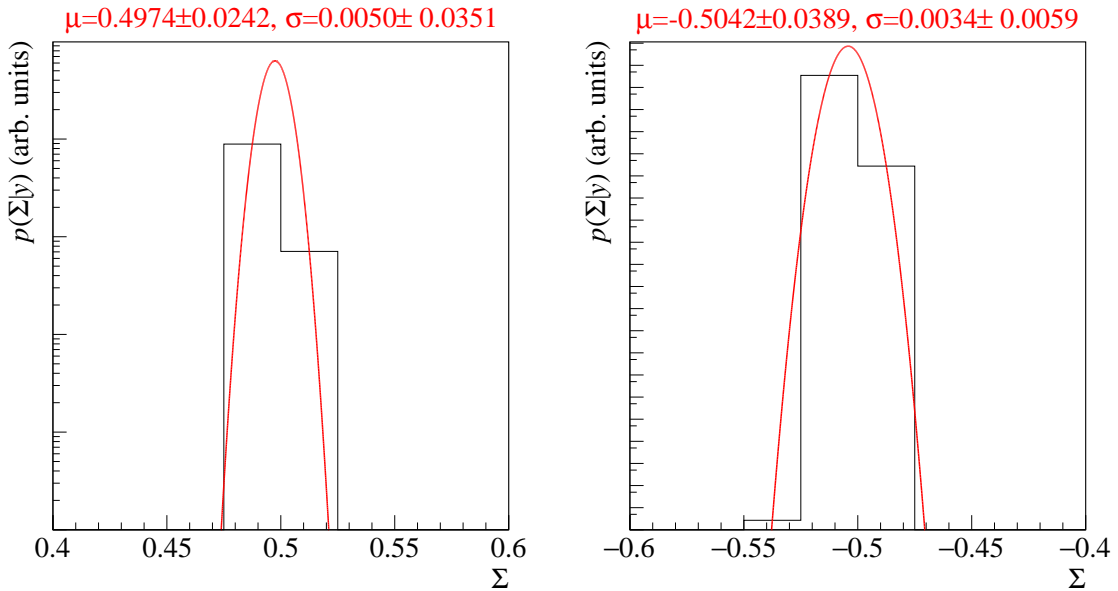


**Figure 4.7:** Combined posterior probabilities using the *pooled likelihood* approach. Left: Signal beam asymmetry, Right: background beam asymmetry. Mean and standard deviation as obtained from a Gaussian fit are shown on top

conclude that the event based fit estimates positions and widths of the posterior distributions correctly.

A check of the relative MCSE and  $\hat{R}$  values of all fit parameters as exemplary shown in Figure 4.8 reveals also that the hyperparameters  $n_{\text{chain}}, n_{\text{samples}}, n_{\text{warm up}}$  are correctly tuned. It is noteworthy that the event based fit creates more precise results regarding the MCSE although less Monte Carlo experiments in total were performed than for the binned fit.

Next to signal and background beam asymmetry the fit also estimates an efficiency function  $\epsilon(\phi)$  that is described by a FOURIER series. The polarization weighted sum of event yields allows to confirm whether a good description of the efficiency is achieved because it is given by the efficiency function modulated only by a constant, see previous section 4.1  $\alpha \tilde{N}^{\parallel} + \beta \tilde{N}^{\perp} = c \cdot \epsilon(\phi)$ . Figure 4.9 shows the weighted sum of event yields with the same binning as used in the binned fit together with a posterior predictive check using the draws of all parameters distributions  $a, b$ . As opposed to the binned fit it is not only performed at each data point but for significantly more points. This mimics a continuous function as is appropriate for an unbinned fit. However, for better visibility the posterior predictive distributions are not built at every point but the efficiency function is plotted for each set of draws

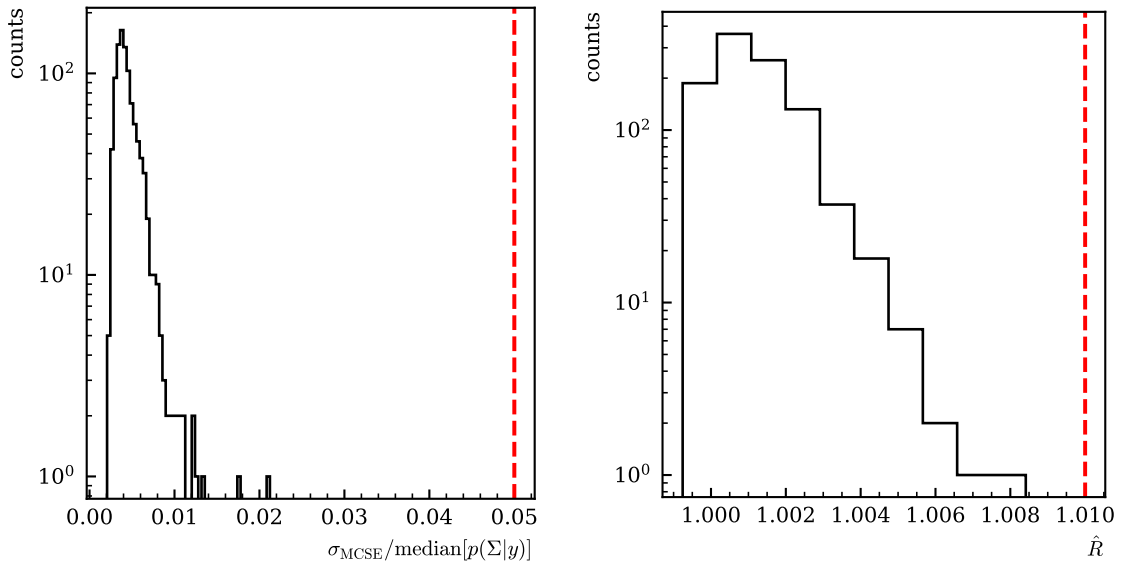


**Figure 4.8:** Left: relative error  $\frac{\sigma_{\text{MCSE}}}{\text{median}[p(\Sigma|y)]}$  associated with the fit parameter  $\Sigma$ . Right:  $\hat{R}$  associated with the fit parameter  $\Sigma$ . Both are shown for all 1000 unbinned fits. The critical values that should not be exceeded are marked by dashed lines.

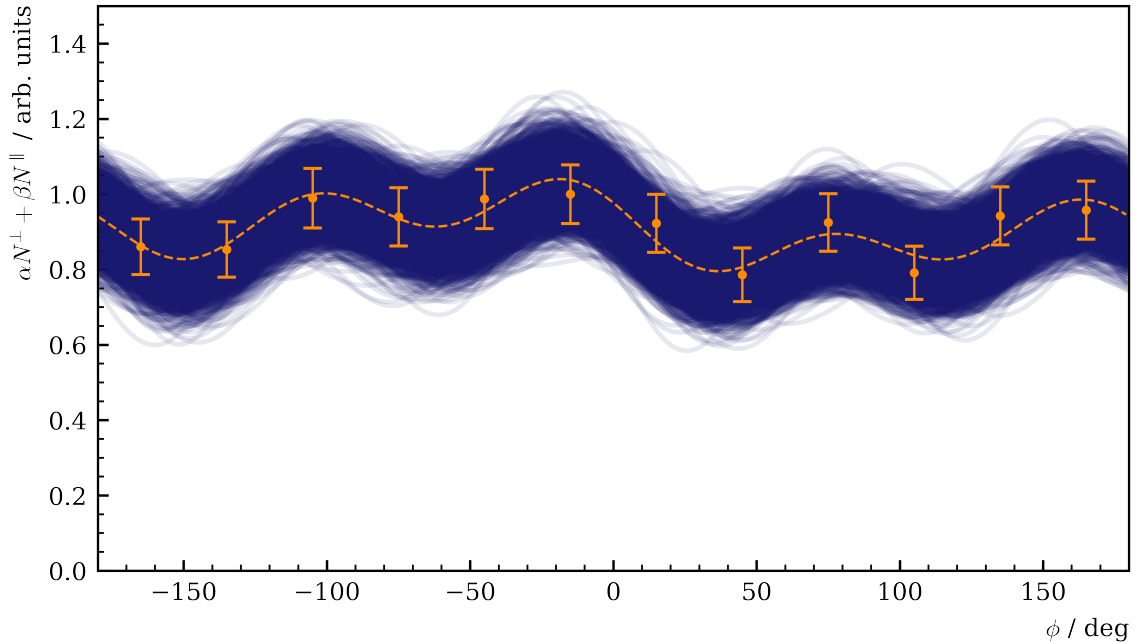


**Figure 4.9:** Posterior predictive check using the draws of the detector coefficients  $a$  and  $b$ . Points with error bars are the polarization weighted sum of event yields. The dashed line is the mean of the predictive values while the solid opaque lines are representative of one simulation draw  $a^{(s)}, b^{(s)}$ .

$a^{(s)}, b^{(s)}, s = 1 \dots 4000$ . No  $p$  values are estimated since they would not be representative of the whole fit. The mean of the posterior predictive distributions is given by the dashed line and agrees within statistical error bars with the simulated data.

### 4.2.2 Application of methods to data

Since both methods were tested successfully using toy Monte Carlo data, both are subsequently applied to real data to extract the beam asymmetry. Since the number of fits is small compared to the amount of fits performed during testing, the amount of posterior draws was increased to 5000 per chain. All other hyperparameters were left the same

$$n_{\text{samples}} = 5000 \quad n_{\text{chain}} = 4 \quad n_{\text{warm up}} = 1000. \quad (4.37)$$

#### Event yield asymmetries

In all bins of beam energy and meson polar angle the binned fit was performed. Similar to the Monte Carlo samples, 12 bins in phi are built to comply with the binning in reference [Afz19], and guarantee comparability.

Figure 4.10 shows the resulting asymmetry  $A(\phi)$  for all angular bins for the energy bin  $1250 \text{ MeV} \leq E_\gamma < 1310 \text{ MeV}$  as orange data points with statistical error bars. Additionally, a  $\chi^2$  fit (orange line) to the asymmetry together with posterior predictive checks as obtained from a fully BAYESIAN fit according to the introduced model (blue distributions) is shown. The goodness of fit is checked via the introduced  $p$ -values  $p = T(A_{\text{rep}} > A)$ , and are shown as black points with propagated error bars on the bottom. The optimal value of  $p = 0.5$  is marked by the dashed line and realizes the mean of the distribution of all  $p$ -values, so that one can assume good description of the data by the fits, see Figure 4.11. This replaces the investigation of the  $\chi^2/\text{NDF}$  distribution in the case of a frequentist fit.

The MCMC diagnostics reveal that all MARKOV chains have converged and explored the available parameter space completely which is characterized by  $\widehat{R} = 1.00$  for all fits. The increment of posterior draws removed any fluctuations in the  $\widehat{R}$  value that was present before. The relative MCSE is below the (self-)defined threshold of  $\frac{\sigma_{\text{MCSE}}}{\text{median}[p(\Sigma|y)]} < 5\%$  for 95% of all fits. The remaining 5% are fits that estimated the beam asymmetry close to 0 such that further incrementing the number of posterior draws will not amend this. Both, relative MCSE and  $\widehat{R}$  associated with the fit parameter  $\Sigma$  of the binned fit, are shown in Figure 4.12. Thus, one can conclude the successful tuning of hyperparameters concerning the BAYESIAN fit.

#### Event based fit

The discussed BAYESIAN event based fit is also performed for all kinematic bins. The MCMC diagnostics reveal good choice of hyperparameters, as Figure 4.13 shows. As already observed during the toy Monte Carlo experiments, the unbinned fit produces more precise results; 98% of all fits exhibit an MCSE below threshold, those bins with error above threshold are again explained by values of the beam asymmetry  $\Sigma \approx 0$ . Good within and between chain convergence is reached, as  $\widehat{R} \lesssim 1.01$  for all fits and parameters shows.

The only illustrative measure regarding the performance of the unbinned fit is the posterior predictive distribution of the detector coefficients  $a, b$ . Figure 4.14 shows the weighted sum of event yields with the same binning as used in the binned fit together with a posterior predictive check using the draws of

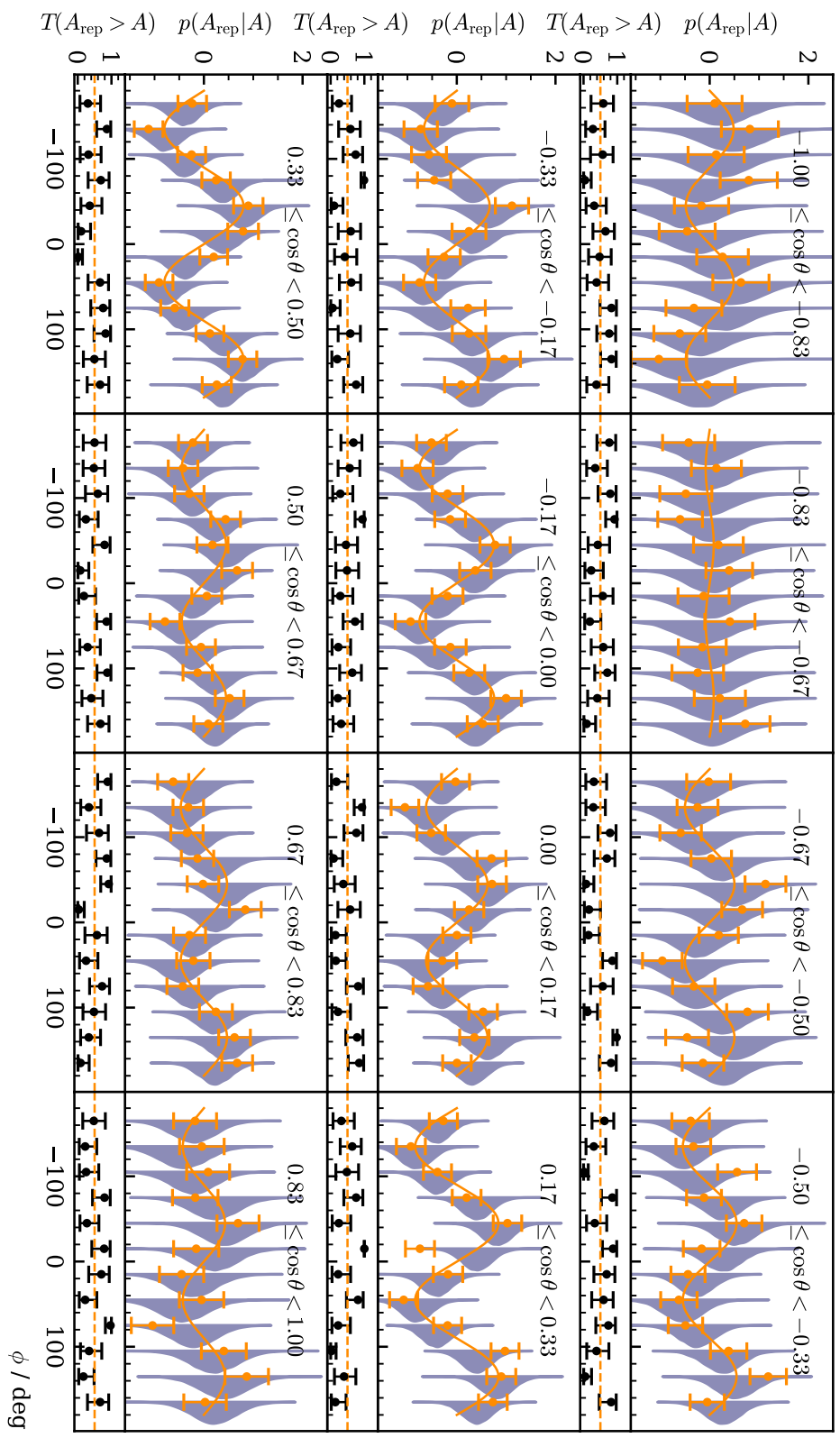


**Figure 4.10:** Posterior predictive checks  $p(A_{\text{rep}}|A)$  from a BAYESIAN fit to the event yield asymmetries for the reaction  $\gamma p \rightarrow p\eta \rightarrow p\gamma\gamma$  for all angular bins of the energy bin  $1250 \text{ MeV} \leq E_\gamma < 1310 \text{ MeV}$ . The data points in the upper plot are the asymmetry  $A(\phi)$ , which was additionally fitted using a  $\chi^2$  fit (solid line). The goodness of fit is shown using  $p$ -values, which give the fraction  $T(A_{\text{rep}} > A)$  of replicated samples greater than the original measured value, with propagated statistical error bars on the bottom of each plot. The expected mean value of  $T(A_{\text{rep}} > A) = 0.5$  is indicated by the dashed line.

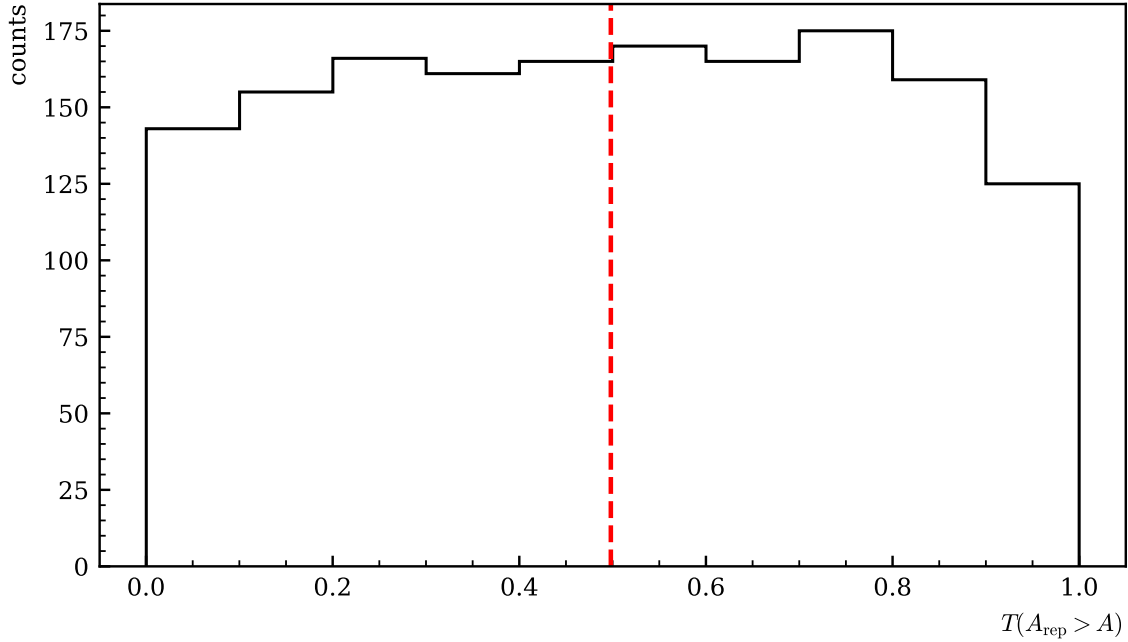


**Figure 4.11:**  $p$  values generated using all fits from all bins in the reaction  $\gamma p \rightarrow p\eta \rightarrow p\gamma\gamma$ . They are centered around their mean at 0.5, which is indicated by the dashed line, and show no bias towards higher or lower values, thus confirming an adequate fit.

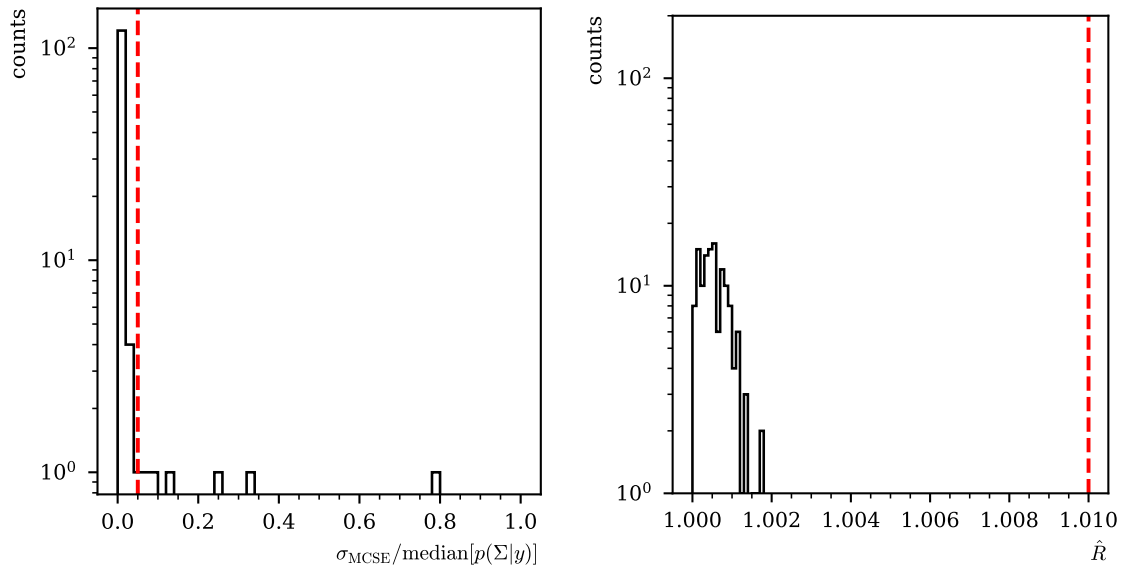


**Figure 4.12:** Left: relative error  $\frac{\sigma_{\text{MCSE}}}{\text{median}[p(\Sigma|y)]}$  associated with the fit parameter  $\Sigma$ . Right:  $\hat{R}$  associated with the fit parameter  $\Sigma$ . Both are shown for all  $11 \cdot 12$  binned BAYESIAN fits to the asymmetry  $A$  ( $\phi$ ) in  $\eta$  photoproduction. The critical values that should not be exceeded are marked by dashed lines.

all parameters distributions  $a, b$  for the kinematic bin  $1250 \text{ MeV} \leq E_\gamma < 1310 \text{ MeV}, 0 \leq \cos \theta < 0.17$ . As opposed to the binned fit it is not only performed at each data point but for significantly more points. This mimics a continuous function as is appropriate for an unbinned fit. However, for better visibility the posterior predictive distributions are not built at every point but the efficiency function is plotted for each set of draws  $a^{(s)}, b^{(s)}, s = 1 \dots 20000$ . No  $p$  values are estimated since they would not be representative of the whole fit. Note that the detector efficiency  $\epsilon(\phi)$  is almost flat as opposed to the simulated efficiency in subsection 4.2.1. This is an overall observation and not specific to the shown kinematic bin and further confirmed by the fact that the sums of all fit coefficients  $a, b$  are distributed around zero. Regardless of the significance of detection inefficiencies the unbinned fit is nevertheless able to obtain good agreement between fit and data; the mean of all posterior predictive distributions (dashed line) agrees within statistical error bars with the data points.

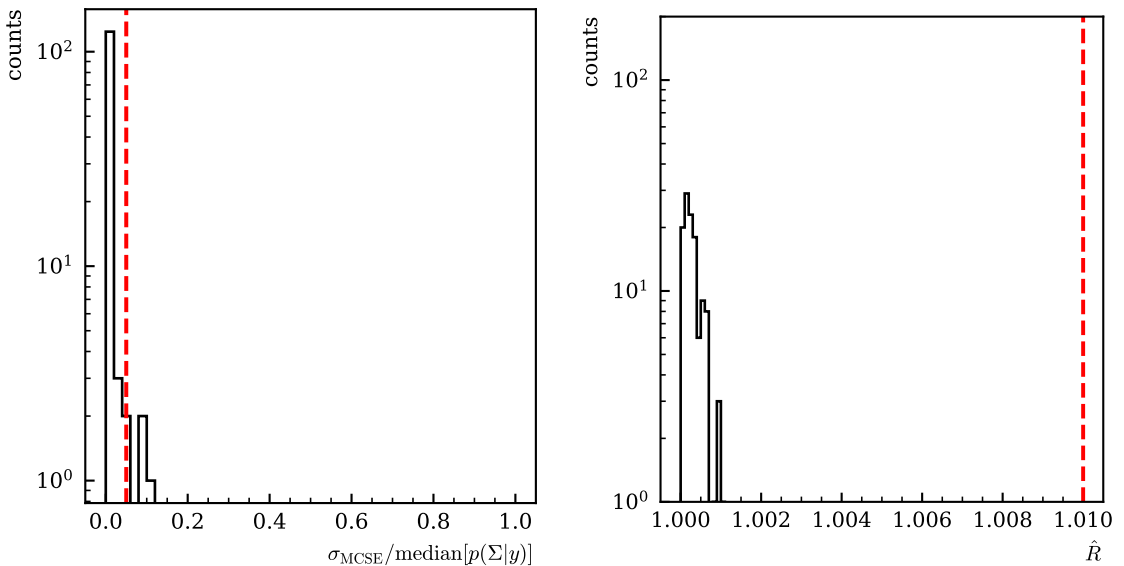


**Figure 4.13:** Left: relative error  $\frac{\sigma_{\text{MCSE}}}{\text{median}[p(\Sigma|y)]}$  associated with the fit parameter  $\Sigma$ . Right:  $\hat{R}$  associated with the fit parameter  $\Sigma$ . Both are shown for all  $11 \cdot 12$  unbinned fits in  $\eta$  photoproduction. The critical values that should not be exceeded are marked by dashed lines.

### 4.2.3 Discussion

The final results for the beam asymmetry obtained with both methods are shown in Figure 4.15 for all bins in beam energy and meson polar angle. Along with the marginal posterior distributions obtained from both introduced methods point estimates from a  $\chi^2$  fit and an unbinned fit [Afz19] are shown. An important intermediate result is that all results agree with each other within statistical error bars or within the width of the marginal posterior distributions. Any effects that lead to slightly distinguishable point estimates from a binned or unbinned fit are propagated directly throughout the BAYESIAN fit; then each distribution is centered around the point estimate of the respective fitting method. The results from the binned and unbinned fit with error bars on average cover 68% of the respective marginal posterior distributions, corresponding to a  $1\sigma$  interval. Thus, in general, the

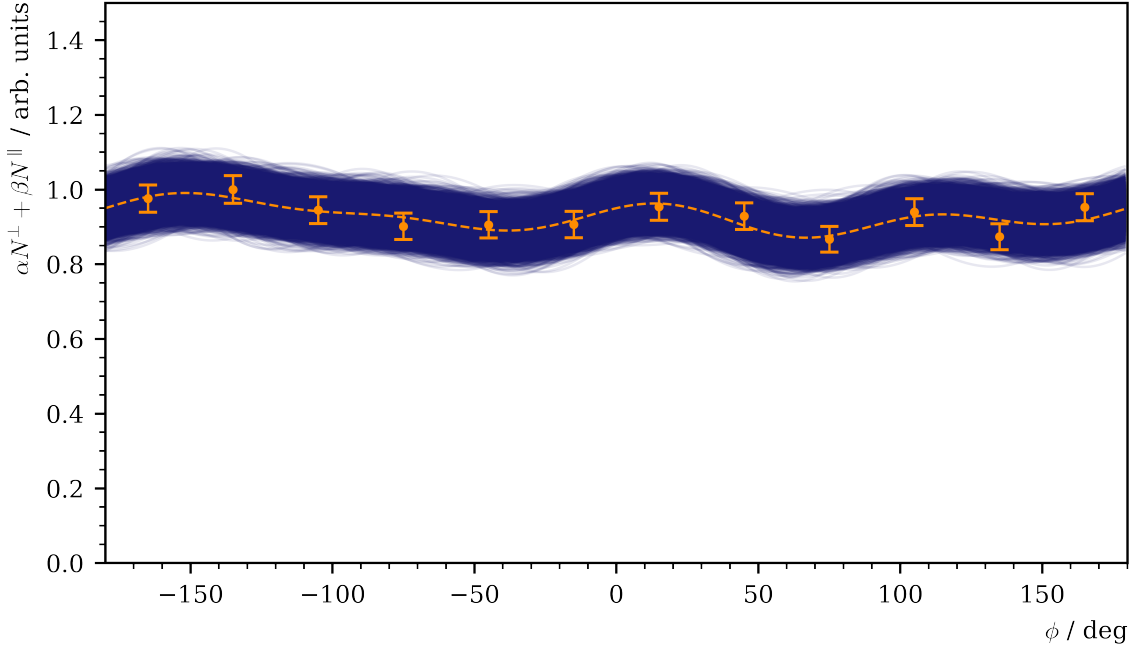


**Figure 4.14:** Posterior predictive check using the draws of the detector coefficients  $a$  and  $b$  for the kinematic bin  $1250 \text{ MeV} \leq E_\gamma < 1310 \text{ MeV}$ ,  $0 \leq \cos \theta < 0.17$ . Points with error bars are the polarization weighted sum of event yields. The dashed line is the mean of the predictive values while the solid opaque lines are representative of one simulation draw  $a^{(s)}, b^{(s)}$ .

application of BAYESIAN methods has proven to give the same results and no systematic error is introduced by the BAYESIAN approach. The effort of implementing the binned or unbinned fit in a BAYESIAN approach is comparable to using standard libraries provided by e.g. *python* [RP22] or *ROOT* [BR97]. Due to the probabilistic structure of the Stan language [Sta22a] implementation of likelihood and prior models is straightforward and the sampling algorithms can be accessed or modified to ones needs intuitively. However, the BAYESIAN fit requires more careful preparation and also diagnostics. On one hand, the choice of priors has to be made. On the other hand, the fitting procedure is inherently different; not only the goodness of fit compared with data has to be checked but also the convergence of the MARKOV chains themselves.

The computational cost also increases greatly in comparison to the traditional frequentist approaches. Especially the unbinned BAYESIAN fit requires a lot of computation time, where the number of data points is of order  $O(10^4)$  as opposed to 12 data points for the binned fit. This can be understood considering the underlying algorithms; the least squares fit and also the unbinned maximum likelihood fit both aim to minimize a given test statistic which is achievable by differentiation. Determining marginal posterior distributions from BAYESIAN inference on the other hand requires (numeric) integration, making it the more complex task which is observable in the consumed computation time. While an unbinned maximum likelihood fit using e.g. *TTree::UnbinnedFit* [ROOo] takes seconds, the BAYESIAN unbinned fit took up to 20 minutes.

Yet, the additional effort is rewarded by the fact that the BAYESIAN fit will yield *distributions* for all parameters as opposed to point estimates with error bars. This is especially useful for polarization

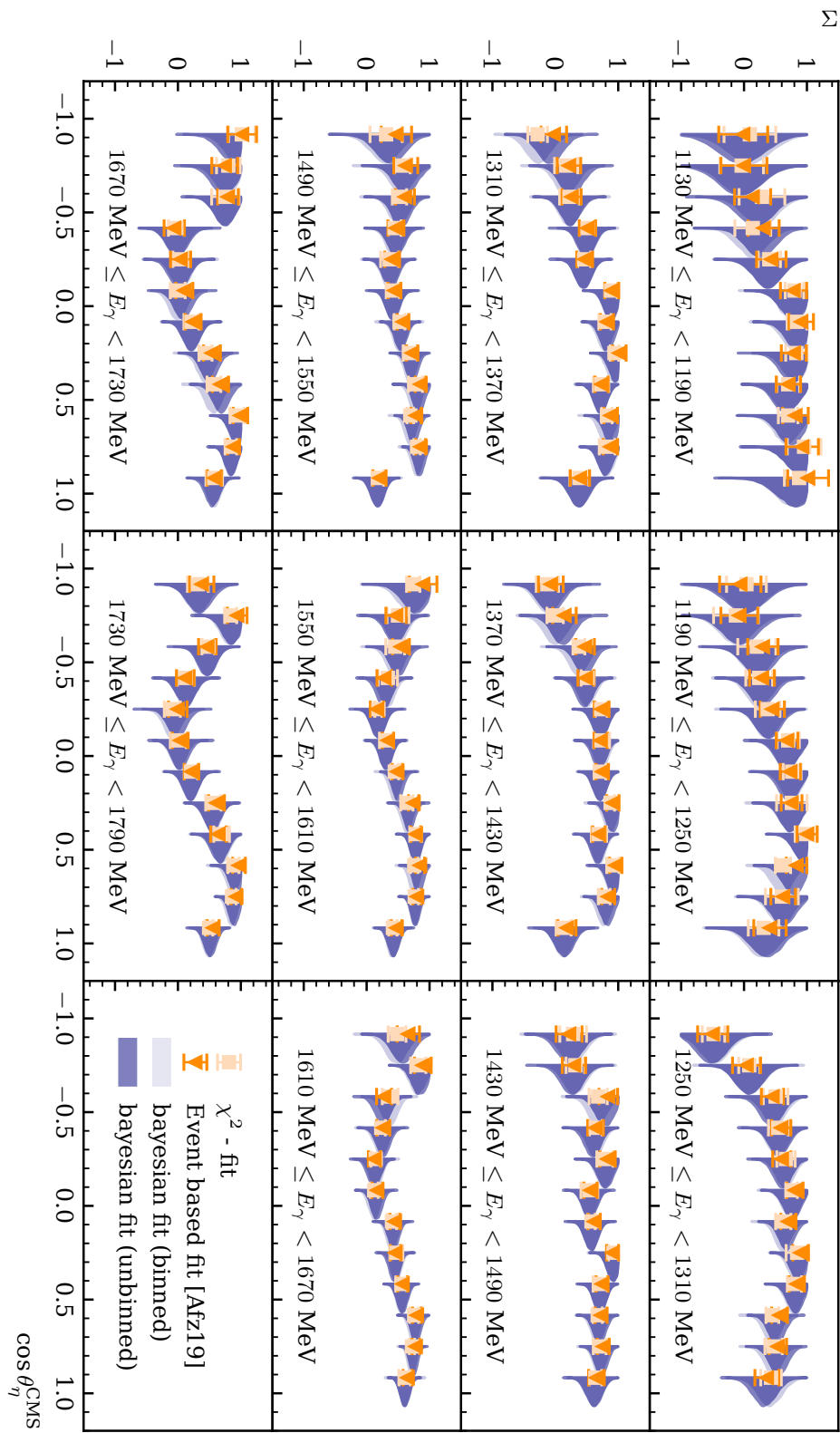


**Figure 4.15:** Final results for the beam asymmetry  $\Sigma$  in  $\eta$  photoproduction off the proton for all kinematic bins obtained with BAYESIAN methods. They are compared with the results of a least squares fit and an unbinned fit as given in reference [Afz19]. All results agree within statistical error bars or within the widths of marginal posterior distributions.

observables which may be used as input for PWA calculations. Here error estimates can be derived from the distributions e.g. as (multiple) standard deviations, the full width at half maximum or similar. If furthermore a BAYESIAN approach is pursued, also the whole distributions may be used. Because the final results are distributions also the structure of these may be analyzed uncovering possible multimodalities as well as distributions differing from i.e. a symmetric GAUSSIAN. Another advantage of the BAYESIAN fit is the ability to truncate the posterior samples to the relevant or allowed parameter space. In the very first energy bin in Figure 4.15 this is visible clearly where several point estimates exceed the physical limit of  $\Sigma = 1$  as opposed to the obtained marginal posteriors. Lastly, the BAYESIAN fit allows much more flexible changes to the fitted model, as will be discussed in the next section 4.3.

### 4.3 Determination of $\Sigma_{\eta'}$

After successfully testing the application of BAYESIAN methods this section will demonstrate the extraction of new results for the beam asymmetry in  $\eta'$  photoproduction off the proton obtained at the CBELSA/TAPS experiment. Only the event based fitting method is applied and the binned fitting of event yield asymmetries is discarded because on the one hand the available statistics will on average give only few counts per bin  $(E_\gamma, \cos \theta, \phi)$  of order  $\mathcal{O}(10^1)$ , depending on the specific number of  $\phi$ -bins. This will result in very large statistical errors per bin that may also not necessarily approximated as GAUSSIAN anymore. On the other hand this could be compensated by choosing fewer bins in  $\phi$  which would however amplify the systematic underestimation of the beam asymmetry which is discussed in appendix C.

The event based fits are performed as unbinned maximum likelihood fit and as an unbinned BAYESIAN fit. New toy Monte Carlo experiments are thrown adapting to the significantly decreased statistics. Also, tests regarding the background contamination of Monte Carlo samples are made, see Chapter 3.

#### 4.3.1 Application of event based fit to toy Monte Carlo data

After selecting all suitable event candidates for  $\gamma p \rightarrow p\eta' \rightarrow p\gamma\gamma$  reactions there still remain significant background contributions which make up roughly 20% of all events averaged over all kinematic bins. Investigation of Monte Carlo simulations of different mesonic final states revealed they are mainly realized by the false reconstruction of  $2\pi^0$  photoproduction events (see chapter 3). It was thus investigated how the presence of two beam asymmetries  $\Sigma_1$  and  $\Sigma_2$  affects the fit. The combined differential cross section is then given by

$$\frac{d\sigma}{d\Omega_{\text{pol}}}(\phi) = \frac{d\sigma^{(1)}}{d\Omega_{\text{pol}}}(\phi) + \frac{d\sigma^{(2)}}{d\Omega_{\text{pol}}}(\phi) \quad (4.38)$$

$$= \frac{d\sigma^{(1)}}{d\Omega_0} \cdot \left(1 - p_\gamma \Sigma_1 \cos(2\phi)\right) + \frac{d\sigma^{(2)}}{d\Omega_0} \cdot \left(1 - p_\gamma \Sigma_2 \cos(2\phi)\right). \quad (4.39)$$

If now the fraction  $\delta$  of events in the final state with beam asymmetry  $\Sigma_2$  is known one can express the unpolarized cross sections via a common combined unpolarized cross section as

$$\frac{d\sigma^{(1)}}{d\Omega_0} = (1 - \delta) \cdot \frac{d\sigma}{d\Omega_0} \quad \frac{d\sigma^{(2)}}{d\Omega_0} = \delta \cdot \frac{d\sigma}{d\Omega_0}. \quad (4.40)$$

Plugging Equation (4.40) into Equation (4.39) then yields

$$\frac{d\sigma}{d\Omega_{\text{pol}}}(\phi) = \frac{d\sigma}{d\Omega_0} \cdot \left(1 - p_\gamma [(1 - \delta) \cdot \Sigma_1 + \delta \cdot \Sigma_2] \cos(2\phi)\right). \quad (4.41)$$

In the presence of background  $\Sigma^{\text{bkg}}$ <sup>10</sup> all measured values for the beam asymmetry  $\Sigma^{\text{meas}}$  are systematically shifted from their true value  $\Sigma^{\text{true}}$ , depending on the amount of background, if the methods described in section 4.1 are used without modification, i.e.

$$\Sigma^{\text{meas}} = (1 - \delta) \cdot \Sigma^{\text{true}} + \delta \cdot \Sigma^{\text{bkg}}. \quad (4.42)$$

This is an important intermediate result: If the background asymmetry  $\Sigma^{\text{bkg}}$  and the corresponding fraction of events  $\delta$  that exhibit this asymmetry are known, the true values  $\Sigma^{\text{true}}$  can be obtained. If  $\Sigma^{\text{bkg}}$  is not known this is a source of systematic error.

Table 4.2 shows all characteristics of the investigated toy Monte Carlo experiments, the values for polarization and statistics per bin were chosen to match the respective average values in the selected data for the  $\gamma p \rightarrow p\eta' \rightarrow p\gamma\gamma$  final state. Furthermore  $\delta = 20\%$  of all events were simulated as background with beam asymmetry  $\Sigma_2$  while the remainder of events is simulated with beam asymmetry  $\Sigma_1$ . The amount of random time background in the prompt peak is set to  $(1 - f) = 0.05$  while the sideband events are weighted by  $w = \frac{13}{200}$  (see section 3.3). The same efficiency function and hyperparameters are employed as previously with the exception of the number of posterior draws which is raised to  $n_{\text{samples}} = 5000$  from the beginning. Because of the smaller amount of data this does not increase the computational cost immensely.

<b>chosen parameters</b>	$p_\gamma^\parallel = 0.3, p_\gamma^\perp = 0.3, \Sigma_1 = 0.5, \Sigma_2 = -0.3, \Sigma_t^{\text{bkg}} = -0.5, f = 0.95, \delta = 0.2$ $w = \frac{13}{200}$
<b>simulation draws</b>	$N_{\text{total}}^\parallel \sim \mathcal{P}(200), N_{\text{total}}^\perp \sim \mathcal{P}(200)$
	signal in prompt      background in prompt      sideband
	$N_{\text{total}}^{\parallel/\perp} \cdot f$ $N_{\text{total}}^{\parallel/\perp} \cdot (1 - f)$ $N_{\text{total}}^{\parallel/\perp} \cdot (1 - f) \cdot 1/w$
<b>efficiency function</b>	$\epsilon(\phi) = 1/10.5 \cdot (9.3 + 0.28 \cdot \cos \phi + 0.24 \cdot \sin 3\phi)$
<b>hyperparameters</b>	$n_{\text{samples}} = 5000, n_{\text{chain}} = 4, n_{\text{warm up}} = 1000$

**Table 4.2:** Summary of the complete setting of all toy Monte Carlo experiments for the event based fit. Table layout adapted from [Afz19].

<sup>10</sup> For clarity, the beam asymmetry associated with random time background will in this section be denoted as  $\Sigma_t^{\text{bkg}}$  and the beam asymmetry associated with background reactions as  $\Sigma^{\text{bkg}}$ .

### Unbinned maximum likelihood fit

To test the unbinned maximum likelihood fit and its response to the presence of background, 10000 toy Monte Carlo bins are created according to table 4.2. The expected beam asymmetry is

$$\Sigma^{\text{meas}} = 0.8 \cdot 0.5 - 0.2 \cdot 0.3 = 0.34. \quad (4.43)$$

Building the normalized residuals with respect to  $\Sigma^{\text{meas}}$  and the random time background asymmetry  $\Sigma_t^{\text{bkg}}$  yields standard normal distributions, see Figures 4.16 and 4.17, thus fulfilling the expectations entirely. This allows Equation (4.42) to be applied on results obtained with this method provided the background beam asymmetry is known. Any errors on  $\Sigma^{\text{bkg}}$  may be propagated in a GAUSSIAN manner. The beam asymmetry is estimated without bias and the errors are correctly estimated as confirmed by  $\mu = 0$  and  $\sigma = 1$  for the normalized residuals within few widths of the statistical errors. Note that the unnormalized distributions are significantly broader than the ones examined in the previous section which is due to the decreased statistics in each bin which already indicates larger statistical errors. The decreased statistics also cause greater variation in the fitted efficiency function that is seen in Figure 4.18, which still describes the data very well.

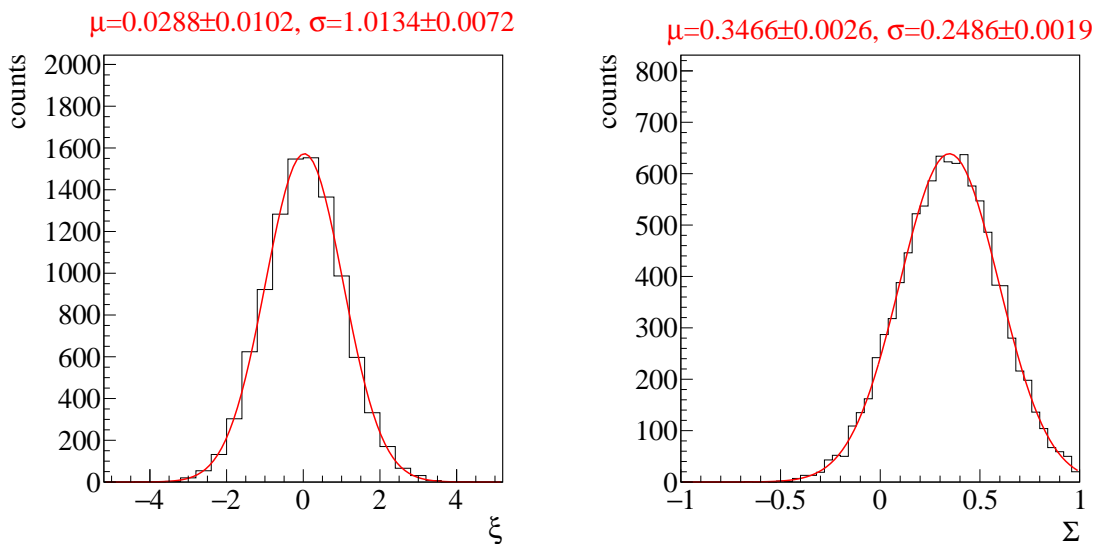


**Figure 4.16:** Normalized residuals (left) and unaltered distribution (right) of all 10000 unbinned maximum likelihood fits for the beam asymmetry  $\Sigma = (1 - \delta) \cdot \Sigma_1 + \delta \cdot \Sigma_2$ . GAUSSIAN fits are performed with results given on top of each plot.

### Unbinned BAYESIAN fit

When performing a BAYESIAN fit a systematic shift like Equation (4.42) as result of background contributions is not easily applicable. The posterior distributions may be shifted by a constant value but including statistical errors of the background beam asymmetry is not possible. To circumvent this, the background beam asymmetry can be included inherently in the likelihood function that is

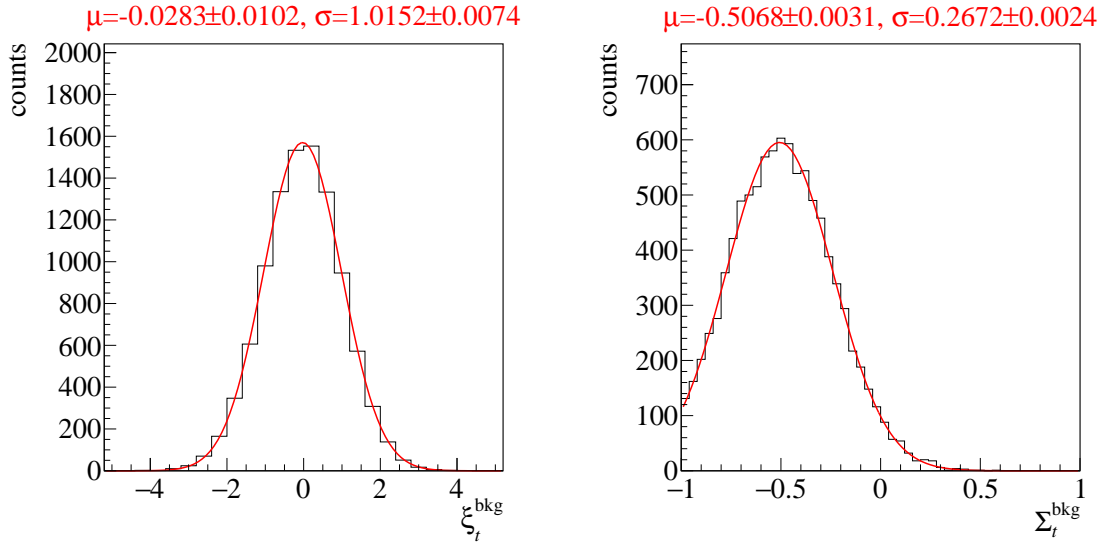


**Figure 4.17:** Normalized residuals (left) and unaltered distribution (right) of all 10000 unbinned maximum likelihood fits for the background beam asymmetry  $\Sigma_t^{\text{bkg}}$ . GAUSSIAN fits are performed with results given on top of each plot.

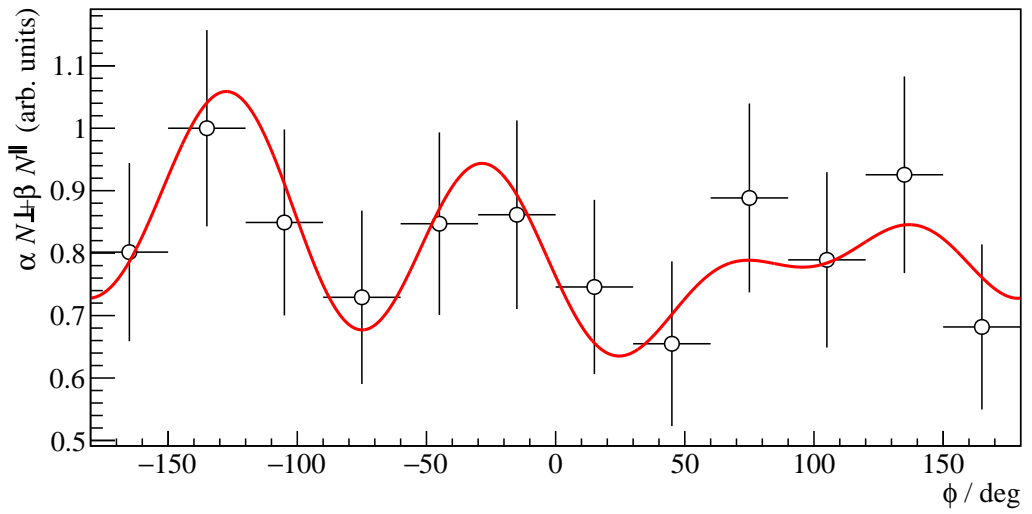


**Figure 4.18:** Fitted efficiency function (red line) applied to the polarization weighted sum of event yields (data points) for one toy Monte Carlo bin. 12 bins in  $\phi$  are built for demonstration.

part of the model being fitted. In practice,  $\delta$  and  $\Sigma_2$  have to be part of the data that is fed into the probabilistic model. In general though  $\Sigma_2$  will have a statistical error, which can be included in the fashion of modeling *missing data* [Sta22a]. Doing so, the value for  $\Sigma_2$  is regarded as an estimate for the true, unknown (or missing) value  $\Sigma_2^{\text{true}}$ . The statistical error  $\tau$  of  $\Sigma_2$  specifies the measurement model assuming **GAUSSIAN** errors

$$\Sigma_2^{\text{true}} \sim \mathcal{N}(\Sigma_2, \tau). \quad (4.44)$$

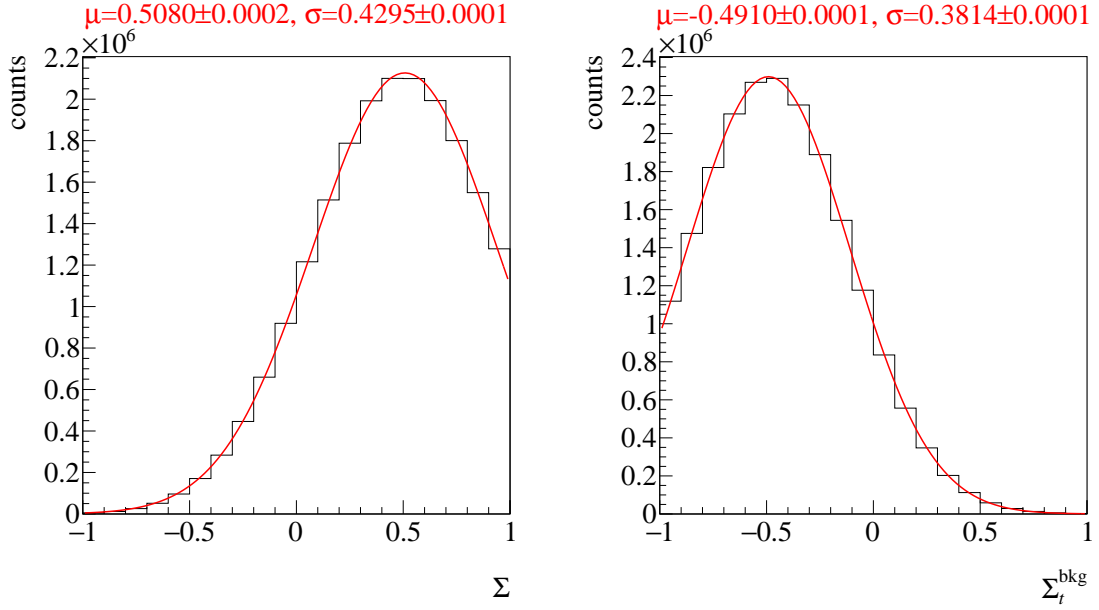
With this  $\Sigma_2^{\text{true}}$  is added as an additional fit parameter to the probabilistic model, so that the likelihood is modified as

$$\begin{aligned} \ln \mathcal{L} = & \sum_{i=1}^n \ln p_{\text{prompt}} \left( \phi_i, p_{\gamma,i} \mid (1 - \delta) \cdot \Sigma_1 + \delta \cdot \Sigma_2^{\text{true}}, a, b, \Sigma_t^{\text{bkg}}, a_t^{\text{bkg}}, b_t^{\text{bkg}} \right) \\ & + \sum_{j=1}^m \ln p_{\text{sideband}} \left( \phi_j, p_{\gamma,j} \mid \Sigma_t^{\text{bkg}}, a_t^{\text{bkg}}, b_t^{\text{bkg}} \right). \end{aligned} \quad (4.45)$$

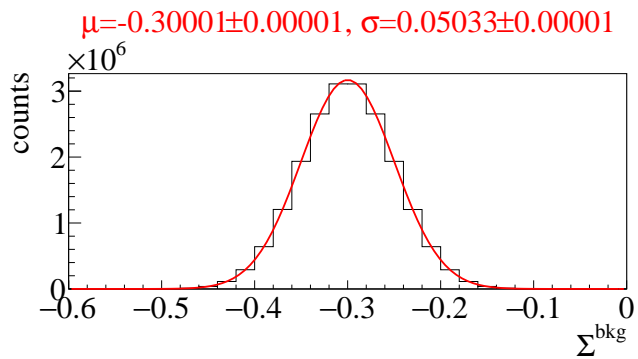
For a complete inference  $\Sigma_2^{\text{bkg}}$  also needs to be assigned a prior, which is chosen to be uniform to keep the number of fit parameters minimal. In total, 1000 bins in accordance with Table 4.2 are fitted with the adapted model that includes a background asymmetry  $\Sigma_2$  with statistical error  $\tau$  which are used to estimate the additional fit parameter  $\Sigma_2^{\text{true}}$ . For the sake of the toy Monte Carlo experiments the measurement error is arbitrarily chosen to be  $\tau = 0.05$  which is similar to the measured errors of the beam asymmetry in  $2\pi^0$  photoproduction [Mah22].

Figure 4.19 shows the combined posteriors for the fit parameters  $\Sigma_1$  and  $\Sigma_t^{\text{bkg}}$  of the event based **BAYESIAN** fit for all generated toy Monte Carlo bins. The posteriors are added up since the truncation of the posteriors biases the results when combining them in a pooled likelihood model or normalized residuals  $\Xi$ . Previous experiments already proved sensible error estimation, i.e. distribution widths, when using the unbinned **BAYESIAN** fit. This is discussed in appendix D. The input parameters are very well reproduced within the statistical error, which is given by the standard deviation of the **GAUSSIAN**. The posterior distribution of  $\Sigma_1$  is wider than the posterior of the background beam asymmetry  $\Sigma_t^{\text{bkg}}$  because an additional measurement of  $\Sigma_2$  with measurement error  $\tau$  is used to estimate  $\Sigma_1$ . This is in complete analogy to shifting the point estimates  $\Sigma^{\text{meas}}$  to their true values  $\Sigma^{\text{true}}$ , as described previously, which will also result in larger statistical error bars according to **GAUSSIAN** error propagation. Since the signal beam asymmetry  $\Sigma_1$  was recognized correctly by the fit it is evident that the combined posterior distributions for  $\Sigma_2$  are in full agreement with the expectations, see figure 4.20. Mean  $\mu$  and standard deviation  $\sigma$  are reproduced exactly as they were modeled as a **GAUSSIAN** fit to the combined posteriors reveals.

It remains to investigate the properties of the employed **MARKOV** chains. First of all one observes that the accuracy of results, i.e. the relative MCSE, suffers from the available statistics which are significantly smaller in comparison with the previously investigated case for the  $p\eta \rightarrow \gamma\gamma$  final state. Only 97% of all unbinned fits fulfill the self set criterion of  $\sigma_{\text{MCSE}}/\text{median}(p(\Sigma|y)) \leq 0.05$  whereas for the toy Monte Carlo experiments in the previous section 4.2 this was the case for *all* unbinned fits. This observation however is not resembling a failing fit but rather the possibility for the data to mimic beam asymmetries close to zero because of the fewer available data points. In these cases the relative MCSE exceeds the threshold as has also been observed before. Convergence and full exploration of the available parameter space on the other hand is guaranteed for all fits because all  $\widehat{R}$  values for all



**Figure 4.19:** Combined (added) posteriors of all 1000 unbinned BAYESIAN fits. Left: Signal beam asymmetry  $\Sigma_1$  Right: Background beam asymmetry  $\Sigma_t^{\text{bkg}}$ . A GAUSSIAN fit is performed with results given on top.



**Figure 4.20:** Combined (added) posteriors of all unbinned BAYESIAN fits for the fit parameter  $\Sigma_2^{\text{true}}$ . A GAUSSIAN fit is performed which reproduces exactly the values that were used for the simulations.

parameters and fits are within the demanded thresholds. Figure 4.5 shows the relative MCSE as well as the  $\hat{R}$  value for the fit parameter  $\Sigma$ .

Lastly, consistency of the fit results with the data that is fitted can be checked as before by a posterior predictive check of the detector coefficients  $a, b$  plugged into the efficiency function  $\epsilon(\phi) = \frac{1}{c} \cdot (\alpha \tilde{N}^{\parallel} + \beta \tilde{N}^{\perp})$  as can be seen in Figure 4.22. Each draw  $a^{(s)}, b^{(s)}, s = 1, \dots, 20000$  is plotted as an opaque blue line. The mean over the posterior draws is indicated by the dashed line and follows the polarization weighted sum of event yields which is shown as data points. The mean agrees within statistical error bars at each point indicating finally a successful fit in every respect.

It has been demonstrated that the chosen BAYESIAN model can describe data generated with two beam asymmetries very well. Note that expanding the existing model from before requires minimal changes since *Stan* [Sta22a] allows modular implementations; only the new parameter  $\Sigma_2^{\text{true}}$  and the new data points  $(\Sigma_2, \tau, \delta)$  have to be added to give correctly centered posteriors that are not anymore systematically shifted. More effort would have to be made to get similar results with the traditional unbinned fitting method described before.

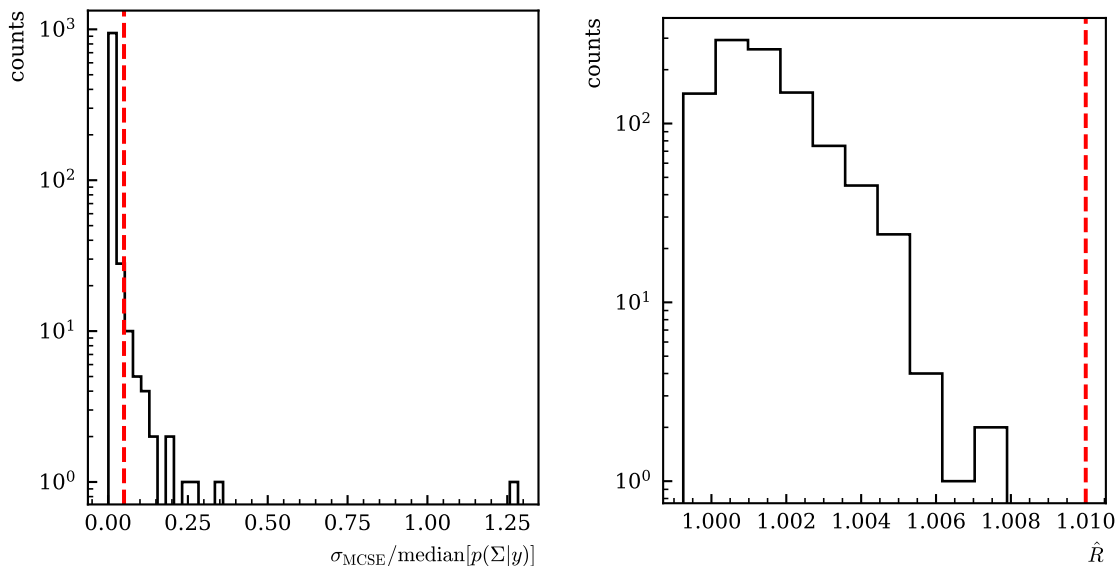


**Figure 4.21:** MCMC diagnostics for the event based BAYESIAN fit. Left: MCSE, Right:  $\hat{R}$ -value. The critical values not to be exceeded are marked by the dashed lines.

### 4.3.2 Application of event based fit to data

Investigation of toy Monte Carlo experiments showed that the presence of polarized background events cause a systematic shift in the extracted beam asymmetry. The shift may be compensated by a modified likelihood function for the BAYESIAN fit or by reversing the shift *after* obtaining intermediate results for  $\Sigma^{\text{meas}}$  with an unbinned maximum likelihood fit. By studying Monte Carlo simulations of various mesonic final states it has been found that the main background contributions in the analysis of the final state  $\gamma p \rightarrow p\eta' \rightarrow p\gamma\gamma$  is given by the false reconstruction of events  $\gamma p \rightarrow p2\pi^0 \rightarrow p4\gamma$ , see chapter 3. Conveniently, this includes the determination of the fraction of background events  $\delta$ , see

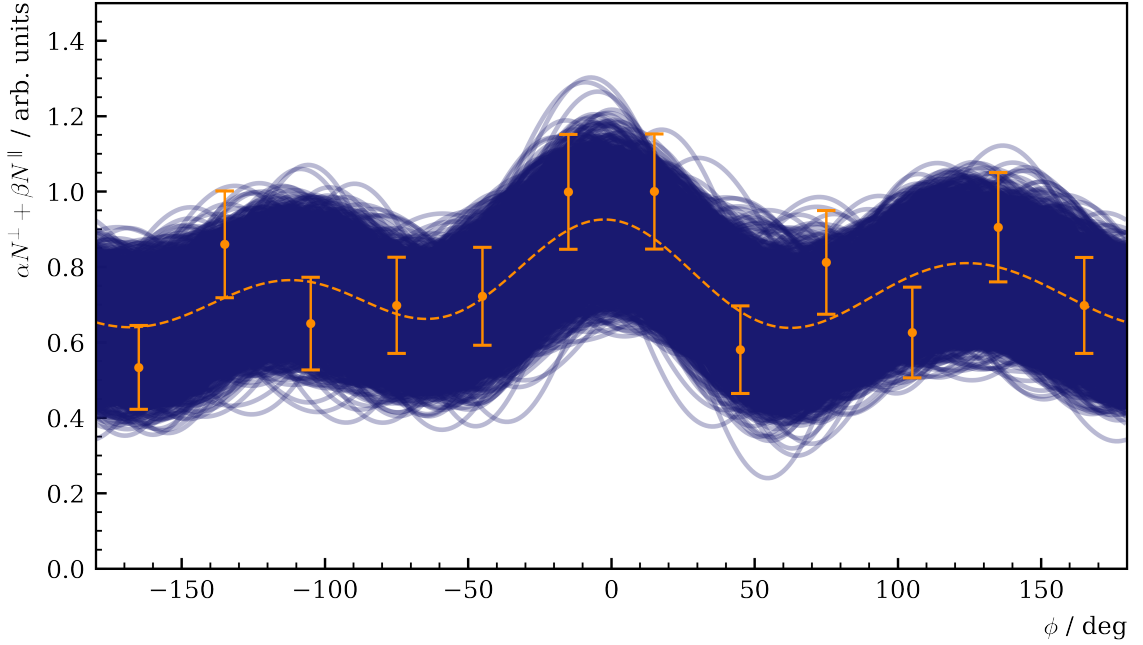


**Figure 4.22:** Posterior predictive checks of one toy Monte Carlo bin using the draws from the marginal posteriors of the detector coefficients  $a, b$  (opaque blue lines). The mean values are marked by the dashed line and follow the distribution of the data points which are the polarization weighted sum of event yields, using 12  $\phi$  bins.

Figure 3.10. Furthermore, preliminary results for the beam asymmetry in double pion photoproduction at the CBELSA/TAPS experiment using the same binning as this analysis [Mah22] were available so that the previously discussed corrections can in fact be applied for each kinematic bin. It is hereby assumed that the *entire* background is realized by  $2\pi^0$  production and the fraction  $\delta$  is determined by an according fit of Monte Carlo spectra. This holds true only approximately for each kinematic bin and is thus a source of systematic error, which is discussed in the next subsection 4.3.3.

Figure 4.23 shows the final results for the beam asymmetry in the reaction  $\gamma p \rightarrow p\eta' \rightarrow p\gamma\gamma$  obtained from data taken at the CBELSA/TAPS experiment. Shown are two sets of results; the dark blue distributions are the results of an unbinned BAYESIAN without any modifications to the original model whatsoever. The dark orange data points are the corresponding results of an unbinned maximum likelihood fit  $\Sigma^{\text{meas}}$ . The light blue distributions however depict the results that were obtained from the modified BAYESIAN model, i.e. with the additional fit parameter  $\Sigma_2^{\text{true}}$ , the light orange data points correspond to the corrected point estimates  $\Sigma^{\text{true}}$  according to Equation (4.42). In addition to the beam asymmetry  $\Sigma_1 = \Sigma_{\eta'}$  the fit also determines marginal posteriors for  $\Sigma_2^{\text{true}} = \Sigma_{2\pi^0}$ . To check consistency of the fit, these posterior distributions are compared to the results  $(\Sigma_2, \tau)$  that were used as input [Mah22], they are shown in Figure 4.24.

Several remarks can be made regarding these results:

- As it has been found studying toy Monte Carlo simulations, the modified BAYESIAN fit again successfully reconstructs two separate beam asymmetries. Figure 4.24 impressively shows the good agreement of input data points  $(\Sigma_2, \tau)$  and posterior of  $\Sigma_2^{\text{true}}$ . On average  $\Sigma_2 \pm \tau$  covers 68% of the posterior distributions, corresponding to a  $1\sigma$  region, proving that no systematic

error is made by introducing the additional fit parameter  $\Sigma_2^{\text{true}}$ .

2. There is very good agreement between point estimates and corresponding posterior distributions. The point estimates give mean and standard deviation of the marginal posteriors to good approximation. If the point estimates are corrected according to Equation (4.42) their statistical error increases. Similarly, the distributions from the modified BAYESIAN fit are wider, agreeing with the corrected point estimates and errors.
3. Errors and distributions widths are rather large, which could be expected due to the small amount of events that could be used to extract the results. However, distributions are rarely truncated because they are mostly centered around  $\Sigma \approx 0$
4. Shifting the final results of the beam asymmetry depending on the amount of background has marginal impact on the absolute scale. Although background contributions are far from negligible they exhibit only asymmetries close to 0 (see Figure 4.24). Thus, the shifted values still agree within statistical error bars or widths with the original values.

To confirm between- and in-chain convergence for all fits, the  $\widehat{R}$ -values of all fit parameters are checked to be  $1 \lesssim \widehat{R} \lesssim 1.01$ . Due to the large number of samples this criterion is fulfilled without complications. Furthermore the relative MCSE with respect to the median of the posterior distributions is checked to confirm the accuracy of all chains. It is  $\sigma_{\text{mcse}}/\text{median}(p(\Sigma|y)) \leq 0.05$  for all but one fit where the beam asymmetry is very close to zero. Figure 4.25 shows both quantities for all fits for the fit parameter  $\Sigma$ .

A last consistency check of the posterior predictive distributions of the efficiency function reveals no results aside from the expectations. Figure 4.26 shows all posterior predictive draws of the detector coefficients  $a^{(s)}, b^{(s)}$  plugged into the efficiency function  $\epsilon(\phi)$ . The mean of all draws describes the polarization weighted sum of event yields within statistical errors. The observed efficiency is less peaked than the simulated one (Figure 4.22), confirming the results that have been found in section 4.2. Yet, more structures are observed compared to the  $p\eta$  final state due to the decreased statistics.

### 4.3.3 Systematic error

There are two major sources for systematic error in the discussed analysis. On one hand, the determination of the polarization degree of the incident photon beam is not exactly accurate and thus influences the fit results which heavily depend on the linear polarization degree. On the other hand, neglecting polarized background events originating from a different reaction that have been falsely regarded as  $2\pi^0$  events when shifting the intermediate results may create systematic errors.

The relative error of the polarization degree can be estimated during the determination process where analytically calculated bremsstrahlung spectra (ANB) are fitted to measured spectra [Afz19]. This allows to give the relative error in the beam energy region that was analyzed as [Afz19]

$$\frac{\Delta p_\gamma}{p_\gamma} = \begin{cases} 0.05, & \text{if } E_\gamma < 1600 \text{ MeV} \\ 0.08, & \text{otherwise.} \end{cases} \quad (4.46)$$

It was assumed that

$$\Sigma^{\text{meas}} = (1 - \delta) \cdot \Sigma^{\text{true}} + \delta \Sigma^{\text{bkg}}, \quad (4.47)$$

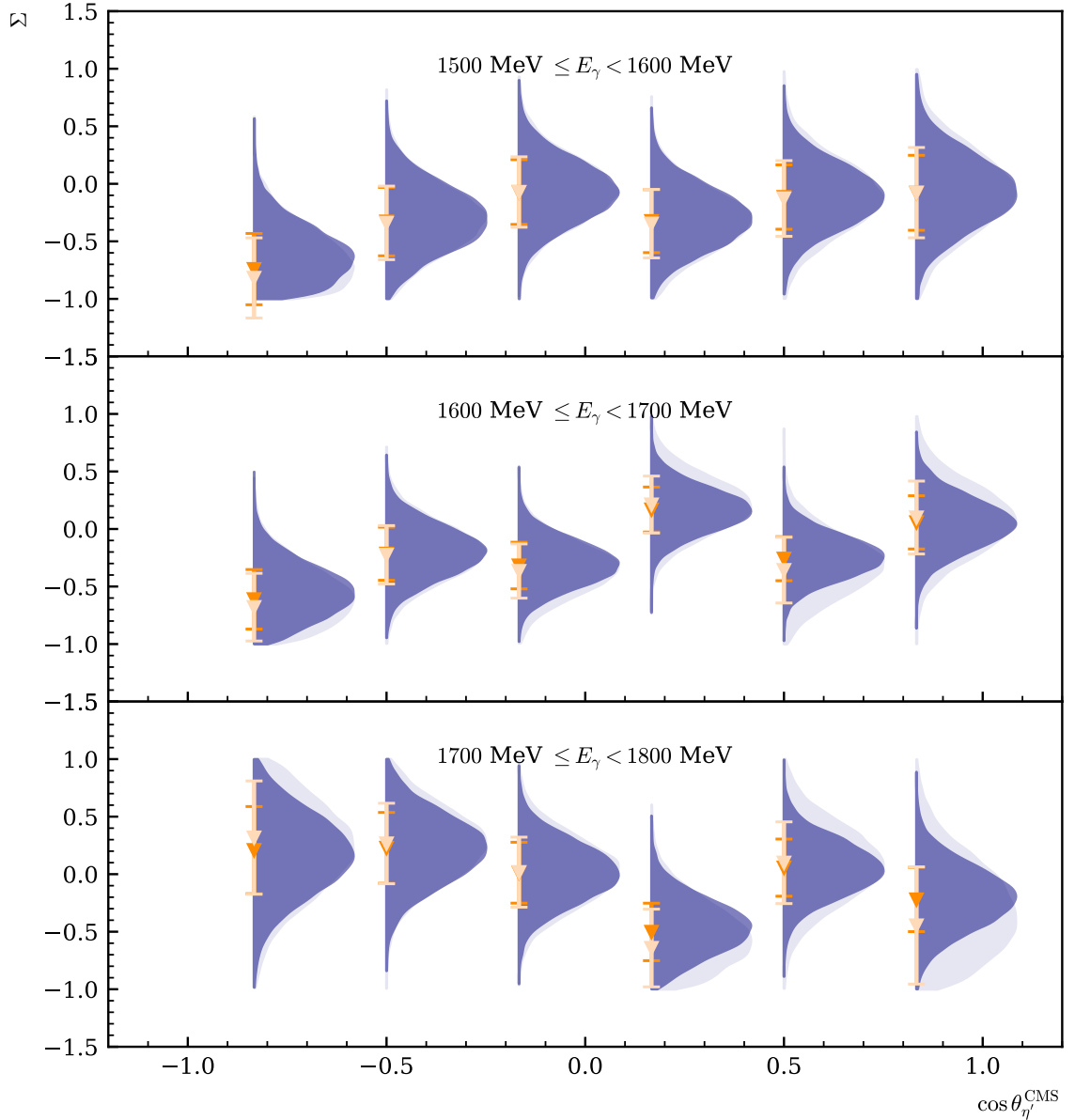


**Figure 4.23:** Final results for the beam asymmetry  $\Sigma$  in  $\eta'$  photoproduction. Two sets of results are shown: The dark blue distributions and orange data points with errorbars are obtained with an unbinned fit that does not consider any background contributions. The light blue distributions and data points are obtained with the modified BAYESIAN fit and by correcting the point estimates according to Equation (4.42), respectively. All errors are statistical errors only.

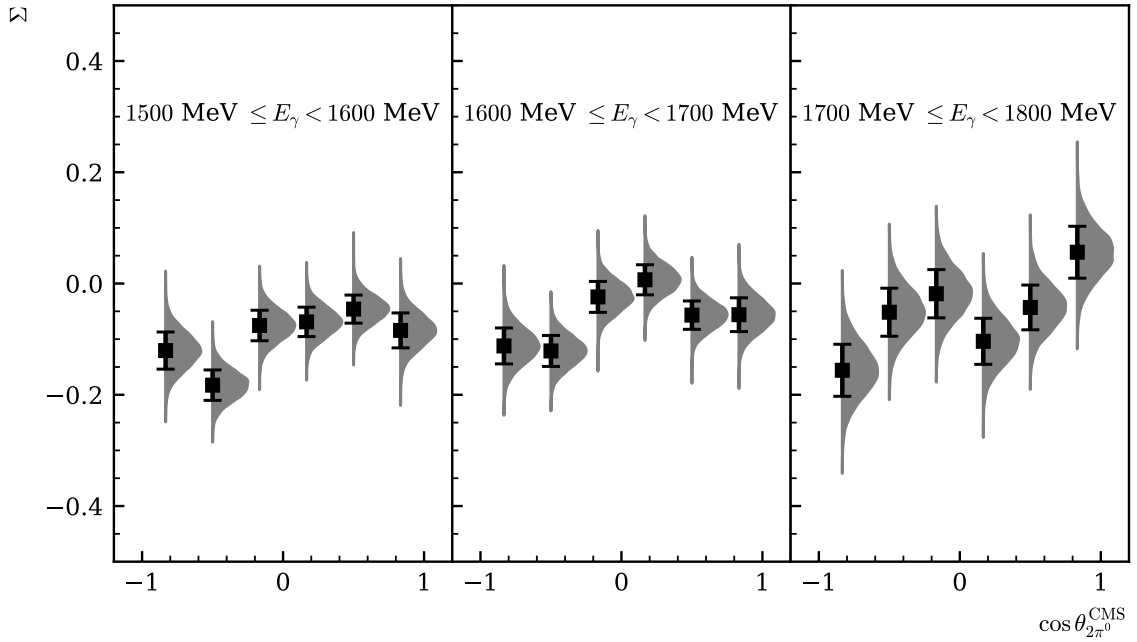


**Figure 4.24:** Results for the additionally fitted  $\Sigma_2^{\text{true}}$  (distributions) compared with the underlying data points [Mah22] with statistical errors. The error bars on average cover  $1\sigma$  of the distributions, indicating a successful fit. All errors are statistical errors only.

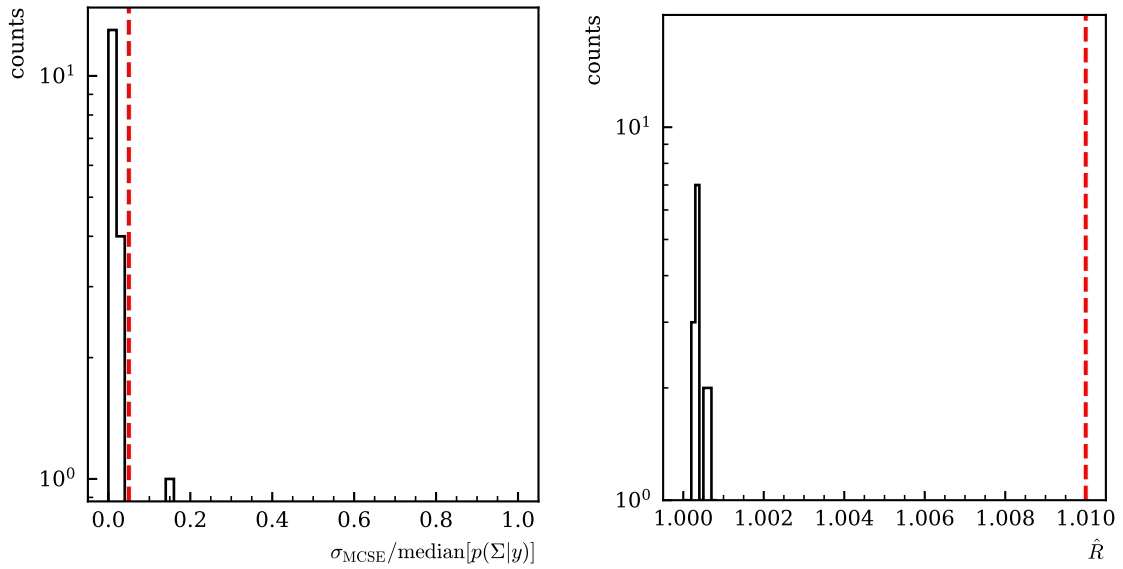


**Figure 4.25:** MCMC diagnostics for the event based BAYESIAN fit. Left: MCSE, Right:  $\hat{R}$ -value. The critical values not to be exceeded are marked by the dashed lines.

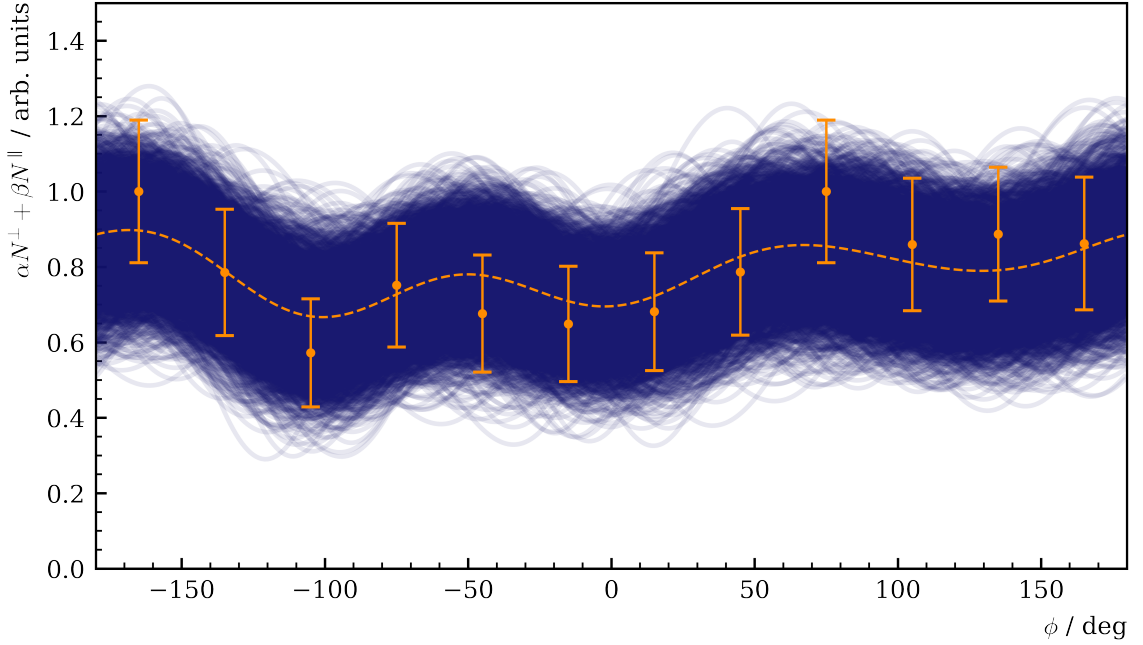


**Figure 4.26:** Posterior predictive checks of the kinematic bin  $1700 \text{ MeV} \leq E_\gamma < 1800 \text{ MeV}, 0.67 \leq \cos \theta < 1$  using the draws from the marginal posteriors of the detector coefficients  $a, b$  (opaque blue lines). The mean values are marked by the dashed line and follow the distribution of the data points which are the polarization weighted sum of event yields, using 12  $\phi$  bins.

with  $\Sigma^{\text{true}} = \Sigma_{\eta'}$  and  $\Sigma^{\text{bkg}} = \Sigma_{2\pi^0}$  and according modifications to the obtained results have been made. However, regarding the entire background contributions to double pion photoproduction holds only approximately in each bin. Actually, the measured value for the beam asymmetry is given by

$$\Sigma^{\text{meas}} = (1 - \delta_1 - \delta_2) \cdot \Sigma_{\eta'} + \delta_1 \Sigma_{2\pi^0} + \delta_2 \Sigma^{\text{bkg}}, \quad (4.48)$$

where  $\delta_1$  is the relative contribution of  $2\pi^0$  production events and  $\delta_2$  the relative contribution of other background events, e.g.  $\pi^0\eta$  production, that have been neglected before that may exhibit an asymmetry  $\Sigma^{\text{bkg}}$ . The systematic uncertainty of  $\Sigma_{\eta'}$  can then be determined by setting  $\Sigma^{\text{bkg}} = \pm 1$  and determining the maximum deviation from the previous results. The results from the unbinned maximum likelihood fit are used which to good approximation also give the median and mean of the posterior distributions.

$$\Delta \Sigma_{\eta'} = \max \left[ \left| \frac{\Sigma^{\text{meas}} - \delta_1 \cdot \Sigma_{2\pi^0} \pm \delta_2 \cdot 1}{1 - \delta_1 - \delta_2} - \frac{\Sigma^{\text{meas}} - \delta \cdot \Sigma_{2\pi^0}}{1 - \delta} \right| \right] \quad (4.49)$$

The two fractions  $\delta_1$  and  $\delta_2$  are determined by fitting the invariant mass spectra of Monte Carlo data bin-wise to the measured data for each kinematic bin, as described in chapter 3. Hereby  $\delta_2$  is determined by subtracting the background fraction  $\delta_1$  obtained from a fit that only allowed  $2\pi^0$  contributions underneath the  $\eta'$  invariant mass peak from the background fractions  $\delta$  obtained fitting

*all* MC spectra to the data. The total absolute systematic error is then given by

$$\Delta\Sigma_{\eta'}^{\text{sys}} = \sqrt{\left(\frac{\Delta p_\gamma}{p_\gamma} \Sigma_{\eta'}\right)^2 + \left(\Delta\Sigma_{\eta'}\right)^2}. \quad (4.50)$$

Figure 4.27 shows all results with systematic uncertainites given on the bottom of each plot.

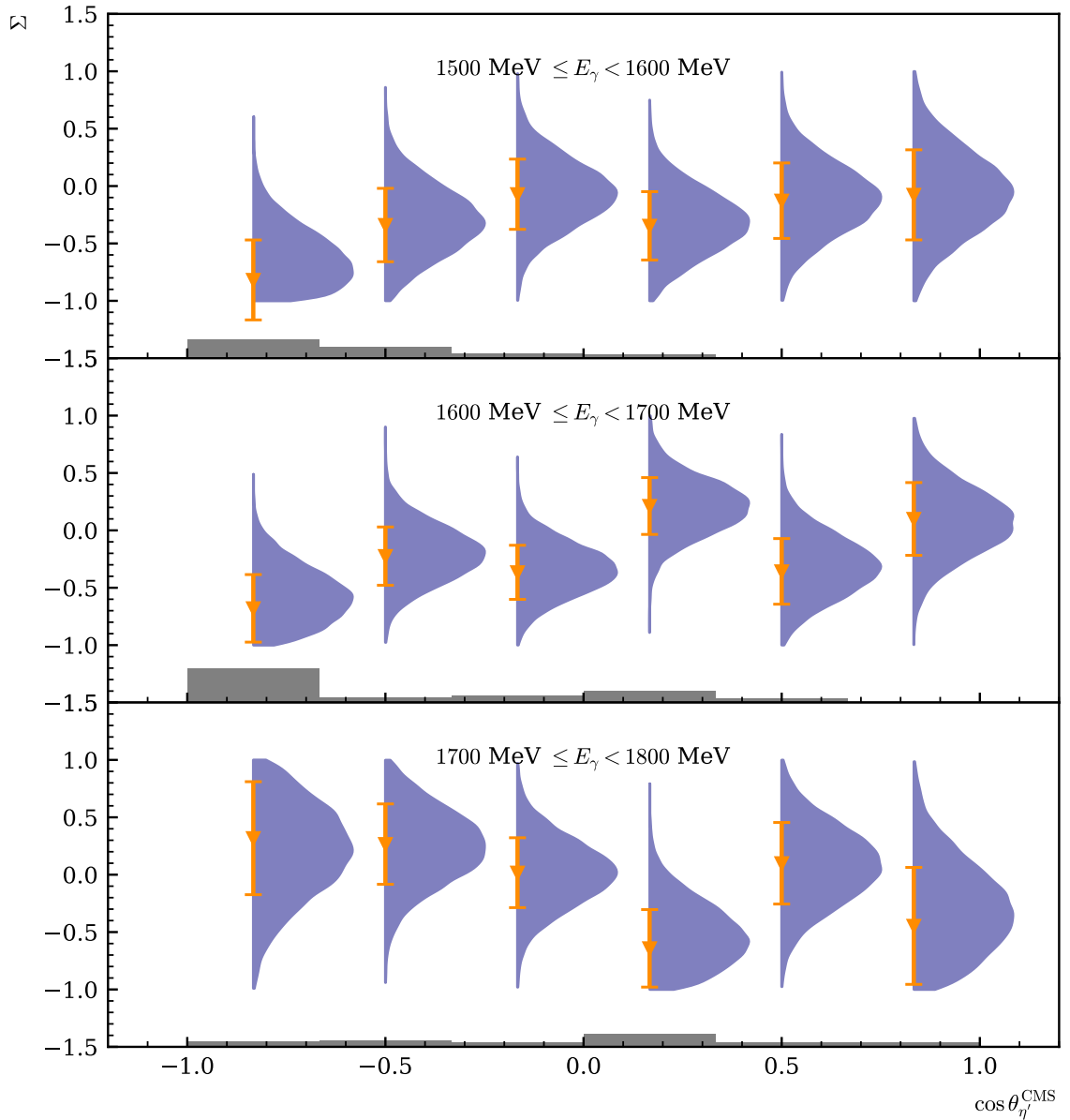


**Figure 4.27:** Final results for the beam asymmetry  $\Sigma_{\eta'}$  for all energy and angular bins. Only the corrected results from the unbinned maximum likelihood fit and distributions from the modified BAYESIAN fit are shown. The bottom of each plot indicates the systematic error as gray bars. It was determined as previously discussed.

# CHAPTER 5

---

## Discussion

---

This chapter will present a discussion of results for the beam asymmetry  $\Sigma$  in the reaction  $\gamma p \rightarrow p\eta' \rightarrow p\gamma\gamma$  obtained with the CBELSA/TAPS experiment. No dedicated discussion of the results obtained for  $\eta$  photoproduction will be given here. Very good agreement between the results for  $\Sigma_\eta$  in this work and reference [Afz19] makes this obsolete, because the findings for  $\Sigma_\eta$  compared to various previous measurements and existing PWA predictions are discussed in reference [Afz19] in detail. However, final remarks regarding the used fitting methods will be made after the results for  $\Sigma_{\eta'}$  obtained in this thesis were compared to existing data, and as a next step compared to existing PWA model predictions.

### 5.1 Comparison of results to existing data

The data situation for any observables in  $\eta'$  photoproduction is scarce because on one hand the production cross section is very small while on the other hand high center of mass energies are needed to observe the reaction  $\gamma p \rightarrow p\eta'$  [Wor+22]. To collect sufficient statistics at these energies, very high energetic photon beams are necessary because the photon beam Intensity  $I(E_\gamma)$  approximately behaves like [Leo94]

$$I(E_\gamma) \propto \frac{1}{E_\gamma}. \quad (5.1)$$

Next to a measurement of the beam asymmetry in  $\eta'$  photoproduction near threshold at GrAAL [Lev+14], there exists one other recent measurement of  $\Sigma_{\eta'}$  at CLAS [Col+17]. In this work the beam asymmetry could be extracted covering the beam energy range of  $1500 \text{ MeV} \leq E_\gamma < 1800 \text{ MeV}$  and is binned as  $(\Delta E_\gamma, \Delta \cos \theta) = (100 \text{ MeV}, 0.33)$ . Thus, only the results from reference [Col+17] are suited for comparison which are binned as  $(\Delta E_\gamma, \Delta \cos \theta) = (54 \text{ MeV}, 0.2)$ . Of all kinematic bins provided by reference [Col+17] only energy bins where the bin centers approximately align with the energy bins chosen in this thesis are considered for further investigation. Figure 5.1 shows the results for the beam asymmetry  $\Sigma_{\eta'}$  compared with results reported by [Col+17]. First of all, one may notice the large difference in statistical errors between the two datasets. This can be explained by considering that the results obtained by COLLINS ET AL. [Col+17] were extracted via the charged decay  $\eta' \rightarrow \pi^+\pi^-\eta \rightarrow 2\pi^+\pi^-2\pi^0$  with a branching ratio of  $\text{BR} = 42.6 \cdot 22.02\% = 9.38\%$  [Wor+22] as

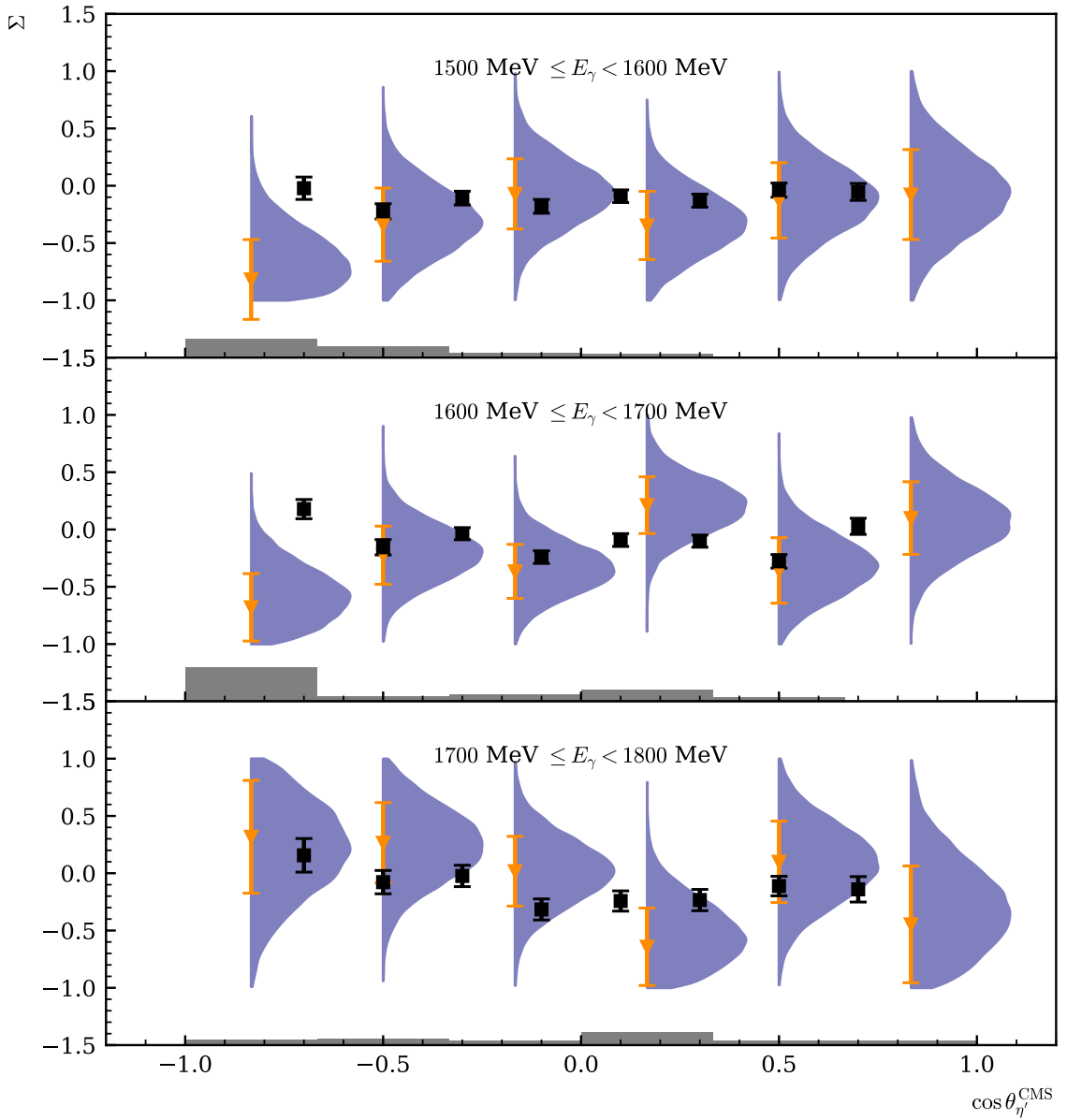


**Figure 5.1:** Results for the beam asymmetry  $\Sigma_{\eta'}$  (orange errorbars and blue distributions) compared with the results for the energy bins  $E_\gamma = 1569 \text{ MeV}$ ,  $E_\gamma = 1676 \text{ MeV}$ ,  $E_\gamma = 1729 \text{ MeV}$  reported in reference [Col+17] (black errorbars). Systematical errors are shown as grey bars.

opposed to the neutral decay  $\eta' \rightarrow \gamma\gamma$  with a branching ratio of  $\text{BR} = 2.2\%$  [Wor+22]. Furthermore, the electrons impinging on the radiator target at CLAS were accelerated to  $4.5 \text{ GeV}$  [Col+17], increasing the statistics in the photon beam energy range of interest compared with CBELSA/TAPS data, where the electrons are only accelerated to  $3.2 \text{ GeV}$ . Aside from the large difference in statistical errors, generally good agreement between the two datasets exists. Most datapoints are compatible within their statistical errors and the angular profile of the beam asymmetry is displayed equivalently. The largest discrepancy between both datasets exists in backwards direction for the first two energy bins; although the angular bins do not exactly match it is noteworthy that there is a sign flip between the different measurements that can not be accounted for by combined statistical and systematical error (for the CLAS measurement a systematic error due to the determination of the photon beam polarization of  $6\%$  is reported [Col+17]). It is not understood why these bins show this particular behavior as no indication towards any additional systematic effects has been found. Note however that without identical binning only vague conclusions regarding the agreement of both datasets can be made. The given datasets allow to identify that there is in general consistency and no large unaccounted systematic uncertainties. Direct comparability can only be achieved if statistics at high center of mass energies are increased at the CBELSA/TAPS experiment.

Due to the placement of the coherent edge the beam asymmetry  $\Sigma_{\eta'}$  could be extracted at beam energies up to  $E_\gamma = 1800 \text{ MeV}$  in this work although the CBELSA/TAPS experiment theoretically provides photon beam energies of maximally  $E_\gamma^{\max} = 3200 \text{ MeV}$ . Yet, the event yield included less than  $10^4 \gamma p \rightarrow p\eta' \rightarrow p\gamma\gamma$  events in the selected energy region collected in roughly four months of beam time. The beam asymmetry in  $\pi^0(\eta)$  photoproduction in reference [Afz19] was determined using  $6.28 \cdot 10^6 (5.24 \cdot 10^5)$  events giving significantly higher precision. Next to small cross section and branching ratio to a neutral final state this illustrates the effect of Eq. 5.1 during data collection leading to large statistical errors and background contributions when determining the beam asymmetry. Furthermore only a coarse binning in  $(E_\gamma, \cos \theta)$  could be chosen to account for the available statistics, denying a detailed investigation of the beam asymmetry  $\Sigma_{\eta'}(E_\gamma, \cos \theta)$ . In order to collect more statistics at high beam energies in future beam times of the CBELSA/TAPS experiment, e.g. to further investigate the reaction  $\gamma p \rightarrow p\eta'$ , either longer beam times and/or shifting the coherent edge towards higher energies should be considered. Also the decay channel  $\eta' \rightarrow \pi^0\pi^0\eta$  may be investigated to increase precision of the existing data. The use of machine learning methods to identify background contributions during event selection [Kre22] could also allow a more precise measurement of the beam asymmetry  $\Sigma_{\eta'}$ .

## 5.2 Comparison of results to PWA calculations

Figure 5.2 shows the new results for the beam asymmetry  $\Sigma$  in  $\eta'$  photoproduction obtained with the CBELSA/TAPS experiment compared with existing PWA-predictions. Shown is the etaMAID2018 solution [Tia+18], as well as the Bonn-Gatchina (BnGa) solution [Ani+18] which already include results from the measurements [Col+17] and [Lev+14] in the fit. This however puts bias towards the fitted data on the PWA solution such that the same remarks regarding agreement of the results of this thesis and the PWA calculations can be made as in the previous section; generally the obtained data points are described well by the PWA predictions with the exception of the backwards direction at the first two energy bins. This indicates that the previous measurements of  $\Sigma_{\eta'}$  had a large influence

on the PWA fits, especially when considering that before these measurements were added, the PWA solutions failed to describe the beam asymmetry in  $\eta'$  photoproduction, generally showing the wrong sign [Col+17]. Thus, similarly to the previous section, only a vague conclusion of general agreement between data points and PWA solutions can be drawn. Further measurements are required to increase the precision of existing PWA models. Following the suggestions of TIAATOR ET AL. [Tia+18] more observable measurements are especially needed near the  $\eta'$  production threshold to resolve discrepancies between different PWA solutions. It is hereby crucial to measure with high precision in small energy bins. In addition to more precise measurements of the differential cross section and the beam asymmetry near threshold the observables  $T$  and  $F$  could be measured as a next step to improve the quality of the PWA solutions [Tia+18]. Figure 5.3 shows all 8 single and double polarization observables near threshold as predicted by different resonance contributions of the etaMAID [Tia+18] (red lines) and Bonn-Gatchina [Ani+18] (black lines) PWA groups. It is evident that the measurements of additional observables will help to eliminate ambiguities in the future.

### 5.3 Final discussion of methods

Next to acquiring new data for the beam asymmetry  $\Sigma$  in the reaction  $\gamma p \rightarrow p\eta'$  the main focus of this thesis laid in the exploration of alternative fitting methods using BAYESIAN statistics. A final résumé is now drawn here with regard to the different strategies used to extract the beam asymmetry  $\Sigma$  in this work.

First tests of the BAYESIAN approach were performed when confirming already published results for the beam asymmetry in  $\eta$  photoproduction [Afz19; Afz+20] and were successively also applied to data obtained from  $\eta'$  photoproduction. Two methods of extracting  $\Sigma$  were discussed;

The combination of normalized event yields into the asymmetry (see section 4.1.1)

$$A(\phi) = \frac{\tilde{N}^\perp - \tilde{N}^\parallel}{p_\gamma^\parallel \tilde{N}^\perp + p_\gamma^\perp \tilde{N}^\parallel} = \Sigma \cos(2(\alpha^\parallel - \phi)). \quad (5.2)$$

allowed to determine the beam asymmetry as a fit parameter for each kinematic bin. Without introducing systematic error the fit could be performed either as a least squares fit or a BAYESIAN fit. The former resulting in a point estimate with statistical errors  $\hat{\Sigma} \pm \sigma_{\hat{\Sigma}}$ , the latter resulting in a marginal posterior distributions  $p(\Sigma|y)$  and both fits were able to give a measure of goodness of fit. It was shown that the obtained statistical error bars provide the width of a  $1\sigma$  interval of the marginal posteriors, indicating that both approaches are indeed equivalent. The implementation of the BAYESIAN fit did not require unreasonably more effort compared to the implementation of a  $\chi^2$ -fit, mainly due to the neat structure of the used programming language Stan [Sta22a]. Computation time of the BAYESIAN fit exceeded the time needed for a  $\chi^2$  fit but not significantly. Nevertheless the nature of MCMC fits required diagnosing the convergence of the fit itself carefully, in total making the BAYESIAN approach more elaborate without increasing the knowledge gained from the fit results significantly because the posteriors are without exception unimodal GAUSSIANS, when they are not truncated by the upper or lower bound for  $\Sigma$ . Yet, any deviations from unimodal GAUSSIAN posteriors could be revealed by using the BAYESIAN approach that also provides great flexibility when using the results as input for PWA calculations. The most important conclusion to be drawn is that a BAYESIAN approach is valid and produces the same results as the so far pursued approach of least-squares fitting because

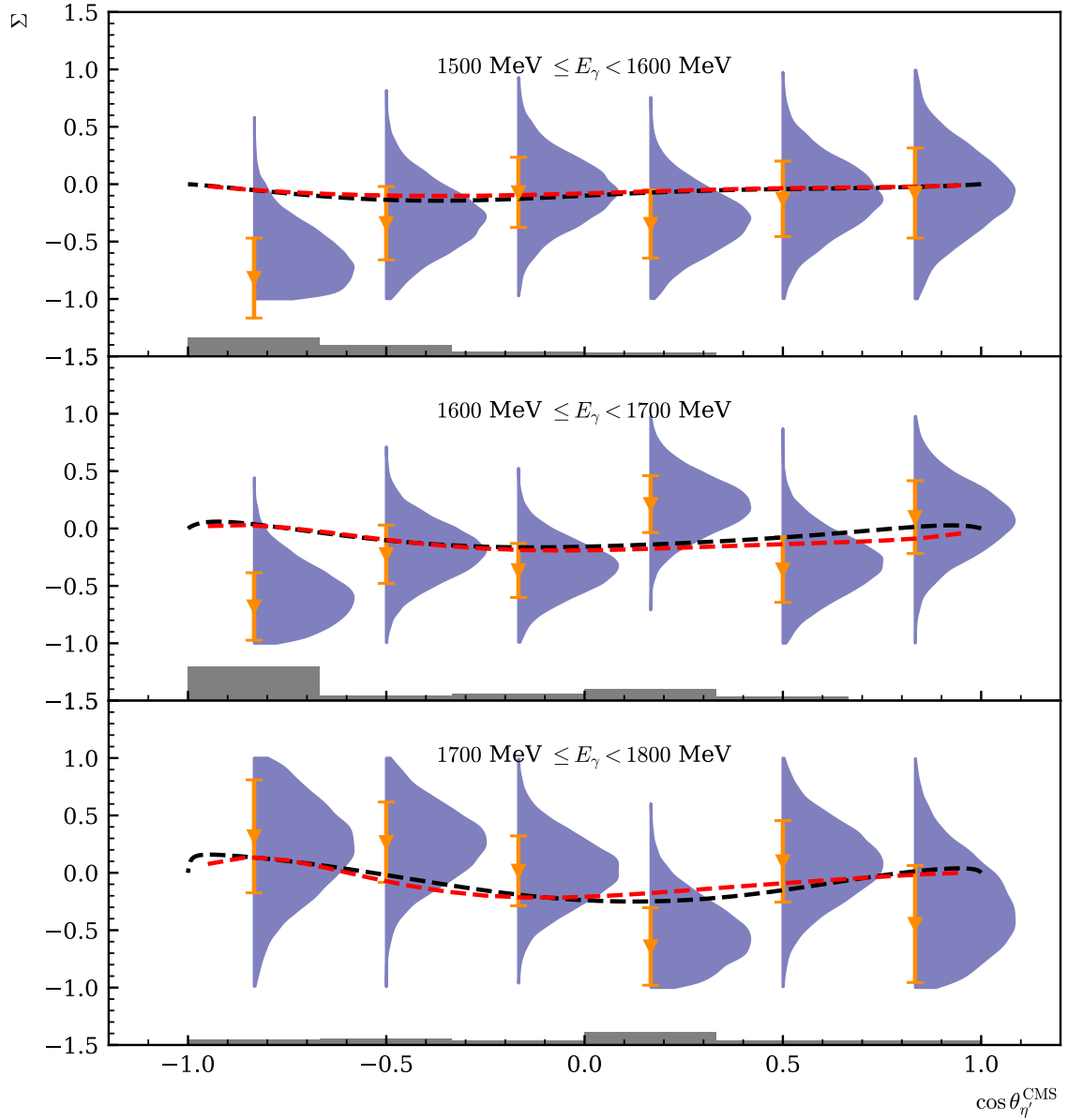


**Figure 5.2:** Results for the beam asymmetry  $\Sigma_{\eta'}$  (orange errorbars and blue distributions) compared with PWA solutions: etaMAID [Tia+18; Tia+] (dashed black line) and BnGa [Ani+18] (dashed red line). The errorbars only depict statistical error, the systematic error is shown as grey bars.

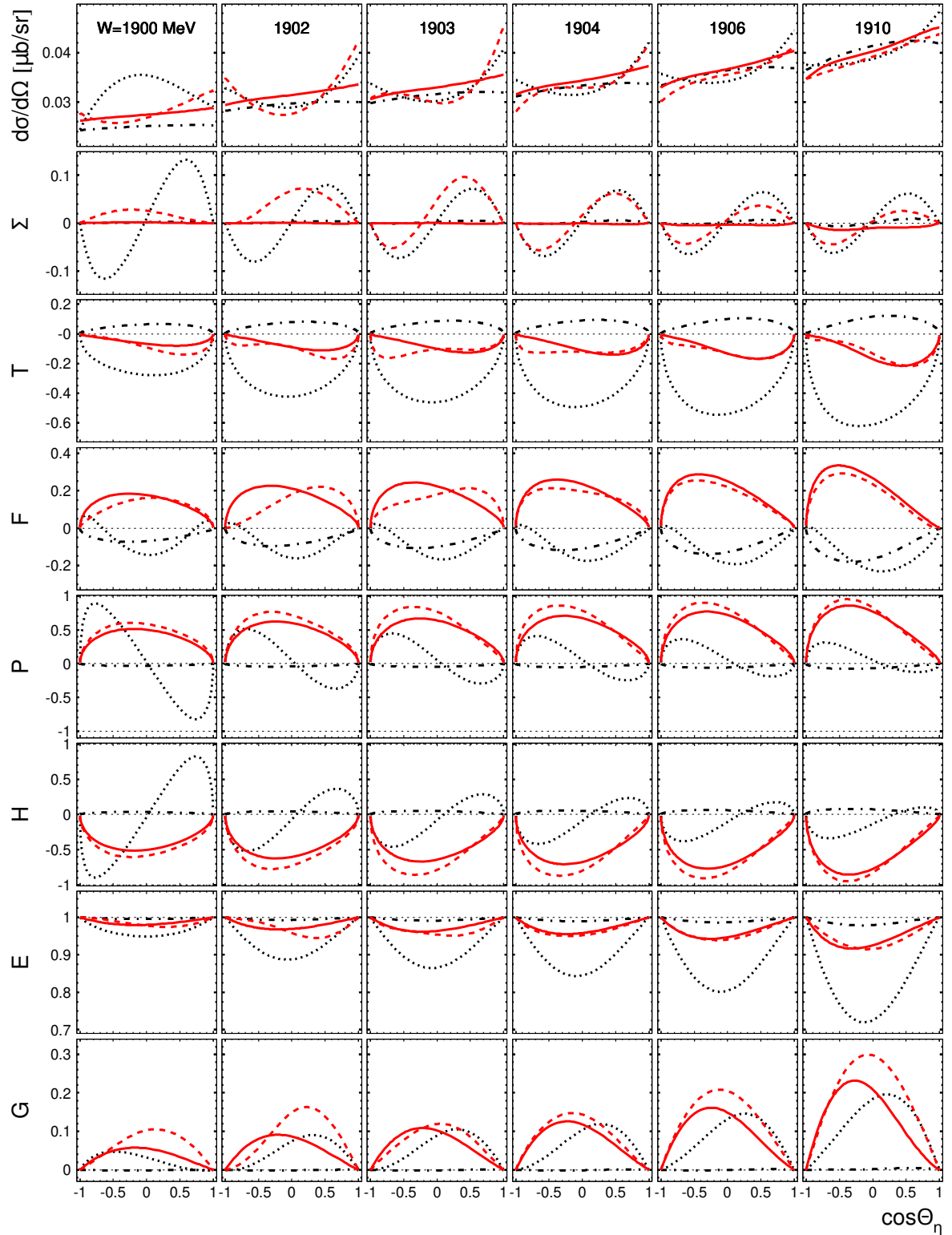


**Figure 5.3:** Different resonance contributions to all eight single and double polarization observables as predicted by etaMAID [Tia+18] and Bonn-Gatchina [Ani+18] PWA solutions near the  $\eta'$  production threshold. Taken from [Tia+18].

creating the same results with different independent methods naturally increases their informative value. However, because the binning of data introduces systematic under- or overestimation of the fit parameter  $\Sigma$  (cf. appendix C) determining the beam asymmetry from the quantity  $A(\phi)$  should be avoided.

The second method that was used to extract the beam asymmetry was an unbinned fit using the likelihood (see section 4.1.2)

$$\begin{aligned} \ln \mathcal{L} = & \sum_{i=1}^n \ln p_{\text{prompt}} (\phi_i, p_{\gamma,i} | \Sigma, a, b, \Sigma^{\text{bkg}}, a^{\text{bkg}}, b^{\text{bkg}}) \\ & + \sum_{j=1}^m \ln p_{\text{sideband}} (\phi_j, p_{\gamma,j} | \Sigma^{\text{bkg}}, a^{\text{bkg}}, b^{\text{bkg}}). \end{aligned} \quad (5.3)$$

The frequentist approach aimed to estimate all parameters with statistical errors by maximizing this likelihood while in a BAYESIAN approach it was embedded into a full probabilistic model, leading to a complete inference for all parameters. Both methods lack a measure of goodness of fit so that toy Monte Carlo experiments were needed to confirm the right working principle which were conducted successfully without revealing bias or sources of systematic errors. Again, the two approaches are found to be equivalent, as estimated from the widths of the distributions and the statistical errors of the point estimates. The same remarks regarding the implementation and interpretation of the two fits as before apply, however computation time for the unbinned BAYESIAN is now significantly larger. While the unbinned maximum likelihood fit takes seconds, for specific kinematic bins the unbinned BAYESIAN fit took up to 20 minutes. Applying the BAYESIAN approach to data selected in the frame of this thesis for the reaction  $\gamma p \rightarrow p\eta' \rightarrow p\gamma\gamma$  furthermore revealed the great advantage of the flexibility fully BAYESIAN models provide; since a significant amount of background reactions from  $2\pi^0$  production is part of the selected data, this had to be considered when determining the beam asymmetry. For the maximum likelihood fit the point estimates had to be shifted *after* the fit, depending on the amount of background. For the BAYESIAN fit however background contributions could be included inherently into the likelihood function, allowing to extract the corrected distributions directly from the fit.

In summary, one can say that the application of BAYESIAN methods when extracting the polarization observable  $\Sigma$  was successful. Equivalence to frequentist methods was shown while at the same time the BAYESIAN fits provide more flexibility and the possibility to investigate the structure of posterior distributions.



# CHAPTER 6

---

## Summary

---

In order to eliminate ambiguities in the invariant amplitudes of pseudoscalar meson photoproduction polarization observables need to be measured, ultimately adding to the understanding of the strong interaction in the non-perturbative regime. Utilizing a linearly polarized photon beam and an unpolarized target, data were taken at the CBELSA/TAPS experiment located at the accelerator ELSA. This allowed the extraction of the beam asymmetry  $\Sigma$  in the beam energy range  $1100 \text{ MeV} < E_\gamma < 1800 \text{ MeV}$ .

The use of BAYESIAN methods for the determination of polarization observables was tested by reproducing high precision data for the beam asymmetry  $\Sigma$  in  $\eta$  photoproduction that were obtained at the CBELSA/TAPS experiment using a binned  $\chi^2$  fit and an unbinned maximum likelihood fit. Instead of point estimates with statistical errors, a BAYESIAN fit result contains marginal posterior distributions for each fit parameter, significantly increasing the amount of information obtained from the fit. In order to acquire these distributions it is necessary to rely on sophisticated MARKOV-chain Monte Carlo methods that increase the computational cost and also require detailed diagnostics. It was found that the BAYESIAN approach gives equivalent results as the traditional frequentist approach and no systematic error is introduced by the choice of fitting method. Since polarization observables are used as input of PWA calculations, providing distributions is a distinct advantage because the user may choose errors derived from the distributions in any way that is appropriate for the chosen model. Also, the BAYESIAN approach allows to truncate the posterior distributions to the physically allowed parameter space in a convenient way that is not applicable to traditional  $\chi^2$  or maximum-likelihood fits. Since the application of BAYESIAN methods to determine polarization observables they were used to determine the beam asymmetry for the  $p\eta'$  final state in the following.

Using the neutral decay  $\eta' \rightarrow \gamma\gamma$  the  $p\eta'$  final state was selected with significant background contributions from the  $p2\pi^0 \rightarrow p4\gamma$  and  $p\pi^0\eta \rightarrow p4\gamma$  final states as has been found investigating Monte Carlo simulations; during reconstruction two photons get lost either because they have not enough energy to surpass the reconstruction threshold for particle energy depositions or because they are combined to one cluster with a nearby high energy photon. Although the acceptance for both reactions after the complete event selection is  $A \ll 1$ , the large difference in the production cross sections as well as the branching ratio to an only-photon final state gave total background contributions of up to 45%. No sensible background reducing cuts have been found. In total  $8 \cdot 10^3$   $p\eta'$  events were retained from which the beam asymmetry  $\Sigma$  was determined using an unbinned maximum likelihood fit and an unbinned BAYESIAN fit. Both methods yielded equivalent results. Hereby the beam asymmetry

for  $2\pi^0$  production was known in the same kinematic binning which allowed to correct the estimated values and distributions according to the respective amount of background contamination. As opposed to the maximum likelihood fit, the BAYESIAN fit allowed to include the background contributions as an additional fit parameter inherently to the chosen probabilistic model. The corrected values and distributions are in fair agreement with previous measurements taken at CLAS using the charged decay  $\eta' \rightarrow \pi^+ \pi^- \eta$  and also agree with PWA predictions within their statistical error. In the energy region  $1100 \text{ MeV} < E_\gamma < 1800 \text{ MeV}$  the new results for the beam asymmetry in  $\eta'$  photoproduction off the proton obtained from CBELSA/TAPS data provide the only addition to existing results from CLAS. However, the precision of the CBELSA/TAPS data can not compete with the CLAS data due to the relatively small number of events that could be reconstructed in the chosen decay channel. Nevertheless, agreement with previous measurements increases the informative value of both datasets that thus contribute to the identification of high-mass  $N^*$  resonances.

The use of BAYESIAN methods to determine polarization observables can be expanded to any measurement of polarization observables and should provide more insight regarding the underlying posterior distributions and at the same time even uncover possible ambiguities. To increase the statistical precision of the existing measurement of the beam asymmetry in  $\eta'$  photoproduction the decay channel  $\eta' \rightarrow \pi^0 \pi^0 \eta$  should be investigated. Also, the use of machine learning methods to classify signal and background contributions in the selected data may be pursued. In the mean time, several upgrades of the CBELSA/TAPS experiment have been installed that promise to improve its trigger capabilities and data taking rates. The measurement of polarization observables in future beamtimes will profit from these improvements and help to further understand the nucleon excitation spectra.

# APPENDIX A

## Illustration of used software tools

### A.1 ExPLORA

Figure A.1 shows an example of a .xml file that was used to call the plugin that was written to select the reaction  $\gamma p \rightarrow p\eta' \rightarrow p\gamma\gamma$ . First of all, several files have to be included in order to acquire certain *containers* that inhibit the raw data of the final state particles. Then the plugin is embedded with the options

- MC (bool) – determines whether Monte Carlo or measured data are analyzed
- PWA (bool) – determines whether used Monte Carlo simulation have PWA weights
- FOURGAMMAS (bool) – determines whether the generated final state has four photons or two
- REALGAMMAS (bool) – determines whether real photons are part of the decay or not (e.g.  $n\pi^+$ )
- allroutes (CBTConfigString) – gives the container that contains the routes of charged particles

```
1  <explora>
2    <!-- Flags can be set and later on used (e.g. as conditions) -->
3    <CBTFlag name="CONFIGS" value="/hadron/krause/git/exploraConfigs"/>
4    <CBTIncludeXML file="${CONFIGS}/Analyse/DataSource/RawData_Prefiltered.xml"/>
5    <!-- Merges particles from different sources in a common container -->
6    <CBTParticleMerger source="CBGammmas,MiniTapsGammmas" container="allgammmas" persistent="no" />
7
8    <!-- Selection plugins ===== -->
9    <!-- Now you have all the particle containers and can start to select events. The analysis of preselected data starts here... -->
10   <CBTIncludeXML file="${CONFIGS}/ReactionSelection/Proton23PED.xml" />
11   <!--This is for 2.5PED events -->
12   <CBTRouteGammaFactory srccontainer="chapirooutes" dstcontainer="chapiroutegammmas"/>
13   <CBTRouteGammaFactory srccontainer="FWPlugVetoRoutes" dstcontainer="fproutegammmas"/>
14   <CBTRouteGammaFactory srccontainer="MiniTapsVetoRoutes" dstcontainer="minitapsroutegammmas"/>
15   <CBTParticleMerger source="chapiroutegammmas, fproutegammmas, minitapsroutegammmas" container="allroutes"/>
16   <!-- = Histogramming ===== -->
17   <!-- The histogrammer creates and fills all the histograms which should be stored in your output file -->
18   <CBTHistogrammer profile="yes" profilehisto="yes">
19     <!--here the written plugin is called -->
20     <CBTetaprimeanalysis MC="FALSE" PWA="FALSE" FOURGAMMAS="FALSE" REALGAMMAS="TRUE" allroutes="allroutes"/>
21   </CBTHistogrammer>
22 </explora>
```

**Figure A.1:** Example .xml file that was used to call the plugin CBTetaprimeanalysis.cpp (line 20) with several self defined options.

## A.2 Stan

In chapter 1 an example fit using *Stan* was shown. Data was fitted that followed a cosine distribution

$$y = a \cdot \cos x + b + \epsilon. \quad (\text{A.1})$$

Here  $y$  is a measured quantity with GAUSSIAN noise  $\epsilon$ ,  $x$  are predictors and  $a$  and  $b$  are fit parameters. Assuming each datapoint  $y_n$  is independent and exhibits an individual noise term  $\epsilon_n \sim \mathcal{N}(0, \sigma_n)$ , the likelihood  $p(y|a, b)$  can be formulated as

$$y_n \sim \mathcal{N}(a \cdot \cos(x_n) + b, \sigma_n) \Leftrightarrow p(y|a, b) = \prod_{i=1}^N \mathcal{N}(y_i|a \cdot \cos(x_i) + b, \sigma_i), \quad (\text{A.2})$$

if there are  $N$  datapoints in total. Specifying e.g. normal priors for the two regression coefficients  $a$  and  $b$  completes the inference

$$a \sim \mathcal{N}(0, 1) \quad b \sim \mathcal{N}(0, 1). \quad (\text{A.3})$$

Figure A.2 shows the implementation of the described model in *Stan*. First of all, all data that is read in has to be defined. Conveniently this can be done using the `vector` class, that corresponds to a list of e.g. all  $x$  values. Next, the parameters of the model are defined and the likelihood and priors are specified. Samples from the posterior predictive distribution are randomly sampled using all simulation draws in a last step.

```

1  data {
2    int<lower=0> n; //number of data points
3    vector[n] x; //predictors
4    vector[n] y; //measurements with
5    vector[n] dy; //corresponding errors
6  }
7  parameters {
8    real a; //amplitude and offset parameters
9    real b;
10 }
11
12 model {
13   y ~ normal(b + a * cos(x), dy); //likelihood
14   a ~ normal(0,1); // prior
15   b ~ normal(0,1); // prior
16 }
17 generated quantities {
18   //posterior predictive check
19   real y_tilde[n] = normal_rng(b + a * cos(x),dy);
20 }
```

**Figure A.2:** Example .stan file that can be used to perform a simple linear fit.

## APPENDIX B

---

# Additional plots and calculations

---

This chapter will give additional calculations and plots which would have interrupted the train of thought unnecessarily in the main part.

## B.1 Statistical error for the asymmetry $A(\phi)$

Let  $\tilde{N}_i^{\parallel/\perp}$  be the normalized event yields at bin  $\phi_i$ . As mentioned in section 4.1, the asymmetry  $A_i$  at bin  $i$  is then given by

$$A_i = \frac{\tilde{N}_i^\perp - \tilde{N}_i^\parallel}{p_\gamma^\parallel \tilde{N}_i^\perp + p_\gamma^\perp \tilde{N}_i^\parallel} = \Sigma \cos(2(\alpha^\parallel - \phi_i)), \quad (\text{B.1})$$

where the event yields are normalized over all  $M$   $\phi$ -bins

$$\tilde{N}_i^{\parallel/\perp} = \frac{N_i^{\parallel/\perp}}{\sum_{j=1}^M N_j^{\parallel/\perp}}.$$

To estimate statistical errors according to GAUSSIAN error propagation, the partial derivatives with respect to  $\tilde{N}_i^{\parallel/\perp}$  have to be built:

$$(\Delta A_i)^2 = \left( \frac{\partial A_i}{\partial \tilde{N}_i^\parallel} \Delta \tilde{N}_i^\parallel \right)^2 + \left( \frac{\partial A_i}{\partial \tilde{N}_i^\perp} \Delta \tilde{N}_i^\perp \right)^2, \quad (\text{B.2})$$

where

$$\left( \frac{\partial A_i}{\partial \tilde{N}_i^{\parallel/\perp}} \right)^2 = \left[ \frac{\tilde{N}_i^{\perp/\parallel} (p_\gamma^\perp + p_\gamma^\parallel)}{(p_\gamma^\parallel \tilde{N}_i^\perp + p_\gamma^\perp \tilde{N}_i^\parallel)^2} \right]^2, \quad (\text{B.3})$$

$$\text{and with } \tilde{N}_i^{\perp/\parallel} = \tilde{N}_i \quad (\text{B.4})$$

$$(\Delta \tilde{N}_i)^2 = \left[ \frac{\partial}{\partial N_i} \left( \frac{N_i}{\sum_j N_j} \right) \cdot \Delta N_i \right]^2 + \sum_{j \neq i} \left[ \frac{\partial}{\partial N_j} \left( \frac{N_i}{\sum_j N_j} \right) \cdot \Delta N_j \right]^2 \quad (\text{B.5})$$

$$= \left[ \frac{\sum_{j \neq i} N_j}{\left( \sum_j N_j \right)^2} \cdot \Delta N_i \right]^2 + \sum_{j \neq i} \left[ -1 \cdot \frac{N_i}{\left( \sum_j N_j \right)^2} \cdot \Delta N_j \right]^2 \quad (\text{B.6})$$

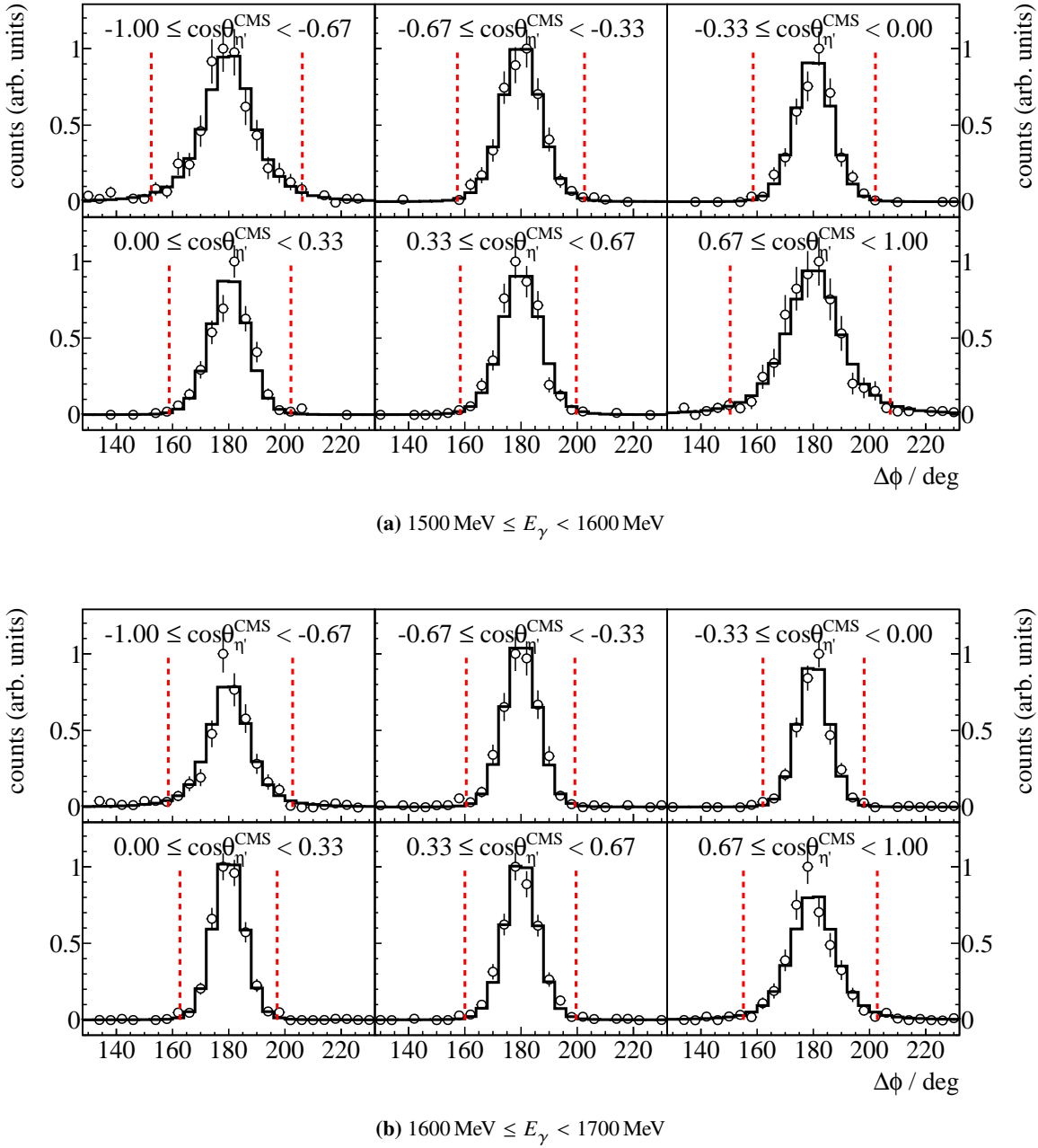
$$= \frac{1}{\left( \sum_j N_j \right)^4} \cdot \left[ \left( \sum_{j \neq i} N_j \cdot \Delta N_i \right)^2 + \sum_{j \neq i} \left( N_i \cdot \Delta N_j \right)^2 \right]. \quad (\text{B.7})$$

One can then further use that  $(\Delta N_i)^2 \approx N_i$ . This holds only approximately, since the histograms are filled  $N$  times with weights  $w_n$  (see chapter 3.3), but since the weights are either  $w = 1$  or  $w \ll 1$

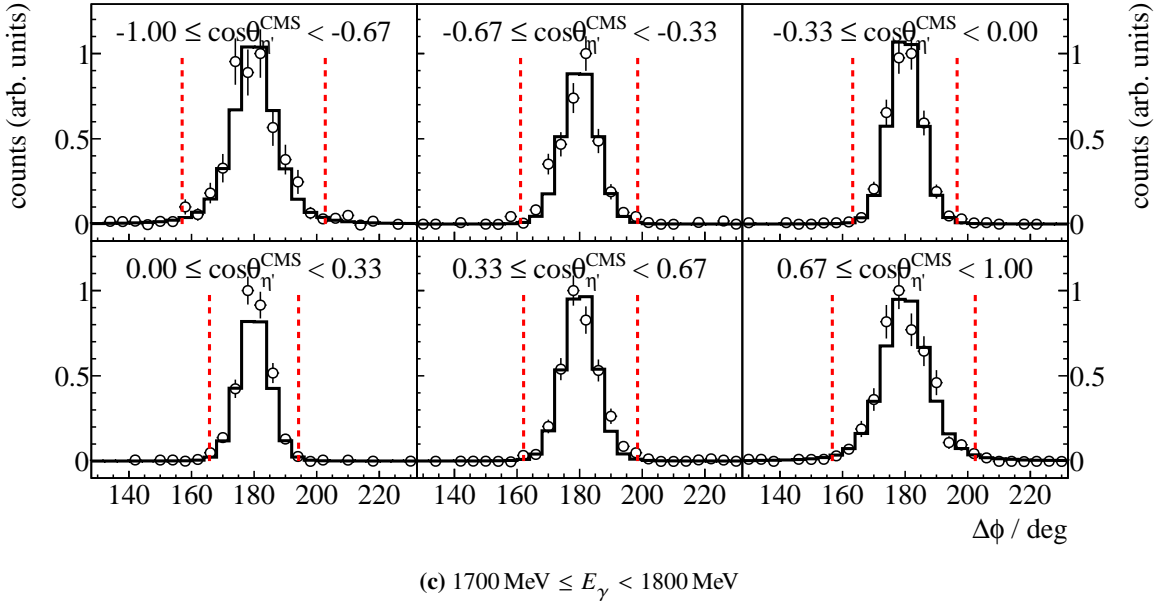
$$\Delta N_i = \sqrt{\sum_{n=1}^N w^2} \approx \sqrt{N_i}. \quad (\text{B.8})$$

## B.2 Kinematic variables for each bin

### B.2.1 Coplanarity



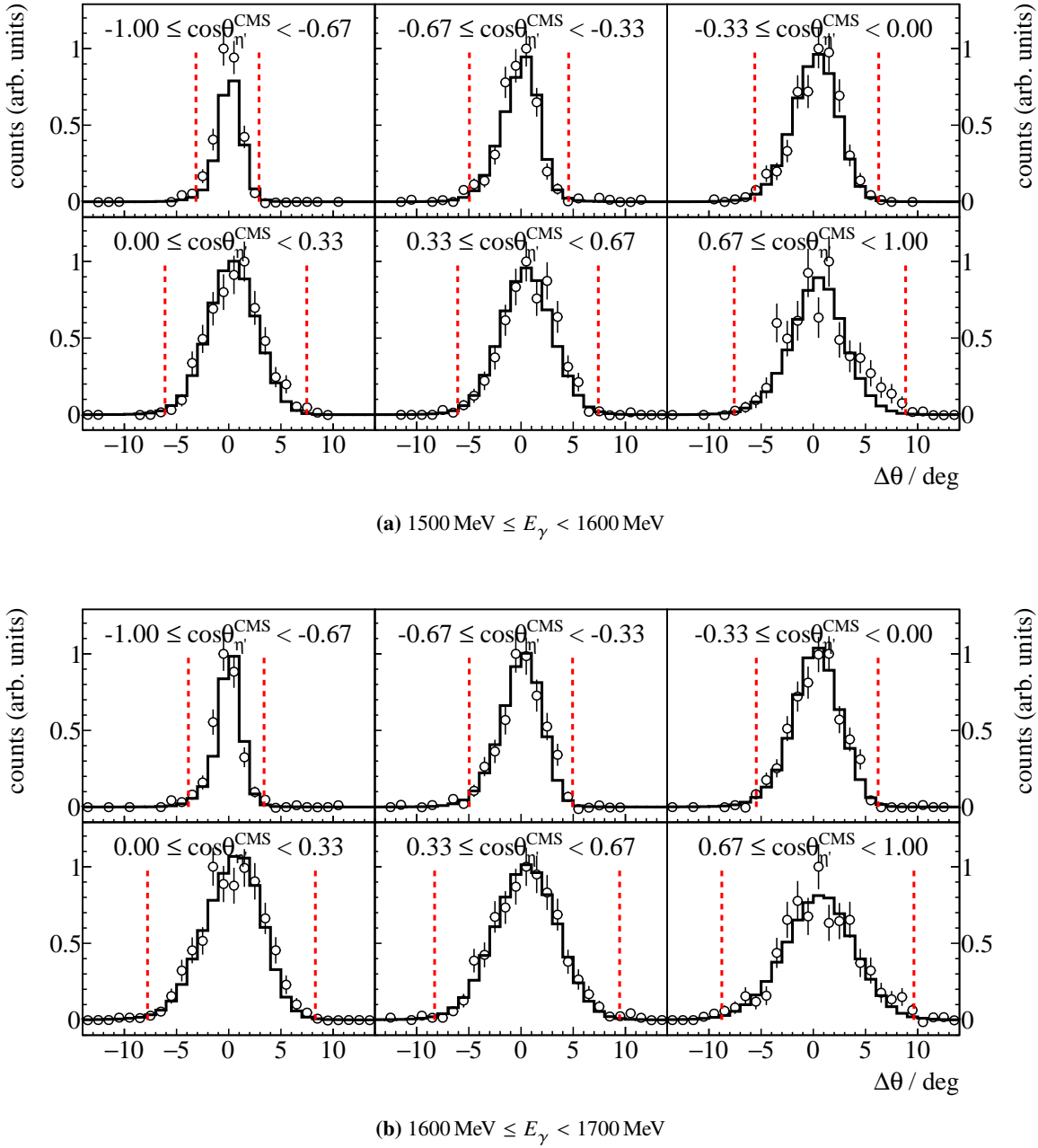
**Figure B.1:** Coplanarity  $\Delta\phi$  for all energy and angular bins. Data points are displayed as open circles, scaled Monte Carlo data belonging to  $\eta'$  photoproduction is displayed as solid histogram. The determined cut ranges are indicated by the dashed red lines.



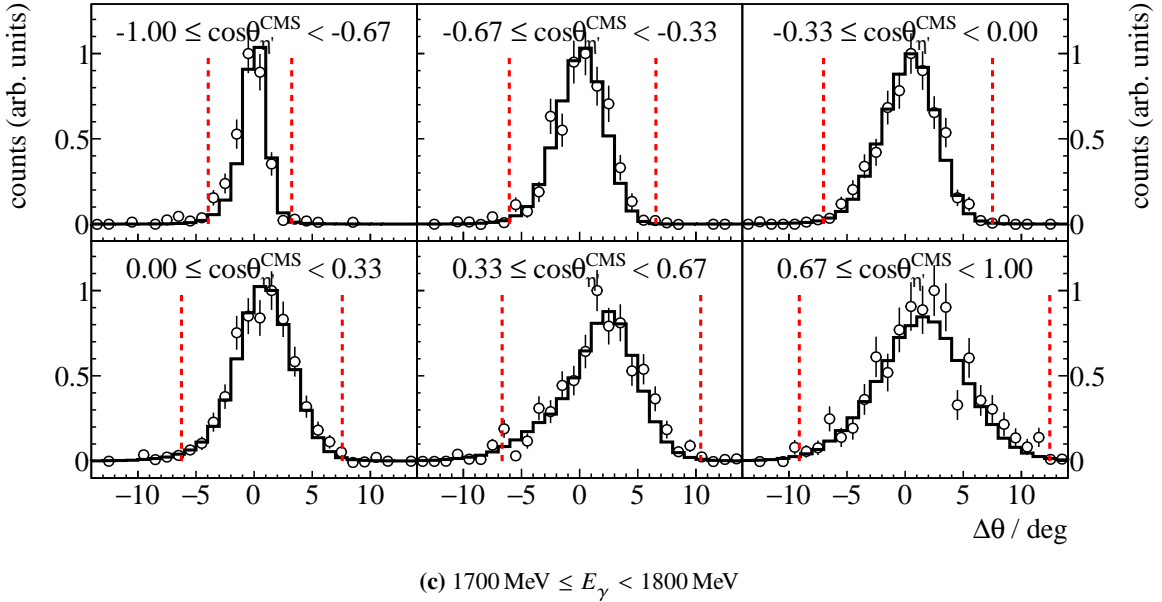
**Figure B.1:** Coplanarity  $\Delta\phi$  for all energy and angular bins. Data points are displayed as open circles, scaled Monte Carlo data belonging to  $\eta'$  photoproduction is displayed as solid histogram. The determined cut ranges are indicated by the dashed red lines.

Figure B.1 shows the coplanarity for all energy and angular bins. Cut ranges were determined from a GAUSSIAN fit to the data points. Only slight dependency on beam energy and meson polar angle can be identified. Only  $\eta'$  Monte Carlo data are fitted because the measured points do not give enough reference points for the fit to identify different contributing final states. There is good agreement between Monte Carlo simulations and measured data.

### B.2.2 Polar angle difference



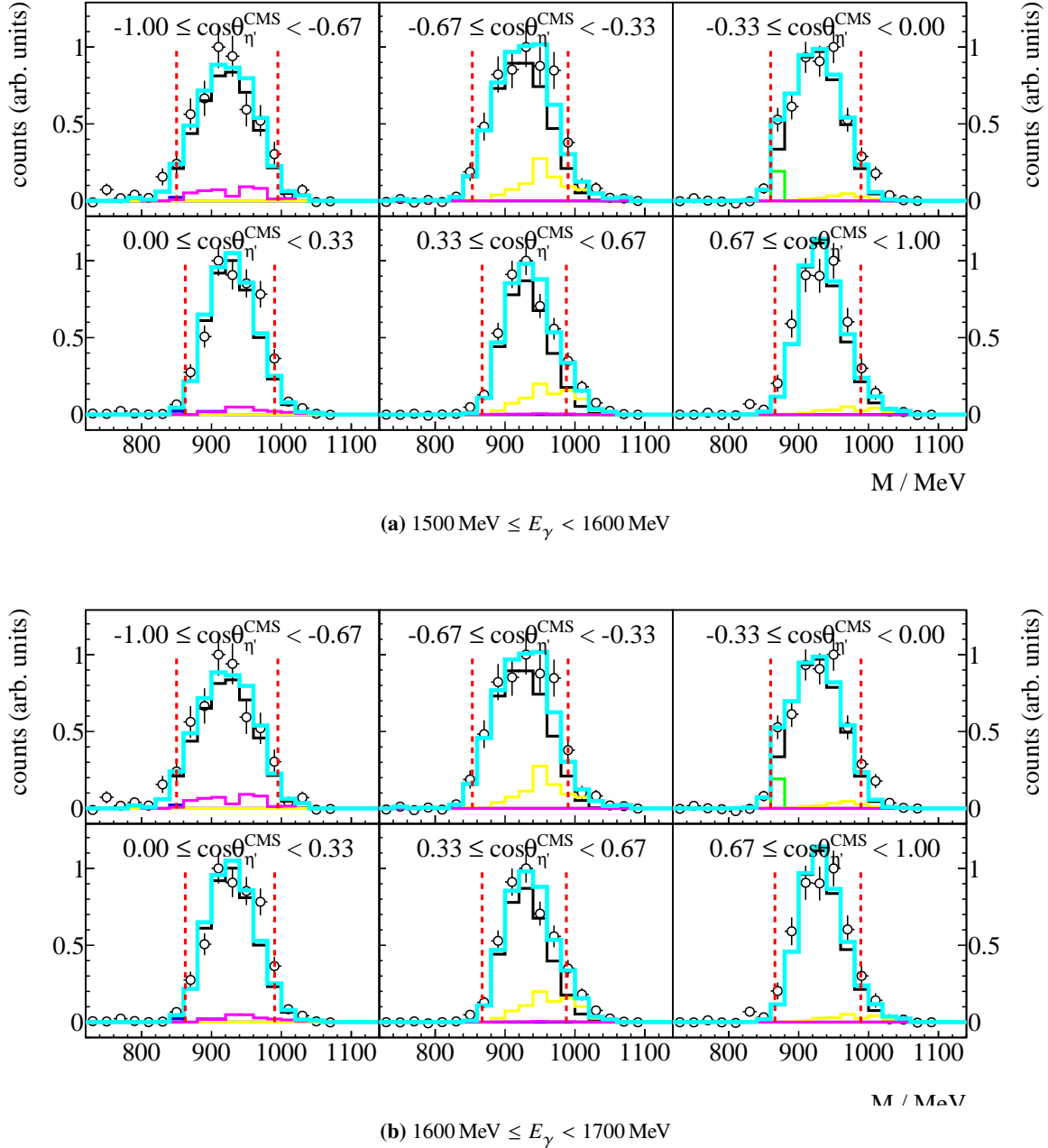
**Figure B.2:** Polar angle difference  $\Delta\theta$  for all energy and angular bins. Data points are displayed as open circles, scaled Monte Carlo data belonging to  $\eta'$  photoproduction is displayed as solid histogram. The determined cut ranges are indicated by the dashed red lines.



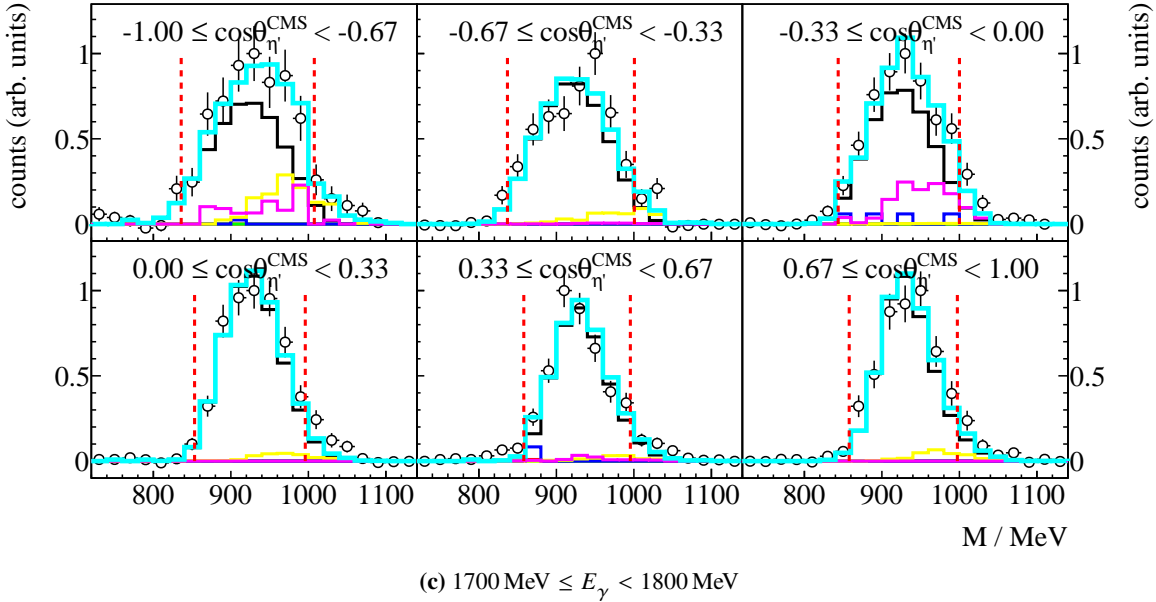
**Figure B.2:** Polar angle difference  $\Delta\theta$  for all energy and angular bins. Data points are displayed as open circles, scaled Monte Carlo data belonging to  $\eta'$  photoproduction is displayed as solid histogram. The determined cut ranges are indicated by the dashed red lines.

Figure B.2 shows the polar angle difference for all energy and angular bins. Cut ranges were determined from a GAUSSIAN fit to the data points. Only slight dependency on beam energy can be identified whereas clear correlation between width of the distribution and meson polar angle exists. This is due to the hit detectors which exhibit different angular resolutions, as has been discussed in the main part. Only  $\eta'$  Monte Carlo data are fitted because the measured points do not give enough reference points for the fit to identify different contributing final states. There is good agreement between Monte Carlo simulations and measured data.

### B.2.3 Missing mass

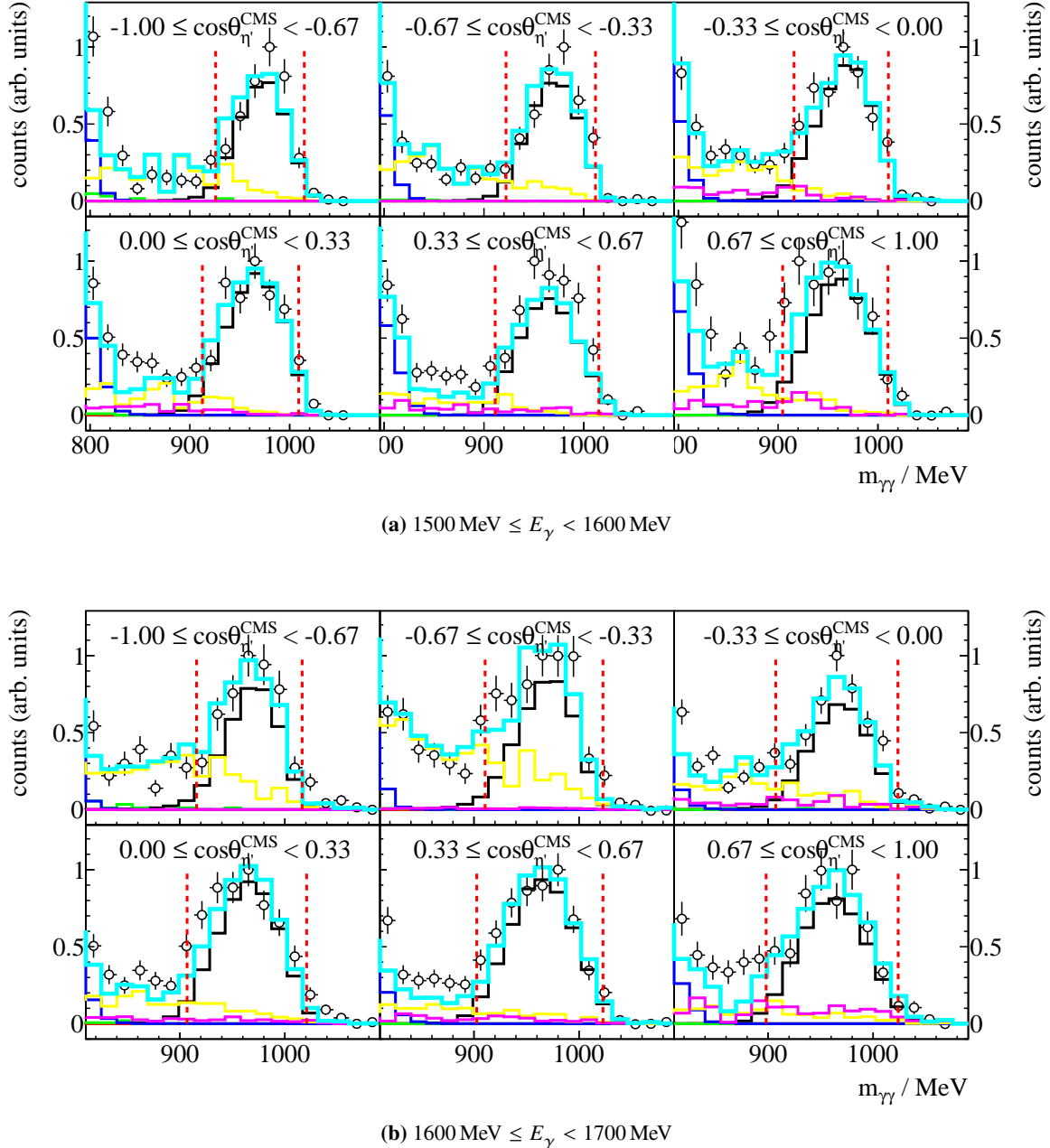


**Figure B.3:** Missing mass  $m_x$  for all energy and angular bins. Data points are displayed as open circles, scaled Monte Carlo data belonging to  $\eta'$  (black),  $2\pi^0$  (yellow) and  $\pi^0\eta$  (magenta) photoproduction is displayed as solid histogram while their sum is displayed as turquoise histogram. The determined cut ranges are indicated by the dashed red lines.



**Figure B.3:** Missing mass  $m_X$  for all energy and angular bins. Data points are displayed as open circles, scaled Monte Carlo data belonging to  $\eta'$  (black),  $2\pi^0$  (yellow) and  $\pi^0\eta$  (magenta) photoproduction is displayed as solid histogram while their sum is displayed as turquoise histogram. The determined cut ranges are indicated by the dashed red lines.

Figure B.3 shows the missing mass for all energy and angular bins. Cut ranges were determined from a Novosibirsk fit to the Monte Carlo data. Only slight dependency on meson polar angle can be identified. Especially at higher beam energies the missing mass peak grows wider with flat background contributions from  $2\pi^0$  and  $\pi^0\eta$  production towards higher masses. The Monte Carlo fit mostly shows consistency with the fit of the invariant mass spectra. However, spectra are to be seen with caution, since the shapes of the two different background contributions are very similar and there is no other reference point in the missing mass spectrum as opposed to the invariant mass. Fits to the invariant mass spectra may reveal background contributions where a fit to the missing mass spectrum failed to find any. There is good agreement between Monte Carlo simulations and measured data.

**B.2.4 Invariant mass**


**Figure B.4:** Invariant mass  $m_{\text{meson}}$  for all energy and angular bins. Data points are displayed as open circles, scaled Monte Carlo data belonging to  $\eta'$  (black),  $2\pi^0$  (yellow),  $\pi^0\eta$  (magenta),  $\pi^0$  (green) and  $\omega$  (blue) photoproduction is displayed as solid histogram while their sum is displayed as turquoise histogram. The determined cut ranges are indicated by the dashed red lines.

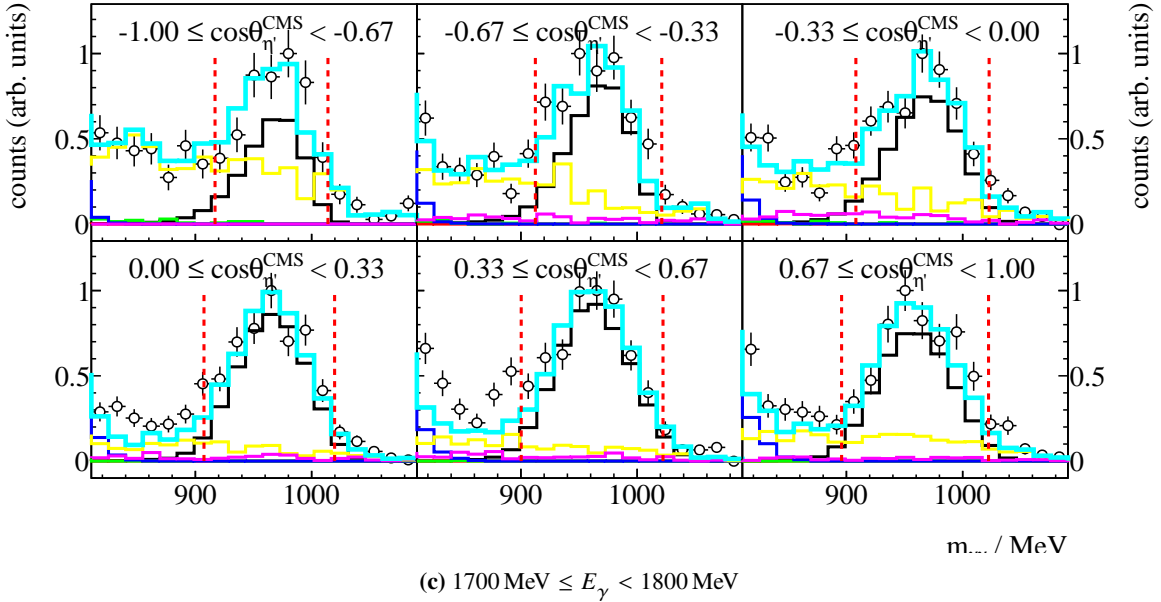


**Figure B.4:** Invariant mass  $m_{\text{meson}}$  for all energy and angular bins. Data points are displayed as open circles, scaled Monte Carlo data belonging to  $\eta'$  (black),  $2\pi^0$  (yellow),  $\pi^0\eta$  (magenta),  $\pi^0$  (green) and  $\omega$  (blue) photoproduction is displayed as solid histogram while their sum is displayed as turquoise histogram. The determined cut ranges are indicated by the dashed red lines.

Figure B.4 shows the invariant mass for all kinematic bins. Hardly any dependence on meson direction and beam energy is observed. However, background contributions are especially observed in very forward and backward direction towards higher beam energies in consistency with findings from the missing mass spectra. A flat background is realized by  $2\pi^0$  and  $\pi^0\eta$  production. There is good agreement between Monte Carlo simulations and measured data.

## APPENDIX C

---

### Discussion of binned fits

---

Investigation of toy Monte Carlo experiments (cf. section 4.3) revealed that the choice of binning leads to systematic errors regarding the parameter  $\Sigma$  when fitting a binned distribution to the equation

$$A(\phi) = \Sigma \cdot \cos(2(\alpha^{\parallel} - \phi)). \quad (\text{C.1})$$

To investigate this further, the distributions  $A(\phi)$  from different toy Monte Carlo experiments where fitted for several binnings in  $\phi$ . Three different Monte Carlo experiments were considered, each corresponding roughly to the expected statistics in one kinematic bin for  $\pi^0$ ,  $\eta$  and  $\eta'$  photoproduction, respectively. For simplicity's sake, only least squares fits are shown here, although similar results were found for BAYESIAN fits also. The equivalency of BAYESIAN and least squares fit has been demonstrated sufficiently up until now. To identify the bias that is introduced by binning the data, 10000 toy Monte Carlo bins for each setting are fitted for  $n = 10, 15, 20, \dots, 100$  bins. Then the dependence from the amount of bins of the mean  $\mu$  of the normalized residuals  $\xi$  as well as the mean  $\chi^2$  value of all fits is investigated. This is shown in Figure C.1; The fitted mean of the normalized posteriors  $\xi$  is plotted against the number of bins (blue data points, left ordinate) as well as the mean  $\chi^2$  of 10000 fits depending on the number of bins (red data points, right ordinate). Clear dependencies can be made out: while too few bins tend to underestimate the true value of the beam asymmetry, too much bins will lead to an overcompensation. For this reason, the functions  $\chi^2(n)$  and  $\mu(n)$  are monotonously rising with increasing number of bins  $n$ . An exception is realized by the samples that simulated the statistics of the  $\eta'$  final state, which can be explained by the fact, that after reaching a certain number of bins, no sensible fit estimates can be made anymore because too few data points are available. A minimum deviation from the nominal value is reached with  $n = 10, 20, 30$  bins for statistics comparable to  $\eta'$ ,  $\eta$  and  $\pi^0$  production respectively. This does not coincide with a minimum  $\chi^2$  necessarily, although the mean  $\chi^2$  values associated with the best estimation of the input value are compatible with 1. Figure C.1 however remarkably shows the influence binning has on the extraction of the beam asymmetry. Since there exist other methods, binned fits should only be used as a sanity check, but generally avoided, to circumvent the introduction of any systematics inherent to binning.

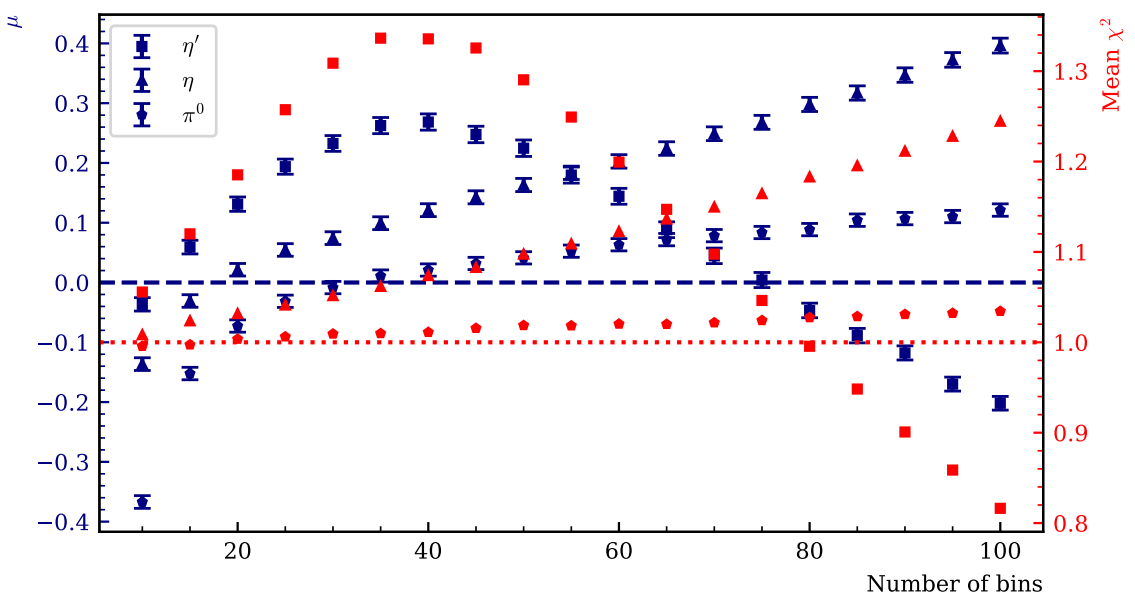


**Figure C.1:** Fit performance in dependence of the number of bins. Left axis shows the mean  $\mu$  of the distribution of the normalized residuals  $\xi$ , right axis shows the mean  $\chi^2$  of all fits. Squares simulate fits with statistics similar to the  $\gamma p \rightarrow p\eta' \rightarrow p\gamma\gamma$  final state, triangles statistics similar to the  $\gamma p \rightarrow p\eta \rightarrow p\gamma\gamma$  final state, pentagons statistics similar to the  $\gamma p \rightarrow p\pi^0 \rightarrow p\gamma\gamma$ . Dotted red line indicates the ideal value of  $\chi^2 = 1$ , while the dashed blue line indicates the ideal mean of the normalized residuals at  $\mu = 0$ .

## APPENDIX D

---

### Investigation of posteriors without truncation

---

In section 4.3 the investigation of posterior distributions from unbinned BAYESIAN fits was incomplete, since the normalized residuals as well as the likelihood pool could not be built with truncated posteriors. This is now supplemented here. After the fits have been repeated without implementing a truncation for the posteriors, all introduced measures to argue good fit quality can be examined. As a reminder, the data were generated with  $\Sigma_1 = 0.5$  and  $\Sigma_t = -0.5$ . Figure D.1 shows the combined posteriors of all fits. The left hand side shows the normalized residuals  $\Xi$  and the right hand side the unnormalized combination of all posteriors. The results completely meet the expectations, the input values for the beam asymmetries are very well reproduced, and the normalized residuals follow a standard normal distribution as GAUSSIAN fits show. Together with the results obtained from the independent likelihood pool (Figure D.2), which is able to reproduce the input values within  $1\sigma$ , this suffices to conclude correct estimation of distribution widths with no inherent bias, as had already been found in section 4.2.3.

**Remark:** It turned out that without the amount of statistics that was used in section 4.2, normal priors centered at 0 for the asymmetries  $\Sigma_t$  and  $\Sigma$  will mislead the fit results for these parameters towards 0 if no lower and upper boundaries are used. Instead the priors were then chosen to be uniform on the interval  $[-2, 2]$ . This imposes boundaries, but will not truncate the posteriors because the distributions are not expected to be this wide. All distributions shown here are generated using this model to complete the full investigation of posteriors. Previous toy Monte Carlo experiments (Figure 4.19) as well as very good agreement between point estimates and posterior distributions (Figure 4.23) together with the results shown here confirm the validity of the fit used in the main part.

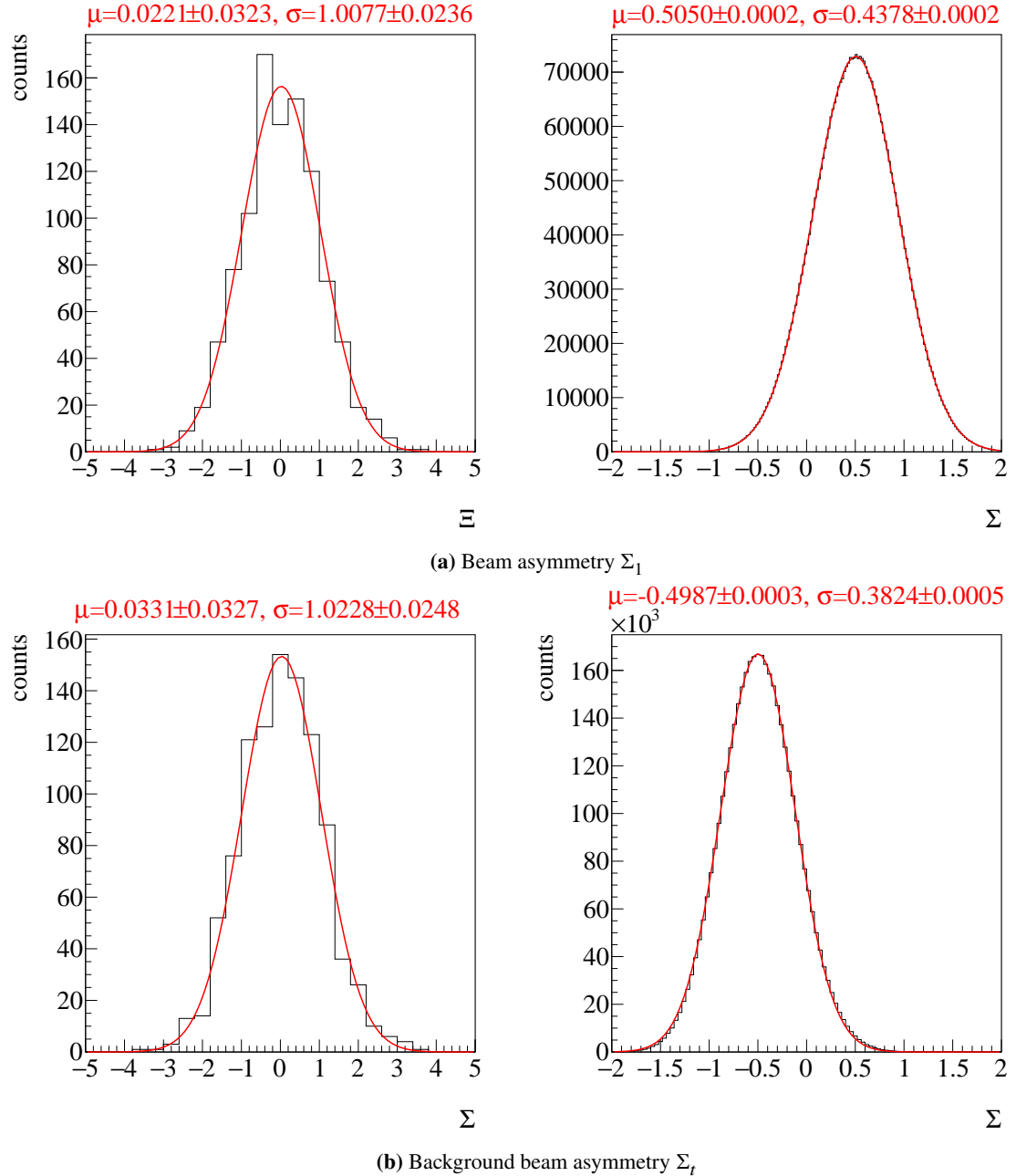


**Figure D.1:** Combined posteriors of all 1000 fits without truncation for the signal beam asymmetry  $\Sigma_1$  and the background beam asymmetry  $\Sigma_t$ . Left: normalized residuals  $\Xi$ , Right: unaltered added posterior distributions. GAUSSIAN fits have been performed with results given on top of each plot.

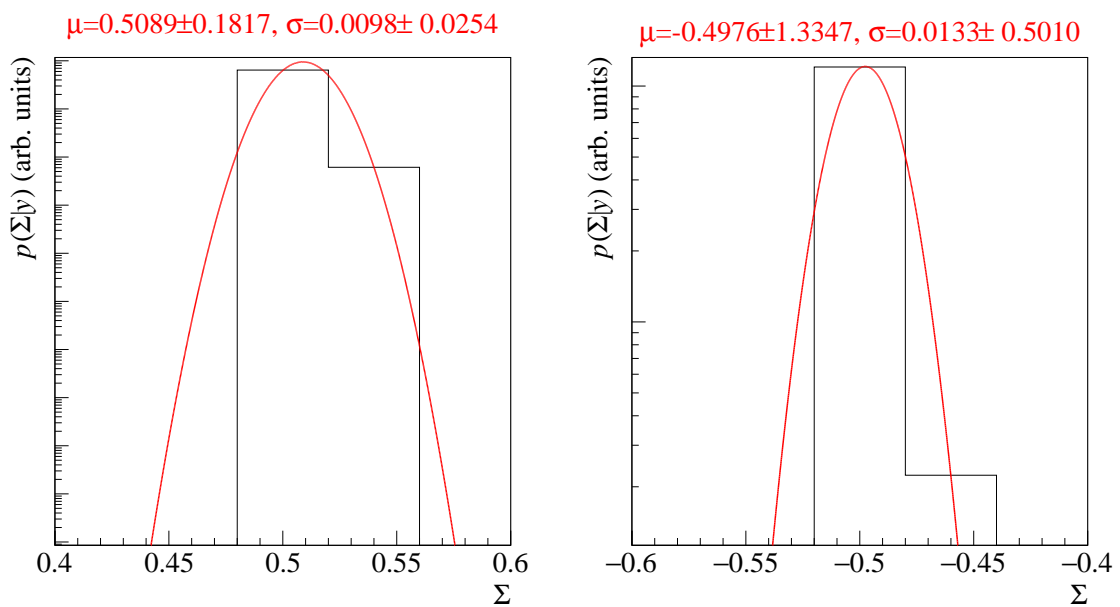


**Figure D.2:** Posterior distributions of  $\Sigma_l$  (left) and  $\Sigma_t$  (right) combined in an independent likelihood pool. GAUSSIAN fits to the distribution confirm the reproduction of the input values within  $1\sigma$ . Note that only very few datapoints were available for the fits, because the distributions overwhelmingly converge into a single bin at  $\pm 0.5$ , hence the large errors on the fit parameters.



# Bibliography

---

- [Wor+22] R. L. Workman et al., *Review of Particle Physics*, PTEP **2022** (2022) 083C01 (cit. on pp. 2–4, 33–35, 38, 40, 48, 95, 97).
- [LMP01] U. Löring, B. Metsch and H. Petry, *The light-baryon spectrum in a relativistic quark model with instanton-induced quark forces*, The European Physical Journal A **10** (2001) 395, ISSN: 1434-601X, URL: <http://dx.doi.org/10.1007/s100500170105> (cit. on pp. 2, 3).
- [Met08] B. Metsch, *Quark models\**, Eur. Phys. J. A **35** (2008) 275 (cit. on p. 3).
- [Ans+93] M. Anselmino, E. Predazzi, S. Ekelin, S. Fredriksson and D. B. Lichtenberg, *Diquarks*, Rev. Mod. Phys. **65** (4 1993) 1199, URL: <https://link.aps.org/doi/10.1103/RevModPhys.65.1199> (cit. on p. 3).
- [KS03] B. Krusche and S. Schadmand, *Study of nonstrange baryon resonances with meson photoproduction*, Prog. Part. Nucl. Phys. **51** (2003) 399, arXiv: [nucl-ex/0306023](https://arxiv.org/abs/nucl-ex/0306023) (cit. on p. 4).
- [Afz19] F. N. Afzal, *Measurement of the beam and helicity asymmetries in the reactions  $\gamma p \rightarrow p\pi^0$  and  $\gamma p \rightarrow p\eta$* , PhD thesis: Rheinische Friedrich-Wilhelms-Universität Bonn, 2019 (cit. on pp. 4, 5, 7, 18, 21, 23, 25, 26, 29, 31–33, 43, 45, 57, 58, 60, 61, 66, 67, 70, 71, 75, 78, 80, 82, 89, 95, 97, 98).
- [DT92] D. Drechsel and L. Tiator, *Threshold pion photoproduction on nucleons*, J. Phys. G **18** (1992) 449 (cit. on p. 4).
- [Bar+18] M. Bartelmann et al., *Theoretische Physik 3 - Quantenmechanik*, Springer Spektrum, 2018, ISBN: 978-3-662-56071-6 (cit. on p. 4).
- [Che+57] G. F. Chew, M. L. Goldberger, F. E. Low and Y. Nambu, *Relativistic Dispersion Relation Approach to Photomeson Production*, Phys. Rev. **106** (6 1957) 1345, URL: <https://link.aps.org/doi/10.1103/PhysRev.106.1345> (cit. on pp. 5, 6).
- [PS95] M. E. Peskin and D. V. Schroeder, *An Introduction to quantum field theory*, Reading, USA: Addison-Wesley, 1995 (cit. on p. 5).
- [San+11] A. M. Sandorfi, S. Hoblit, H. Kamano and T.-S. H. Lee, *Determining pseudoscalar meson photoproduction amplitudes from complete experiments*, Journal of Physics G: Nuclear and Particle Physics **38** (2011) 053001, ISSN: 1361-6471, URL: <http://dx.doi.org/10.1088/0954-3899/38/5/053001> (cit. on pp. 6, 59).

## Bibliography

---

- [CT97] W.-T. Chiang and F. Tabakin,  
*Completeness rules for spin observables in pseudoscalar meson photoproduction*,  
Physical Review C **55** (1997) 2054, ISSN: 1089-490X,  
URL: <http://dx.doi.org/10.1103/PhysRevC.55.2054> (cit. on p. 6).
- [Wun18] Y. Wunderlich, *The complete experiment problem of pseudoscalar meson photoproduction in a truncated partial wave analysis*,  
PhD thesis: Rheinische Friedrich-Wilhelms-Universität Bonn, 2018 (cit. on p. 6).
- [Afz12] F. N. Afzal, *Analysis of Crystal Barrel Data - Measurement of the double polarization observable E in the reaction  $\vec{\gamma}\vec{p} \rightarrow \eta' p$* ,  
Master thesis: Rheinische Friedrich-Wilhelms-Universität Bonn, 2012 (cit. on pp. 6, 33).
- [FTS92] C. G. Fasano, F. Tabakin and B. Saghai,  
*Spin observables at threshold for meson photoproduction*, Phys. Rev. C **46** (1992) 2430  
(cit. on p. 7).
- [Wun+17] Y. Wunderlich, F. Afzal, A. Thiel and R. Beck,  
*Determining the dominant partial wave contributions from angular distributions of single- and double-polarization observables in pseudoscalar meson photoproduction*,  
The European Physical Journal A **53** (2017),  
URL: <https://doi.org/10.1140%2Fepja%2Fepja2017-12255-0> (cit. on p. 7).
- [Gel+14] A. Gelman et al., *Bayesian Data Analysis*, vol. 3, Chapman & Hall/CRC, 2014  
(cit. on pp. 7–10, 12–14, 62).
- [SS05] D. Sivia and J. Skilling, *Data Analysis – A Bayesian Tutorial*, vol. 2,  
Oxford University Press, 2005 (cit. on p. 8).
- [Tro08] R. Trotta, *Bayes in the sky: Bayesian inference and model selection in cosmology*,  
Contemporary Physics **49** (2008) 71,  
URL: <https://doi.org/10.1080%2F00107510802066753> (cit. on p. 8).
- [Nor97] J. R. Norris, *Markov Chains*,  
Cambridge Series in Statistical and Probabilistic Mathematics,  
Cambridge University Press, 1997 (cit. on p. 9).
- [Met+53] N. Metropolis, A. W. Rosenbluth, M. N. Rosenbluth, A. H. Teller and E. Teller,  
*Equation of State Calculations by Fast Computing Machines*,  
The Journal of Chemical Physics **21** (1953) 1087,  
eprint: <https://doi.org/10.1063/1.1699114>,  
URL: <https://doi.org/10.1063/1.1699114> (cit. on p. 9).
- [Has70] W. K. Hastings,  
*Monte Carlo sampling methods using Markov chains and their applications*,  
Biometrika **57** (1970) 97, ISSN: 0006-3444,  
eprint: <https://academic.oup.com/biomet/article-pdf/57/1/97/23940249/57-1-97.pdf>,  
URL: <https://doi.org/10.1093/biomet/57.1.97> (cit. on p. 9).

- 
- [Dua+87] S. Duane, A. Kennedy, B. J. Pendleton and D. Roweth, *Hybrid Monte Carlo*, Physics Letters B **195** (1987) 216, ISSN: 0370-2693, URL: <https://www.sciencedirect.com/science/article/pii/037026938791197X> (cit. on p. 9).
- [Sta22a] Stan development team, *Stan Modeling Language Users Guide and Reference Manual*, vol. 2.29, 2022, URL: <https://mc-stan.org> (cit. on pp. 10–12, 14, 16, 31, 63, 66, 79, 85, 87, 98).
- [KN98] C. Kaya and L. Noakes, “Geodesics and an optimal control algorithm”, vol. 5, 1998 4918 (cit. on p. 10).
- [HG14] M. D. Hoffman and A. Gelman, *The No-U-Turn Sampler: Adaptively Setting Path Lengths in Hamiltonian Monte Carlo*, Journal of Machine Learning Research **15** (2014) 1593, URL: <http://jmlr.org/papers/v15/hoffman14a.html> (cit. on pp. 10, 63, 66).
- [GR92] A. Gelman and D. B. Rubin, *Inference from Iterative Simulation Using Multiple Sequences*, Statistical Science **7** (1992) 457, URL: <https://doi.org/10.1214/ss/1177011136> (cit. on p. 10).
- [Veh+19] A. Vehtari, A. Gelman, D. Simpson, B. Carpenter and P.-C. Bürkner, *Rank-normalization, folding, and localization: An improved  $\hat{R}$  for assessing convergence of MCMC*, arXiv e-prints, arXiv:1903.08008 (2019) arXiv:1903.08008, arXiv: 1903.08008 [stat.CO] (cit. on pp. 10–12, 70).
- [AS72] M. Abramowitz and I. Stegun, *Handbook of Mathematical Functions*, Dover Publishing, 1972 (cit. on p. 12).
- [Gey92] C. J. Geyer, *Practical Markov Chain Monte Carlo*, Statistical Science **7** (1992) 473, URL: <https://doi.org/10.1214/ss/1177011137> (cit. on p. 12).
- [Gey11] C. J. Geyer, *Handbook of Markov Chain Monte Carlo*, ed. by S. Brooks, A. Gelman, G. L. Jones and X.-L. Meng, Chapman and Hall / CRC, 2011 (cit. on p. 12).
- [Sto61] M. Stone, *The Opinion Pool*, The Annals of Mathematical Statistics **32** (1961) 1339, URL: <https://doi.org/10.1214/aoms/1177704873> (cit. on p. 12).
- [MD94] J. Manyika and H. Durrant-Whyte, *Data Fusion and Sensor Management: A Decentralized Information-Theoretic Approach*, Ellis Horwood, 1994 (cit. on p. 13).
- [BS10] C. Bailer-Jones and K. Smith, *Combining probabilities*, Gaia Technical Notes (2010), URL: [https://www.mpi-a.de/gaia/publications/tech\\_notes](https://www.mpi-a.de/gaia/publications/tech_notes) (visited on 29/08/2022) (cit. on p. 13).
- [Bar89] R. J. Barlow, *Statistics, A Guide to the Use of Statistical Methods in the Physical Sciences*, Wiley, 1989 (cit. on pp. 15, 62, 67).
- [BC16] W. M. Bolstad and J. M. Curran, *Introduction to Bayesian statistics*, John Wiley & Sons, 2016 (cit. on pp. 17, 18).

## Bibliography

---

- [Afz+20] F. Afzal et al.,  
*Observation of the  $p\eta'$  Cusp in the New Precise Beam Asymmetry  $\Sigma$  Data for  $\gamma p \rightarrow p\eta'$* ,  
Phys. Rev. Lett. **125** (15 2020) 152002,  
URL: <https://link.aps.org/doi/10.1103/PhysRevLett.125.152002>  
(cit. on pp. 18, 60, 98).
- [TAW22] A. Thiel, F. Afzal and Y. Wunderlich, *Light Baryon Spectroscopy*,  
Progress in Particle and Nuclear Physics **125** (2022) 103949,  
URL: <https://doi.org/10.1016/j.ppnp.2022.103949> (cit. on p. 18).
- [Wil+09] M. Williams et al., *Differential cross sections for the reactions  $\gamma p \rightarrow p\eta$  and  $\gamma p \rightarrow p\eta'$* ,  
Phys. Rev. C **80** (4 2009) 045213,  
URL: <https://link.aps.org/doi/10.1103/PhysRevC.80.045213> (cit. on p. 18).
- [Cre+09] V. Crede et al., *Photoproduction of eta and eta-prime mesons off protons*,  
Phys. Rev. C **80** (2009) 055202, arXiv: [0909.1248 \[nucl-ex\]](https://arxiv.org/abs/0909.1248)  
(cit. on pp. 18, 40, 45, 48).
- [Lev+14] P. Levi Sandri et al., *First Measurement of the  $\Sigma$  Beam Asymmetry in  $\eta'$  Photoproduction off the Proton near Threshold*, (2014) (cit. on pp. 18, 95, 97).
- [Col+17] P. Collins et al.,  
*Photon beam asymmetry  $\Sigma$  for  $\eta$  and  $\eta'$  photoproduction from the proton*,  
Physics Letters B (2017) (cit. on pp. 18, 95–98).
- [Ani+18] A. Anisovich et al., *Proton- $\eta'$  interactions at threshold*,  
Physics Letters B **785** (2018) 626, ISSN: 0370-2693, URL: <https://www.sciencedirect.com/science/article/pii/S0370269318304908>  
(cit. on pp. 18, 97–100).
- [Tia+18] L. Tiator et al.,  
*Eta and etaprime photoproduction on the nucleon with the isobar model EtaMAID2018*,  
The European Physical Journal A **54** (2018),  
URL: <https://doi.org/10.1140/epja/s1018-12643-x>  
(cit. on pp. 18, 97–100).
- [Noë22] J. F. Noël,  
*Truncated partial wave analysis of the reaction  $\gamma p \rightarrow p\pi^0$  using Bayesian statistics*,  
Master thesis: Rheinische Friedrich-Wilhelms-Universität Bonn, 2022 (cit. on p. 18).
- [Krö22] P. Krönert, *Thesis in preparation*,  
PhD thesis: Rheinische Friedrich-Wilhelms-Universität Bonn, 2022 (cit. on p. 18).
- [Leo94] W. R. Leo,  
*Techniques for Nuclear and Particle Physics Experiments, A How-to Approach*, vol. 2,  
Springer-Verlag Berlin Heidelberg GmbH, 1994 (cit. on pp. 22, 27, 28, 95).
- [Hei54] W. Heitler, *The Quantum Theory of Radiation*, Oxford University Press, 1954  
(cit. on p. 22).
- [Dem10] W. Demtröder, *Experimentalphysik 3, Atome, Moleküle, Festkörper*, vol. 4,  
Springer-Verlag Berlin Heidelberg New York, 2010 (cit. on p. 22).

- 
- [Nat+03] F. Natter, P. Grabmayr, T. Hehl, R. Owens and S. Wunderlich, *Monte Carlo simulation and analytical calculation of coherent bremsstrahlung and its polarisation*, Nuclear Instruments and Methods in Physics Research Section B: Beam Interactions with Materials and Atoms **211** (2003) 465 (cit. on p. 23).
- [Els+09] D. Elsner et al., *Linearly polarised photon beams at ELSA and measurement of the beam asymmetry in  $\pi^0$  photoproduction off the proton*, The European Physical Journal A **39** (2009) 373, URL: <https://doi.org/10.1140/2Fepja%2F12008-10708-1> (cit. on p. 23).
- [Kam10] S. Kammer, *Strahlpolarimetrie am CBELSA/TAPS Experiment*, PhD thesis: Rheinische Friedrich-Wilhelms-Universität Bonn, 2010, URL: <https://hdl.handle.net/20.500.11811/4539> (cit. on p. 23).
- [For10] K. Fornet-Ponse, *Die Photonenmarkierungsanlage für das Crystal-Barrel/TAPS-Experiment an ELSA*, PhD thesis: Rheinische Friedrich-Wilhelms-Universität Bonn, 2010, URL: <https://hdl.handle.net/20.500.11811/4507> (cit. on p. 24).
- [Har08] J. Hartmann, *Zeitkalibrierung und Photonenflussbestimmung für das Crystal-Barrel-Experiment and ELSA*, Diploma thesis: Rheinische Friedrich-Wilhelms-Universität Bonn, 2008 (cit. on pp. 24, 25, 27–29).
- [Wal] D. Walther, *Crystal Barrel, A  $4\pi$  photon spectrometer*, URL: <https://www.cb.uni-bonn.de> (visited on 27/09/2021) (cit. on pp. 24, 28).
- [Ham09] C. Hammann, *Aufbau eines Flüssigwasserstofftargets zur Durchführung von Kalibrationsmessungen am Crystal-Barrel Experiment an ELSA*, Diploma thesis: Rheinische Friedrich-Wilhelms-Universität Bonn, 2009 (cit. on pp. 24, 25).
- [Fös00] A. Fösel, *Entwicklung und Bau des Innendetektors für das Crystal Barrel Experiment an ELSA/Bonn*, PhD thesis: Friedrich-Alexander-Universität Erlangen-Nürnberg, 2000 (cit. on p. 25).
- [Suf+05] G. Suft et al., *A scintillating fibre detector for the Crystal Barrel experiment at ELSA*, Nucl. Instrum. Meth. A **538** (2005) 416 (cit. on p. 25).
- [PDG] PDG, *Atomic and Nuclear Properties*, URL: <https://pdg.lbl.gov/2022/AtomicNuclearProperties/index.html> (visited on 04/08/2022) (cit. on pp. 25, 27, 28).
- [Ake+92] E. Aker et al., *The Crystal Barrel spectrometer at LEAR*, Nucl. Instrum. Meth. A **321** (1992) 69 (cit. on pp. 26, 27).
- [Urb17] M. Urban, *Design eines neuen Lichtpulsersystems sowie Aufbau und Inbetriebnahme der neuen APD Auslese für das Crystal-Barrel-Kalorimeter*, PhD thesis: Rheinische Friedrich-Wilhelms-Universität Bonn, 2017 (cit. on pp. 26, 27, 34).

## Bibliography

---

- [Jun04] J. Junkersfeld,  
*Kalibration des Crystal-Barrel-ELSA Detektors mit Hilfe der Reaktion  $\gamma p \rightarrow p\pi^0$* ,  
Diploma thesis: Rheinische Friedrich-Wilhelms-Universität Bonn, 2004 (cit. on p. 27).
- [Bet30] H. Bethe, *Zur Theorie des Durchgangs schneller Korpuskularstrahlen durch Materie*,  
Annalen der Physik **397** (1930) 325, eprint:  
<https://onlinelibrary.wiley.com/doi/pdf/10.1002/andp.19303970303>,  
URL:  
<https://onlinelibrary.wiley.com/doi/abs/10.1002/andp.19303970303>  
(cit. on p. 27).
- [Hon14] C. Honisch, *Design, Aufbau und Test einer neuen Ausleseelektronik für das Crystal-Barrel-Kalorimeter*,  
PhD thesis: Rheinische Friedrich-Wilhelms-Universität Bonn, 2014 (cit. on p. 27).
- [Wen04] C. Wendel, *Entwicklung eines Szintillations-Detektors zur Identifikation geladener Teilchen im Crystal-Barrel Vorwärtsdetektor*,  
Diploma thesis: Rheinische Friedrich-Wilhelms-Universität Bonn, 2004 (cit. on p. 27).
- [Geh15] S. Gehring, *Test des Szintillationsdetektors zur Identifikation geladener Teilchen im Crystal-Barrel-Vorwärtsdetektor*,  
Bachelor thesis: Rheinische Friedrich-Wilhelms-Universität Bonn, 2015 (cit. on p. 27).
- [Gab+94] A. Gabler et al.,  
*Response of TAPS to monochromatic photons with energies between 45 and 790 MeV*,  
Nuclear Instruments and Methods in Physics Research Section A: Accelerators, Spectrometers, Detectors and Associated Equipment **346** (1994) 168, ISSN: 0168-9002,  
URL:  
<https://www.sciencedirect.com/science/article/pii/0168900294907013>  
(cit. on pp. 27, 28).
- [Str96] H. Ströher, *Electromagnetic and Hadronic Probes of Nuclear Matter: Portrait of the European Photon Detector TAPS*, Nuclear Physics News **6** (1996) 7,  
eprint: <https://doi.org/10.1080/10506899609411060>,  
URL: <https://doi.org/10.1080/10506899609411060> (cit. on p. 27).
- [Nov91] R. Novotny, *The BaF/sub 2/photon spectrometer TAPS*,  
IEEE Transactions on Nuclear Science **38** (1991) 379 (cit. on p. 27).
- [Kai07] D. Kaiser,  
*Aufbau und Test des Gas- Čerenkov-Detektors für den Crystal-Barrel-Aufbau an ELSA*,  
Diploma thesis: Rheinische Friedrich-Wilhelms-Universität Bonn, 2007 (cit. on p. 28).
- [McG08] W. McGehee, *The Gamma Intensity Monitor of the Crystal-Barrel-Experiment*,  
Bachelor thesis: Massachusetts Institute of Technology, 2008 (cit. on p. 28).
- [Die08] J. Dielmann, *Entwicklung, Aufbau und Test eines Detektors zur Bestimmung des Photonenflusses an der Bonner Photonenmarkierungsanlage*,  
Diploma thesis: Rheinische Friedrich-Wilhelms-Universität Bonn, 2008 (cit. on p. 29).
- [Win06] A. Winnebeck, *Entwicklung und Implementierung eines universellen, FPGA basierten Triggermoduls für das Crystal-Barrel-Experiment and ELSA*,  
Diploma thesis: Rheinische Friedrich-Wilhelms-Universität Bonn, 2006 (cit. on p. 29).

- 
- [Hof18] P. Hoffmeister,  
*Das Datenerfassungssystem für das Crystal-Barrel/TAPS-Exoeriment an ELSA*,  
PhD thesis: Rheinische Friedrich-Wilhelms-Universität Bonn, 2018 (cit. on p. 29).
- [Fle01] H. Flemming, *Entwurf und Aufbau eines Zellularlogik-Triggers für das Crystal-Barrel-Experiment an der Elektronenbeschleunigeranlage ELSA*,  
PhD thesis: Rheinische Friedrich-Wilhelms-Universität Bonn, 2001 (cit. on p. 29).
- [Sch+] C. Schmidt et al., *Extended Pluggable Object-oriented Root Analysis*,  
url: <https://explora.cb.uni-bonn.de> (visited on 10/08/2022) (cit. on p. 30).
- [BR97] R. Brun and F. Rademakers, *ROOT — An object oriented data analysis framework*,  
Nucl. Instrum. Meth. A **389** (1997) 81, issn: 0168-9002, url: <https://www.sciencedirect.com/science/article/pii/S016890029700048X>  
(cit. on pp. 30, 62, 65, 66, 79).
- [MU49] N. Metropolis and S. Ulam, *The Monte Carlo Method*,  
Journal of the American Statistical Association **44** (1949) 335, PMID: 18139350,  
eprint: <https://www.tandfonline.com/doi/pdf/10.1080/01621459.1949.10483310>, URL:  
<https://www.tandfonline.com/doi/abs/10.1080/01621459.1949.10483310>  
(cit. on p. 30).
- [Bru+87] R. Brun, F. Bruyant, M. Maire, A. C. McPherson and P. Zanarini, *GEANT3*, (1987)  
(cit. on p. 30).
- [Kal11] F. Kalischewski, *Development of a new simulation for the CBELSA/TAPS experiment using Virtual Monte Carlo*,  
Diploma thesis: Rheinische Friedrich-Wilhelms-Universität Bonn, 2011 (cit. on p. 30).
- [AKN+] A. Anisovich, E. Klempt, V. Nikonov et al., *Bonn-Gatchina Partial Wave Analysis*,  
url: <https://pwa.hiskp.uni-bonn.de/> (visited on 10/08/2022) (cit. on p. 30).
- [Ani+12] A. V. Anisovich et al.,  
*Properties of baryon resonances from a multichannel partial wave analysis*,  
The European Physical Journal A **48** (2012),  
url: <https://doi.org/10.1140%2Fepja%2F12012-12015-8> (cit. on p. 30).
- [Mah22] P. Mahlberg, *Thesis in Preparation*,  
PhD thesis: Rheinische Friedrich-Wilhelms-Universität Bonn, 2022  
(cit. on pp. 30, 56, 85, 88, 91).
- [RP22] G. van Rossum and the Python development team,  
*The Python Language Reference, Release 3.10.5*, 2022,  
url: <https://docs.python.org/3.10/reference/index.html>  
(cit. on pp. 31, 62, 79).
- [Cmd22] CmdStanPy development team, *CmdStanPy*, 2022,  
url: <https://github.com/stan-dev/cmdstanpy> (visited on 29/08/2022)  
(cit. on p. 31).

## Bibliography

---

- [McK10] W. McKinney, “Data Structures for Statistical Computing in Python”, *Proceedings of the 9th Python in Science Conference*, ed. by S. van der Walt and J. Millman, 2010 56 (cit. on p. 31).
- [Kum+19] R. Kumar, C. Carroll, A. Hartikainen and O. Martin, *ArviZ a unified library for exploratory analysis of Bayesian models in Python*, Journal of Open Source Software **4** (2019) 1143, URL: <https://doi.org/10.21105/joss.01143> (cit. on p. 31).
- [Dah08] T. Dahlke, *Bestimmung einer winkelabhängigen Energiekorrekturfunktion für das TAPS-Kalorimeter des Crystal-Barrel/TAPS-Experiments and ELSA*, Diploma thesis: Rheinische Friedrich-Wilhelms-Universität Bonn, 2008 (cit. on p. 34).
- [GP08] M. Grüner and D.-M. Piontek, *Hit reconstruction in ChaPI*, CB-TR16 Note 003 (2008) (cit. on p. 34).
- [Ike+00] H. Ikeda et al., *A detailed test of the CsI(Tl) calorimeter for BELLE with photon beams of energy between 20-MeV and 5.4-GeV*, Nucl. Instrum. Meth. A **441** (2000) 401 (cit. on pp. 40, 42).
- [Har17] J. Hartmann, *Measurement of Double Polarization Observables in the Reactions  $\gamma p \rightarrow p\pi^0$  and  $\gamma p \rightarrow p\eta$  with the Crystal Barrel/TAPS Experiment at ELSA*, PhD thesis: Rheinische Friedrich-Wilhelms-Universität Bonn, 2017, URL: <https://hdl.handle.net/20.500.11811/7258> (cit. on pp. 45, 63, 66).
- [Die+20] M. Dieterle et al., *Helicity-Dependent Cross Sections for the Photoproduction of  $\pi^0$  Pairs from Nucleons*, Physical Review Letters **125** (2020), URL: <https://doi.org/10.1103%2Fphysrevlett.125.062001> (cit. on p. 48).
- [Käs+18] A. Käser et al., *First measurement of helicity-dependent cross sections in  $\pi^0\eta$  photoproduction from quasi-free nucleons*, Physics Letters B **786** (2018) 305, URL: <https://doi.org/10.1016%2Fj.physletb.2018.10.006> (cit. on p. 48).
- [Bar+05] O. Bartholomy et al., *Neutral-PionPhotoproduction off Protons in the Energy Range  $0.3 \text{ GeV} < E_\gamma < 3 \text{ GeV}$* , Physical Review Letters **94** (2005), URL: <https://doi.org/10.1103%2Fphysrevlett.94.012003> (cit. on p. 48).
- [Sta+11] A. Starostin et al., *Measurement of  $3\pi^0$  photoproduction on the proton from threshold to 1.4 GeV*, 2011, URL: <https://arxiv.org/abs/1101.3744> (cit. on p. 48).
- [Mur+20] N. Muramatsu et al., *Differential cross sections, photon beam asymmetries, and spin density matrix elements of  $\omega$  photoproduction off the proton at  $E_\gamma = 1.3 - 2.4 \text{ GeV}$* , Phys. Rev. C **102** (2 2020) 025201, URL: <https://link.aps.org/doi/10.1103/PhysRevC.102.025201> (cit. on p. 48).

- 
- [Str+76] W. Struczinski et al., *Study of photoproduction on hydrogen in a streamer chamber with tagged photons for  $1.6 \text{ GeV} < E_\gamma < 6.3 \text{ GeV}$*  *Topological and reaction cross sections*, Nuclear Physics B **108** (1976) 45, ISSN: 0550-3213, URL: <https://www.sciencedirect.com/science/article/pii/0550321376901231> (cit. on p. 48).
- [Dug+09] M. Dugger et al.,  $\pi^+$  photoproduction on the proton for photon energies from 0.725 to 2.875 GeV, Physical Review C **79** (2009), URL: <https://doi.org/10.1103/physrevc.79.065206> (cit. on p. 48).
- [Pov+14] B. Povh, K. Rith, C. Scholz, F. Zetsche and W. Rodejohann, *Teilchen und Kerne, Eine Einführung in die physikalischen Konzepte*, vol. 9, Springer Spektrum, 2014 (cit. on p. 61).
- [Vir+20] P. Virtanen et al., *SciPy 1.0: Fundamental Algorithms for Scientific Computing in Python*, Nature Methods **17** (2020) 261 (cit. on p. 62).
- [sci] *scipy, scipy.optimize.curve\_fit, Function Documentation*, URL: [https://docs.scipy.org/doc/scipy/reference/generated/scipy.optimize.curve\\_fit.html](https://docs.scipy.org/doc/scipy/reference/generated/scipy.optimize.curve_fit.html) (visited on 28/06/2022) (cit. on p. 62).
- [ROOa] ROOT, *TH1 Class reference*, URL: <https://root.cern.ch/doc/master/classTH1.html#a63eb028df86bc86c8e20c989eb23fb2a> (visited on 28/06/2022) (cit. on p. 62).
- [Sta22b] Stan development team, *Prior Choice Recommendations*, 2022, URL: <https://github.com/stan-dev/stan/wiki/Prior-Choice-Recommendations> (visited on 02/07/2022) (cit. on p. 62).
- [ROOb] ROOT, *TTree Class reference*, URL: <https://root.cern.ch/doc/master/classTTree.html#a3e6bf252ab8653b47cc9116950f3ee7b> (visited on 28/06/2022) (cit. on pp. 65, 79).
- [JR75] F. James and M. Roos, *Minuit - a system for function minimization and analysis of the parameter errors and correlations*, Computer Physics Communications **10** (1975) 343, ISSN: 0010-4655, URL: <https://www.sciencedirect.com/science/article/pii/0010465575900399> (cit. on p. 65).
- [ROOc] ROOT, *TF1 Class reference*, URL: <https://root.cern.ch/doc/master/classTF1.html#a410b0219e18e80d3e305b4d97374c077> (visited on 28/06/2022) (cit. on pp. 66, 67).
- [Kre22] J. Kreit, *Thesis in preparation*, Bachelor thesis: Rheinische Friedrich-Wilhelms-Universität Bonn, 2022 (cit. on p. 97).
- [Tia+] L. Tiator et al., *etaMAID Partial Wave analysis*, URL: <https://maid.kph.uni-mainz.de/eta2018/eta-observ.html> (visited on 15/08/2022) (cit. on p. 99).



# List of Figures

---

1.1	Running coupling of QCD depending on the momentum transfer $Q$ . The colored data points represent different methods to obtain a value for $\alpha_s$ . For a detailed review see [Wor+22].	2
1.2	Calculated nucleon (isospin $I = 1/2$ ) resonances compared to measurements. Left in each column are the calculations [LMP01], the middle shows the measurements and PDG rating [Wor+22]	3
1.3	FEYNMAN diagram for the s-channel photoproduction of pseudoscalar mesons, adapted from [Afz19].	4
1.4	Five different MCMC simulations for a bivariate normal distribution, with starting points marked by black squares. Left: After 50 iterations no convergence is yet to be seen. Middle: After 1000 iterations the chains are closer to convergence. Right: Removing the first halve of simulation draws leaves a set of draws from the target distribution. Taken from [Gel+14]	9
1.5	Randomly generated data with GAUSSIAN noise (errorbars) following the function $y(x) = 1 \cdot \cos(x) + 1$ (red line).	15
1.6	Marginal posteriors of the parameters $\theta_1$ and $\theta_2$ as obtained from MCMC sampling. The histograms represent the posterior draws, the black solid line shows a Kernel-Density-Estimate (KDE) to smooth the distribution. The solid vertical red line shows the most probable value determined from the KDE, while the dashed red vertical lines show a $1\sigma$ interval around the mean $\mu$ . The blue error bars show the results obtained from a $\chi^2$ fit.	16
1.7	Posterior predictive check of the fitted model. For each drawn sample of $\theta$ a random number according to the sampling distribution $p(y \theta)$ is drawn for every predictor $x_i$ . The $p$ value is then determined from the posterior predictive distribution.	17
2.1	Overview of the experimental hall of the CBELSA/TAPS experiment. The electron beam from ELSA enters at the bottom left. M. GRÜNER in [Afz19]	21
2.2	Illustration of the bremsstrahlung process: An electron $e^-$ is deflected in the COLOUMB field of a nucleus in the radiator material. A photon $\gamma$ is emitted and so the momentum $q$ is transferred.	22
2.3	Left: Incoherent (green) and crystal (blue) bremsstrahlung intensities as a function of the photon energy. Right: The enhancement spectrum is given as the ratio of crystal to incoherent intensity spectrum. The dashed line at the bottom shows the calculated polarization degree. Both spectra are generated using ANB calculations. Taken from [Afz19].	23

2.4	The goniometer holds several radiators that can be inserted onto the beam axis (b). Also available is a MØLLER coil with radiator (a) [Wal]. . . . .	24
2.5	Top-down view of the tagging system consisting of dipole magnet (red) and scintillating bars and fibers [For10]. Electrons are deflected by the magnet after the bremsstrahlung process. . . . .	24
2.6	Schematic overview of the liquid hydrogen target. Two tubes connected to a heat exchanger and the Kapton cell allow filling it with liquid hydrogen. M. GRÜNER in [Afz19]. . . . .	25
2.7	The inner detector with three layers of scintillating fibers. The inner two layers are tilted with respect to the outer layer. D. WALTHER in [Afz19]. . . . .	26
2.8	Crystal barrel calorimeter and forward detector are built such that they enclose the target and the inner detector. The forward detector consists of the first three rings (green base) of crystals which are additionally covered by plastic scintillators for charged particle identification. The definition of polar angle $\theta$ and azimuthal angle $\phi$ in the LAB system are indicated as well. D. WALTHER in [Urb17] . . . . .	26
2.9	The MiniTAPS detector is made up of 216 BaF <sub>2</sub> crystals (grey). In front of each crystal, plastic scintillators are mounted for charged particle information. Taken from [Wal]. . . . .	28
2.10	The two detectors FluMo and GIM are used to monitor the photon flux at different reaction rates. D. WALTHER in [Afz19]. . . . .	29
2.11	Comparison of the ANB calculated enhancement spectra (blue) to the measured enhancement spectra (black data points). The right hand side shows the calculated polarization degree. The upper row shows the plots for the coherent edge position at 1750 MeV and the lower row shows the coherent edge position at 1850 MeV. Taken from [Afz19]. . . . .	32
3.1	Distribution of event classes in $\eta' \rightarrow \gamma\gamma$ production . . . . .	35
3.2	Time information of all final state particles and the beam photon for 3PED $\eta'$ production . . . . .	36
3.3	Reaction time $t_r$ for 3PED and 2.5PED $\eta'$ production. The yellow region indicate the sidebands while the purple colored interval is the selected prompt peak. . . . .	37
3.4	Coplanarity of the $p\eta'$ final state with all other cuts applied for the energy bin $1500 \text{ MeV} \leq E_\gamma < 1600 \text{ MeV}$ . The vertical dashed lines show the cut ranges obtained from a gaussian fit to the data (open circles). The solid black histograms represent fitted MC data of $\eta' \rightarrow \gamma\gamma$ . . . . .	41
3.5	Polar angle difference of the $p\eta'$ final state with all other cuts applied for the energy bin $1500 \text{ MeV} \leq E_\gamma < 1600 \text{ MeV}$ . The vertical dashed lines show the cut ranges obtained from a gaussian fit to the data (open circles). The solid black histograms represent fitted MC data of $\eta' \rightarrow \gamma\gamma$ . . . . .	42
3.6	Missing mass of the $p\eta'$ final state with all other cuts applied for the energy bin $1500 \text{ MeV} \leq E_\gamma < 1600 \text{ MeV}$ . The vertical dashed lines show the cut ranges obtained from a fit to data (open circles) employing a Novosibirsk function. The solid colored histograms represent fitted MC data from relevant photoproduction reactions: in black $\eta'$ , in green $\pi^0$ , in red $\eta$ , in blue $\omega$ , in yellow $2\pi^0$ , magenta $\pi^0\eta$ . The turquoise histogram is the sum of all MC histograms. . . . .	43

3.7	Invariant mass of the $p\eta'$ final state with all other cuts applied for all energy and angular bins. The open circles represent the measured data, the solid colored histograms fitted MC data from relevant photoproduction reactions: in black $\eta'$ , in green $\pi^0$ , in red $\eta$ , in blue $\omega$ , in yellow $2\pi^0$ and in magenta $\pi^0\eta$ . The turquoise histogram is the sum of all MC histograms. . . . .	44
3.8	Invariant mass of the $p\eta'$ final state with all other cuts applied for the energy bin $1500 \text{ MeV} \leq E_\gamma < 1600 \text{ MeV}$ . The vertical dashed lines show the cut ranges obtained from a gaussian fit to the $\eta'$ MC data (solid black histogram). The open circles represent the measured data, the solid colored histograms fitted MC data from relevant photoproduction reactions: in black $\eta'$ , in green $\pi^0$ , in red $\eta$ , in blue $\omega$ , in yellow $2\pi^0$ and in magenta $\pi^0\eta$ . The turquoise histogram is the sum of all MC histograms. . . . .	44
3.9	Acceptance for the reaction $\gamma p \rightarrow p\eta'$ after all cuts that have been discussed so far for 2.5PED and 3PED events . . . . .	45
3.10	Fraction of background events in the analyzed beam energy and angular bins. . . . .	46
3.11	Acceptance for possible background contributions . . . . .	47
3.12	Generated energies of $\gamma_3$ and $\gamma_4$ in $2\pi^0$ and $\pi^0\eta$ photoproduction MC data. The threshold of 20 MeV is marked by a vertical red line. $E_{\gamma_4}$ is shown on the top, $E_{\gamma_3}$ is shown on the bottom of each figure. . . . .	49
3.13	$E_\gamma^{\text{gen}}$ vs. $E_\gamma^{\text{rec}}$ of $\gamma_1$ and $\gamma_2$ for $2\pi^0$ (top) and $\pi^0\eta$ (bottom) production. The slope $E_\gamma^{\text{gen}} = E_\gamma^{\text{rec}}$ is marked by a solid line. . . . .	51
3.14	Polar angle difference $\Delta\theta$ between $\gamma_2$ and $\gamma_3$ of the $\pi^0\eta$ final state. . . . .	52
3.15	Illustration of the misidentification process during reconstruction. Enumeration of photons is now arbitrary. . . . .	52
3.16	Generated CMS angle $\cos\theta_{\text{gen.}}$ vs. reconstructed CMS angle $\cos\theta_{\text{rec.}}$ for both background reactions. The slope $\cos\theta_{\text{gen.}} = \cos\theta_{\text{rec.}}$ is indicated by the solid line. . . . .	53
3.17	Detector hits of the recoil proton, as obtained from MC data for the production of $\eta'$ , $2\pi^0$ and $\pi^0\eta$ . CB: Crystal Barrel, FW: forward detector, MT: MiniTAPS . . . . .	55
3.18	Difference in measured and calculated beam energy. Data points are shown as open circles, MC data as solid histograms: in black $\eta'$ , in green $\pi^0$ , in red $\eta$ , in blue $\omega$ , in yellow $2\pi^0$ and in magenta $\pi^0\eta$ . The turquoise histogram is the sum of all MC histograms. . . . .	56
3.19	Invariant mass spectrum passing different stages in the event selection process. In the end clear peaks for all possibly produced mesons are visible. The vertical lines indicate the mean cut ranges over all energy and angle bins. . . . .	57
3.20	Invariant mass spectrum passing different stages in the event selection process. In the end clear peaks for all possibly produced mesons are visible. Taken from [Afz19]. . . . .	58
4.1	Left: Definition of the angles $\alpha, \phi, \varphi$ . Right: Photon momentum $\vec{k}$ and polarization $\vec{\epsilon}$ define the beam polarization plane while the reaction plane is defined by the recoil proton $p$ and produced meson $M$ . . . . .	59

4.2 Posterior predictive checks $p(A_{\text{rep}} A)$ from a BAYESIAN fit to the event yield asymmetries for 12 toy Monte Carlo bins are shown as distributions. The data points in the upper plot are the asymmetry $A(\phi)$ , which was additionally fitted using a $\chi^2$ fit (solid line). The goodness of fit is shown using $p$ -values, which give the fraction $T(A_{\text{rep}} > A)$ of replicated samples greater than the original measured value, with propagated statistical error bars on the bottom of each plot. The expected mean value of $T(A_{\text{rep}} > A) = 0.5$ is indicated by the dashed line.	68
4.3 $p$ values of all toy Monte Carlo bins. They are centered around their mean at 0.5, which is indicated by the dashed line, and show no bias towards higher or lower values, thus confirming an adequate fit.	69
4.4 Left: Combined posterior distributions of all 10000 fits normalized by their respective standard deviation. Right: Unaltered combined posterior distributions of all 10000 fits. A GAUSSIAN fit was performed to determine mean $\mu$ and standard deviation $\sigma$ of the distributions with results given on top.	69
4.5 Left: relative error $\frac{\sigma_{\text{MCSE}}}{\text{median}[p(\Sigma y)]}$ associated with the parameter $\Sigma$ . Right: $\hat{R}$ associated with the fit parameter $\Sigma$ . Both are shown for all 10000 unbinned fits. The critical values that should not be exceeded are marked by dashed lines.	71
4.6 Combined posteriors for the beam asymmetries $\Sigma$ and $\Sigma^{\text{bkg}}$ from all 1000 event based fits. Left: Residuals $\Xi$ Right: Unnormalized posterior distributions. A GAUSSIAN fit is performed on the distributions with results for mean $\mu$ and standard deviation $\sigma$ on top.	72
4.7 Combined posterior probabilities using the <i>pooled likelihood</i> approach. Left: Signal beam asymmetry, Right: background beam asymmetry. Mean and standard deviation as obtained from a Gaussian fit are shown on top	73
4.8 Left: relative error $\frac{\sigma_{\text{MCSE}}}{\text{median}[p(\Sigma y)]}$ associated with the fit parameter $\Sigma$ . Right: $\hat{R}$ associated with the fit parameter $\Sigma$ . Both are shown for all 1000 unbinned fits. The critical values that should not be exceeded are marked by dashed lines.	74
4.9 Posterior predictive check using the draws of the detector coefficients $a$ and $b$ . Points with error bars are the polarization weighted sum of event yields. The dashed line is the mean of the predictive values while the solid opaque lines are representative of one simulation draw $a^{(s)}, b^{(s)}$ .	74
4.10 Posterior predictive checks $p(A_{\text{rep}} A)$ from a BAYESIAN fit to the event yield asymmetries for the reaction $\gamma p \rightarrow p\eta \rightarrow p\gamma\gamma$ for all angular bins of the energy bin $1250 \text{ MeV} \leq E_\gamma < 1310 \text{ MeV}$ . The data points in the upper plot are the asymmetry $A(\phi)$ , which was additionally fitted using a $\chi^2$ fit (solid line). The goodness of fit is shown using $p$ -values, which give the fraction $T(A_{\text{rep}} > A)$ of replicated samples greater than the original measured value, with propagated statistical error bars on the bottom of each plot. The expected mean value of $T(A_{\text{rep}} > A) = 0.5$ is indicated by the dashed line.	76
4.11 $p$ values generated using all fits from all bins in the reaction $\gamma p \rightarrow p\eta \rightarrow p\gamma\gamma$ . They are centered around their mean at 0.5, which is indicated by the dashed line, and show no bias towards higher or lower values, thus confirming an adequate fit.	77

4.12 Left: relative error $\frac{\sigma_{\text{MCSE}}}{\text{median}[p(\Sigma y)]}$ associated with the fit parameter $\Sigma$ . Right: $\widehat{R}$ associated with the fit parameter $\Sigma$ . Both are shown for all $11 \cdot 12$ binned BAYESIAN fits to the asymmetry $A(\phi)$ in $\eta$ photoproduction. The critical values that should not be exceeded are marked by dashed lines. . . . .	77
4.13 Left: relative error $\frac{\sigma_{\text{MCSE}}}{\text{median}[p(\Sigma y)]}$ associated with the fit parameter $\Sigma$ . Right: $\widehat{R}$ associated with the fit parameter $\Sigma$ . Both are shown for all $11 \cdot 12$ unbinned fits in $\eta$ photoproduction. The critical values that should not be exceeded are marked by dashed lines. . . . .	78
4.14 Posterior predictive check using the draws of the detector coefficients $a$ and $b$ for the kinematic bin $1250 \text{ MeV} \leq E_\gamma < 1310 \text{ MeV}, 0 \leq \cos \theta < 0.17$ . Points with error bars are the polarization weighted sum of event yields. The dashed line is the mean of the predictive values while the solid opaque lines are representative of one simulation draw $a^{(s)}, b^{(s)}$ . . . . .	79
4.15 Final results for the beam asymmetry $\Sigma$ in $\eta$ photoproduction off the proton for all kinematic bins obtained with BAYESIAN methods. They are compared with the results of a least squares fit and an unbinned fit as given in reference [Afz19]. All results agree within statistical error bars or within the widths of marginal posterior distributions.	80
4.16 Normalized residuals (left) and unaltered distribution (right) of all 10000 unbinned maximum likelihood fits for the beam asymmetry $\Sigma = (1 - \delta) \cdot \Sigma_1 + \delta \cdot \Sigma_2$ . GAUSSIAN fits are performed with results given on top of each plot. . . . .	83
4.17 Normalized residuals (left) and unaltered distribution (right) of all 10000 unbinned maximum likelihood fits for the background beam asymmetry $\Sigma_t^{\text{bkg}}$ . GAUSSIAN fits are performed with results given on top of each plot. . . . .	84
4.18 Fitted efficiency function (red line) applied to the polarization weighted sum of event yields (data points) for one toy Monte Carlo bin. 12 bins in $\phi$ are built for demonstration.	84
4.19 Combined (added) posteriors of all 1000 unbinned BAYESIAN fits. Left: Signal beam asymmetry $\Sigma_1$ Right: Background beam asymmetry $\Sigma_t^{\text{bkg}}$ . A GAUSSIAN fit is performed with results given on top. . . . .	86
4.20 Combined (added) posteriors of all unbinned BAYESIAN fits for the fit parameter $\Sigma_2^{\text{true}}$ . A GAUSSIAN fit is performed which reproduces exactly the values that were used for the simulations. . . . .	86
4.21 MCMC diagnostics for the event based BAYESIAN fit. Left: MCSE, Right: $\widehat{R}$ -value. The critical values not to be exceeded are marked by the dashed lines. . . . .	87
4.22 Posterior predictive checks of one toy Monte Carlo bin using the draws from the marginal posteriors of the detector coefficients $a, b$ (opaque blue lines). The mean values are marked by the dashed line and follow the distribution of the data points which are the polarization weighted sum of event yields, using 12 $\phi$ bins. . . . .	88
4.23 Final results for the beam asymmetry $\Sigma$ in $\eta'$ photoproduction. Two sets of results are shown: The dark blue distributions and orange data points with errorbars are obtained with an unbinned fit that does not consider any background contributions. The light blue distributions and data points are obtained with the modified BAYESIAN fit and by correcting the point estimates according to Equation (4.42), respectively. All errors are statistical errors only. . . . .	90

---

4.24 Results for the additionally fitted $\Sigma_2^{\text{true}}$ (distributions) compared with the underlying data points [Mah22] with statistical errors. The error bars on average cover $1\sigma$ of the distributions, indicating a successful fit. All errors are statistical errors only. . . . .	91
4.25 MCMC diagnostics for the event based BAYESIAN fit. Left: MCSE, Right: $\widehat{R}$ -value. The critical values not to be exceeded are marked by the dashed lines. . . . .	91
4.26 Posterior predictive checks of the kinematic bin $1700 \text{ MeV} \leq E_\gamma < 1800 \text{ MeV}, 0.67 \leq \cos \theta < 1$ using the draws from the marginal posteriors of the detector coefficients $a, b$ (opaque blue lines). The mean values are marked by the dashed line and follow the distribution of the data points which are the polarization weighted sum of event yields, using 12 $\phi$ bins. . . . .	92
4.27 Final results for the beam asymmetry $\Sigma_{\eta'}$ for all energy and angular bins. Only the corrected results from the unbinned maximum likelihood fit and distributions from the modified BAYESIAN fit are shown. The bottom of each plot indicates the systematic error as gray bars. It was determined as previously discussed. . . . .	94
5.1 Results for the beam asymmetry $\Sigma_{\eta'}$ (orange errorbars and distributions) compared with the results for the energy bins $E_\gamma = 1569 \text{ MeV}, E_\gamma = 1676 \text{ MeV}, E_\gamma = 1729 \text{ MeV}$ reported in reference [Col+17] (black errorbars). Systematical errors are shown as grey bars. . . . .	96
5.2 Results for the beam asymmetry $\Sigma_{\eta'}$ (orange errorbars and distributions) compared with PWA solutions: etaMAID [Tia+18; Tia+] (dashed black line) and BnGa [Ani+18] (dashed red line). The errorbars only depict statistical error, the systematic error is shown as grey bars. . . . .	99
5.3 Different resonance contributions to all eight single and double polarization observables as predicted by etaMAID [Tia+18] and Bonn-Gatchina [Ani+18] PWA solutions near the $\eta'$ production threshold. Taken from [Tia+18]. . . . .	100
A.1 Example .xml file that was used to call the plugin CBTetaprimeanalysis.cpp (line 20) with several self defined options. . . . .	105
A.2 Example .stan file that can be used to perform a simple linear fit. . . . .	106
B.1 Coplanarity $\Delta\phi$ for all energy and angular bins. Data points are displayed as open circles, scaled Monte Carlo data belonging to $\eta'$ photoproduction is displayed as solid histogram. The determined cut ranges are indicated by the dashed red lines. . . . .	109
B.1 Coplanarity $\Delta\phi$ for all energy and angular bins. Data points are displayed as open circles, scaled Monte Carlo data belonging to $\eta'$ photoproduction is displayed as solid histogram. The determined cut ranges are indicated by the dashed red lines. . . . .	110
B.2 Polar angle difference $\Delta\theta$ for all energy and angular bins. Data points are displayed as open circles, scaled Monte Carlo data belonging to $\eta'$ photoproduction is displayed as solid histogram. The determined cut ranges are indicated by the dashed red lines. . . . .	111
B.2 Polar angle difference $\Delta\theta$ for all energy and angular bins. Data points are displayed as open circles, scaled Monte Carlo data belonging to $\eta'$ photoproduction is displayed as solid histogram. The determined cut ranges are indicated by the dashed red lines. . . . .	112

B.3 Missing mass $m_x$ for all energy and angular bins. Data points are displayed as open circles, scaled Monte Carlo data belonging to $\eta'$ (black), $2\pi^0$ (yellow) and $\pi^0\eta$ (magenta) photoproduction is displayed as solid histogram while their sum is displayed as turquoise histogram. The determined cut ranges are indicated by the dashed red lines.	113
B.3 Missing mass $m_X$ for all energy and angular bins. Data points are displayed as open circles, scaled Monte Carlo data belonging to $\eta'$ (black), $2\pi^0$ (yellow) and $\pi^0\eta$ (magenta) photoproduction is displayed as solid histogram while their sum is displayed as turquoise histogram. The determined cut ranges are indicated by the dashed red lines.	114
B.4 Invariant mass $m_{\text{meson}}$ for all energy and angular bins. Data points are displayed as open circles, scaled Monte Carlo data belonging to $\eta'$ (black), $2\pi^0$ (yellow), $\pi^0\eta$ (magenta), $\pi^0$ (green) and $\omega$ (blue) photoproduction is displayed as solid histogram while their sum is displayed as turquoise histogram. The determined cut ranges are indicated by the dashed red lines.	115
B.4 Invariant mass $m_{\text{meson}}$ for all energy and angular bins. Data points are displayed as open circles, scaled Monte Carlo data belonging to $\eta'$ (black), $2\pi^0$ (yellow), $\pi^0\eta$ (magenta), $\pi^0$ (green) and $\omega$ (blue) photoproduction is displayed as solid histogram while their sum is displayed as turquoise histogram. The determined cut ranges are indicated by the dashed red lines.	116
C.1 Fit performance in dependence of the number of bins. Left axis shows the mean $\mu$ of the distribution of the normalized residuals $\xi$ , right axis shows the mean $\chi^2$ of all fits. Squares simulate fits with statistics similar to the $\gamma p \rightarrow p\eta' \rightarrow p\gamma\gamma$ final state, triangles statistics similar to the $\gamma p \rightarrow p\eta \rightarrow p\gamma\gamma$ and final state, pentagons statistics similar to the $\gamma p \rightarrow p\pi^0 \rightarrow p\gamma\gamma$ . Dotted red line indicates the ideal value of $\chi^2 = 1$ , while the dashed blue line indicates the ideal mean of the normalized residuals at $\mu = 0.1$	118
D.1 Combined posteriors of all 1000 fits without truncation for the signal beam asymmetry $\Sigma_1$ and the background beam asymmetry $\Sigma_t$ . Left: normalized residuals $\Xi$ , Right: unaltered added posterior distributions. GAUSSIAN fits have been performed with results given on top of each plot.	120
D.2 Posterior distributions of $\Sigma_1$ (left) and $\Sigma_t$ (right) combined in an independent likelihood pool. GAUSSIAN fits to the distribution confirm the reproduction of the input values within $1\sigma$ . Note that only very few datapoints were available for the fits, because the distributions overwhelmingly converge into a single bin at $\pm 0.5$ , hence the large errors on the fit parameters.	121



# List of Tables

---

1.1	Summary of the particles of the SM . . . . .	1
1.2	Allowed quantum numbers for the intermediate resonance state $N^*$ in $\eta/\eta'$ -photoproduction. Adapted from [Afz19]. . . . .	5
1.3	All 16 non redundant polarization observables in pseudoscalar meson photoproduction [San+11]. Table adapted from [Afz12]. . . . .	6
1.4	Key differences between BAYESIAN statistics and Frequentist statistics, contents taken from [BC16]. . . . .	18
2.1	Summary of the key parameters of the 2013 beam time at CBELSA/TAPS taken for the measurement of the beam asymmetry $\Sigma$ . Taken from [Afz19]. . . . .	31
3.1	The five most probable decay modes of the $\eta$ and $\eta'$ meson. The most probable further decay with according branching ratio is shown in brackets.[Wor+22] . . . . .	33
3.2	Examined MC reactions that were used in sum for the fit . . . . .	39
3.3	Fit functions and cut ranges for each kinematic variable . . . . .	40
3.4	Total cross sections $\sigma$ in the energy range 1500 to 1800 MeV, branching ratios (BR) to $n\gamma$ final states, maximum acceptance $\tilde{A}$ for signal and possible background contributions as well as the expected signal to background ratio $R$ . References [Die+20] and [Käs+18] give the cross sections only up to roughly 1500 MeV, the given values are thus upper bounds. For the same reason, from reference [Sta+11] only a lower bound can be estimated. For all other reactions a rough mean over the energy bins of interest is built. If the references provide only differential cross sections a crude integration in each angular bin is performed. In case only very few ( $O(10^1)$ ) decays pass event selection, the acceptance is built in one global bin only for the respective reactions. This is indicated by the horizontal line. . . . .	48
3.5	Relative loss in signal and background events if a cut on $\Delta E$ is applied. . . . .	54
4.1	Summary of the complete setting of all toy Monte Carlo experiments for the event based fit. Values and table layout adapted from [Afz19]. . . . .	71
4.2	Summary of the complete setting of all toy Monte Carlo experiments for the event based fit. Table layout adapted from [Afz19]. . . . .	82